The Dissertation Committee for Javad Behseresht Certifies that this is the approved version of the following dissertation:

Physical Controls on Hydrate Saturation Distribution in the Subsurface

Committee:

Steven L. Bryant, Supervisor

Marc A. Hesse

Kishore K. Mohanty

Maša Prodanović

Mukul M. Sharma

Physical Controls on Hydrate Saturation Distribution in the Subsurface

by

Javad Behseresht, B.P.E.; B.S.E.E.; M.S.E.

Dissertation

Presented to the Faculty of the Graduate School of

The University of Texas at Austin

in Partial Fulfillment

of the Requirements

for the Degree of

Doctor of Philosophy

The University of Texas at Austin

December 2012

Dedication

To the best parents ever

***Z*ahra and *A*vaz**

And to my lovely wife

***S*aeedeh**

For their endless love, support and encouragement

Acknowledgements

I would like to thank all those who made this dissertation possible.

I am especially grateful to my advisor Dr. Steven L. Bryant for his invaluable advices and all his guidance throughout this project. He was always supportive, encouraging and willing to share his ever more fascinating ideas which were crucial to the success of this work. I am particularly thankful for the collaborative environment and numerous opportunities he gave me to present my work in several conferences and to the audience in the community. I must thank also the members of my dissertation committee, Dr. Hesse, Dr. Mohanty, Dr. Prodanović and Dr. Sharma for their sound advices and inputs towards the completion of this work. Financial support of this research by the department of energy is greatly appreciated.

I am also grateful to Glen Baum, Roger Terzian, Frankie Hart and Gary Miscoe for their day-to-day support to facilitate our academic life. I would also like to extend my gratitude to Joanna Castillo for her assistance with conference posters and presentations in several occasions.

I am indebted to many of my friends and colleagues who shaped this dissertation in many ways through their instructive and fruitful discussions. Specifically I would like to thank Mohsen Rezaveisi and Aboulghasem Kazeminia for their indispensable help and knowledge sharing about numerical modeling of convection-diffusion phenomena. I am very grateful to my wife, Saeedeh, who patiently spent countless hours on helpful technical discussions with me in different stages of this work. I also enjoyed technical discussions with my colleagues Mohammad Mirzaei, Mahdi Shirdel, Abdoljalil Varavei, Christopher Blyton and Yao Peng. I would like to thank my awesome friends Amir

Frooqnia, Mohsen Rezaveisi, Aboulghasem Kazeminia, Rohollah Abdollahpour, Elena Rodriguez, Mehdi Haghshenas, Babak Fallahazad, Ali Moinfar, Mahdi Shirdel, and AmirReza Rahmani, whose moral support has been critical along my graduate studies, as well as Saeid Enayatpour, Ali Naderi, Ali Afsharpour, Rouzbeh Ghanbarnezhad, Siyavash Motealleh, Ali Goudarzi, Soheil Ghanbarzadeh, Mohammad Lotfollahi, Mohsen Taghavaifar, Hamed Darabi and many others whom I did not cite explicitly. Finally, I would like to express my highest gratitude to my lovely wife Saeedeh who was always caring, supportive and patient with my long work hours.

Physical Controls on Hydrate Saturation Distribution in the Subsurface

Javad Behseresht, Ph.D.

The University of Texas at Austin, 2012

Supervisor: Steven L. Bryant

Many Arctic gas hydrate reservoirs such as those of the Prudhoe Bay and Kuparuk River area on the Alaska North Slope (ANS) are believed originally to be natural gas accumulations converted to hydrate after being placed in the gas hydrate stability zone (GHSZ) in response to ancient climate cooling. A mechanistic model is proposed to predict/explain hydrate saturation distribution in "converted free gas" hydrate reservoirs in sub-permafrost formations in the Arctic. This 1-D model assumes that a gas column accumulates and subsequently is converted to hydrate. The processes considered are the volume change during hydrate formation and consequent fluid phase transport within the column, the descent of the base of gas hydrate stability zone through the column, and sedimentological variations with depth. Crucially, the latter enable disconnection of the gas column during hydrate formation, which leads to substantial variation in hydrate saturation distribution. One form of variation observed in Arctic hydrate reservoirs is that zones of very low hydrate saturations are interspersed abruptly between zones of large hydrate saturations. The model was applied on data from Mount Elbert well, a gas hydrate stratigraphic test well drilled in the Milne Point area of the ANS. The model is consistent with observations from the well log and interpretations of seismic anomalies in the area. The model also predicts that a considerable amount of fluid (of order one pore volume of gaseous and/or aqueous phases) must migrate within

or into the gas column during hydrate formation. This work offers the first explanatory model of its kind that addresses "converted free gas reservoirs" from a new angle: the effect of volume change during hydrate formation combined with capillary entry pressure variation versus depth.

Mechanisms by which the fluid movement, associated with the hydrate formation, could have occurred are also analyzed. As the base of the GHSZ descends through the sediment, hydrate forms within the GHSZ. The net volume reduction associated with hydrate formation creates a “sink” which drives flow of gaseous and aqueous phases to the hydrate formation zone. Flow driven by saturation gradients plays a key role in creating reservoirs of large hydrate saturations, as observed in Mount Elbert. Viscous-dominated pressure-driven flow of gaseous and aqueous phases cannot explain large hydrate saturations originated from large-saturation gas accumulations. The mode of hydrate formation for a wide range of rate of hydrate formation, rate of descent of the BGHSZ and host sediments characteristics are analyzed and characterized based on dimensionless groups. The proposed transport model is also consistent with field data from hydrate-bearing sand units in Mount Elbert well. Results show that not only the petrophysical properties of the host sediment but also the rate of hydrate formation and the rate of temperature cooling at the surface contribute greatly to the final hydrate saturation profiles.

Table of Contents

List of Tables

List of Figures

Chapter 1: Introduction

Natural gas is known to be the premium energy resource for this century for two main reasons: (i) gas burns cleanly and produces less carbon dioxide, compared to oil or coal and (ii) as liquid fuels are better used as raw materials for generating petrochemicals, many fuel-consumer devices are converted into natural gas dependent devices (Sloan, 2003). Examples of the latter are gas burning cars and gas-fired power plants that are newly introduced to the market. In addition to the recently found unconventional gas shale resources, such as huge shale gas reservoirs in the North America, there are areas containing abundant untapped reserves of gas. These areas include deep ocean sediments with much higher pressure and Arctic sediments with much lower temperatures than used to be encountered in conventional gas reservoirs. However, in such unusual temperature and pressure conditions natural gas, in the presence of water, will tend to exist as non-flowing crystalline solids called gas hydrates (Sloan, 2003).

Prospecting for gas hydrates as a resource has only recently begun to adopt the perspective of exploring for petroleum systems (Collett et al., 2009). This approach uses different types of information, such as geophysical and geologic data, to detect a source of methane gas, locate migration pathways through which methane gas was transported to the hydrate stability zone, a resource-grade unit (e.g. coarse-grained sands) to host natural gas hydrate within the stability region, and in some cases a structural or stratigraphic seal/trap for the hydrate-bearing unit (Ruppel, 2011). The petroleum systems approach for inferring the gas hydrate distribution in the subsurface sediments was originally proposed and applied to permafrost-associated hydrate settings above conventional hydrocarbon reservoirs on the Alaskan North Slope (Hunter et al., 2004) and the Canadian Beaufort's Mackenzie Delta (Osadetz and Chen, 2004).

1.1) WHAT ARE GAS HYDRATES?

Clathrates of natural gas (Gas hydrates) are crystalline ice-like compounds that form from gas molecules caged in a lattice of water molecules (Sloan, 1998). Gas hydrates are formed at low temperatures and generally high pressures (e.g. temperatures below 25˚C and pressures greater than 1.5 MPa for natural gas hydrates) which are typical of relatively shallow depths in oceanic sediments (Koh et al., 2002; Kvenvolden, 1988) or deeper sediments in the Arctic (Collett, 1993).

Gas hydrates are generally divided into three groups of structures: (i) structure I, (ii) structure II and (iii) structure H. Cubic structure I hydrates are the most common among naturally occurring gas hydrates (Koh et al., 2002) and contains small, i.e. 0.4-0.55 nm, guest molecules (Sloan, 2003). Cubic structure II, however, occurs in mostly man-made environments with generally larger guest molecules, i.e. 0.6-0.7 nm. Finally, hexagonal structure H occurs only with mixture of large, i.e. 0.8-0.9 nm, and small guest

gas molecules and are found in both natural and man-made environments (Sloan, 1998). Each structure is composed of unit cages of host water molecules, known as “cavity” and each cavity is described by a combination of numbers such as 5^x6^y. The latter nomenclature indicates a water cage composed of x pentagonal and y hexagonal faces. Sloan (2003) has neatly summarized the main three structures of methane hydrate (Fig. 1-1). The structure of the water lattice depends on the size of the “guest” gas molecule or gas composition (Koh et al., 2002). For example, as shown in Fig. 1-1, small molecules such as methane and carbon dioxide tend to form structure I hydrate composing of two 5^{12} and six $5^{12}6^2$ cages and a total of 46 water molecules. Considering the anecdotal occurrence of type H hydrates, most hydrate science, and thus applications, focuses on type I and type II gas hydrates (Sloan, 1998). In this dissertation we mainly consider type I hydrates due to their predominance in the Earth’s natural environment. The proposed model, however, is conveniently extendable to type II hydrates as well.

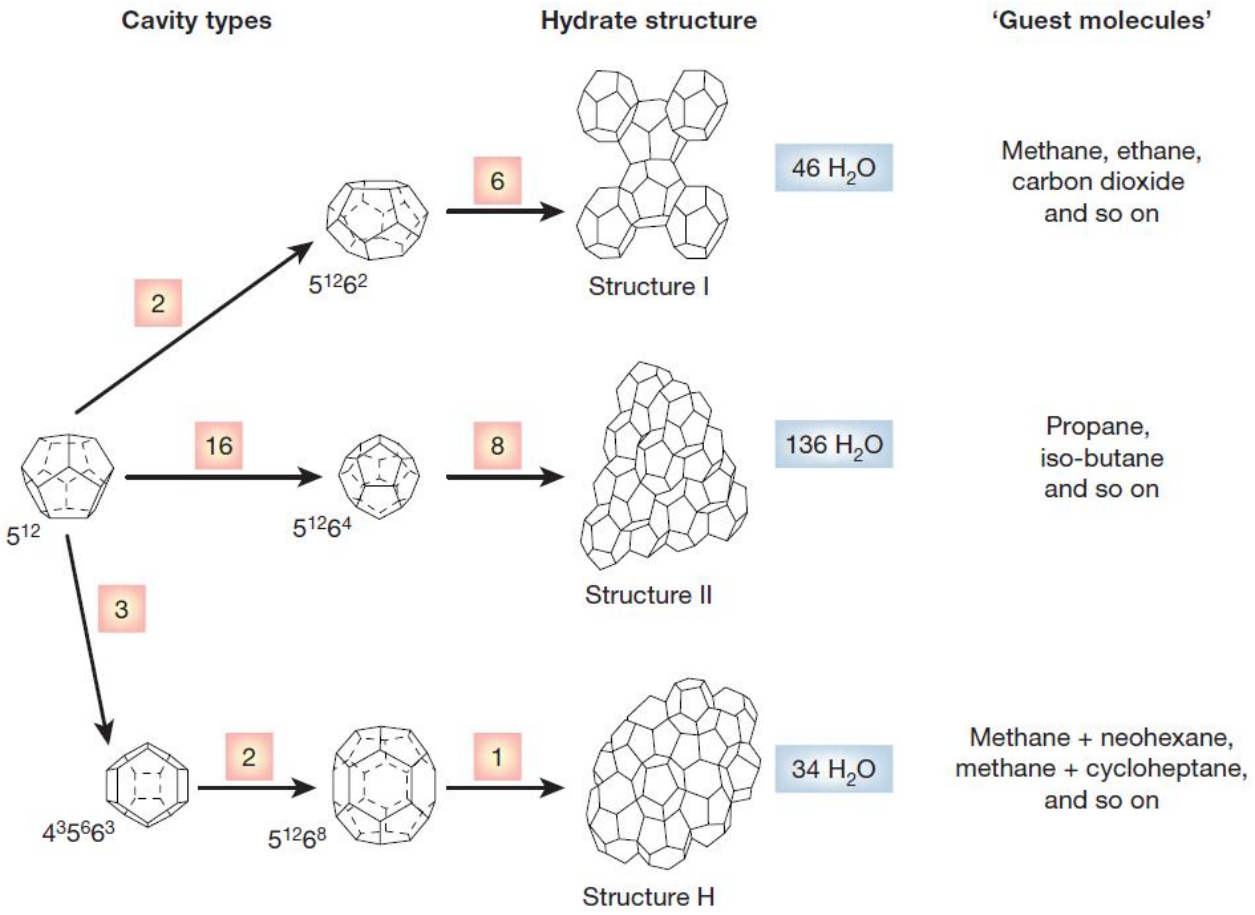

Fig. 1-1-Three main hydrate structures (I, II and H) are shown. Nomenclature: $5^{12}6^2$ shows a cage of water with 12 pentagonal and two hexagonal faces. The numbers in red squares show the number of each type of cage constructing a hydrate structure (Sloan, 2003).

Methane hydrates are considered the most important type of natural gas hydrate based on their global volumetric extent as well as their areal distribution (Ruppel, 2011).

1.2) IMPORTANT IMPLICATIONS OF GAS HYDRATES

There are many well-known applications, and thus motivations, for hydrate research and engineering. In this section a brief overview of some of these applications,

including energy recovery, geohazards, climate change, gas transportation and storage as well as flow assurance are presented. Each of the aforementioned applications is a result of some key physical properties that hydrates exhibit. For example, as mentioned earlier, hydrates are solid and their densities are greater than typical hydrocarbon fluids, i.e. gas and oil. The latter has practical implications for flow assurance and safety in pipelines. Moreover, the fact that hydrates concentrate their guest molecules leads to some other applications such as hydrates serving as potential in situ source of energy, or hydrates being used in transporting stranded gas or hydrates may be part of the reason behind climate change (Sloan, 2003). Some of these applications and implications are briefly discussed here.

1.2.1) Flow Assurance

Probably the most important and urgent consideration of hydrates is in the flow assurance of oil and gas pipelines. All hydrocarbon-producing wells produce an amount of undesirable water which may be combined with hydrocarbons that are in hydrate guest-size range if the flowing mixed phases are cooled enough. Considering that hydrates are non-flowing solid compounds hydrate formation in oil and gas pipelines plugs transmission lines and could lead to costly production stoppages (Sloan, 2003).

In order to avoid pipeline blockage, the flowing phases, containing undesired water, should be maintained outside the hydrate stability pressure-temperature window. However, many of the transmission pipelines are well within hydrate-formation window owing to (i) the low temperatures, such as the deep sea floor temperature of typically 277 K, and (ii) the commission for operating at high pressure to achieve economic energy densities (Sloan, 1998). This unfortunate situation, in turn, calls for hydrate-inhibition methods.

A well adopted hydrate-inhibition method for providing flow assurance in energy industry is injecting hydrogen-bonding fluids, such as alcohols, in relatively large concentrations into the flowing phases at the wellhead. The injected inhibitor fluids would then compete with solid-phase hydrates for the available water and, in effect, shift the hydrate stability zone towards colder temperatures and higher pressures. More recent types of hydrate inhibitors are also available, such as kinetic inhibitors and anti-agglomerates, which are rapidly being adopted in the oil and gas industry (Mehta et al., 2003; Sloan, 2003).

1.2.2) Safety

Another key issue associated with the presence of hydrates in pipelines is to ensure hydrate safety and prevent the annual loss of lives and properties. This problem is mainly caused by the density of hydrates, with a specific gravity of about 0.9, being larger than that of typical hydrocarbon fluids, with a specific gravity of about 0.8 (Sloan, 1998).

When hydrates in pipelines start dissociating, they first detach from the pipe walls and thus start traveling at high speeds, measured at 300 km hr^{-1}, through the pipe. This event would make the downstream gas compressed and leads to pipeline blowouts (Sloan, 2000).

Another safety issue regarding hydrates arises when pipelines are locally heated in order to dissociate the hydrates. Very often the released gas is contained by the end of the hydrate plug until the pressure becomes too high and thus bursts the pipeline (Sloan, 2000). This safety issue is the result of a key property of gas hydrates-the ability of

hydrates to compress substantial amounts of gas in hydrate form. This capability, on the other hand, accompanies some prizes and useful implications.

1.2.3) Energy Recovery-The Prize

The energy density in gas hydrates is almost the same as that of a compressed gas owing to the fact that guest gas molecules are separated almost 0.5 nm by water cages. As a result, a cubic meter of methane hydrate would contain almost 0.8 m^3 of water and more than 160 m^3 of methane at standard temperature and pressure. Clathrates energy density, however, is still less than the energy density of liquefied natural gas (Sloan, 2003).

A large fraction of the Earth's hydrocarbon fuel is stored in clathrate hydrates. Estimates of the size of these hydrocarbon pools suggest that the amount of methane trapped in hydrates is almost 300 times that in conventional US reserves (Sloan, 1998). Globally, the most well accepted estimates (Kvenvolden, 1988) suggest that the amount of energy stored in the form of hydrate is twice that stored in other fossil fuels, including oil, gas and coal, combined. However, despite the substantial increase in data regarding gas hydrate occurrence along with more elaborate numerical modeling, the estimates of the amount of methane locked up in the form of hydrate has been varying over the past decade (Ruppel, 2011), ranging from 1.4 to 1.7×10^7 TCF (Buffett and Archer, 2004; Milkov, 2004) to 4.2×10^6 TCF (Klauda and Sandler, 2003). Most recently, Boswell and Collett (2011) concluded that a more reasonable figure for the amount of methane trapped in the form of hydrate would be 10^5 TCF. In any case, all these estimates are too huge to be ignored, especially compared to other gas reserves in conventional and unconventional resources, and thus suggest methane hydrates as a promisingly vast

energy resource. Yet, almost 10% of the aforementioned estimates of gas in place (GIP), being the amount of methane trapped in resource-grade deposits, is believed to ever produce commercial quantities of gas (Ruppel, 2011).

Majority of the estimates of gas hydrates have originated from indirect seismic observations which use a bottom simulating reflector (BSR). BSR is used as an indication of the base of a hydrate-bearing interval in the subsurface. These indications, however, are not always reliable as in many occasions hydrates occur without exhibiting bottom simulating reflections or BSR does not indicate the presence of hydrate (Sloan, 2003). Fig. 1-2 reflects the global reserves of natural gas hydrates where solid circles show the inferred hydrate bearing sites, e.g. through detecting a BSR. As expected, majority of the hydrate bearing zones are offshore along the continental margins and on shore in the Arctic where the right combination of pressure and temperature, appropriate for hydrate to form and be stable, is more plausible.

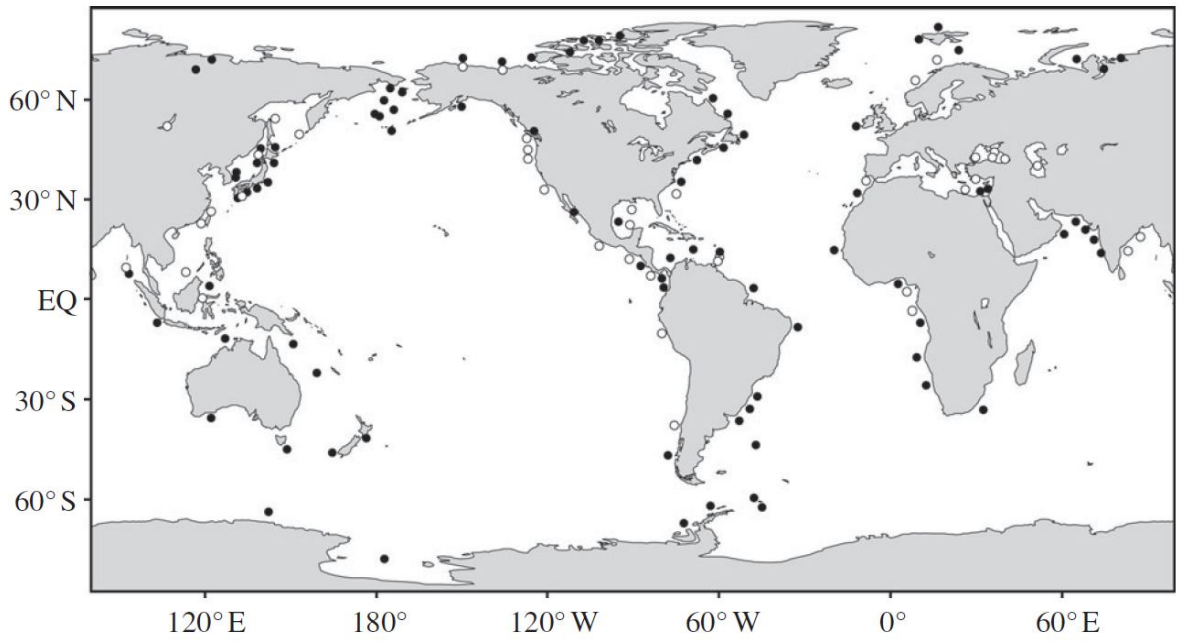

Fig. 1-2-Global map of identified gas hydrate reserves. Solid circles represent locations at which hydrate reserves were inferred, e.g. based on presence of a BSR, while hollow circles indicate the hydrate reserves from which hydrate-bearing cores were actually retrieved (Maslin et al., 2010).

Most of the global natural hydrate resources are biogenic (Sloan, 1998), i.e. the guest gas molecules originated from degraded plants and animal matters buried in the sea floor at low temperatures over geologic time. Along with biogenic-sourced hydrates there are abundant evidences of hydrates with thermogenic deeper gas sources like those observed in Gulf of Mexico (Milkov and Sassen, 2002) or Caspian Sea (Soloviev et al., 1987). Also many of the Arctic terrestrial hydrate reservoirs such as those of the Alaskan North Slope are also believed to have a thermogenic source of gas (Collett, 1993).

1.2.4) Climate Change

The importance of gas hydrates in the global climate systems has only been realized in the last two decades. For example, as recently reported by Kennett et al. (2003) as little as 15,000 years ago release of methane from methane hydrates caused a significant increase in global temperature, i.e. global warming (Kennett et al., 2003). This Late Quaternary climate change scenario is also called '*the hydrate gun hypothesis*' (Sloan, 2003).

A similar, but less controversial, hypothesis suggests that an ancient (about 55.5 million years ago) 4 to 8˚C temperature rise over a short period of time (1000 years), known as the *Late Palaeocene Thermal Maximum* (LPTM), might be explained by a massive oceanic release of methane from methane hydrates (Dickens et al., 1997, 1995; Kaiho et al., 1996).

The aforementioned hypotheses are just two of many ongoing hypotheses regarding the active role of methane hydrates in the global climate change. The global climate changes are not, however, all triggered by methane hydrates. A reverse process can potentially take place meaning that global warming could trigger a massive methane release from hydrate accumulations.

1.2.5) Geohazards

As mentioned earlier gas hydrates are generally stable under high pressures and low temperatures. Therefore, gas hydrates can act as a serious geohazards in the near future owing to global warming and its consequent effect on the stability of both marine and terrestrial gas hydrate deposits. Notwithstanding, it is not yet certain whether the future global warming would cause a significant methane release (Maslin et al., 2010).

The reason for this uncertainty is that the heat conductance through marine sediments could be a slow enough process to allow for a new equilibrium state for methane hydrates with minor amounts of gas escaping.

Models of the global inventory of hydrates and trapped methane bubbles show that a global warming of 3˚C can release huge amounts, in the range of 35 to 940 GtC, of carbon. This substantial amount of carbon can, in turn, add an additional 0.5˚C to the global temperature (Maslin et al., 2010).

The global warming is believed to be more severe in permafrost areas with temperature increases of over 12˚C predicted for major parts of North America and Northern Asia. Therefore, the gas hydrate destabilization in permafrost areas is even more certain than that in marine systems. Besides, as ice sheets in Antarctic and Greenland shrinks due to global warming, the coastal regions and close-by continental slopes would rise through isostacy. Consequently, the hydrostatic pressure would decrease and this reduction in pressure can potentially lead to massive slope failure and boost the risk of tsunamis (Maslin et al., 2010).

1.2.6) Gas Storage and Transportation

Owing to the ability of hydrate in condensing and storing a huge amount of gas, Gudmundsson and Borrehaug (1996) suggested that it is economically feasible to transport stranded gas in the form of gas hydrate (Gudmundsson and Børrehaug, 1996). However, there are still debates on whether gas hydrates can act as an economic means of gas transportation. Mannel and Puckett (2008) performed thorough investigation of several designs for the production, shipping, and regasification of natural gas hydrates. Their studies suggest that natural gas hydrates are economically less favorable than LNG

for natural gas transportation primarily owing to the lower energy density of natural gas hydrates compared to LNG. They emphasized, however, that gas hydrates are economically feasible for natural gas storage due to the lower costs of natural gas hydrates synthesis compared to that for LNG.

1.3) HABITATS OF NATURAL GAS HYDRATES

As mentioned in section (1.2.3) all the inferred and recovered hydrate reserves are generally limited to either offshore area along the continental margins or in the Arctic regions below the permafrost. Boswell and Collett (2006) proposed the hydrate resource pyramid, shown in Fig. 1-3, capturing the distribution of locked up methane among major types of methane hydrate habitats (Boswell and Collett, 2006). The pyramid also shows that only a small portion of the global hydrate reserves is likely to be considered as an economically feasible gas resource. Moreover, this pyramid reflects the probable chronology for developing these major hydrate habitats as energy resource.

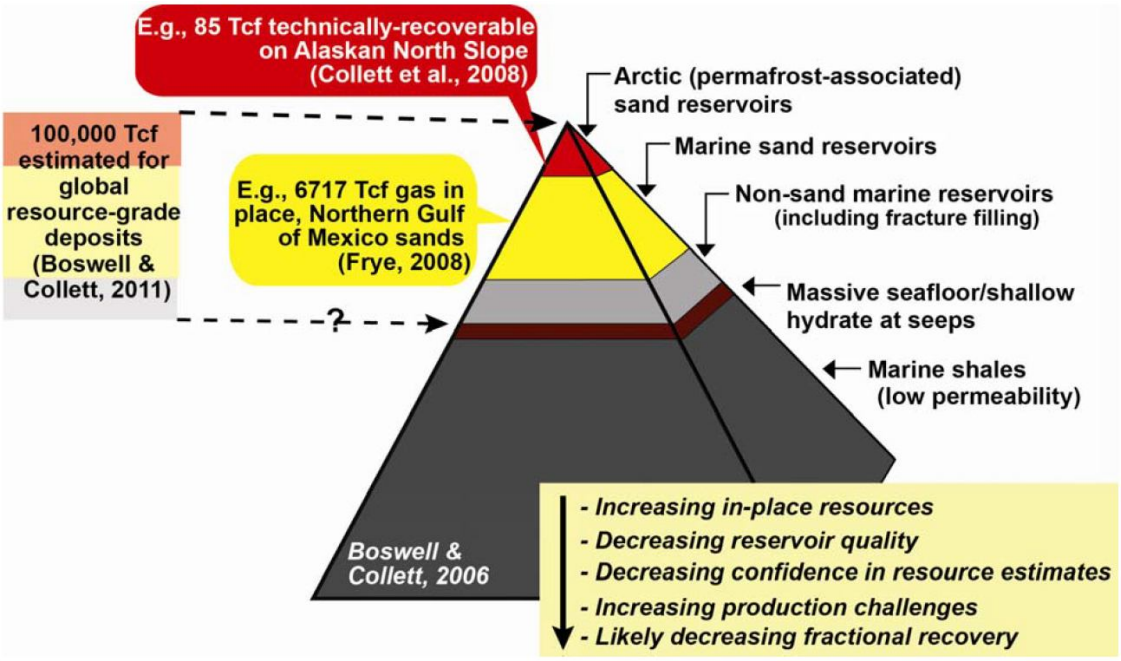

Fig. 1-3- Hydrate resource pyramid originally proposed by Boswell and Collett (2006) categorizing different habitats for the natural gas hydrates around the globe. This figure is modified by Ruppel (2011).

In deep ocean sediments hydrates occur in various morphologies (Sloan, 1998; Waite et al., 2009). Hydrates have been observed as disseminated grains filling pores (Dallimore and Collett, 2005; Fujii et al., 2008) and as complex networks of filled fractures and veins in fine grained sediments (Hadley et al., 2008; Holland et al., 2008). Beneath the Indian Ocean (offshore India) most of the recovered gas hydrate was found to exist in “combination reservoirs”, characterized as either pore-filling grains or as fracture-filling (in clay dominated sediments) (Collett et al., 2009).

In the Arctic such as Alaska’s North Slope (ANS), strata several meters thick, containing large saturations (65%-75%) of gas hydrate are often separated by layers of varying thickness that contain little or no hydrate (Boswell et al., 2011). In addition, gas

hydrates in permafrost regions have been commonly reported to occur with pore-filling morphology in sand-rich sediments (Dallimore and Collett, 2005).

In the following, each of these two major hydrate-bearing settings is discussed in more detail based on the hydrate resource pyramid shown in Fig. 1-3.

1.3.1) Arctic sand reservoirs

The smallest portion of the above pyramid, at the top, represents the volume fraction of global natural gas hydrates which is located in the Arctic permafrost-associated areas. Notwithstanding the small proportion of permafrost-associated gas hydrates, these settings are believed to be the first to be commercialized for gas production. To date, the permafrost-associated settings are the only locations where gas production from dissociating hydrate in the subsurface has been documented (Ruppel, 2011). Examples of short-term, i.e. several days, gas production from these settings are the production tests carried out in the Mackenzie Delta area of Canada at the Mallik well in 2002 and 2007 (Dallimore and Collett, 2005; Hancock et al., 2005; Kurihara et al., 2008; Takahisa, 2005), on the Alaskan North Slope at the Mount Elbert well in 2008 (Hunter et al., 2011) and the CO_2 injection test in the Prudhoe Bay area on the Alaskan North Slope in spring 2012 (Schoderbek and Boswell, 2011). It is worth mentioning that hydrates in the subpermafrost sediments often exhibit pore-filling morphologies. Fig. 1-4 shows a hydrate-bearing core recovered from the Mallik well in which Hydrates are clearly visible in between the sand grains as white materials.

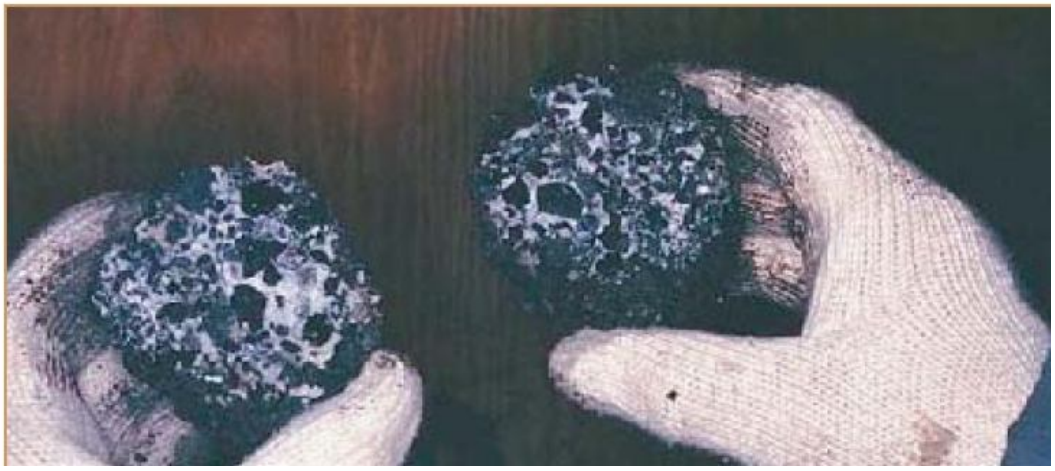

Fig. 1-4- A core extracted from a hydrate-bearing interval at the Mallik well in Mackenzie Delta, Canada. Gas hydrates are clearly visible in white color in between sand grains (Geological Survey of Canada).

Fig. 1-5 shows the gas hydrate stability region for a typical permafrost-associated setting. The hydrate stability region is the region to the left of the phase boundary (red curve) where the geotherm (blue curve) is cooler than the temperature of the phase boundary. As specified on the figure, the gas hydrate within the sediment is stable from within the bottom part of the permafrost and extends hundreds of meters down from the base of the permafrost. It is important to note that this figure merely specifies where gas hydrates can be stable and does not give any information regarding where hydrates actually occur in the subsurface. In fact, this figure represents an ideal situation for hydrate formation, that is both gas and water are present so that gas hydrates would occur where the pressure, temperature and other relevant conditions, such as salinity, are appropriate.

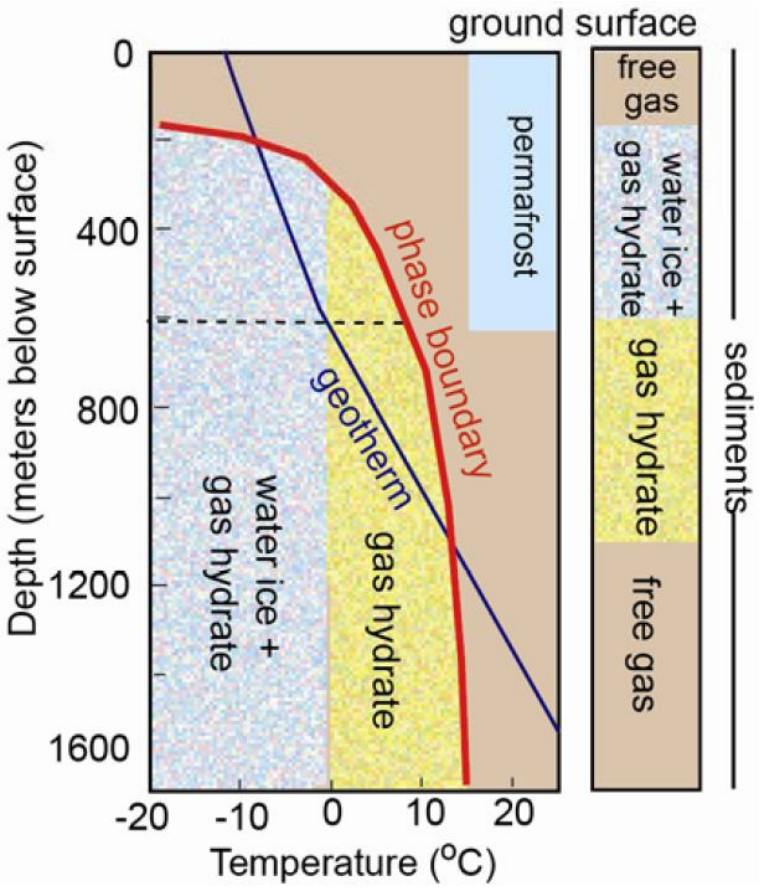

Fig. 1-5- The stability region for natural gas hydrate, i.e. area to the left of the red phase boundary, for permafrost-associated settings. This diagram shows the region where gas hydrates are stable, but does not necessarily reflect where hydrates actually occur in nature. For a typical permafrost geothermal gradient, hydrates are theoretically stable from the bottom part of the permafrost-bearing sediment and extend down to several hundred meters below the permafrost (Ruppel, 2011).

The geothermal gradient in permafrost-associated area is generally much lower than that in marine systems. For example, a typical temperature gradient within the permafrost is about 1.3˚C per 100 m and this gradient would be about 2˚C per 100 m in sediments below the permafrost. It is worth mentioning that the ambient temperature and the thickness of the permafrost-bearing sediment are of supreme importance in determining the hydrate stability depth range (Maslin et al., 2010). Fig. 1-6 highlights the

hydrate stability depth range for two cases with different depths of permafrost base. In case 1, the base of permafrost is at depth 100m and thus the geotherm temperature is estimated to be always warmer than the temperature at the phase boundary. Therefore, there is no place at which the physical condition is appropriate for hydrate formation. In case 2, however, since the base of permafrost is at a deeper depth, i.e. 750 m, a part of the geotherm falls well within the hydrate stability region and thus the depth interval highlighted in thick gray color is where hydrate can be stable.

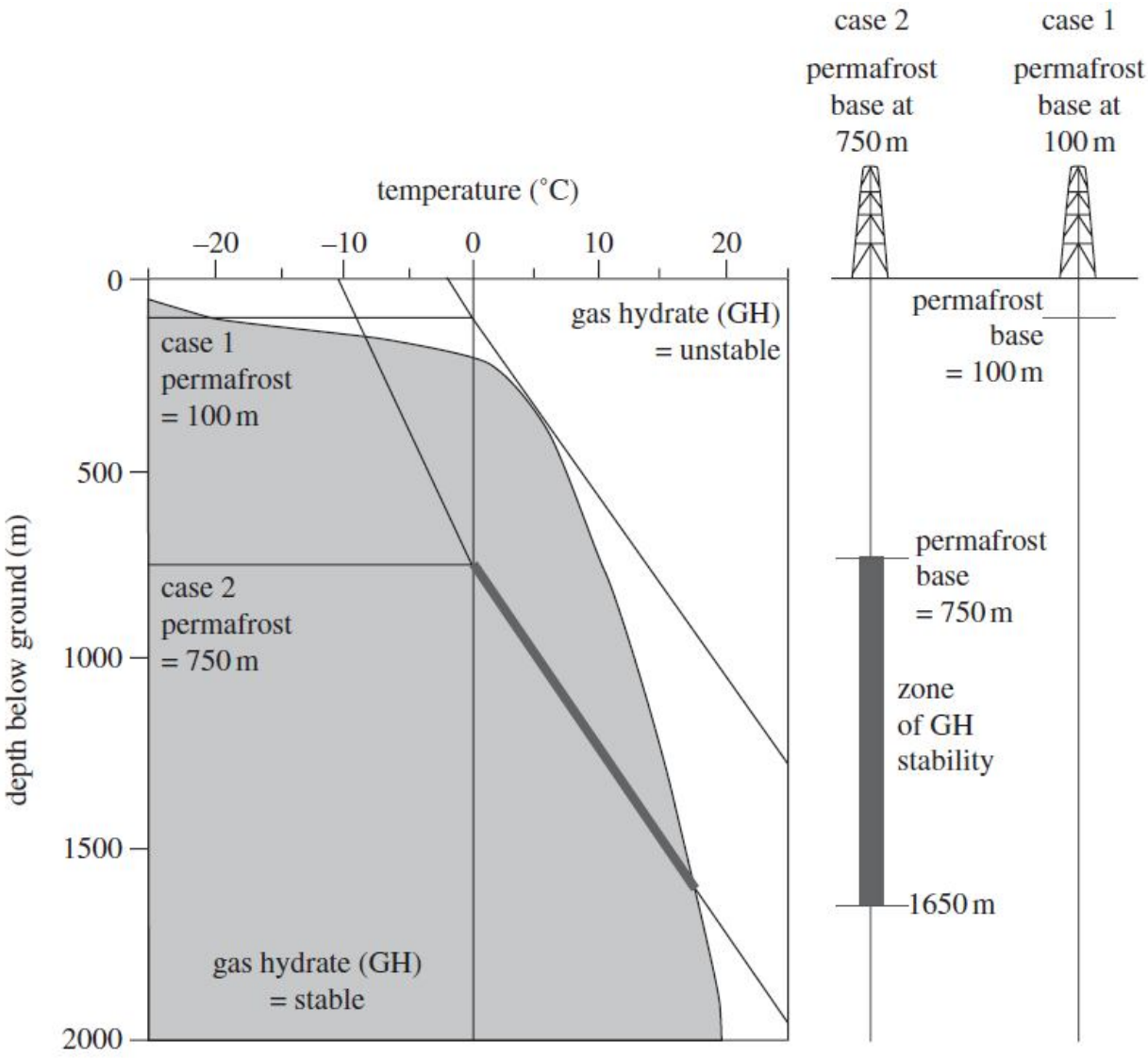

Fig. 1-6-The hydrate stability region in polar areas is a strong function of the ambient temperature and thickness of the permafrost. Case 1 shows a case where the base of permafrost is at 100m while in case 2 the base of permafrost is at 750 m below the ground level. In case 1 there is no hydrate stability depth range while in case 2 a depths range of 900 m thick exists within which hydrate can be stable (Maslin et al., 2010).

1.3.2) Marine Sediments

As discussed earlier, majority of global natural gas hydrate reserves are found offshore along the continental margins. However, there are a broad range of marine sediments in which methane hydrates are inferred or observed. As shown in Fig. 1-3, Boswell and Collett (2006) categorized marine hydrate systems into three main categories: (i) marine sand reservoirs, (ii) non-sand marine sediments and (iii) low permeability marine sediments.

Fig. 1-7 shows the gas hydrate stability region for a typical marine setting. Similar to that for the sub-permafrost case, the hydrate stability region is the region to the left of the phase boundary (red curve) where the geotherm (blue curve) is cooler than the temperature of the phase boundary. As is identified on the figure, the gas hydrate is theoretically stable in the lower part of the ocean, where ocean temperature is cooler than the phase boundary temperature, and extends to about 200 meters into the sediment below the seafloor.

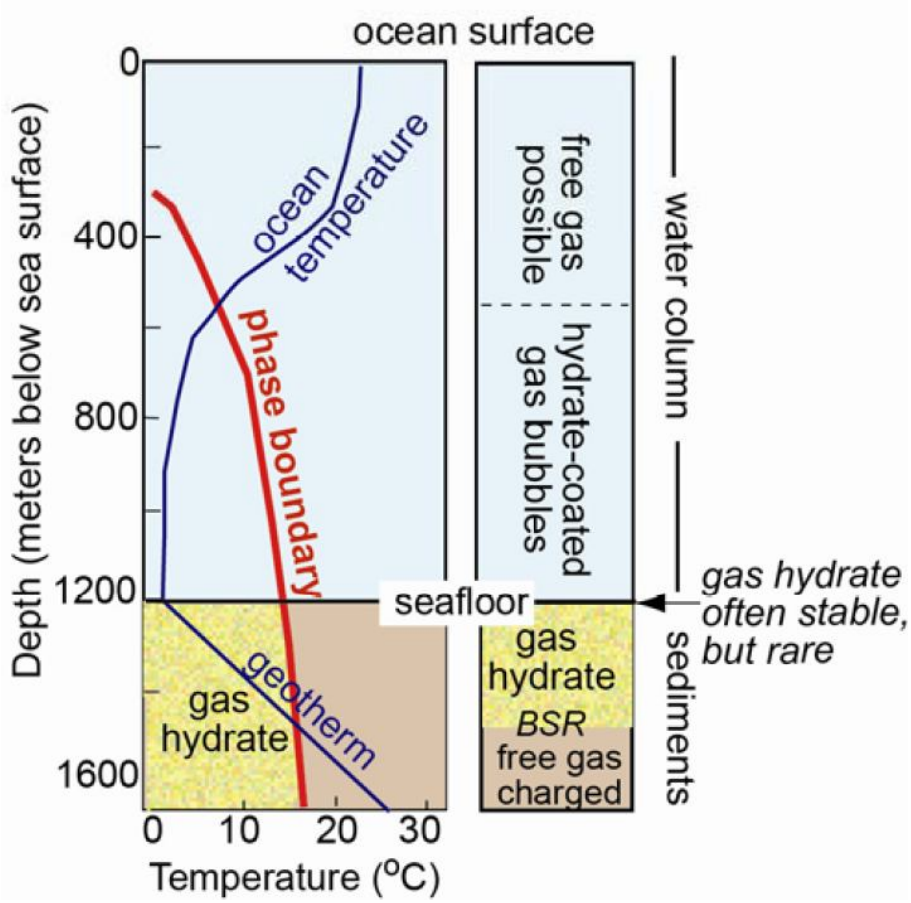

Fig. 1-7- The stability region for natural gas hydrate, i.e. area to the left of the red phase boundary, for marine settings. As mentioned earlier, such a diagram shows the region where gas hydrates are stable, but does not necessarily reflect where hydrates actually occur in nature. For a typical marine system at an arbitrary sea floor depth of 1200m and the geothermal gradient shown here, hydrates are theoretically stable in the lower part of the water column and extend down into the sediment until a depth, here ~200 m below sea floor, below which geotherm is warmer than the temperature of the phase boundary (Ruppel, 2011).

Similar to that discussed for sub-permafrost settings, section (1.3.1) , for marine systems the ambient temperature and the water depth are of paramount importance in determining the hydrate stability range. Fig. 1-8 highlights the hydrate stability depth range for three cases with different water depths but the same temperature of 0˚C at the

seafloor. In case 1, the water depth is 100m and thus the geotherm temperature is estimated to be always warmer than the temperature at the phase boundary. Therefore, there is no place at which the physical condition is appropriate for hydrate formation. In case 2, however, since the water depth is higher, i.e. 400 m, a part of the geotherm falls within the hydrate stability region and thus the depth interval highlighted in thick gray color is where hydrate can be stable. In case 3 a deeper water depth, i.e. 1000 m, is considered. As shown in Fig. 1-8, geotherm falls within the hydrate stability region over a larger depth range, i.e. from 1000m to 1600m. In fact, in marine systems as the depth of the seafloor increases the gas hydrate stability zone (GHSZ), if one exists, becomes thicker (Dickens, 2003).

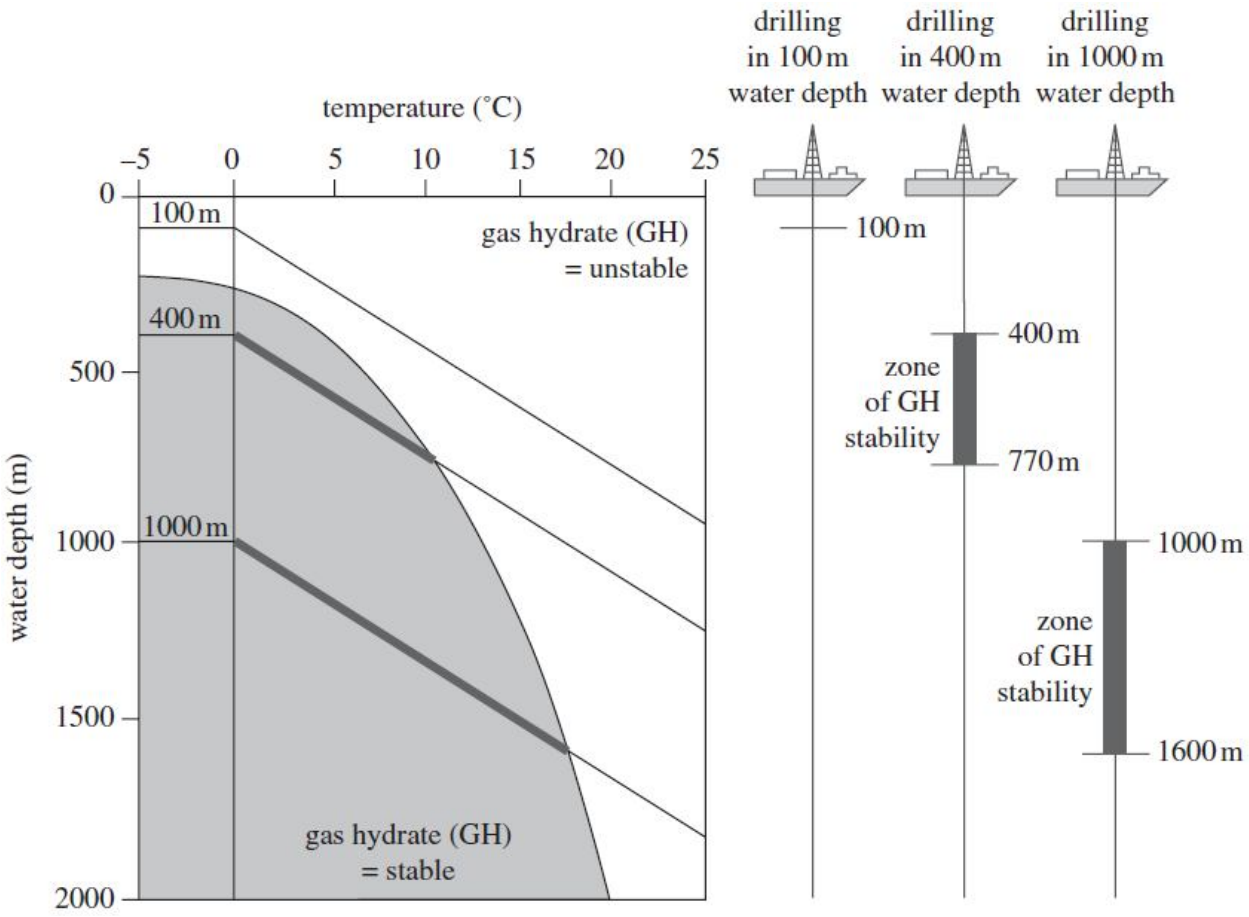

Fig. 1-8- The hydrate stability region in marine areas is a strong function of the ambient temperature and water depth. Case 1 shows a case where the water depth is 100m while in case 2 the water depth is 400 m and in case 3 the water depth is 1000m. In all three cases, though, the sea floor temperature is assumed to be 0˚C. In case 1 there is no hydrate stability depth range while in cases 2 and 3 depth ranges of several hundred meters exist within which gas hydrates can be stable. As the water depth increases a thicker hydrate stability zone is expected (Maslin et al., 2010).

In the following, marine sediments are briefly discussed under the three main categories adopted by Boswell and Collett (2006).

1.3.2.1) Marine sand reservoirs

Permeable marine sands are below permafrost-associated settings in the hydrate reserves pyramid in Fig. 1-3. Marine permeable sands are believed to be the main target for long-term production from gas hydrate reserves (Ruppel, 2011). Resource-grade gas hydrate reservoirs are described based on a combination of reservoir quality and hydrate saturation. Using such delineation scheme it is known that highly permeable marine sands containing moderate to high hydrate saturation are the best targets for natural gas production (Ruppel, 2011). Hydrate in these settings is mostly found as pore-filling morphologies. A recent example of such resource-grade reserves are the geologic units in Gulf of Mexico with inferred hydrate saturations as high as 80% detected through logging while drilling (Boswell et al., 2009).

1.3.2.2) Non-sand marine sediments

This category of hydrate bearing sediment can be described as less permeable, usually smaller grain, sediments with hydrates found mostly in fractures (Cook et al., 2010). Many examples of hydrates filling pervasive fractures through low-permeability sediments, e.g. silt and clay, are reported in the literature including the observations in Korean and Indian margins (Cook and Goldberg, 2008; Cook et al., 2010; Lee and Collett, 2009) and Gulf of Mexico (Cook et al., 2008). Although the overall hydrate saturation within these settings might be low, producing from these fractures can theoretically yield a substantial amount of gas. Besides, similar to that for shale gas, these fractures can serve as conduit for rapidly transporting the gas through otherwise sediments with low conductivity (Ruppel, 2011).

1.3.2.3) Low permeability marine sediments

Low permeability marine sediments come at the base of hydrate resource pyramid (Fig. 1-3). These setting are believed to host most of the global hydrate resource; however, due to their very low hydrate saturation they seem unlikely to become economic resources for gas production (Ruppel, 2011).

Something common among all the aforementioned gas hydrate settings is that these deep-water marine and permafrost areas are all much farther away to production and distribution infrastructure compared to most of conventional and unconventional reserves such as shale and coalbed. Obviously among the above gas hydrate habitats those closer to the existing infrastructures would most probably be the initial commercial scale hydrate-associated gas production. That is why researchers believe that the first commercial gas production would occur on the Alaskan North Slope near preexisting infrastructures and the produced gas could immediately be used for running on-sire operations (Hancock et al., 2004; Howe, 2004). In this dissertation also the main discussion would be on Arctic sub-permafrost hydrate-bearing settings due to their more urgent, in terms of onset of economic production, attention for further research compared to marine systems.

1.4) PREVIOUS MODELS FOR HYDRATE FORMATION IN THE SUBSURFACE SEDIMENTS

Methane hydrate systems in marine area have been the subject of extensive research in recent years. Several researches have suggested that hydrate forms through the upward movement of methane gas through Hydrate Stability Zone (HSZ) (Hyndman and Davis, 1992; Rempel and Buffett, 1997). Rempel and Buffett used a conceptual pore scale model to predict the methane hydrate saturation. Their model took the temperature

and its effect on gas/water equilibrium into account and showed a strong effect of gas/water equilibrium on hydrate saturation. They obtained, however, a hydrate saturation of only 1% which is much less than many of recent field observations (Boswell et al., 2009; Seol and Kneafsey, 2008).

Torres et al. (2004) developed a one dimensional, non-steady state, transport reaction model to simulate the observed chloride at the southern summit Hydrate Ridge, Cascadia margin off Oregon. They observed that the massive gas hydrate deposits, which coexist with highly saline pore fluids at the summit of hydrate ridge, cannot be explained by methane transport only through the dissolved phase. They came to the conclusion that methane transport as a free gas phase is necessary to be considered in order to explain the observed methane hydrate saturations in the summit of hydrate ridge (Torres et al., 2004). The necessity of presence of gas as a free phase to explain the formation of large saturations of hydrate was also shown by others (Liu and Flemings, 2006; Xu and Ruppel, 1999).

Liu and Flemings developed an equilibrium model for simulating the methane venting through the HSZ at southern Hydrate Ridge, offshore Oregon (Liu and Flemings, 2006, 2007). They suggested a high methane flux, as if methane is flowing in single phase, due to buoyancy. Hydrate formation in their model was limited by salinity build-up only, and not by the available amount of gas, as they assumed an unlimited amount of free gas passing through the HSZ. They assumed that methane transports upward through some fractures throughout the HSZ and that the formation of hydrate will provide a barrier against lateral movement of methane and thus methane keeps venting out through this hydrate-chimney to the sea floor. Other models have also been developed based on

methane flow through the GHSZ (Bhatnagar et al., 2007; Davie and Buffett, 2001; Garg et al., 2008).

A conceptual model of hydrate formation in marine sediments at pore scale was developed by (Clennell et al., 1999; Henry et al., 1999). Besides, several conceptual models were proposed for the formation of hydrate at the interface between water and CO_2 including: (i) growth of hydrate into CO_2 (Shindo et al., 1993), hydrate growth in both CO_2 and water, also known as duplex suspension layer model, (Lund et al., 1994) and (iii) hydrate growth into water only (Teng et al., 1996). Tohidi and his colleagues conducted visualization experiments in glass micro models and showed that in a system with two phases present, gas hydrate starts forming at the two phase interface (Tohidi et al., 2001), because the hydrate component concentrations greatly exceed the mutual fluid solubilities. The solid hydrate film at the interface, in turn, acts as a barrier preventing further contact of the bulk-fluid phases. Therefore, for continued clathrates hydrate formation fluid surface renewal is required (Sloan, 2003).

At the field scale, numerical simulations of hydrate-bearing systems have been accomplished with most of the emphasis on improving techniques for production from hydrate-settings through thermal and depressurization techniques for dissociating in situ hydrates (Moridis, 2003; Moridis et al., 2004).

To better understand the hydrate-bearing systems, in both marine and terrestrial settings, there is also a need to account for simultaneous flow of methane gas and brine in the subsurface. As mentioned earlier, the necessity to account for multiphase flow, rather than gas-saturated aqueous phase flow as a single phase, as well as the inherent heterogeneity in the host sediments has been highlighted before (Ginsburg and Soloviev, 1997; Milkov and Xu, 2005; Soloviev et al., 1987; Tréhu et al., 2004).

In summary, the above predictive hydrate formation/distribution models can be divided into two categories: (A) Models assuming formation of hydrate from methane dissolved in water in which accumulation is driven by methane-saturated water entering the gas hydrate stability zone (GHSZ) or by providing methane from a biogenic source (Bhatnagar et al., 2007; Buffett, 2000; Ginsburg, 1998; Hensen and Wallmann, 2005; Hyndman and Davis, 1992; Xu and Ruppel, 1999) and (B) models assuming formation of hydrate at the interface between gaseous and aqueous phases in which accumulation is driven by methane gas phase entering the GHSZ (Liu and Flemings, 2006, 2007; Torres et al., 2004). One motivation for the latter class of models, as mentioned earlier, was that observed chloride concentrations and gas hydrate distributions could not be explained without assuming transport of free gas through GHSZ (Torres et al., 2004).

The model categories (A) and (B) address marine hydrate reservoirs. While there is no comparably mechanistic model of hydrate formation for terrestrial hydrate accumulations, i.e. subpermafrost hydrate reservoirs, in the literature, the overall process has been delineated. Boswell et al. (2011) listed several aspects of gas hydrate accumulations in the Arctic that support the interpretation of conversion of free gas accumulation to gas hydrate accumulations. The accepted scenario for Arctic hydrate reservoirs such as those of the Milne Point Unit (MPU), Prudhoe Bay and Kuparuk River area in ANS is that gas first accumulated in shallow traps. A GHSZ was then established and ultimately expanded to encompass the gas reservoir in response to ancient climate cooling, i.e. imposition of Arctic conditions (Collett, 1993). Fig. 1-9 shows the hydrate saturation profile interpreted based on acoustic and resistivity logs in several wells in Prudhoe Bay, Kuparuk River and Milne Point units.

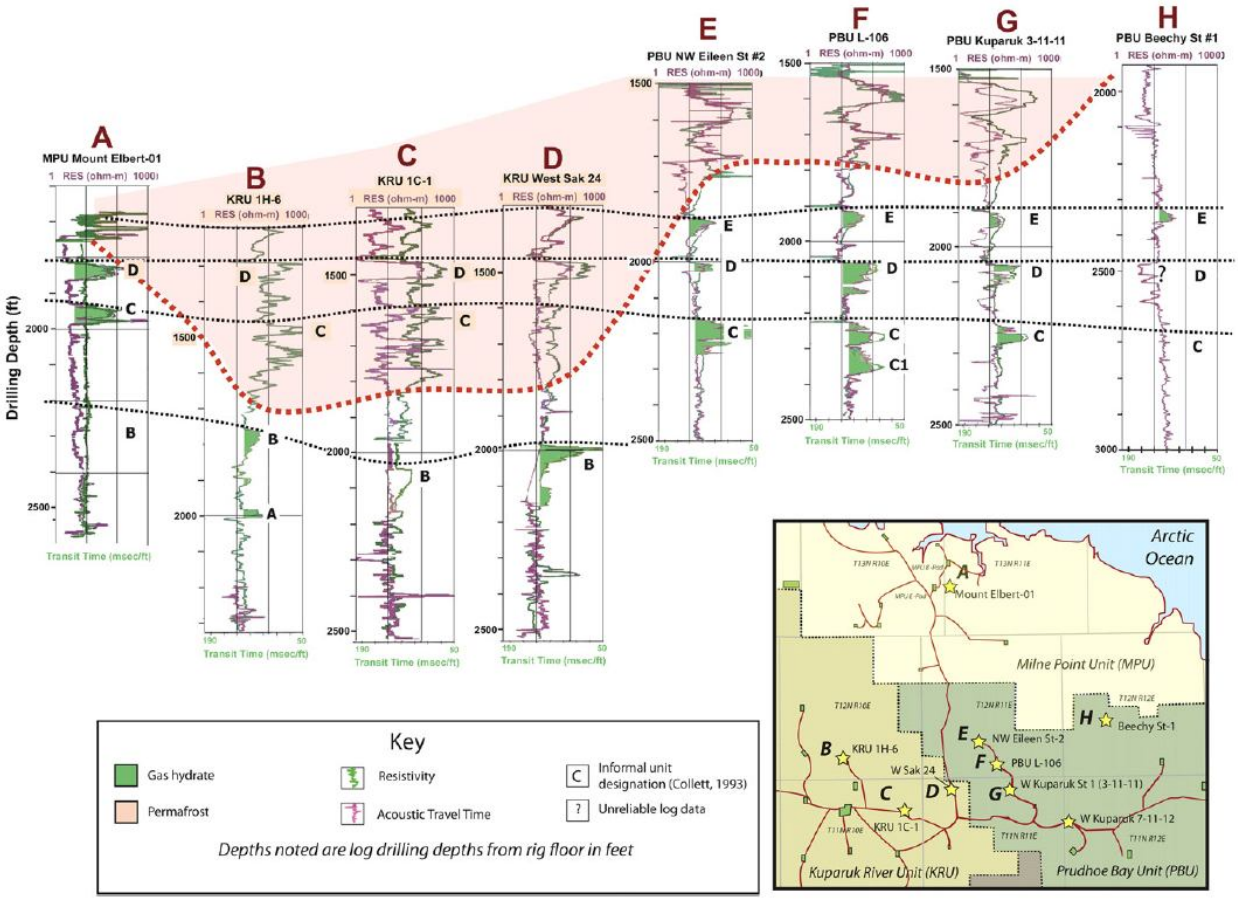

Fig. 1-9-Occurrence of natural gas hydrate (green) interpreted from acoustic and resistivity logs in eight of the wells drilled in eastern Kuparuk River, western Prudhoe Bay and southern Milne Point units (Boswell et al., 2011). The black letters shows the sand unit names informally designated by Collett (1993).

In this dissertation a more detailed model of the process of hydrate accumulation is proposed, based on the latter Arctic scenario. A major difference between this model and the marine models (A) and (B) is that instead of presuming fluxes of fluid(s) to the GHSZ, we presume that the base of GHSZ moves down to (and through) an existing petroleum system. Fluid flux occurs in our model (and plays an important role in determining saturation) but only as a response to BGHSZ motion. This downward movement of the BGHSZ occurred in the ANS roughly 1.8 Ma (Collett, 1993; Dai et al.,

2011). For simplicity we also assume that CH_4 is the only constituent of the gas phase and the only guest molecule in the hydrate.

1.5) PROBLEM DESCRIPTION AND HYPOTHESES

The motivation for a detailed process model here is that the previous presentations of the above concept, i.e. descent of the GHSZ through a pre-established gas column, (Boswell et al., 2011; Collett, 1993; Collett et al., 2011; Dai et al., 2011) did not explore the physical basis for how this conversion of gas accumulation to hydrate might proceed, nor did they consider implications and effects of variable geology/petrophysics as well as volume change during hydrate formation on the response of a free-gas/water system to the imposition of gas hydrate stability conditions. All these effects, however, seem to play key roles in how hydrate saturation distributes in the subsurface.

1.5.1) Problem Description

Observations in the well-characterized Prudhoe Bay (PBU), Kuparuk River (KPU) and Milne Point (MPU) hydrate accumulations of Fig. 1-9, e.g. in Mount Elbert well, suggest that the above effects could be significant. For example, large saturations of hydrate are often restricted to the upper part of the sand units (Fig. 1-10b). Several interpretations of rather abrupt changes between large (50% to 75%) and small (0% to 15%) saturations have been reported. In the upper hydrate-bearing sand unit of Mount Elbert well, known as Unit D (Collett, 1993), this observation could be interpreted as the occurrence of high quality (large porosity and large intrinsic permeability) sand at the top of the unit. However, in the lower hydrate-bearing sand unit, known as Unit C (Collett, 1993), this is not the case (Boswell et al., 2011). The top section of Unit C contains the major hydrate saturation (Fig. 1-10b) while it possesses a significantly lower porosity and

intrinsic permeability than the lower section containing little or no hydrate (Boswell et al., 2011). Moreover, reservoir sands in the MPU are only partially filled with hydrate and often exhibit a sharp basal contact. For example within the D Unit log and core data exhibit an abrupt decrease in hydrate saturation, S_h, from >65% to <10% despite the gradational increase in shale content and decrease in reservoir quality and porosity (Boswell et al., 2011). Hence it is difficult to postulate a straightforward relation between reservoir quality and hydrate saturation in the Mount Elbert well. Boswell et al. (2011), however, favor a lithologic control on hydrate saturation in Unit D which does not hold for Unit C in Mount Elbert well.

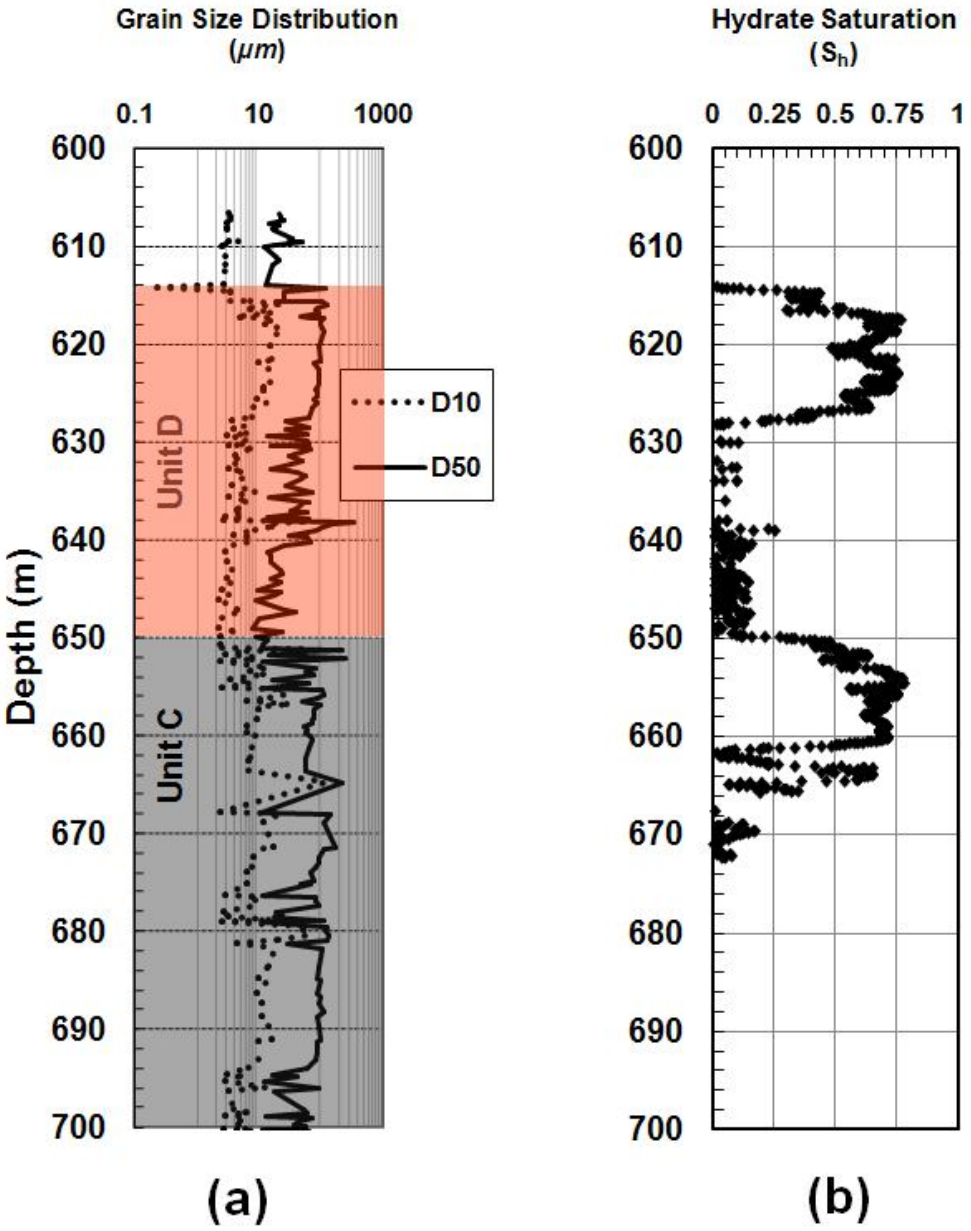

Fig. 1-10- Data from Mount Elbert stratigraphic test well, drilled in the Milne Point unit of Alaska North Slope: (a) 10th percentile, D_{10}, and 50th percentile, D_{50}, of grain size distribution versus depth determined from laser-grain-size analyses (Rose et al., 2011); (b) Gas hydrate saturation, S_h, determined from the TCMR-repeat-pass-plus-density log based on NMR-DEN POR method (Lee and Collett, 2011). The shown interval of interest includes the informally labeled C and D units of Collett (1993).

Another possible explanation for such abrupt variations in hydrate saturation at some specific points is that they simply reflect the variation of the original gas saturation distribution. Unit D may have been only partially filled with gas for variety of reasons -- a shallow spill point, the stratigraphic seal could hold only a modest gas column, or an interruption in the gas migration path caused insufficient charge. But partial charge is not a necessary condition for such abrupt changes in hydrate saturation in an individual reservoir: in this research we show that the volume changes associated with hydrate formation along with variation in grain size distribution with depth lead to a patchy hydrate saturation distribution even of a fully charged reservoir. Whatever the extent of charge, this explanation assumes that the conversion to hydrate occurs after the reservoir is no longer connected to the source of gas.

The partial charge explanation becomes more critical in the case of a vertical sequence of partially filled hydrate reservoirs. This explanation would require no vertical communication between the original gas accumulations in Units D and C, i.e. a sufficiently large capillary entry pressure for the sediment at the base of Unit D. The requisite entry pressure depends in turn on the height of gas column resulting from the charge of Unit C.

Based on the above unanswered questions regarding the detailed physical processes led to the observed hydrate saturation distributions in the Arctic, three key hypotheses are proposed and evaluated in this dissertation.

1.5.2) Hypotheses to Be Tested

One key hypothesis tested during this research is as follows: characteristic features associated with hydrate occurrence in the Arctic are consistent with three

conditions: i) the establishment of gas phase saturation within the sediment when the base of gas hydrate stability zone (BGHSZ) was located above the sediment package or when no GHSZ was present at all; ii) sufficient variation of grain size distribution with depth and iii) volume reduction during hydrate formation, i.e. hydrate occupies less volume than its constituents (CH_4, H_2O) in their respective phases. The latter is presumably true in all natural hydrate-bearing sediments, including Arctic sediments. The first condition is also commonly satisfied in the Arctic; the second depends on local depositional history.

Another hypothesis evaluated here is that capillarity-driven, rather than viscous dominated pressure-driven, transport of aqueous and gaseous phase in the course of hydrate formation is key to the observed modern hydrate saturation profiles. In other words, the Arctic hydrate accumulations, such as that in Mount Elbert well, are very unlikely to be explained without considering flow due to saturation gradients.

The final hypothesis proposed and tested here is that the rate of temperature cooling, i.e. the rate of descent of the BGHSZ, as well as the rate of hydrate formation exhibits a paramount effect on the resulting hydrate saturation profile from a preexisting gas accumulation. More specifically, the faster the temperature cooling the less sharp the basal contacts in the Arctic hydrate-bearing sands.

1.6) OBJECTIVES AND MODEL DESCRIPTION

1.6.1) Objectives

The primary objectives of this research are as follows:

- Develop a stoichiometric transport-associated hydrate formation model from a free gas and an aqueous phase

- Develop a quasi-1D capillarity-based model that enables predicting/explaining hydrate saturation profiles in "*converted free gas reservoirs*", considering three key elements:
    - Descent of the BGHSZ through the initial gas accumulation
    - Volume change and gas/water transport into the GHSZ during hydrate formation
    - Variation in grain size distribution versus depth
- Develop a transient 1-D hydrate formation model for "*converted free gas reservoirs*" providing *a priori* on the relative volumes of gaseous and aqueous phases transported to the GHSZ during hydrate formation, considering three key elements:
    - Descent of the BGHSZ through the initial gas accumulation
    - Volume change and gas/water transport into the GHSZ during hydrate formation
    - Rate of descent of the BGHSZ and rate of hydrate formation
- Investigate the key fluid phases *transport mechanisms* and effects of *rate of descent* of the BGHSZ during hydrate formation in "*converted free gas reservoirs*"

1.6.2) Physical Phenomena Critical to the Proposed Models

Grain size varies with depth in most depositional environments. When gas accumulates in a sediment, these variations play an important role on the gas/water saturation profile. Fig. 1-11a shows schematically a stack of four distinct sediment layers with different grain size distributions. Each layer thus has a different characteristic curve of capillary pressure versus saturation, as shown in Fig. 1-11b. Capillary pressure, P_c, is defined as the difference between the non-wetting phase pressure, in this case gas pressure P_g, and wetting phase, aqueous phase pressure P_w, i.e. $P_c=P_g-P_w$. Capillary pressure curve shows the relationship describing the capillary pressure required for establishing a given gas phase saturation in a sediment originally filled with water. The top layer (layer 1) has the smallest grains, and the corresponding capillary pressure curve shows a much larger capillary entry pressure than other layers. If gas enters this stack of sediments from the bottom of layer 4 (Fig. 1-11a) and begins to accumulate, the capillary pressure increases with gas column height above the entry point as shown in Fig. 1-11c. The capillary pressure at any height combined with the corresponding drainage curve (Fig. 1-11b) yields the gas/water saturation profile shown in Fig. 1-11d. The fine-grained layer 1 acts as a seal for the gas accumulation in Fig. 1-11d. Note that the BGHSZ is above the gas column and thus no hydrate is present in Fig. 1-11d. Fig. 1-11e shows the situation when the BGHSZ has descended all the way down the gas column and thus the gas accumulation (Fig. 1-11d) has turned into hydrate. Note that the initially single gas column (Fig. 1-11d) turned into discrete, concentrated hydrate deposits at the top section of two of the formations (Fig. 1-11e). The resulting hydrate saturation profile in Fig. 1-11e exhibits a similar distribution to the Mount Elbert well (Fig. 1-10b). More detailed

explanation of how vertical heterogeneity, i.e. grain size variation versus depth, can lead to such discrete, concentrated hydrate deposits is provided in a later section.

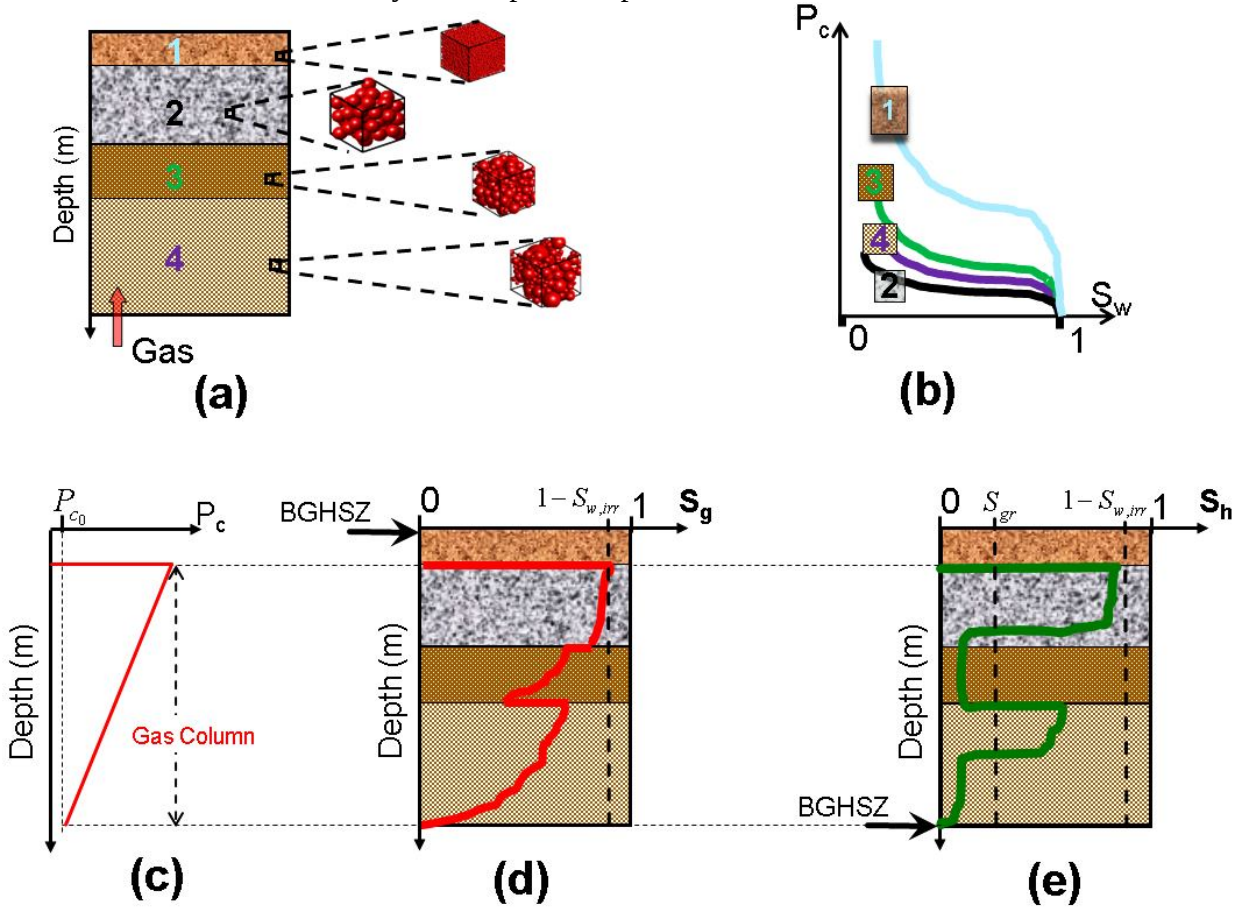

Fig. 1-11-(a) Sediment layers with different grain size distributions. The characteristic capillary pressure for each layer is shown in (b). Gas enters the bottom layer and accumulates below the fine-grained layer at top of sediment package. (c) Capillary pressure profile within the gas column, combined with the characteristic curves of (b), determines the gas saturation profile (d) through the sediments. Note that gas accumulation has occurred while BGHSZ is shallower than the gas column and thus no hydrate is being formed so far. (e) As BGHSZ descends along the sediment column, a hydrate saturation profile is established which can be very different from the initial gas saturation profile and need not correlate with sediment layering.

The other physical phenomenon essential to our model is that the volume occupied by a mole of methane hydrate is smaller than the volume occupied by gas and aqueous phases containing the same number of moles of CH_4 and H_2O as the hydrate. This volume shrinkage can be shown through stoichiometry of hydrate forming from methane and water. Next chapter will discuss this aspect of the model in detail. This volume reduction would in turn draw a flux of gaseous and aqueous phase into the hydrate formation zone, i.e. GHSZ. Methane which is transported to the GHSZ, i.e. methane drawn from the free gas still residing below the BGHSZ, to help fill the void space is then converted to hydrate inside the GHSZ. As discussed below, the relative ratio of transported gaseous and aqueous phases affects the resulting hydrate saturation profile.

The rate of salinity transport would also play an important role on the observed amount of hydrate. It can limit the amount of hydrate formed if a large amount of gas is available compared to the amount of water, or if we have a closed system. This is because the inclusion of H_2O into the hydrate from the aqueous phase causes salinity to build up in the aqueous phase, reaching a critical value above which hydrate cannot form or be stable (Liu and Flemings, 2007). Ultimately the pore-level geometric configuration of each phase within the sediment governs the relative rates at which water, methane and salinity are transported through the sediment. We will not consider the salinity effect in this model, assuming that the aqueous phase has a small initial salinity and that any buildup is rapidly dissipated into an unlimited reservoir of brine.

Heat transfer will also affect the hydrate formation. If the latent heat of formation is not dissipated, the local temperature will increase, making hydrate unstable. Considering that the heat diffusion coefficient (typically 10 m^2/yr.) is about 500 times faster than salinity transport coefficient (typically 0.02 m^2/yr.), salinity build up is more

likely the limiting factor (Clennell et al., 1999; Iversen and Jorgensen, 1993). Therefore, we neglect the effect of heat transfer in this work.

This dissertation focuses on the conversion of an accumulated gas saturation to hydrate as the BGHSZ moves down. Subsequently, hydrate dissociates if the BGHSZ moves upwards, leaving the gas bearing region out of GHSZ. Cycles of hydrate formation and dissociation could take place during geological time. For example, such movements of the BGHSZ are reported (Fig. 1-12) in MacKenzie delta region (Majorowicz et al., 2008; Torres et al., 2011). Similar oscillations of the BGHSZ in Mount Elbert well were reported by Dai et al. (2011); however, the hydrate-bearing section of the Mount Elbert well, i.e. Units C and D, remained well inside the GHSZ and were not disturbed by the oscillations of the BGHSZ.

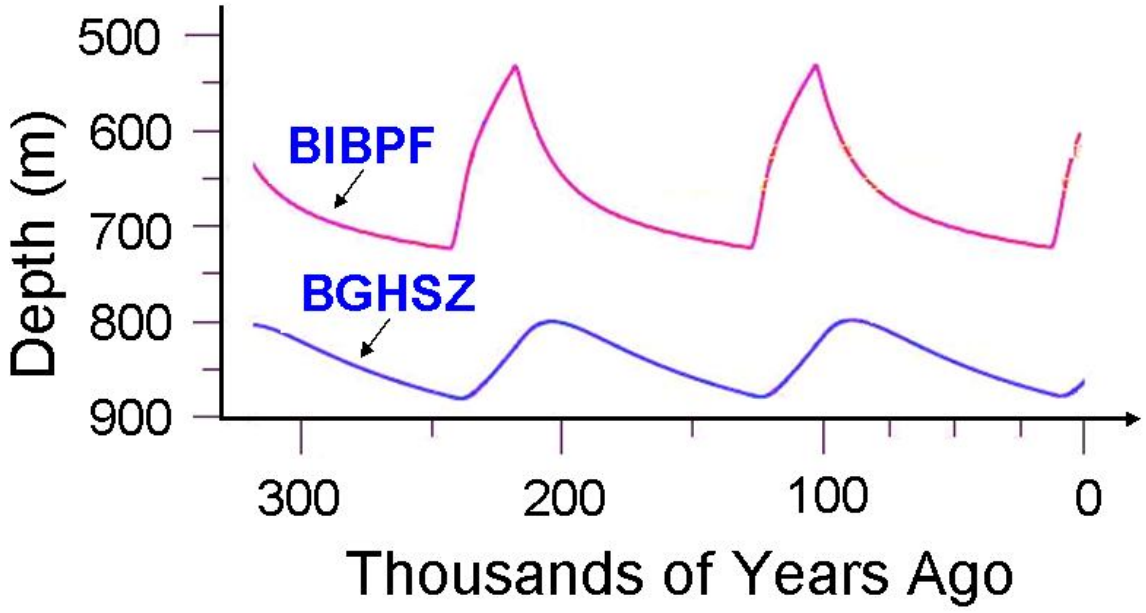

Fig. 1-12- Results of glacial surface forcing on permafrost, based on thermal conductivity, latent heat, heat flow and observed gas hydrate thickness in the MacKenzie delta region: BGHSZ (base of gas hydrate stability zone) and BIBPF (base of ice-bearing permafrost) cycle with geological time (Majorowicz et al., 2008)

1.6.3) Model Applicability

Because the conversion to hydrate drives substantial fluid migration, the structural setting of the gas accumulations also affects the final hydrate distribution. The model analyzed in this research is for the limiting case of horizontal layers, in which fluid migration is only in the vertical direction. In this case the process is essentially one-dimensional. The advantage of the 1-D hydrate formation model is that it permits analysis of some key processes involved in conversion of gas accumulations to hydrate reservoirs. Because the Mount Elbert well has been characterized in considerable detail, it provides an opportunity to test some key implications of the model. Several features observed in Mount Elbert data are replicated by this 1-D model, suggesting that it would be useful to extend the process model to 2- and 3-D geology. But it is beyond the scope of this dissertation to explain the Mount Elbert accumulation per se, and in any case the one-dimensionality of the model is too simple for that task. The Mount Elbert well, as shown in Fig. 1-13, is located on a monoclinal structure that dips less than 2˚ to the NNE (Boswell et al., 2011; Collett, 1993; Inks et al., 2009). Moreover, Boswell et al. (2011) reported complex combination of stratigraphic and structural controls, e.g. lateral heterogeneity within the sand units, lateral trapping by normal faults or the effect of Mount Elbert fold on hydrate saturation distribution, which cannot be captured by a 1-D model. As the dip angle increases from 0˚, gas can migrate along dip as well as vertically; the limiting case treated here does not consider for lateral flow components and thus provides a lower bound on the saturation profile for dipping beds. Conductive faults, Fig. 1-13, provide another possible route for fluid migration at Mount Elbert well on the upthrown side of a large normal fault (Boswell et al., 2011). These may have contributed to the flow at the time of hydrate formation, but we assume all faults are sealing.

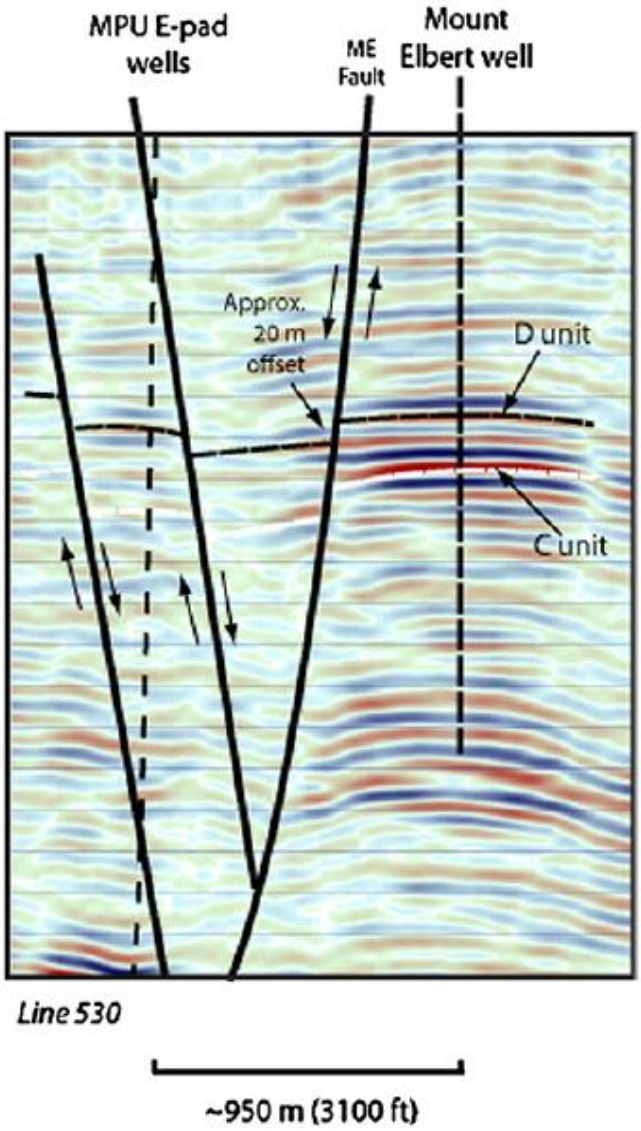

Fig. 1-13- Mount Elbert well, is located on a monoclinal structure that dips less than 2˚ to the NNE (Boswell et al., 2011; Collett, 1993; Inks et al., 2009).

In summary, the timing, the pathway, the extent of charge and the dip angle are key controls on final hydrate distribution in a multilayer column of sediment. The model presented here quantitatively addresses the extent-of-charge explanation discussed earlier (i.e. original gas reservoirs in multiple layers are not in communication across layers),

and more importantly it generalizes the extent-of-charge model to show how a stack of partially filled hydrate reservoirs can result even from initially communicating layers that host a single continuous column of gas.

Chapter 2: A Stoichiometric Transport-associated Model for Hydrate Formation from Free Gas and Aqueous Phases

2.1) BACKGROUND

Formation of hydrate accompanies a volume change, in the sense that the volume occupied by a mole of methane hydrate, i.e. the amount of hydrate containing one mole of gas, is smaller than the volume occupied by gas and aqueous phases containing the same number of moles of CH_4 and H_2O as the hydrate. This reduction in volume accompanying hydrate formation follows from hydration number, N, in the hydrate lattice, $CH_4.N(H_2O)$, and typical densities of the respective phases. Hydrates are known to be non-stoichiometric, meaning that N varies with variation in hydrate cage occupancy which is in turn a function of pressure, temperature and overall gas composition (Sloan, 2003), with values of N=6.05±0.06 (Handa, 1986; Ripmeester and Ratcliffe, 1988) for methane hydrate. For simplicity we use a constant value of N=6, which is consistent with

an average density of 914 kg/m^3 for methane hydrate (Sloan, 1998). As a numerical example of the volume reduction associated with hydrate formation, consider a vessel containing 0.5 m^3 of methane and 0.5 m^3 of pure water held at a constant pressure of 6.5 MPa and temperature of 2˚C during hydrate formation. At these conditions the phase densities are about 55 kg/m^3 (gas) and 1000 kg/m^3 (aqueous). For N = 6, the molecular weight of hydrate would be 124. All the gas will be consumed to form hydrate, and the hydrate volume is V_h=0.5×55/16×124/914≈0.23m^3. It can be shown that almost 0.18 m^3 of water is used to form the latter amount of hydrate. Therefore, at the current thermodynamic condition the final hydrate volume, 0.23 m^3, is almost one third of the consumed volumes of methane and water combined.

In this chapter a stoichiometric hydrate formation model is proposed to predict the hydrate saturation profile from an initial gaseous and aqueous phase volume fraction, S_g and S_w, respectively. The model is established for a system containing free gaseous and aqueous phases and will consider hydrate formation in both closed and open systems. The proposed model for open systems will then be used to predict hydrate saturation profiles resulting from preexisting gas saturation distributions in host sediments. Conceptually, as hydrate forms from a fixed volume of gas phase in a sediment, void space becomes available. Here “void space” is shorthand for the volume change accompanying hydrate formation. The void space will either be filled by influx of fluid phase(s) or accommodated by compaction of the sediment. In this dissertation, however, we assume no compaction occurs during conversion to hydrate. By the end of this chapter we will see that in any case the volume changes are too large to be accommodated only by compaction.

2.2) VOLUME CHANGE FOR HYDRATE FORMATION FROM GASEOUS AND AQUEOUS PHASES

A simple box model is used to compute the volume change as hydrate forms. A box (with a volume V_{tot}) is originally filled by methane and water existing as two pure phases (Fig. 2-1a). The initial methane/water volumes are fixed and no hydrate is present initially. Suppose an increment of hydrate, δV_h, forms at the interface between gas and water phase as the result of stoichiometric conversion of the corresponding increments of methane and water, δV_g and δV_w. The relationship between the volume increments depends on the densities of the phases, i.e. hydrate, gaseous and aqueous. Temperature and pressure are assumed to be appropriate for hydrate formation and constant during hydrate formation. Therefore, gas and aqueous phases have constant densities during hydrate formation. Mathematically we have:

$$\delta V_w + \delta V_g = \delta V_h + \delta V \qquad (2.1)$$

Wherein δV denotes the overall reduction in volume occupied by the phases. As a consequence of this volume change, considering that a constant pressure and temperature is assumed, depending on having a closed or open box two different consequences will emerge.

For a closed box (no fluid-transport in or out of the box) the only way to keep the pressure and temperature constant is by changing the volume of the box, i.e. the total volume of the box will shrink by an amount of δV. This would correspond to compaction (grain rearrangement to reduce porosity) in a natural system. In natural systems, though, we expect open systems wherein fluid phases can leave or enter. We will first analyze hydrate formation in a closed system where no fluid flow in/out of the control volume takes place. Then we would further generalize the model for a natural system which is open to flow of both gas phase and aqueous phase.

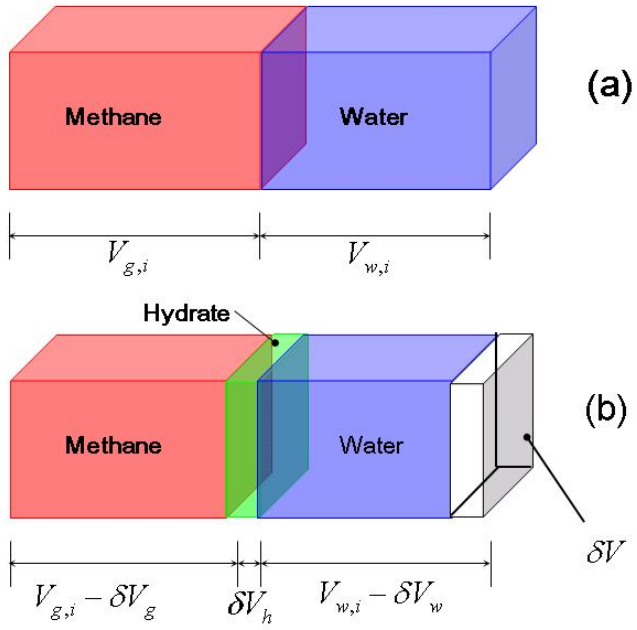

Fig. 2-1- The box model to compute the volume change due to hydrate formation. (a) The initial gaseous/aqueous phase volumes are fixed, $V_{g,i}+V_{w,i}=V_{tot}$. No hydrate is present initially. (b) An increment of hydrate, δV_h, forms at the interface between gaseous and aqueous phases, consuming δV_g of gaseous phase and δV_w of aqueous phase.

2.3) MODEL OF HYDRATE FORMATION FROM FREE GAS AND AQUEOUS PHASE: CLOSED SYSTEM

Fig. 2-2a shows a cylinder with a movable piston, initially containing methane and water under a pressure and temperature, *P* and *T*, condition suitable for hydrate formation. For simplicity water is assumed to be fresh; therefore, salinity build-up will not limit the hydrate formation (limiting case). Hydrate starts growing at the interface of methane and water (Fig. 2-2b) and will keep forming until one of the original phases (gaseous or aqueous) is fully consumed.

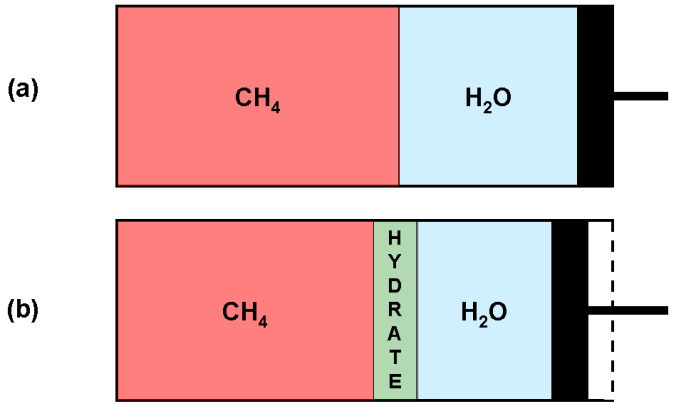

Fig. 2-2- (a) A cylinder with movable piston is initially filled with water and methane under pressure, *P*, and temperature, *T*. (b) The system of cylinder and piston after an increment of hydrate is formed. The volume reduction is illustrated as white area on the right hand side of the cylinder.

Since the suitable pressure and temperature condition is provided, as mentioned earlier hydrate will keep forming until the system runs out of one or both of the constituents (water, methane or both). Therefore, two general final situations can be imagined for a system initially filled with $n_{g,i}$ moles of gas and $n_{w,i}$ moles of water: (i) *Excess water* case where the amount of water is more than the stoichiometric requirement to convert all the available methane into hydrate; (ii) *Excess gas* case where the amount of water is less than the stoichiometric requirement to convert all the available methane into hydrate. To convert $n_{g,i}$ moles of methane into methane hydrate, $n_{w,i}=N\times n_{g,i}$ moles of water is required; where N is methane hydration number.

2.3.1) Excess water: Amount of water exceeds stoichiometric requirement

In this case the total number of moles of water, $n_{w,i}$, is more than the stoichiometric amount of water required to convert the total amount of methane into hydrate, $N\times n_{g,i}$. Therefore, all the gas is consumed to form $n_{h,f}$ moles, equivalent to a

volume, $V_{h,f}$, of methane hydrate. A typical final state of the system in this case is shown in Fig. 2-3d. The initial volumes of gaseous and aqueous phases, $V_{g,i}$ and $V_{w,i}$, are related to the initial moles of the phases through Eqs. (2.2) and (2.3):

$$V_{w,i} = n_{w,i}\bar{V}_w \tag{2.2}$$

$$V_{g,i} = n_{g,i}\bar{V}_g \tag{2.3}$$

where $\bar{V}_w$ and $\bar{V}_g$ are molar volumes of aqueous phase and gas phase, respectively. Molar volume of a component is equal to the molecular weight, MW_c, of the component divided by its density, ρ_c, i.e.:

$$\bar{V}_c = \frac{MW_c}{\rho_c} \; ; \; c = w, g, h \tag{2.4}$$

Similarly for the final volume of methane hydrate, $V_{h,f}$, we have:

$$V_{h,f} = n_{h,f}\bar{V}_h \tag{2.5}$$

Furthermore, based on hydrate stoichiometry:

$$n_{h,f} = \frac{V_{h,f}}{\bar{V}_h} = n_{g,i} = \frac{V_{g,i}}{\bar{V}_g} \tag{2.6}$$

Therefore,

$$V_{h,f} = V_{g,i}\frac{\bar{V}_h}{\bar{V}_g} \tag{2.7}$$

The final volume of water, $V_{w,f}$, after converting all the available methane into methane hydrate, would be:

$$V_{w,f} = V_{w,i} - \underbrace{Nn_{g,i}\bar{V}_w}_{Consumed} = V_{w,i} - N\frac{\bar{V}_w}{\bar{V}_g}V_{g,i} \tag{2.8}$$

From Eqs. (2.7) and (2.8), the final total volume of the system would be:

$$V_{tot,f} = V_{w,f} + V_{h,f} = V_{w,i} + V_{g,i}\left(\frac{\bar{V}_h - N\bar{V}_w}{\bar{V}_g}\right) \tag{2.9}$$

Therefore, the amount of volume reduction in the excess water case, $\Delta V_{EW} = V_{tot,i} - V_{tot,f}$, would be:

$$\Delta V_{EW} = \underbrace{(V_{g,i} + V_{w,i})}_{Init.\ Vol.} - V_{tot,f} = V_{g,i}\left(1 - \frac{\bar{V}_h - N\bar{V}_w}{\bar{V}_g}\right) \tag{2.10}$$

Final methane hydrate volume, $V_{h,f}$, and volume change, ΔV_{EW}, may be normalized by the initial system volume, $V_{g,i}+V_{w,i}$, as:

$$\frac{V_{h,f}}{V_{tot,i}} = \frac{V_{h,f}}{V_{g,i} + V_{w,i}} = \frac{V_{g,i}}{V_{g,i} + V_{w,i}}\frac{\bar{V}_h}{\bar{V}_g} = S_{g,i}\frac{\bar{V}_h}{\bar{V}_g} \tag{2.11}$$

$$\frac{\Delta V_{EW}}{V_{tot,i}} = S_{g,i}\left(1 - \frac{\bar{V}_h - N\bar{V}_w}{\bar{V}_g}\right) \tag{2.12}$$

In Eqs. (2.11) and (2.12), $S_{g,i}$ represents the initial volume fraction of methane inside the cylinder (closed system).

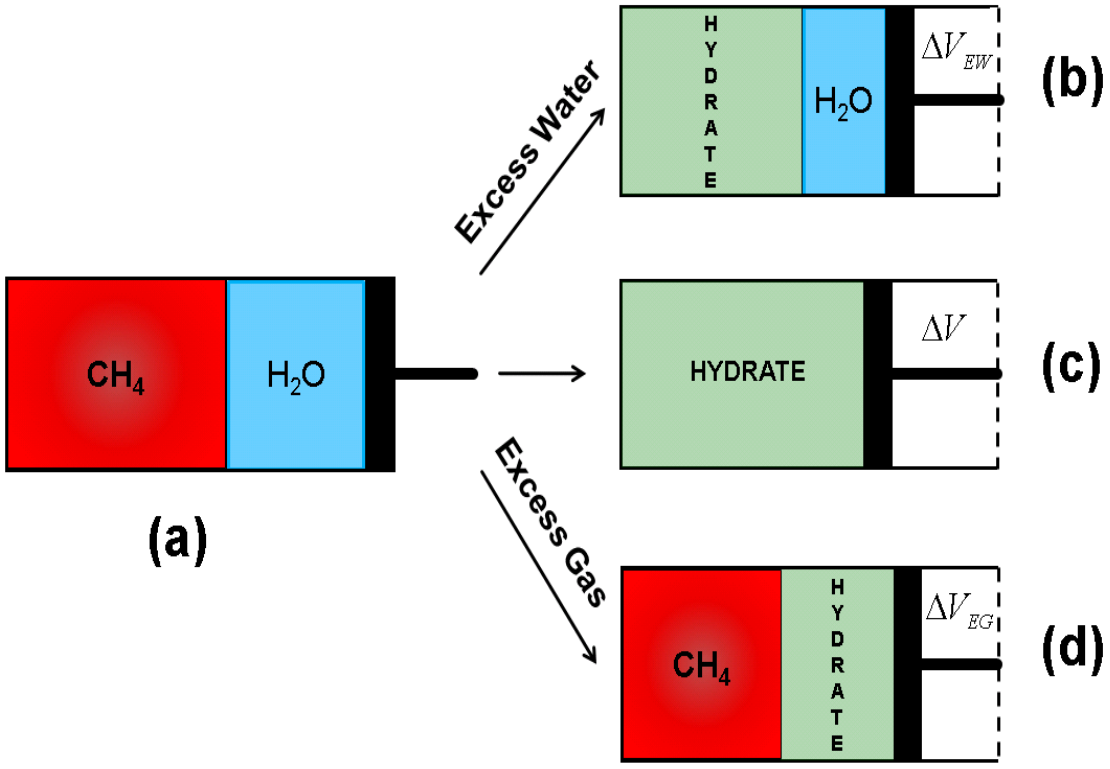

Fig. 2-3-(a) Closed system: $n_{g,i}$ moles of methane and $n_{w,i}$ moles of water at constant T, P appropriate for hydrate formation; (b) Final state of the system if the initial amount of water is more than the stoichiometric requirement (excess water); (c) final state of the system when the amounts of gas and water are at the exact stoichiometric requirement $n_{w,i}=N\times n_{g,i}$; (d) Final state of the system when the initial amount of methane is more than the stoichiometric requirement (excess methane).

2.3.2) Excess methane: Amount of water is less than stoichiometric requirement

In this case, there is less water than the amount required for converting the initial amount of methane into hydrate, i.e. $n_{w,i}<N\times n_{g,i}$. Therefore, the initial water would be completely used to form hydrate (Fig. 2-3d) and the final methane hydrate volume would be:

$$V_{h,f} = \frac{1}{N}\frac{\bar{V}_h}{\bar{V}_w}V_{w,i} \tag{2.13}$$

Thus the final volume of methane, $V_{g,f}$, would be:

$$V_{g,f} = V_{g,i} - \underbrace{\frac{1}{N}\frac{\bar{V}_g}{\bar{V}_w}V_{w,i}}_{Consumed} \tag{2.14}$$

Therefore, the final total volume for the excess methane case would be:

$$V_{tot,f} = V_{g,f} + V_{h,f} = V_{g,i} + \frac{1}{N}\left(\frac{\bar{V}_h - \bar{V}_g}{\bar{V}_w}\right)V_{w,i} \tag{2.15}$$

Hence, the amount of volume reduction in the excess methane case, $\Delta V_{EG} = V_{tot,i} - V_{tot,f}$, would be:

$$\Delta V_{EG} = \underbrace{(V_{g,i} + V_{w,i})}_{Init.\ Vol.} - V_{tot,f} = V_{w,i}\left(1 - \frac{\bar{V}_h - \bar{V}_g}{N\bar{V}_w}\right) \tag{2.16}$$

Similar to the excess water case, the normalized hydrate volume and the normalized volume change can be calculated by Eqs. (2.17) and (2.18).

$$\frac{V_{h,f}}{V_{tot,i}} = \frac{1}{N}\frac{\bar{V}_h}{\bar{V}_w}S_{w,i} \tag{2.17}$$

$$\frac{\Delta V_{EG}}{V_{tot,i}} = \left(1 - \frac{\bar{V}_h - \bar{V}_g}{N\bar{V}_w}\right)S_{w,i} \tag{2.18}$$

In the above equations, $S_{w,i}$ denotes the initial volume fraction of the aqueous phase.

In addition to the two general cases introduced in (2.3.1) and (2.3.2), there exists a theoretical case which takes place only if the gaseous and aqueous phases are initially at the exact stoichiometric balance for hydrate formation, i.e. $n_{w,i}=N\times n_{g,i}$. In this

case, the final state of the system will be having hydrate only (Fig. 2-3c). Performing a similar analysis to those discussed earlier, it can be shown that the final total volume in this case would be:

$$V_{tot,f} = V_{h,f} = \frac{1}{N}\frac{\bar{V}_h}{\bar{V}_w}V_{w,i} = V_{g,i}\frac{\bar{V}_h}{\bar{V}_g} \tag{2.19}$$

Final total volume normalized by the initial volume of the system gives:

$$\frac{V_{tot,f}}{V_{tot,i}} = \frac{1}{N}\frac{\bar{V}_h}{\bar{V}_w}S_{w,i} = \frac{\bar{V}_h}{\bar{V}_g}S_{g,i} \tag{2.20}$$

And the normalized system volume change is:

$$\Delta V = S_{w,i}\left(1-\frac{\bar{V}_h-\bar{V}_g}{N\bar{V}_w}\right) = S_{g,i}\left(1-\frac{\bar{V}_h-N\bar{V}_w}{\bar{V}_g}\right) \tag{2.21}$$

Note that the above is true only if $n_{w,i}=N\times n_{g,i}$ or equivalently $S_{w,i} = \frac{N\bar{V}_w}{\bar{V}_g}S_{g,i}$.

Fig. 2-4 shows a color map of methane hydrate volume normalized by the initial system volume, $V_{h,f}/V_{tot,i}$, as a function of methane density and initial volume fraction of methane inside the closed system. Note that methane density is a function of pressure and temperature of the system; therefore, the effect of pressure and temperature is reflected here in terms of methane density. The normalized methane hydrate volumes are confined between 0 and ~$0.55V_{tot,i}$ over the methane gas density range shown in Fig. 2-4. The latter covers the methane density values under typical pressures and temperatures of hydrate-bearing sediments in the subsurface.

Fig. 2-5 shows a color map of the volume change normalized by the initial total volume, $\Delta V / V_{tot,i}$, as a function of initial methane density and initial volume fraction of methane inside the closed system. This figure along with Fig. 2-4, may be used to estimate the final hydrate volume and the remaining phase volume (aqueous phase or gaseous phase) in a closed system. The white dashed line in Fig. 2-4 and Fig. 2-5 indicates the boundary between excess water and excess methane cases. More specifically, the area to the right of the white dashed line represents excess methane situations and the left side of the dashed line represents excess water cases. It can be shown that the white dashed line is described by Eq. (2.22).

$$\rho_g = \frac{1}{N}\left(\frac{1-S_{g,i}}{S_{g,i}}\right)\left(\frac{MW_g}{MW_w}\right) \tag{2.22}$$

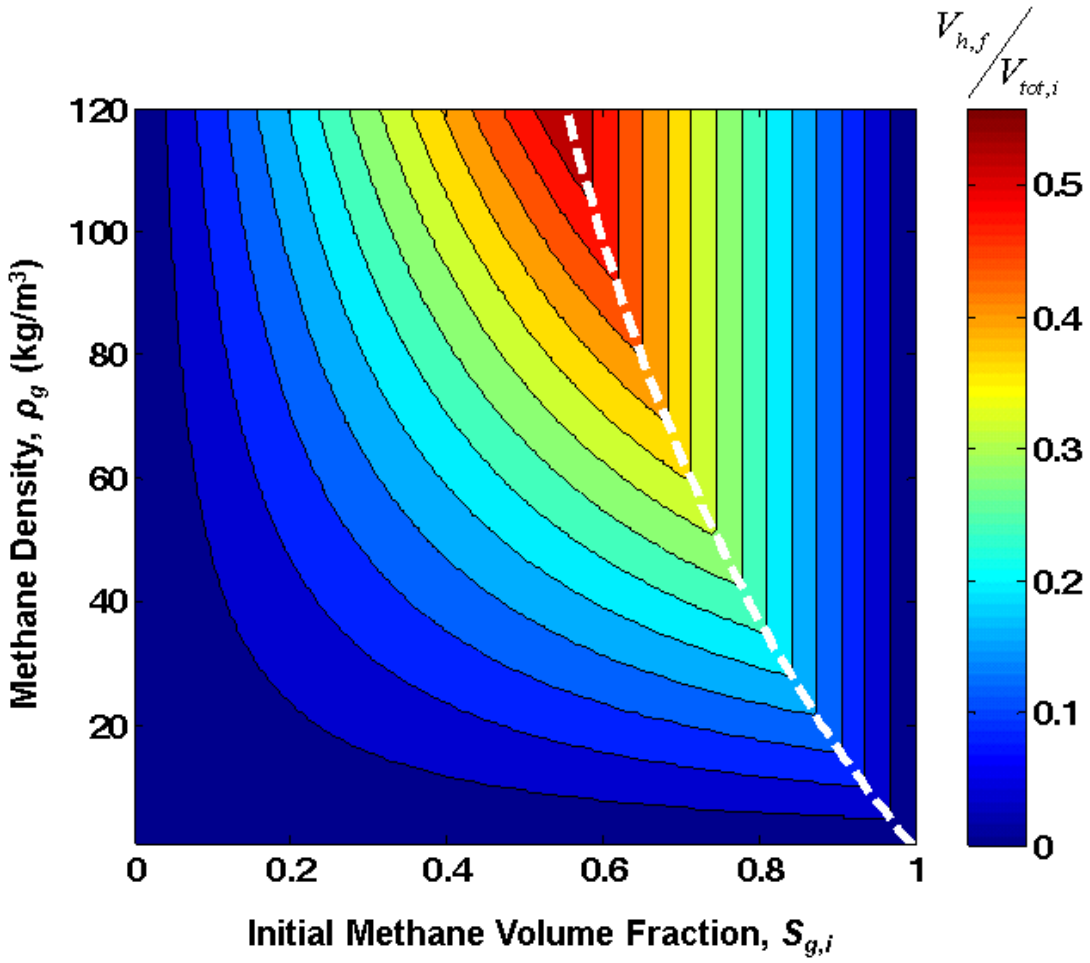

Fig. 2-4. Volume of methane hydrate normalized by the initial total volume, $V_{h,f}/V_{tot,i}$, as a function of initial methane volume fraction and methane density. The white dashed line indicates the boundary between excess water and excess methane cases.

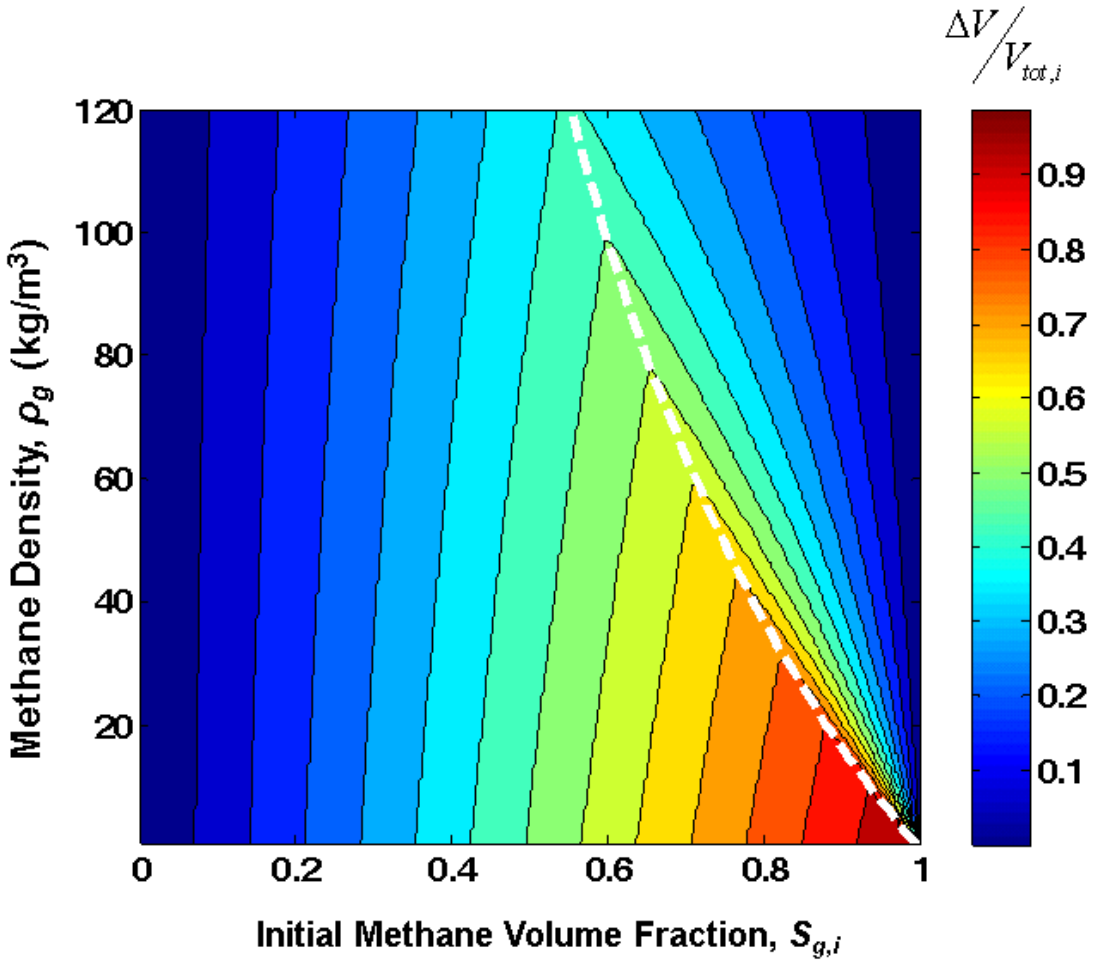

Fig. 2-5. Total volume change normalized by the initial total volume, $\Delta V/V_{tot,i}$ as a function of initial methane volume fraction and methane density. The white dashed line indicates the boundary between excess water and excess methane cases.

Fig. 2-6 shows hydrate volume and total final volume normalized by the initial total volume, when $\rho_g = 55 kg/m^3$, versus initial volume fraction of gas inside a closed system. The solid line indicates the normalized methane hydrate volume and the dashed line is the normalized final total volume. In fact, the difference between the dashed line and the solid line is the normalized volume of the remaining phase (either gaseous phase

or aqueous phase). The red area shows that the remaining phase is gas (excess methane) and the blue area indicates that the remaining phase is aqueous (excess water).

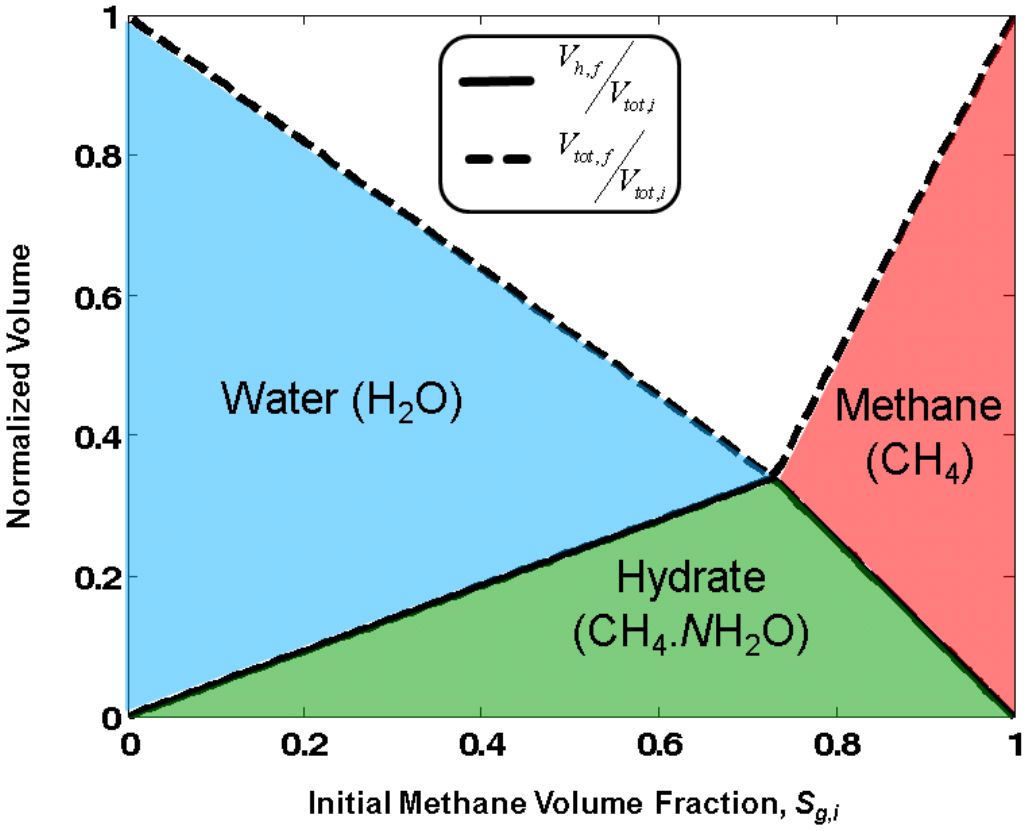

Fig. 2-6. Hydrate Volume and total final volume normalized by the initial total volume, for ρ_g = 55 kg/m^3, versus initial volume fraction of gas inside a closed system.

Hydrate formation in closed systems was investigated. However, in natural systems such as the subsurface porous media, open systems (where fluid phases can leave or enter) are expected rather than closed systems. Therefore, it is of higher interest to investigate hydrate formation in open systems. Section (2.4) focuses on methane hydrate formation in an open system, where methane and water are both allowed into the system during hydrate formation.

2.4) MODEL OF HYDRATE FORMATION FROM FREE GAS AND AQUEOUS PHASE: OPEN SYSTEM

In the model of Fig. 2a, both water and methane are allowed to enter the box to compensate for the volume reduction during hydrate formation and thus maintain the pressure. Hydrate will keep forming until either methane or water is exhausted. Two general cases can be considered in terms of the initial and transported amounts of water, $n_{w,i}$ and Δn_w, and methane, $n_{g,i}$ and Δn_g.

2.4.1) Excess water: Amount of water exceeds stoichiometric requirement

In this case the total number of moles of water, $n_{w,i} + \Delta n_w$, is more than the stoichiometric amount of water required to convert the total amount of methane into hydrate, $N(n_{g,i} + \Delta n_g)$. Therefore, all the gas is consumed to form n_h moles, equivalent to a volume $V_{h,f}$, of methane hydrate and thus,

$$V_{w,f} = V_{tot} - V_{h,f} \tag{2.23}$$

where V_{tot} denotes the total volume of the box and $V_{w,f}$ is the final water volume inside the box. Furthermore,

$$n_{h,f} = \frac{V_{h,f}}{\bar{V}_h} = (n_{g,i} + \Delta n_g) = \frac{V_{g,i} + \Delta V_g}{\bar{V}_g} \tag{2.24}$$

where $V_{g,i}$ denotes the initial gaseous phase volume in the box and ΔV_g is the gaseous phase volume transported into the box. $\bar{V}_h$ and $\bar{V}_g$ are the molar volumes of hydrate and methane, respectively.

The final volume occupied by aqueous phase would be:

$$V_{w,f} = V_{w,i} + \Delta V_w - \underbrace{N \times V_h \frac{\bar{V}_w}{\bar{V}_h}}_{Consumed\ H_2O} \tag{2.25}$$

$V_{w,i}$ and $V_{w,f}$ denote the initial and final water volume inside the box, respectively. ΔV_w is the volume of the aqueous phase transported into the box. Rewriting the right hand side of Eq. (2.25) in terms of moles yields:

$$V_{w,f} = \left[n_{w,i} + \Delta n_w - N(n_{g,i} + \Delta n_g) \right] \bar{V}_w \tag{2.26}$$

The hydrate volume can be written in terms of the initial moles of gas in the box and the molar ratio of gas transported, $R_n = \Delta n_g / (\Delta n_g + \Delta n_w)$, into the box:

$$V_{h,f} = \left[\frac{R_n \left(\bar{V}_g - \bar{V}_w \right) + \bar{V}_w}{R_n \left(\bar{V}_h - (N+1) \bar{V}_w \right) + \bar{V}_w} \right] n_{g,i} \bar{V}_h \tag{2.27}$$

Fig. 2-7b illustrates a typical final state of the system in the case of excess water.

Eqs. (2.23) and (2.26) give the volume of water that enters the box in terms of the final hydrate volume:

$$\Delta V_w = V_{tot} - V_{w,i} + V_{h,f} \left(N \frac{\bar{V}_w}{\bar{V}_h} - 1 \right) \tag{2.28}$$

Similarly, Eq. (2.24) gives the volume of gas that enters the box:

$$\Delta V_g = \frac{\bar{V}_g}{\bar{V}_h} V_h - V_{g,i} \tag{2.29}$$

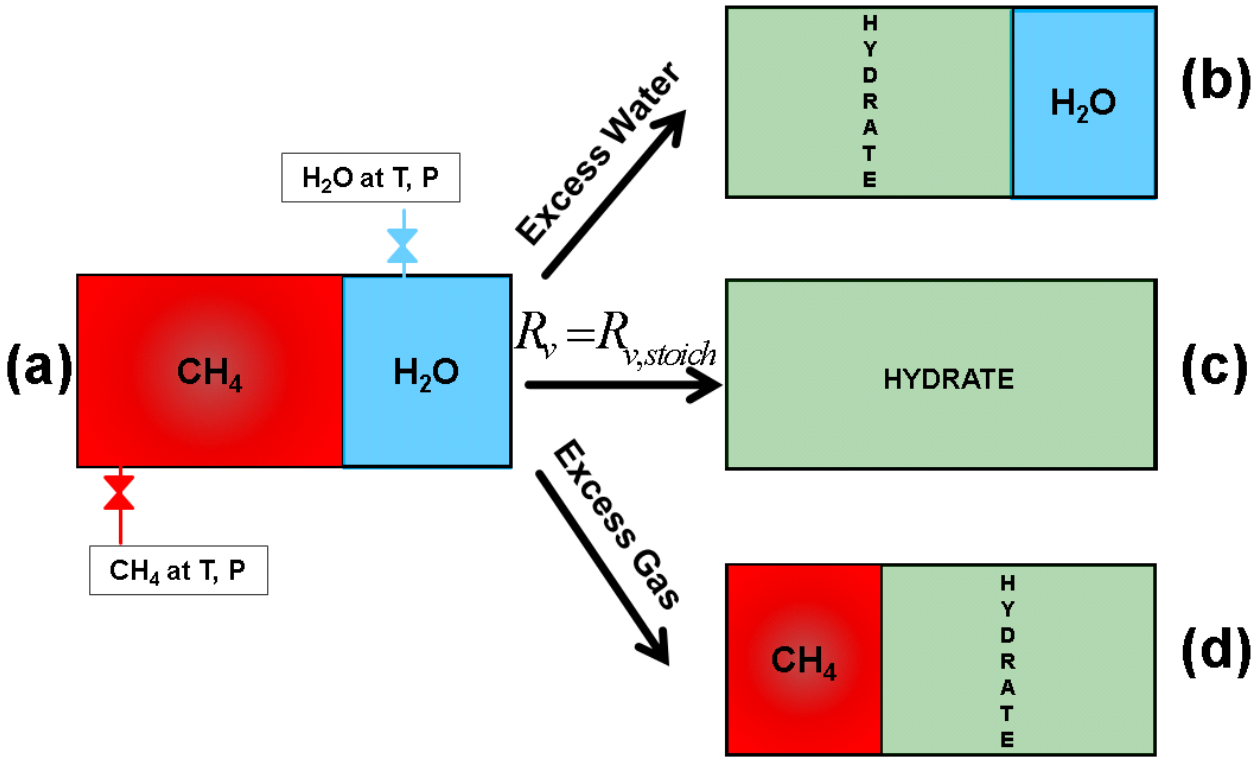

Fig. 2-7. Hydrate formation in an open system: prescribed volumes of CH_4 and H_2O phases are initially present, and CH_4 and H_2O can enter so that T, P are constant during hydrate formation; (b) final state when the total amount of water (initial amount + the amount entered) is more than the stoichiometric requirement (excess water); (c) final state when the total amount of gas and water are at the exact stoichiometric ratio; (d) final state of the open system when the total amount of gas (initial amount + amount entered) is more than the stoichiometric gas requirement (excess gas).

Eqs. (2.28) and (2.29) give the total phase volume transported into the box, $\Delta V_w + \Delta V_g$, as a function of the final hydrate volume, $V_{h,f}$:

$$\Delta V_w + \Delta V_g = K_{trans} V_{h,f} \tag{2.30}$$

where K_{trans} is as follows:

$$K_{trans} = \frac{N\bar{V}_w + \bar{V}_g}{\bar{V}_h} - 1 \tag{2.31}$$

In fact, K_{trans} is the total phase (gaseous + aqueous) volume transported into the box (or any hydrate formation zone) per unit volume of hydrate formed, so that the total system volume is fixed. Note that K_{trans} is independent of the initial amounts of gaseous and aqueous phases.

2.4.2) Excess methane: Amount of water is less than stoichiometric requirement

In this case, there is more methane than the amount required for converting the total amount of water into hydrate, i.e.:

$$n_{g,i} + \Delta n_g > \frac{1}{N}(n_{w,i} + \Delta n_w) \tag{2.32}$$

Therefore, all the water is consumed to form $n_{h,f}$ moles, equivalent to a volume $V_{h,f}$ of methane hydrate. Fig. 2-7d illustrates a typical final state of the box in the case of excess methane. A development analogous to that in Section (2.4.1) yields the final hydrate volume as a function of R_n and the volumes of methane and water that enter the box:

$$V_{h,f} = \left[\frac{R_n\left(\bar{V}_g - \bar{V}_w\right) + \bar{V}_w}{R_n\left((N+1)\bar{V}_g - \bar{V}_h\right) + \left(\bar{V}_h - \bar{V}_g\right)} \right] n_{w,i}\bar{V}_h \tag{2.33}$$

$$\Delta V_g = V_{tot} - V_{g,i} + V_h\left(\frac{\bar{V}_g}{\bar{V}_h} - 1\right) \tag{2.34}$$

$$\Delta V_w = N\frac{\bar{V}_w}{\bar{V}_h}V_h - V_{w,i} \tag{2.35}$$

Eqs. (2.34) and (2.35) show that the total phase volume transported into the box, $\Delta V_w+\Delta V_g$, is governed by Eq. (2.30) regardless of having an excess water or excess methane case.

Fig. 2-7c shows a special case where the final state of the system is having hydrate only. This happens only if

$$\frac{n_{w,i}+\Delta n_w}{n_{g,i}+\Delta n_g}=N \tag{2.36}$$

Combining Eqs. (2.24) and (2.36) gives $\Delta n_g=\Delta n_{g,stoich}$, required for this special case to happen, as:

$$\Delta n_{g,stoich}=\frac{V_{tot}}{\bar{V}_h}-n_{g,i} \tag{2.37}$$

Eqs. (2.36) and (2.37) give:

$$\Delta n_{w,stoich}=N\frac{V_{tot}}{\bar{V}_h}-n_{w,i} \tag{2.38}$$

Eqs. (17) and (18) show that the value of R_n for this special case, Eq. (2.39), depends on the initial state, $n_{g,i}$ and $n_{w,i}$. For a given initial phase content, $R_n < R_{n,stoich}$ represents an excess aqueous phase case while $R_n > R_{n,stoich}$ shows an excess gas case.

$$R_{n,stoich}=\frac{\Delta n_{g,stoich}}{\Delta n_{g,stoich}+\Delta n_{w,stoich}} \tag{2.39}$$

Based on the formulations in (2.4.1) and (2.4.2) , assuming V_{tot} is fixed, two independent parameters exist. For example, one choice of independent parameters is $n_{g,i}$

and Δn_g, from which a final V_h and $V_{g,f}$ (or V_h and $V_{w,f}$ depending on values of independent parameters) is obtained. Another choice is $n_{g,i}$ and V_h from which Δn_g and Δn_w and thus R_n is obtained.

2.5) APPLICATION OF THE HYDRATE FORMATION MODEL TO NATURAL POROUS MEDIA AS OPEN SYSTEMS

In order to use the above hydrate formation model in porous media as open systems, it is useful to express the box model in terms of phase saturations in a volume of sediment containing an initial gaseous/aqueous phase saturations (Fig. 2-8). To do so, one pore volume of the sediment (porosity times total sediment volume) can be considered as the open box in the model. Dividing the preceding expressions by V_{tot} (=1 pore volume), $V_{g,i}$, $V_{g,f}$, $V_{w,i}$, $V_{w,f}$ and $V_{h,f}$ are replaced by phase saturations, $S_{g,i}$, $S_{g,f}$, $S_{w,i}$, $S_{w,f}$ and $S_{h,f}$, respectively. Similarly, the transported phase volumes ΔV_w and ΔV_g are replaced by dimensionless volumes, $\Delta V_{w,d}$ and $\Delta V_{g,d}$. For instance, Eq. (2.30) can be extended to calculate the total pore volumes of gas and aqueous phase transported into a sediment as a function of hydrate saturation, as in Eq. (2.40).

$$\Delta V_{g,d} + \Delta V_{w,d} = K_{trans} S_{h,f} \tag{2.40}$$

We define R_v as a volumetric version of R_n, convenient for calculations in sediments:

$$R_v = \frac{\Delta V_g}{\Delta V_g + \Delta V_w} = \frac{\Delta n_g \bar{V}_g}{\Delta n_g \bar{V}_g + \Delta n_w \bar{V}_w} \tag{2.41}$$

It can be shown that R_v and R_n are related as:

$$R_v = \frac{R_n \bar{V}_g}{R_n \left(\bar{V}_g - \bar{V}_w \right) + \bar{V}_w} \tag{2.42}$$

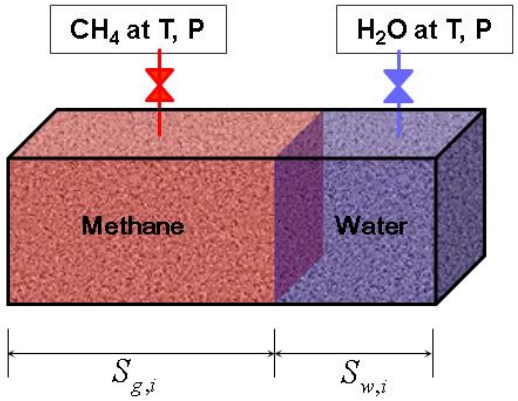

Fig. 2-8. A sediment box containing an initial methane gas and water saturation of $S_{g,i}$ and $S_{w,i}$, respectively. Methane and water are shown separated merely for the sake of illustration.

When the model is applied to gas accumulations in sediment, two independent parameters are constrained accordingly. For example, one constrained parameter is the initial gas saturation inside the sediment, $S_{g,i}$. However, constraining ΔV_g (or R_v) requires more study. Here we treat R_v as a free parameter and examine how system behavior changes with R_v. An alternative is to consider $S_{g,i}$ and S_h as constrained parameters and determine R_v (or ΔV_g and ΔV_w).

Combining Eqs. (2.27) and (2.42) and replacing volumes with saturations, gives the final hydrate saturation for the excess water case as a function of R_v and initial gas saturation, $S_{g,i}$, as:

$$S_{h,f} = \frac{\bar{V}_h}{R_v \left(\bar{V}_h - \bar{V}_g - N\bar{V}_w \right) + \bar{V}_g} S_{g,i} \tag{2.43}$$

Similarly, for the excess methane case Eq. (2.44) holds.

$$S_{h,f} = \frac{\bar{V}_h}{R_v\left(-\bar{V}_h + \bar{V}_g + N\bar{V}_w\right) + \bar{V}_h - \bar{V}_g}\left(1 - S_{g,i}\right) \tag{2.44}$$

Fig. 2-9 shows the corresponding curves for a set of values for initial gas/water saturation within a control volume of sediment (with unit pore volume). Temperature and pressure were assumed T=2˚C and P=6.5MPa (averaged temperature and averaged hydrostatic pressure over depth along the hydrate-bearing interval in the Mount Elbert well). Using Peng-Robinson equation of state methane density was calculated to be 55 kg/m^3 at the latter pressure and temperature. Density of aqueous and hydrate phases were taken as 1000 kg/m^3 and 914 kg/m^3, respectively. Each curve in Fig. 2-9 passes through S_h=1 when R_v=$R_{v,stoich}$. Using either Eq. (2.43) or (2.44) it can be shown that $R_{v,stoich}$ can be written as a function of initial gas saturation, and molar volumes of aqueous, gaseous and hydrate phases, Eq. (2.45).

$$R_{v,stoich} = \frac{S_{g,i}\bar{V}_h - \bar{V}_g}{\bar{V}_h - \bar{V}_g - N\bar{V}_w} \tag{2.45}$$

Regardless of the initial phase saturations, for values of R_v<$R_{v,stoich}$ the final state has only hydrate and water phases present (excess water) and for R_v>$R_{v,stoich}$ the final state has hydrate and gas phases only (excess gas). Therefore, for values of $S_{g,i}$ for which Eq. (2.45) gives a value of $R_{v,stoich}$ >1, the final state of the system would be having hydrate and aqueous phase only, regardless of the value of R_v. The reason is that if $R_{v,stoich}$ >1, then for any value of 0< R_v <1 , R_v would be smaller than $R_{v,stoich}$. In fact this latter case,

$R_{v,stoich}$ >1, happens over a small range of $S_{g,i}$ which satisfies inequality (2.46). Under the above pressure and temperature (T=2˚C and P=6.5MPa), this happens when $S_{g,i}$< 0.2.

$$S_{g,i} < 1 - \frac{N\bar{V}_w}{\bar{V}_h} \tag{2.46}$$

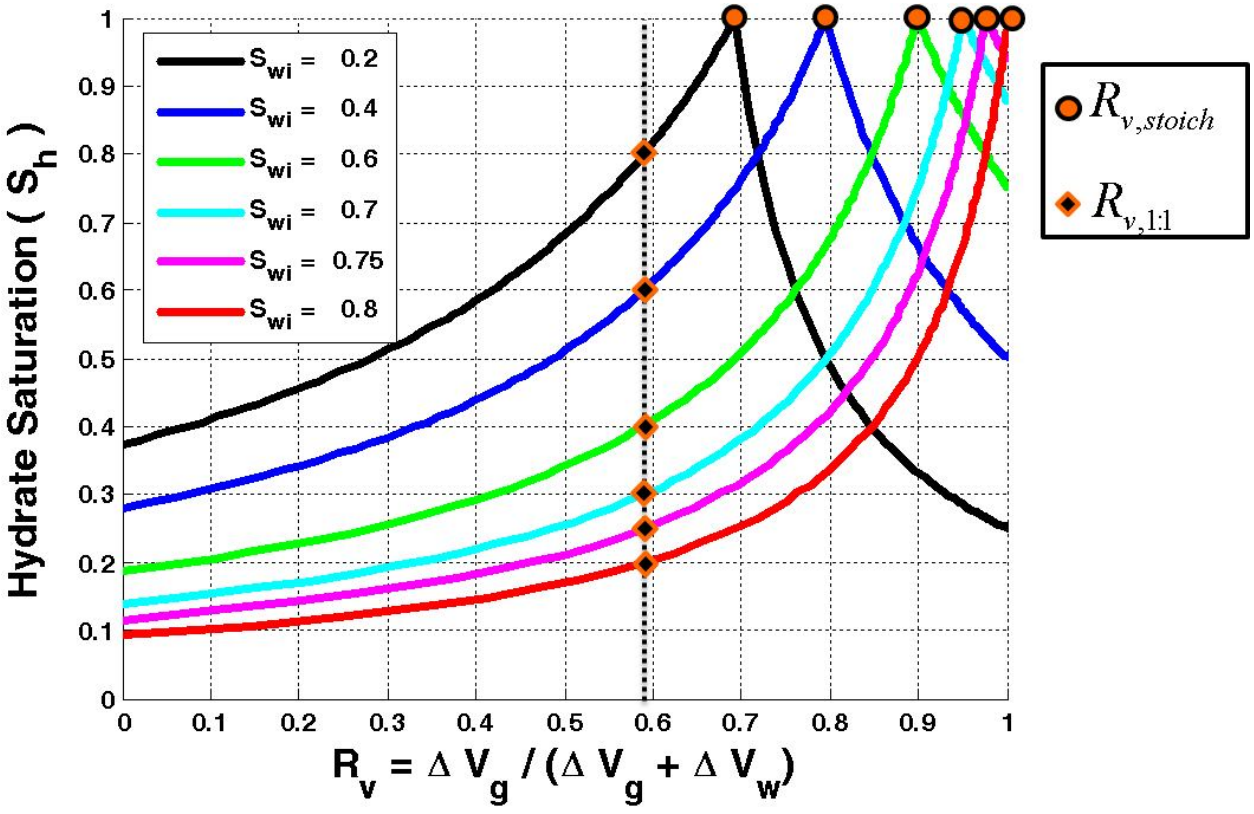

Fig. 2-9. Final hydrate saturation in an open volume of sediment at 2°C, 6.5 MPa depends strongly on initial water saturation and R_v. Special points at which S_h is the maximum possible value are shown as $R_{v,stoich}$ on the curves. To the left of $R_{v,stoich}$ the final state consists of hydrate and water; to the right, of hydrate and gas. Neutral points at which S_h=$S_{g,i}$ are shown as $R_{v,1:1}$ on the curves, which is equal to 0.59 at this temperature and pressure.

The value of R_v at which $S_h=S_{g,i}$ is denoted $R_{v,1:1}$, shown as diamonds in Fig. 2-9. If the final hydrate saturation S_h is larger than initial gas saturation $S_{g,i}$, then the final water saturation $S_{w,f}$ must be less than $S_{w,i}$. In this case the hydrate formation process must have involved drainage (reducing the wetting phase saturation). Conversely, if $S_h<S_{g,i}$, thus $S_{w,f}>S_{w,i}$, then the conversion required imbibition. The value of $R_{v,1:1}$ thus represents a neutral point between imbibition occurring during hydrate formation for $R_v<R_{v,1:1}$ and drainage occurring for $R_v>R_{v,1:1}$. It can be shown that the value of $R_{v,1:1}$ depends only on the phase densities and hydration number, N and is independent of initial saturations:

$$R_{v,1:1}=\frac{\bar{V}_g-\bar{V}_h}{N\bar{V}_w+\bar{V}_g-\bar{V}_h} \tag{2.47}$$

Other information of interest provided by the above hydrate formation model would be the dimensionless volumes, volumes normalized by the total pore volume inside the sediment box in which hydrate forms, of aqueous phase ($\Delta V_{w,d}$) and gaseous phase ($\Delta V_{g,d}$) transported into the sediment. Combining Eqs. (2.40), (2.43), and (2.44) and using the definition of R_v, pore volumes of transported gaseous phase can be expressed as:

$$\Delta V_{g,d}=\begin{cases} R_v K_{trans}\dfrac{\bar{V}_h}{R_v\left(\bar{V}_h-\bar{V}_g-N\bar{V}_w\right)+\bar{V}_g}S_{g,i} & ;R_v<R_{v,stoich} \\ R_v K_{trans} & ;R_v=R_{v,stoich} \\ R_v K_{trans}\dfrac{\bar{V}_h}{R_v\left(-\bar{V}_h+\bar{V}_g+N\bar{V}_w\right)+\bar{V}_h-\bar{V}_g}\left(1-S_{g,i}\right) & ;R_v=R_{v,stoich} \end{cases} \tag{2.48}$$

where K_{trans} is defined as in Eq. (2.31). The aqueous phase transported volume then can be calculated from Eq. (2.48) using the calculated value of $\Delta V_{g,d}$ from Eq. (2.48) as:

$$\Delta V_{w,d} = K_{trans} S_{h,f} - \Delta V_{g,d} \tag{2.49}$$

Fig. 2-10 shows transported methane, transported water and the total methane and water transported, calculated from Eqs. (2.48) and (2.49), versus R_v for an initial water saturation of $S_{w,i}$ = 0.2 ($S_{g,i}$ = 0.8). Note that in the excess water case, the amount of transported methane is a much stronger function of R_v compared to the amount of transported water which remains almost constant with R_v. In the excess methane case, both transported water and methane change sharply with R_v. An interesting point is that the total amount of fluid transported is in the order of one pore volume which is quite substantial.

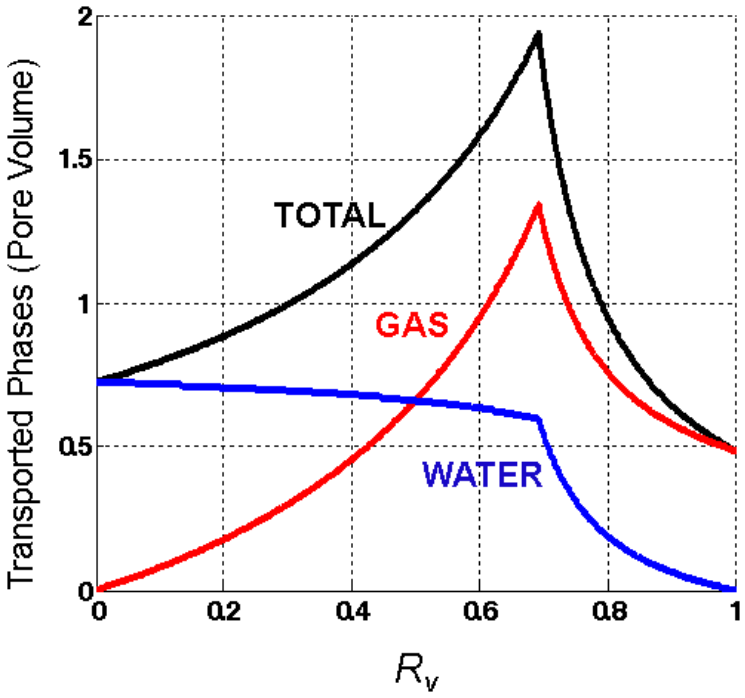

Fig. 2-10. Transported methane, $\Delta V_{g,d}$, transported water, $\Delta V_{w,d}$, and total phase transported, $\Delta V_{g,d} + \Delta V_{w,d}$, during hydrate formation versus R_v for a sediment with initial water saturation of $S_{w,i} = 0.2$ ($S_{g,i} = 0.8$).

From this point in this dissertation, hydrate formation analyses are mainly based on the above saturation-based (using volumetric transport ratio, R_v) equations for open systems, mainly Eqs. (2.43), (2.44) and (2.40), with the main parameters discussed being R_v, $R_{v,1:1}$, $R_{v,stoich}$ and K_{trans}.

In the following chapter hydrate formation inside a sediment column containing a pre-established gas column is investigated.

Chapter 3: Gas reservoir Conversion to Hydrate: Bed-Scale Volumetric and Sedimentological Considerations

3.1) BACKGROUND

In chapter 2 a stoichiometric transport-associated hydrate formation model was introduced. Adopting the aforementioned model, this chapter investigates hydrate formation inside a 1-D sediment column containing a gas accumulation. First a homogenous sediment column is considered and ultimately hydrate formation inside heterogeneous sediments, i.e. with varying grain size distribution, are considered to reveal the paramount sedimentological control on hydrate saturation distribution in "*converted free gas reservoirs*". A key premise here is that the gas column (representing an ancient gas reservoir) is converted to hydrate as the sediment column is gradually cooled from the top. The latter, as mentioned in chapter 1, would be equivalent to moving the GHSZ down through the gas column and gradually converting the gas column into hydrate.

3.2) EFFECT OF VOLUME CHANGE DURING HYDRATE FORMATION ON THE RESULTING HYDRATE SATURATION PROFILE FROM A FINITE COLUMN OF GAS IN A *HOMOGENEOUS* SEDIMENT COLUMN

The model introduced in chapter 2 applies to a box of sediment with known initial gas/water saturation. By treating a sediment interval as a column of many such boxes, a given gas/water saturation distribution along the column and a chosen value for R_v uniquely determine the hydrate saturation profile. Accumulations are considered as a vertical stack of sediment boxes here since the proposed models in this dissertation are 1-D models. However, the latter consideration would not be appropriate for 3-D modeling because the box model does not account for lateral variations in sediment properties.

Consider a column of methane gas and water, in which the gaseous phase is no longer connected to original source of charge, established below a seal in a homogeneous sediment. Fig. 3-1a shows gas saturation versus depth when the BGHSZ is at the top of the gas column. As the BGHSZ descends, Fig. 3-1b, the gas and water above the BGHSZ achieve the thermodynamic condition suitable for hydrate formation, hydrate forms, and the model of chapter 2 applies.

Fig. 3-1b shows the case in which both gaseous (red arrow) and aqueous (blue arrow) phases enter the vacant space created during hydrate formation. The phase volumes that enter depend on $S_{g,i}$ and R_v. The methane that enters is then converted to hydrate. As mentioned above, the gas column is assumed disconnected from the original source of charge; therefore, the transported methane is provided from below the hydrate formation zone within the same column of gas. Consequently, a volume of water, ΔV_w^{GWC}, imbibes from below the gas column to replace the transported gas. This causes the gas-water contact (GWC) to rise, establishing a residual gas saturation at the base of the accumulation, as shown in Fig. 3-1c. As the BGHSZ descends and the GWC rises, these

two levels will meet at a certain depth and thereafter the BGHSZ enters the residual gas zone below the GWC. When the BGHSZ enters the residual gas zone, R_v would be zero during hydrate formation since no gas can flow at residual gas saturation, S_{gr}. The continuation of this process as the BGHSZ descends ultimately yields a hydrate profile with large saturations in the upper portion of the column and small saturations below (Fig. 3-1d). This profile differs qualitatively from the initial gas saturation profile (Fig. 3-1a) and is a characteristic result of the model.

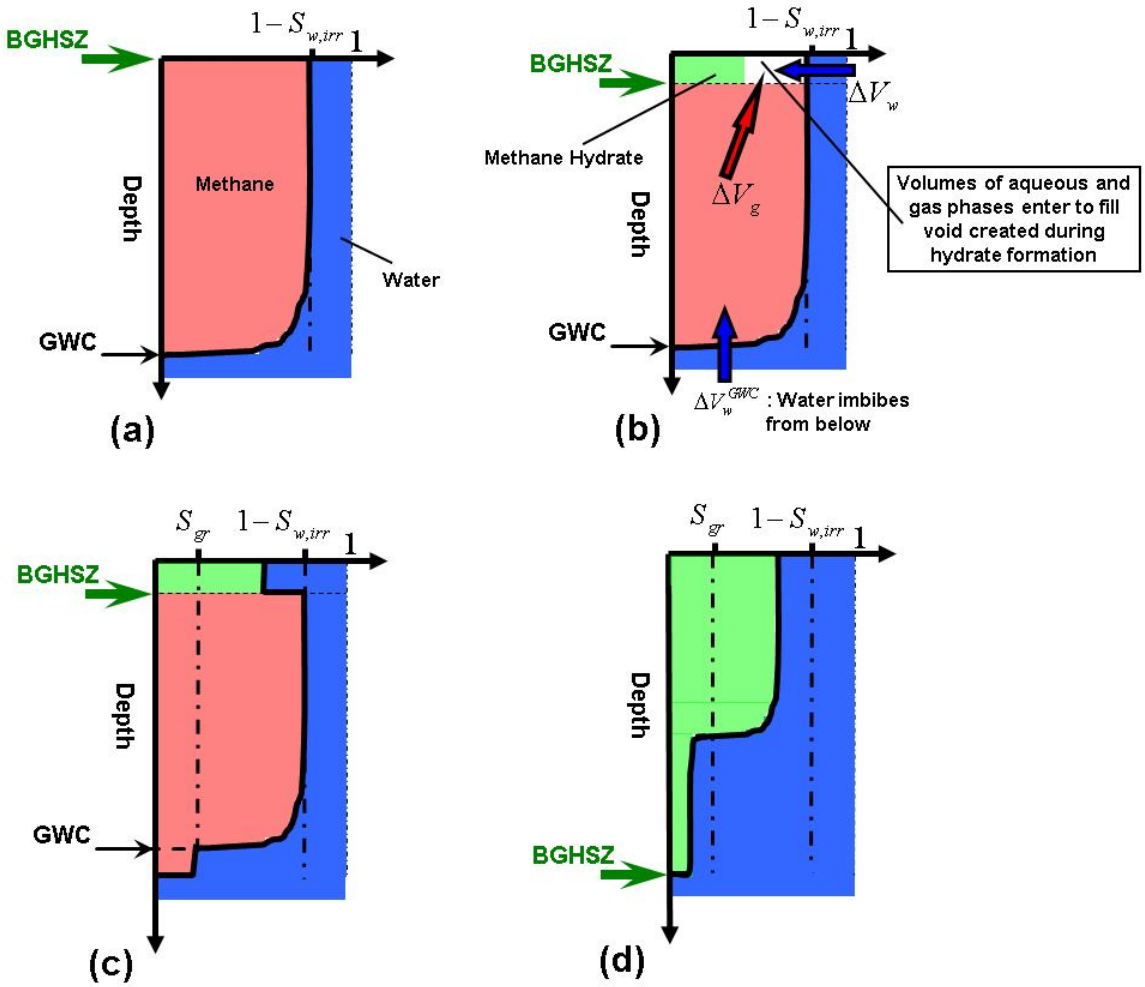

Fig. 3-1-(a) The initial state of a gas accumulation below a seal in a homogeneous sediment which is below the BGHSZ. (b) After little descent of the BGHSZ. The volume reduction during hydrate formation is shown in white. Gaseous and aqueous phases move into GHSZ to compensate for the volume change. (c) The migrated gas forms more hydrate; the final hydrate saturation in the sediment layer newly located in GHSZ can be estimated from the box model of Fig. 1-11 and Fig. 2-7 if a value of R_v is assumed. (d) The hydrate saturation profile $S_h(z)$ after the BGHSZ has descended to the lowermost part of the gas column differs significantly from $S_{g,i}(z)$ of (a). This is a consequence of the volume change during hydrate formation in a finite vertical column of gas.

3.3) EFFECT OF HETEROGENEITY (GRAIN SIZE VARIATION ALONG DEPTH) ON SATURATION DISTRIBUTION

In contrast to the homogeneous sediment column shown in Fig. 3-1, heterogeneity is expected in natural sediments. Grain size variation with depth causes variation in capillary entry pressure along the sediment column.

The reduction in gas-water capillary pressure along the gas column, due to the rise of GWC, will have two implications in heterogeneous sediments. First, the gas phase saturation at each depth decreases, with the amount of decrease depending on the characteristic capillary curve for the sediment at each depth. Second, the capillary pressure at one or more depths may fall below the capillary entry pressure for sediment at that depth. If this occurs the initially single column of gas breaks into two (or more) columns of gas no longer in communication with each other. Therefore, the capillary entry pressure profile is crucial in our model. Fig. 3-2 illustrates hydrate formation from a pre-established gas accumulation below a seal in a heterogeneous sediment composed of four distinct homogeneous layers (Fig. 3-2a). The gas accumulation is cooled from the top, i.e. the BGHSZ descends, and consequently converted into hydrate. As the BGHSZ descends, the gas above the BGHSZ as well as some gas migrated from below would form hydrate above the BGHSZ. Similar to that for a homogeneous case, the migrated gas from below is replaced by aqueous phase, resulting in ascent of GWC. The gas-water capillary pressure decreases and intersects the capillary entry pressure at the top of the bottom-most layer and thus the initially single gas column breaks into two non-communicating gas columns: gas columns I and II (Fig. 3-2b). Therefore, gas column II would not contribute in further hydrate formation within gas column I. When the BGHSZ reaches the top of gas zone II, all the gas above this point is converted into hydrate (Fig. 3-2c). The final hydrate saturation profile (Fig. 3-2d), after the BGHSZ has descended to

the lowermost part of the gas column, differs significantly from the initial gas saturation profile shown in Fig. 3-2a. This is a consequence of the volume change during hydrate formation in a finite column of gas, combined with the vertical variation in capillary entry pressure of the host sediment.

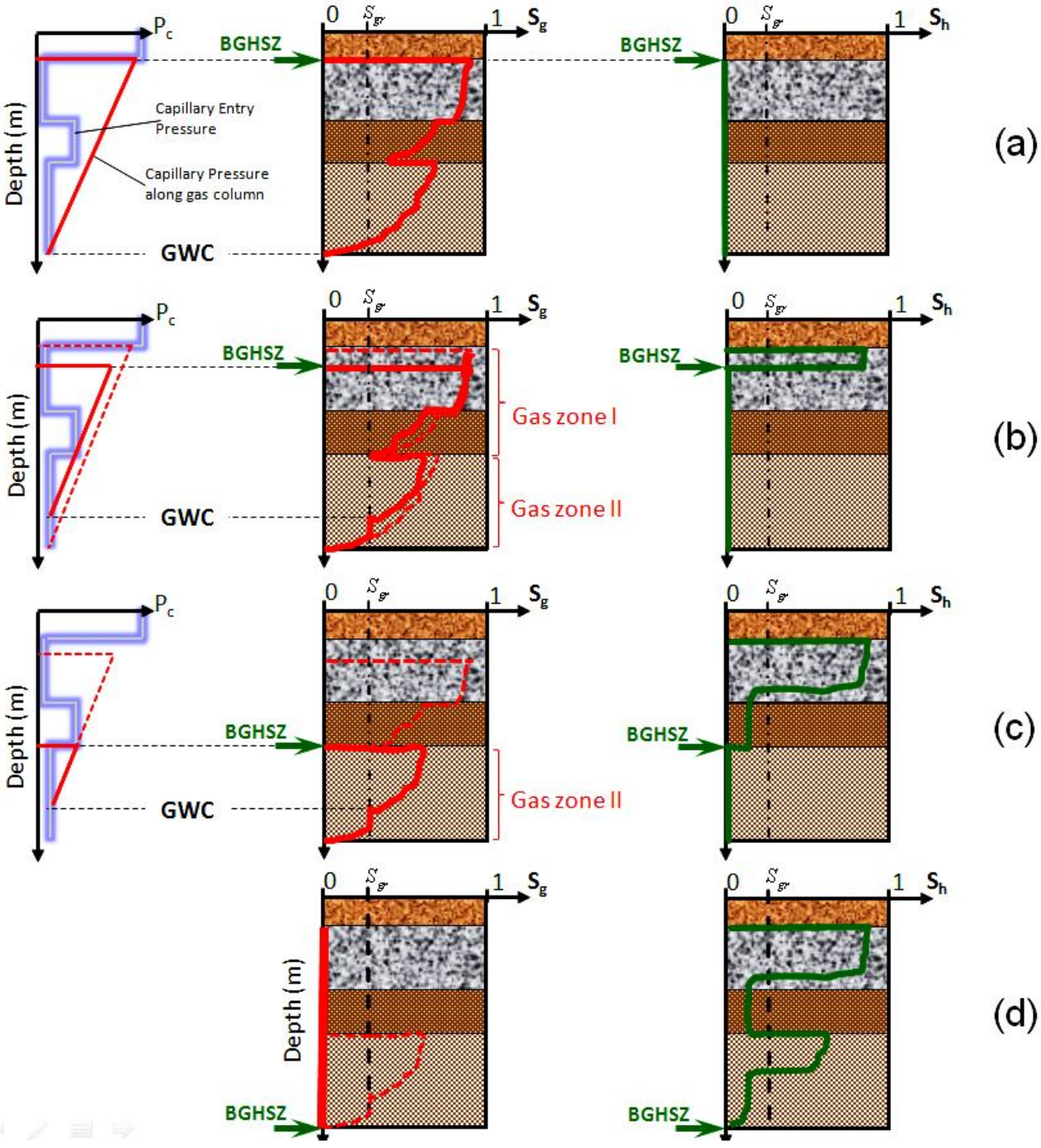
Pc
Depth (m)
BGHSZ
Capillary Entry Pressure
Capillary Pressure along gas column
GWC
0
S_{gr}
1
Sg
Sh
(a)
Gas zone I
Gas zone II
(b)
(c)
(d)

Fig. 3-2- Hydrate formation from a pre-established gas accumulation in a heterogeneous sediment. The gas accumulation is cooled from the top, i.e. the BGHSZ descends, and consequently converted to hydrate from top to bottom. The left column shows profile of capillary entry pressure versus depth (glowing blue line) as well as profile of capillary pressure along the gas column versus depth (red line). The middle column shows gas saturation versus depth along the sediment, and the right column shows hydrate saturation versus depth. (a) Capillary pressure, gas saturation and hydrate saturation versus depth when the BGHSZ is at the top of the gas column. (b) After little descent of the BGHSZ the gas above the BGHSZ as well as some gas migrated from below would form hydrate above the BGHSZ; the final hydrate saturation in the sediment layer newly located in GHSZ can be estimated from the box model of Fig. 1-11 and Fig. 2-7 if a value of R_v is assumed. The migrated gas from below is replaced by aqueous phase, resulting in ascent of GWC. The capillary pressure decreases and intersects the capillary entry pressure at the top of the bottom-most layer. Therefore, the gas below this point would not contribute in further hydrate formation above this point. Capillary pressure and gas saturation of the previous step is shown in dashed line. (c) When the BGHSZ reaches the top of gas zone II, all the gas above this point is converted into hydrate. (d) The hydrate saturation profile $S_h(z)$ after the BGHSZ has descended to the lowermost part of the gas column differs significantly from $S_{g,i}(z)$ of (a).

Measurements of capillary entry pressure are rare, but grain size distributions are often available. Thus we develop a simple relationship between grain size parameters and capillary entry pressure.

The capillary entry pressure for a very well sorted granular media has been related to average grain radius, r_{avg}, as:

$$P_{c,entry} \approx \frac{6\sigma}{r_{avg}} \tag{3.1}$$

where σ is the interfacial tension between the two fluid phases (i.e. gaseous and aqueous phase). Eq. (3.1) has been shown both experimentally (Dawe et al., 1992; Hilpert et al., 2000; Mason and Mellor, 1995) and analytically (Behseresht et al., 2009; Mason and Mellor, 1995).

In poorly sorted sediments Eq. (3.1) is not accurate. However capillary entry pressure is correlated with permeability, which in turn is correlated with grain size distribution. Breyer's equation, Eq. (3.2), relates hydraulic conductivity, K, to grain size distribution in sandy sediments.

$$K = 6\times10^{-4}\,\frac{\rho g}{\mu}\log\left(\frac{500}{U}\right)D_{10}^{2} \tag{3.2}$$

where g is acceleration due to gravity, μ is the dynamic viscosity of the phase flowing through the sediment, ρ is the mass density of the flowing phase, D_{10} is the 10^{th} percentile of grain size in the sediment and U, the coefficient of grain uniformity, is defined as:

$$U = \frac{D_{60}}{D_{10}} \tag{3.3}$$

Permeability, k, is related to hydraulic conductivity by:

$$k = K\frac{\mu}{\rho g} \tag{3.4}$$

Combining Eqs. (3.2) and (3.4) gives:

$$k = 6\times10^{-4}\log(\frac{500}{U})D_{10}^{2} \tag{3.5}$$

Since Eq. (3.1) works best for very well sorted granular media, we find an "equivalent" grain size, r_{eq} of a very well sorted sand that has the same permeability as a poorly sorted sediment. The permeability of very well sorted sediments with grain radius, r, is (Bryant et al., 1993):

$$k = 2.7\times10^{-3}r^{2} \tag{3.6}$$

Combining Eq. (3.5) and (3.6) determines the "equivalent" grain size, r_{eq}:

$$r_{eq} = 0.4714\sqrt{\log(\frac{500}{U})}D_{10} \tag{3.7}$$

We next assume that the capillary entry pressure of the "equivalent well sorted sand" is a good estimate of the capillary entry pressure for the poorly sorted sediment. That is, Eq. (3.1) is used with $r_{avg}=r_{eq}$ to calculate the capillary entry pressure of sediment.

3.4) RESULTS: MODEL APPLICATION TO MOUNT ELBERT WELL

The model was applied to field data from Mount Elbert gas hydrate stratigraphic test well. As mentioned in chapter 1, researchers have suggested that such hydrate accumulations are free gas accumulations converted to hydrate after being placed in the GHSZ (Boswell et al., 2011; Collett et al., 2011). As discussed earlier, Mount Elbert well indicates two zones of large gas hydrate saturation (the D and C sand Units) in the stratigraphically highest portions of those sands (Boswell et al., 2011). High resolution grain size distribution data are also available from the well (Winters et al., 2011).

Analyzing the grain size distribution in different depths of Mount Elbert well data (Winters et al., 2011) reveals that the coefficient of uniformity for majority of depths fall

in the range of $1<U<20$ (Fig. 3-3). In addition, the grain sizes mostly fall between 60 μm and 600 μm. Therefore, the Breyer's estimate of permeability should be applicable (Odong, 2008). Interfacial tension between gas and aqueous phases was estimated to be 65 mN/m at 2°C and 6.5 MPa (Jho et al., 1978). Brine salinity in Mount Elbert well is very small, 4 to 11 ppt, (Torres et al., 2011) and thus has a density very close to that of fresh water, 1000 kg/m^3. Based on these properties and Eq. (3.7), the capillary entry pressure versus depth was calculated from grain size distribution at each depth. Profiles of the 10th and 50th percentile of grain size in sand Units D and C are shown in Fig. 1-10a. The corresponding capillary entry pressure profile is shown as connected dots in Fig. 3-4a.

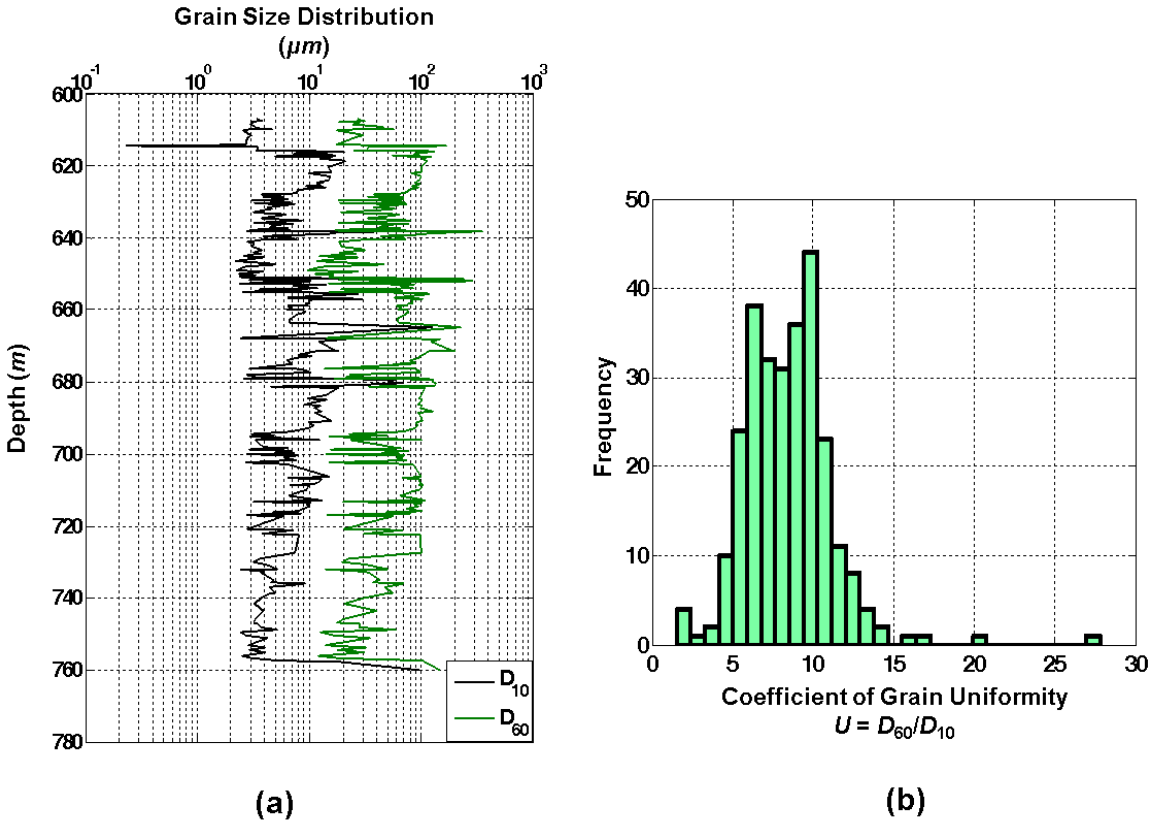

Fig. 3-3- Data from Mount Elbert stratigraphic test well, drilled in the Milne Point unit of Alaska North Slope: (a) 10th percentile, D_{10}, and 60th percentile, D_{60}, of grain size distribution versus depth determined from laser-grain-size analyses (Rose et al., 2011); (b) Coefficient of grain uniformity for 275 samples taken from Mount Elbert depth range of 600m to 760m.

We first consider a hypothetical gas accumulation equivalent to a gas column extending from 614 m to 673 m (i.e. within sand Units D and C) prior to the descent of BGHSZ. The small size of the closure at the top of Unit D (Boswell et al., 2011) would not permit such an accumulation. The purpose of this assumption is to illustrate quantitatively the effect of grain size variation. It is also assumed that the accumulation was no longer connected to the source of charge. Fig. 3-4a shows the estimated gas

saturation profile (red solid line) in the gas reservoir prior to its conversion to hydrate. The profile is obtained from the capillarity characteristics of the host sediment and the presumed depth (673 m) of the original GWC. The latter determines $P_c(z)$ the gas-water capillary pressure profile (dashed line in Fig. 3-4a), which in combination with the estimated capillary entry pressure determines the initial profile of S_g, similar to that explained in Fig. 1-11. For most of the gas column, gas saturation was estimated to be very large, close to 1-$S_{w,irr}$; which was then approximated by 1-$S_{w,irr}$ for simplicity. The smaller gas saturations between 646 m and 650 m are due to the fact that the capillary pressure is only slightly larger than the capillary entry pressure in that interval. Based on nuclear magnetic resonance (NMR) test results reported by Winters *et al.* (2011) the irreducible water saturation, $S_{w,irr}$, varies widely along the hydrate-bearing interval of Mount Elbert well. However, here for simplicity and without affecting the overall behavior of the model $S_{w,irr}$ is assumed to be 20% for the entire column (Behseresht et al., 2009). Imbibition, i.e. aqueous phase displacing gas phase, does occur when hydrate begins to form, forcing gas phase to move upward to the hydrate stability zone. The residual gas saturation at the end of the imbibition, S_{gr}, is assumed to be 30% (Peng et al., 2009).

This long column of gas was supported beneath the clay-rich layer observed at depth of 614 m in Fig. 3-4a. In this hypothetical initial state the gas column is barely connected because the capillary pressure is very close to the capillary entry pressure value at the base of Unit D (depth 650 m, indicated with a hollow circle).

The final input for the model is the value of R_v. For this illustration we set R_v = 0.55 throughout the sediment. As described in section (3.5.2) this value makes physical sense and here we show that it predicts a value of large hydrate saturation similar to the

observed value within major hydrate-bearing sections in Mount Elbert well. The effect of different values of R_v will be discussed in section (3.5.2) .

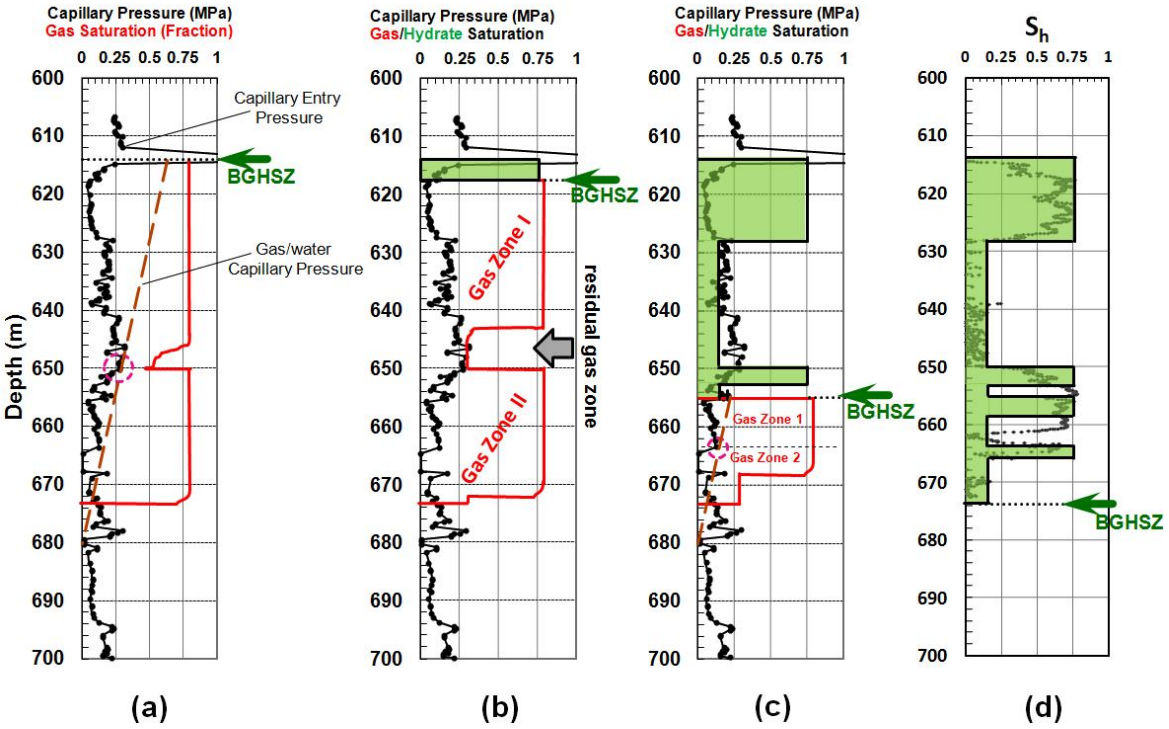

Fig. 3-4- Illustration of model of Fig. 3-2 with grain size distribution from Mount Elbert well and a hypothetical initial gas column. (a) Capillary entry pressure, estimated from grain size distribution and Eqs. (3.1) through (3.7), versus depth (connected dots) along with estimated initial gas saturation (red solid line) when the BGHSZ was above the zone in which hydrate is currently present. Gas/water capillary pressure along the gas column is shown as dashed line. The gas saturation profile changes as the BGHSZ moves down through the gas column and hydrate forms. (b) The BGHSZ has moved 3.5 meters downward. Gas transported from the lower portion of Unit D and water imbibed from below to create gas zone I. Gas zones I and II are no longer in communication due to the capillary barrier between them (shown with an hollow circle) at 650 m. (c) Gas saturation profile (red) when BGHSZ has moved downward through the gas column to a depth of 655m and the resulting hydrate saturation (green fill). Indicated gas zones 1 and 2 are no longer communicating due to the capillary barrier (shown with an hollow circle) at 664 m. (d) Final hydrate saturation profile (using R_v=0.55) after BGHSZ has moved below the bottom of gas column. The log derived hydrate saturations (Lee and Collett, 2011) are shown as dots. Agreement of the magnitudes of saturation is meaningful, but the agreement in locations of the changes between large and small saturation is meaningful only if the structural geology of the environment at the time of formation, 1.8 Ma, would have allowed for the assumed initial gas profile (see text).

As the BGHSZ moves downward into the gas column the GWC rises, the gas-water capillary pressure is reduced along the gas column, and the gas saturation decreases to residual saturation below the new position of the GWC. Crucially, the gas-water capillary pressure falls below the capillary entry pressure of the sediment at 650 m. Because the initial capillary pressure at 650 m is so close to the capillary entry pressure, this happens with the first increment of hydrate formation. Therefore, the originally connected gas column starts acting as two non-communicating columns of gas almost immediately after hydrate starts forming. As a consequence of the early disconnection of the gas in Units C and D the gas that migrates to the GHSZ in Unit D comes only from within Unit D itself. Fig. 3-4b shows an intermediate step when the BGHSZ is at a depth of about 618 m. Note that gas moving to fill the void due to hydrate formation now rises from the bottom of the upper portion of the accumulation, establishing a residual gas saturation between 644 m and 650 m. Water must imbibe into the base of Unit D to replace the migrated gas in this 1-D model.

Fig. 3-4c illustrates the situation after the BGHSZ has descended to a depth of about 655 m. In addition to the initial gas saturation between 650 m and 655 m, some gas from the lower portion of Unit C has been used to form hydrate in the top section of this unit. For R_v= 0.55 the resulting hydrate saturation is 0.75 (cf. Fig. 2-9). The capillary pressure profile intersects the capillary entry pressure profile at a depth of 665 m. Thus the remaining gas column comprises two disconnected regions labeled gas zone 1 and gas zone 2 (Fig. 3-4c). As the BGHSZ keeps moving downward water imbibes from below into the lower part of gas zone 1 to compensate for the volume of gas that moves into the top section of gas zone 1 during hydrate formation. Meanwhile, gas zone 2 saturations

remain essentially unchanged from their initial profile, because the gas zone 1 was disconnected from gas zone 2 prior to hydrate formation in gas zone 1.

The hydrate saturation profile once the BGHSZ has moved to the bottom of the gas column (a depth of about 673m) is shown in Fig. 3-4d. Our prediction is shown as green area and the log-derived hydrate saturations are shown as dots. As mentioned in section (3.2) , in the imbibed portions of the gas zones (e.g. 629 m to 650 m in Unit D), R_v is zero; therefore, when the BGHSZ descends into these portions, only aqueous phase moves to fill the void space that accompanies hydrate formation. For S_{gr} = 0.3, Fig. 2-9 (curve for $S_{w,i}$ = 0.7 evaluated at R_v = 0) yields a hydrate saturation S_h = 0.13.

The key points of this scenario are that the final hydrate saturation profile differs qualitatively from the initial gas saturation profile, and that the model predicts large hydrate saturations of 0.75 in the upper portions of Units C and D, with intervals of small hydrate saturations of 0.13 interspersed between them. The fact that the changes in saturation occur at the same locations as in the well log (Fig. 3-4d) is meaningful only if the structural geology of the formation, also, would have allowed for this initial state (gas column from 614 m to 673 m) over 1.8 million years ago. Otherwise, the coincidence of locations of change in saturations with those from well logs would be fortuitous, because this illustration assumes vertical flow in a gas column from 614 m to 673 m that would not have existed in nature due to the present shallow spill point in Unit D (Boswell et al., 2011). The values of large and small saturation are meaningful, however, and will be discussed in the next section.

3.5) DISCUSSION

3.5.1) Comparing the model behavior with observations from well logs and seismic

For the illustration above, the model predicts a uniform, small saturation of about 13% hydrate in the depth ranges of 628-650 and 666-674 meters. This is the consequence of converting residual gas saturation to hydrate, with the assumption that no additional gas migrated to the BGHSZ as it descended. In this illustration, the one dimension of the model is in the vertical direction. But the same qualitative behavior would occur if the one dimension were along dip in a layer in which gas has accumulated downdip from a crest. That is, as the BGHSZ descends through the dipping accumulation, the required flow of gas and water to the GHSZ would take place along dip, leaving residual gas saturation downdip. Thus the 1-D model would predict a region of large hydrate saturation filling the layer from the crest down to a certain depth above the original GWC, and a region of small hydrate saturation from this depth down to the original GWC. The depth at which the transition from large to small saturation occurred would depend on the size of the original accumulation and grain size variation within the layer in the along-dip direction.

The extension of this idea to an anticline is straightforward: the model predicts small (but not zero) hydrate saturation on the flanks of a structure extending down to the original GWC, with large saturation at the top of the structure. Local pockets of large or small saturation within this gross delineation are possible depending on the variability in grain size. Applying this idea to Mount Elbert, if gas had accumulated within the upper portion of Unit D so as to extend from the top of the structure (i.e. at depth of 614 m in the Mount Elbert well) down toward the flanks, the model would predict a large hydrate saturation in the upper portion of Unit D at and near the center of the structure, with small

hydrate saturations in the upper portion of Unit D along the flanks. This prediction is consistent with observations at Mount Elbert. The well log shows large hydrate saturation in the uppermost 14 m of Unit D. The magnitude of the seismic anomaly is large in the vicinity of the Mount Elbert well, which is located at the top of the structure, and the magnitude decreases toward the flanks of the Mount Elbert accumulation. A reduction of hydrate saturation, alone or in combination with a reduction in reservoir quality, is consistent with a reduction in the magnitude of seismic anomaly (Boswell et al., 2011).

Assuming R_v = 0.55 yields a final hydrate saturation of 75% in the upper portion of unit D. This is similar to the values of the log-derived hydrate saturation profile in the top 14 m of Unit D. It is appropriate to compare the magnitudes of hydrate saturation, even though the initial condition for the illustration is not the same as the situation at Mount Elbert prior to the descent of BGHSZ. The hydrate formation process in the model is local, so that the final hydrate saturation at any depth depends on the initial gas saturation at that depth but not on which direction the fluids move to reach that location. Hence it reasonable to conclude that 55% of the fluid volume that moved into the zone of large hydrate saturation at Mount Elbert was gas. The implications of this value of R_v are discussed below in more detail.

The initial condition assumed in the illustration leads to underestimating the thickness of the large hydrate saturation portion in Unit C between 650 m and 660 m. The reason is that the mass of methane in the hydrate exceeds the mass of methane assumed in the initial gas accumulation in Unit C (Fig. 3-4a). As discussed in Section (3.5.4.2) , increasing the initial gas charge in the vertical section along the Mount Elbert well does not change the predicted profile in Unit C. Thus the model provides an inherent test of its applicability: if vertical fluid movement within a plausible initial gas accumulation yields

less hydrate than observed, then flow must have been along dip (presuming the accumulation is in a suitable structure).

3.5.2) Effect of R_v on hydrate saturation profile

The model presented in this chapter imposes no *a priori* constraint on the value of R_v in the upper portions of Units C and D. It is of interest then to examine the effect of this parameter on the results. The value of $R_{v,stoich}$ for the Mount Elbert well case, with $S_{g,i} \approx 0.8$, is about 0.69 (see Fig. 2-9); therefore, for $R_v > 0.69$ the final state will be hydrate and gas phase only. At Mount Elbert well hydrate and water only are observed, (Lee and Collett, 2011) and thus we should have had $R_v < R_{v,stoich}$. As mentioned earlier in this chapter, the present model requires the GWC to move upward and gas-water capillary pressure along the gas column to decrease during hydrate formation. A consequence of this decrease in capillary pressure is that some imbibition must occur throughout the gas zone, i.e. the aqueous phase saturation S_w must increase. In this case the value of R_v must be less than $R_{v,1:1}$ (the ratio at which S_w does not change from its initial value). For temperature and pressure conditions of the depth interval of interest, $R_{v,1:1}$ is about 0.59. This expectation is consistent with the value of $R_v = 0.55$ that gave large values of S_h similar to those observed in upper portion of Unit D (Fig. 3-4).

As R_v decreases, less gas enters and the final hydrate saturation decreases (see Fig. 2-9). For $R_v < R_{v,stoich}$, regardless of the value of R_v the model converts the entire initial mass of methane in the gas column into hydrate. Thus, smaller R_v leads to greater thicknesses of hydrate at smaller saturations in the upper portion of each unit and correspondingly thinner intervals in which residual gas has been converted to hydrate. Fig. 3-5 shows the hydrate saturation profile when we repeat the illustration example for R_v values of 0 (no gas movement at all), 0.23 and 0.48, along with the log-derived

hydrate saturations in Mount Elbert well. Comparison with Fig. 3-4d suggests that while R_v = 0.55 gives values of the large saturation that are consistent with upper portion of Unit D, R_v may have been smaller, i.e. some value between 0.23 and 0.48 which are shown in Fig. 3-5, as BGHSZ passed through Unit C. It can be shown that R_v is controlled not only by the relative mobilities of gaseous and aqueous phases and capillarity properties of the host sediment but also by the rate of hydrate formation and the rate of descent of the BGHSZ. Therefore, value of R_v is expected to convey useful information about the multi-phase flow properties of host sediment, as well as the rate of hydrate formation. These issues will be discussed in detail in chapter 5.

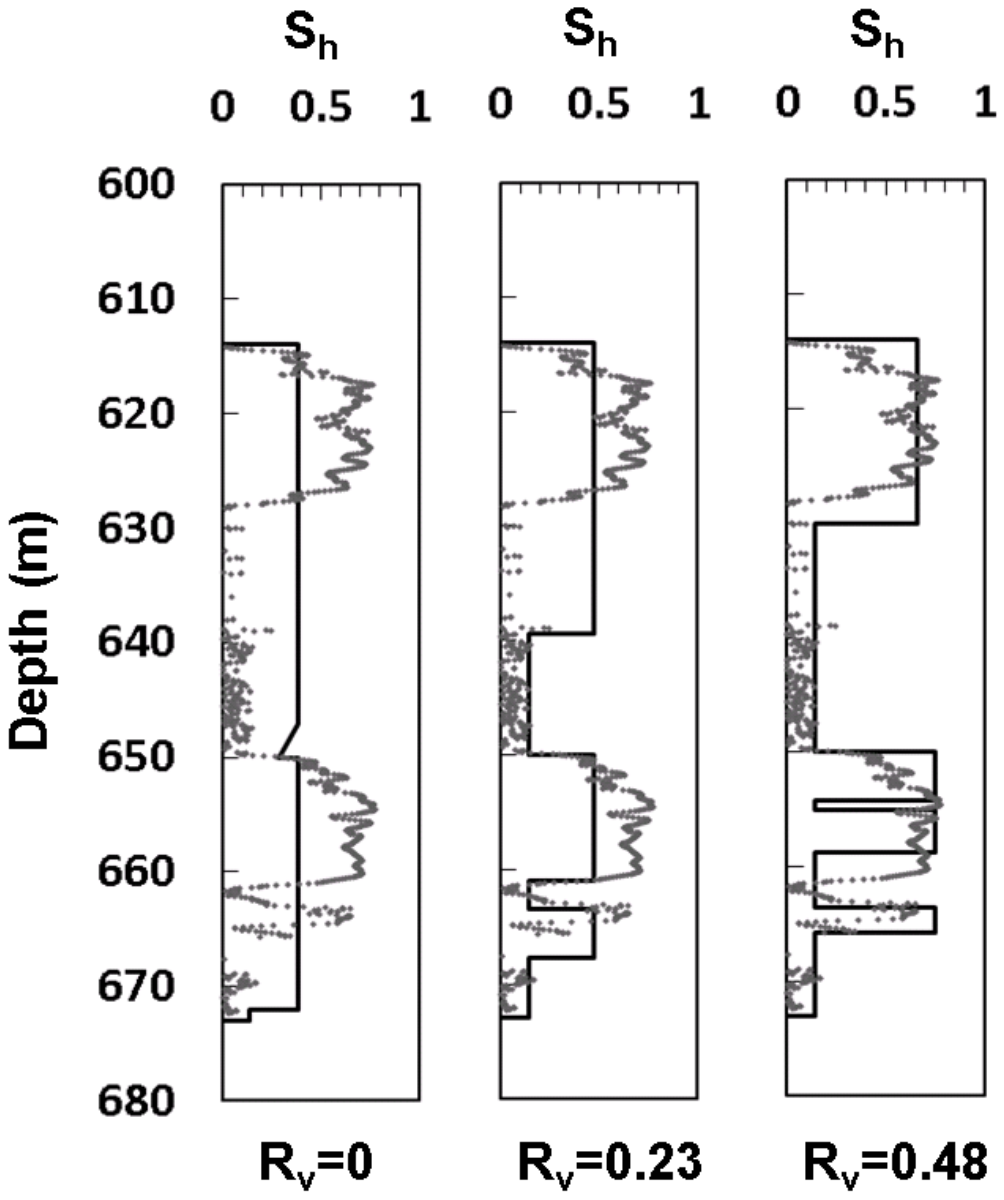

Fig. 3-5- Estimated hydrate saturation profile for three values of R_v along with log-derived hydrate-saturation data from Mount Elbert well (Lee and Collett, 2011). Note that mentioned values of R_v are used for non-residual gas saturations, forming the major hydrate saturations. For hydrate formation within imbibed intervals, i.e. where the gas saturation has decreased to its residual phase value (e.g. between 630 m and 650 m in the panel for R_v =0.48), no gas flow is possible and R_v =0 is used in those intervals. As with Fig. 3-4, comparison of the magnitudes of saturation is meaningful.

3.5.3) Volume of fluid transported into the hydrate-bearing zone

The total transported pore volumes of fluid change linearly with the final hydrate saturation, Eq. (2.40), with a slope of $K_{trans} \approx 1.9$ for the assumed P and T within the depth interval of interest in Mount Elbert well. Eq. (2.40) shows that the amount of fluid transported into the hydrate-bearing zone is substantial, around 1.4 pore volumes in upper portions of units C and D in Mount Elbert well (Fig. 3-6). The volume of gaseous and aqueous phases, i.e. red area and blue area, respectively, can be calculated either from Fig. 2-10, using a value of $R_v = 0.55$ adopted for Mount Elbert, or from Eqs. (2.48) and (2.49). Clearly such volume changes could not be accommodated by compaction of the sediment. In the lower portions of each unit, 0.3 PV of aqueous phase would have moved into the GHSZ to meet the stoichiometric requirement of converting gas to hydrate. In addition, 0.5 PV of aqueous phase, the difference between $S_{g,i}$ and S_{gr} ($\Delta V_{w,d}^{GWC}$ shown in dark blue in Fig. 3-6) had to enter to replace the gas transported from the imbibed zones (lower portion of each disconnected gas sub-column). Behseresht and Bryant (2011) report that capillary dominated, rather than pressure-driven viscous dominated, flow, is key to the required phase flow for converting a free gas accumulation, with large initial gas saturation, to large hydrate-saturation accumulations. This would also have useful implications in determining the time-scale over which such hydrate accumulations are formed. The magnitude of fluid phase transported is also important in hydrate-dissociation studies, e.g. when the BGHSZ rises through an existing hydrate accumulation, and pressure build-up evaluation when hydrate dissociates, because the same volume of fluid must be exported from the sediment.

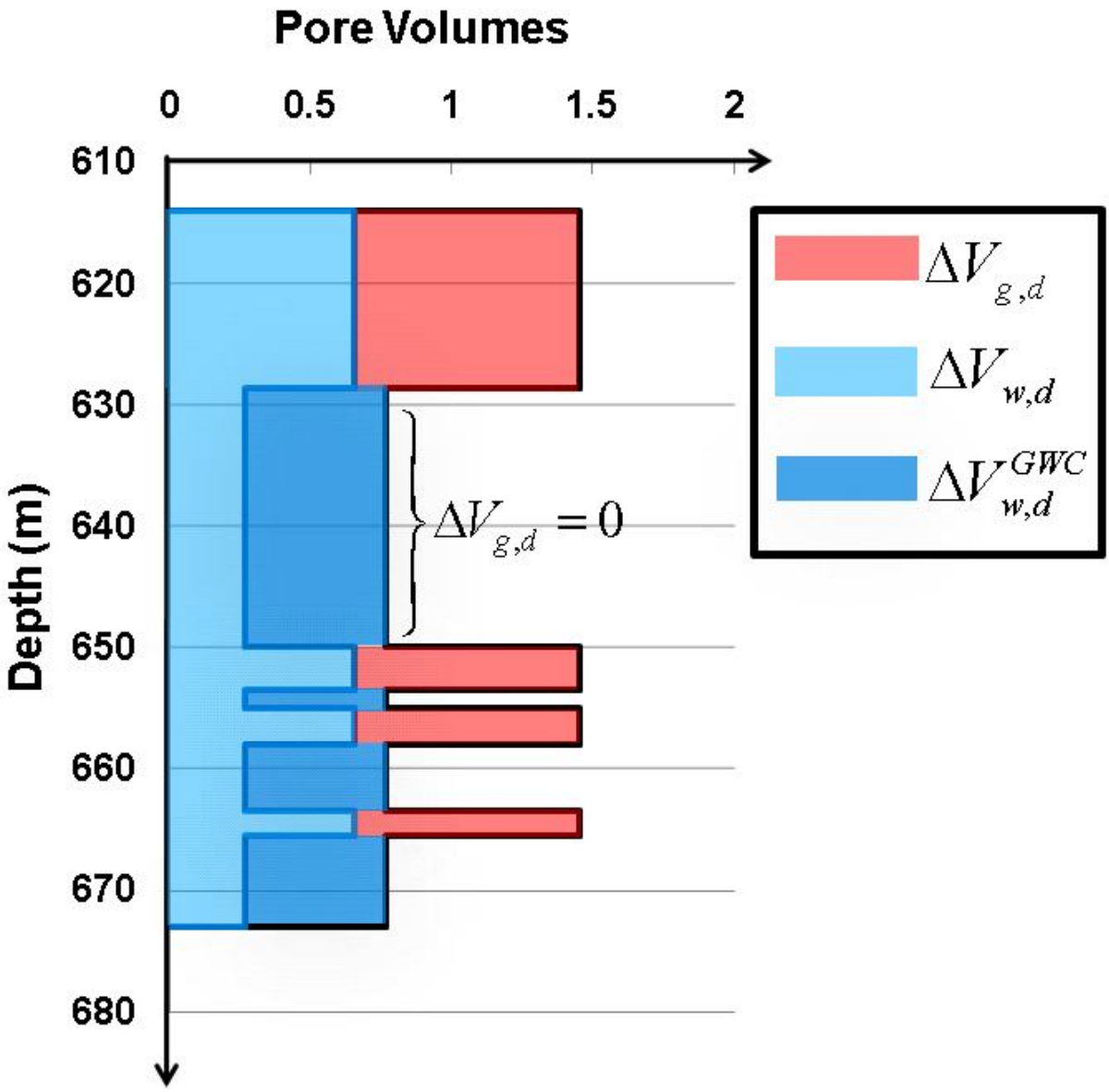

Fig. 3-6- The model predicts that considerable volumes of fluid (red: gas phase to GHSZ from deeper in the gas column; dark blue: aqueous phase to replace migrated gas; light blue: aqueous phase into GHSZ) have been transported during hydrate formation in Mount Elbert well. The upper portion of each unit accommodated a total of 1.4 pore volumes of gas and aqueous phases. This volume is in addition to the one pore volume initially filled with aqueous and gas phase.

3.5.4) Effect of the extent of initial gas charge on modern hydrate saturation distribution

We now consider two other initial gas saturation profiles: a) a partial charge that resulted in thinner and consequently noncommunicating gas accumulations in Units D and C (Fig. 3-7) and b) a greater charge that resulted in an initially continuous gas accumulation spanning Units D and C beyond the modern hydrate-bearing interval (Fig. 3-8).

3.5.4.1) Initially noncommunicating gas accumulations in Units D and C

Fig. 3-7a shows the initial gas saturation profiles within Units C and D. The column height above the GWC at 668 m in Unit C does not provide enough capillary pressure to breach the seal at the base of Unit D. Thus the gas accumulations in zones I and II are noncommunicating. Furthermore, gas only partially fills the Unit D sand because the effective GWC is at the base of Unit D, and the capillary pressure thus does not exceed the capillary entry pressure at 640m. Following gas accumulations I and II being disconnected, the gas that migrates to the GHSZ in Unit D comes only from within Unit D itself. Fig. 3-7b shows an intermediate step when the BGHSZ is at a depth of about 618 m. Note that gas moving to fill the void due to hydrate formation now rises from the bottom of the upper portion of the accumulation in zone I, establishing a residual gas saturation between 628 m and 640 m.

Fig. 3-7c illustrates the situation after the BGHSZ has descended to a depth of about 655 m. In addition to the initial gas saturation between 651 m and 655 m, some gas from the lower portion of Unit C has been used to form hydrate in the top section of this unit. The capillary pressure profile intersects the capillary entry pressure profile at a depth of 665 m. Thus the remaining gas column comprises two disconnected regions

labeled gas zone 1 and gas zone 2 (Fig. 3-7c). As the BGHSZ keeps moving downward water imbibes from below into the lower part of gas zone 1 to compensate for the volume of gas that moves into the top section of gas zone 1 during hydrate formation. Meanwhile, gas zone 2 saturations remain essentially unchanged from their initial profile, because the gas zone 1 was disconnected from gas zone 2 prior to hydrate formation in gas zone 1.

The hydrate saturation profile once the GHSZ has encompassed the whole gas column is shown in Fig. 3-7d. Our prediction is shown as green area and the log-derived hydrate saturations are shown as dots. As mentioned in section (3.2) , in the imbibed portions of the gas zones (e.g. 623 m to 640 m in Unit D), R_v is zero; therefore, when the BGHSZ descends into these portions, only aqueous phase moves to fill the void space that accompanies hydrate formation. Therefore, similar to that in Fig. 3-4, the hydrate saturation in imbibed zones is estimated to be S_h = 0.13. However, compared to that in Fig. 3-4, much less hydrate forms in Unit D since much less gas is initially present, and no gas can migrate into Unit D from Unit C.

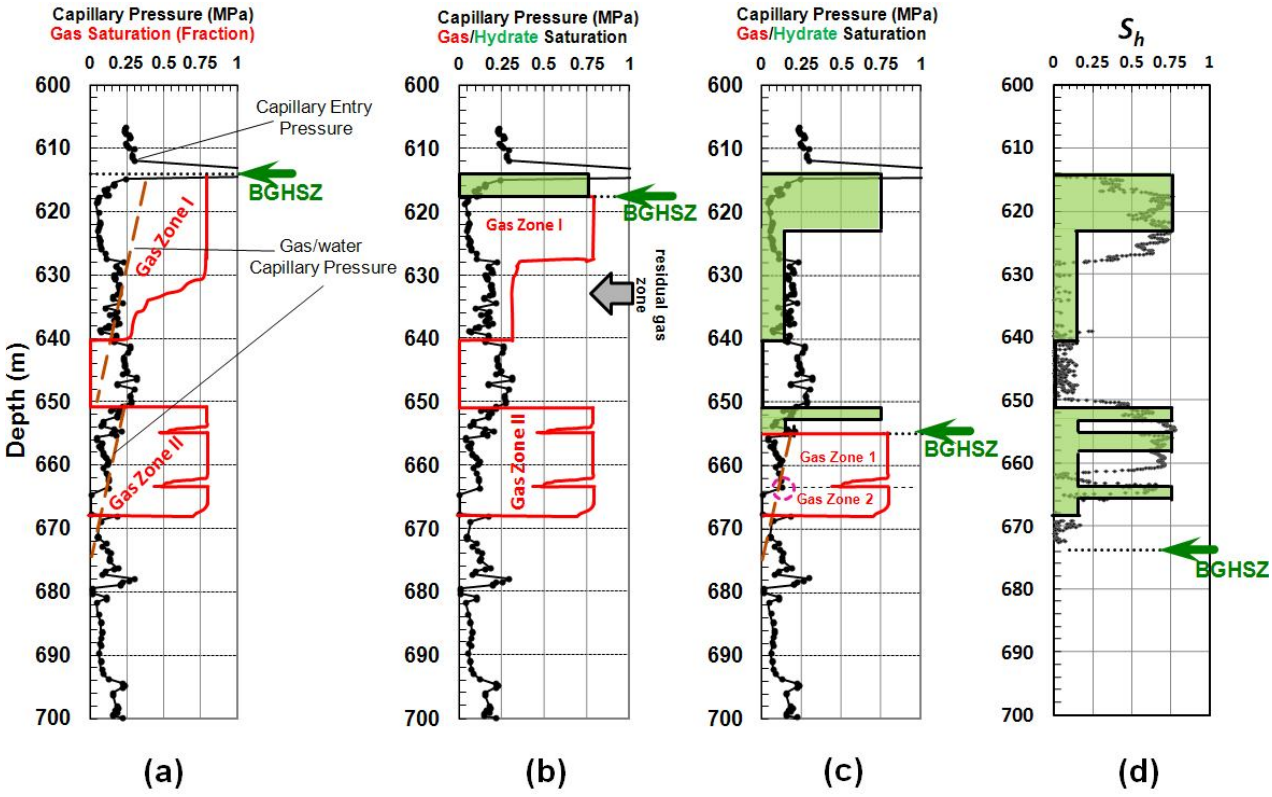

Fig. 3-7- Illustration of model of Fig. 3-2 with grain size distribution from Mount Elbert well and a hypothetical initial gas column. Unlike the case investigated in Fig. 3-4, here the initial gas column is a result of partial charge process so that two noncommunicating gas accumulations are established in Units D and C (a) Capillary entry pressure, estimated from grain size distribution and Eqs. (3.1) through (3.7), versus depth (connected dots) along with the two noncommunicating gas accumulations, gas zone I and II, when the BGHSZ was above the zone in which hydrate is currently present. Gas/water capillary pressure along the two gas zones are shown as dashed lines. (b) The BGHSZ has moved 3.5 meters downward. Gas transported from the lower portion of Unit D and water imbibed from below and has decreased the gas saturation to S_{gr} below 628m in gas zone I. (c) Gas saturation profile (red) when BGHSZ has moved downward through the gas column to a depth of 655m and the resulting hydrate saturation (green fill). Indicated gas zones 1 and 2 are no longer communicating due to the capillary barrier (shown with an hollow circle) at 664 m. (d) Final hydrate saturation profile (using R_v=0.55) after BGHSZ has moved below the bottom of gas column. The log derived hydrate saturations (Lee and Collett, 2011) are shown as dots.

3.5.4.2) Initially continuous gas accumulation spanning Units D and C beyond the modern hydrate-bearing interval

Fig. 3-9b-2 shows the hydrate saturation profile after converting a thicker initial column of gas (Fig. 3-9b-1) for which the GWC is at 694m. In this case the hydrate accumulation in Unit D is thicker, because substantial gas moves into Unit D from Unit C before the two units are disconnected. The predicted profile between 650m and 673m is similar to that shown in Fig. 3-4d. This is because the gas column below 678 m becomes disconnected from the gas above that point as the GWC rises. This creates a second effective GWC at 678 m, and when this secondary GWC rises to 673 m, the gas within Unit D becomes disconnected from that in Unit C just as in Fig. 3-4. Thus the absence of hydrate in the good quality sand below 665 m in Unit C would not necessarily indicate insufficient original gas charge. The eventual conversion of the gas below 678 m yields another major hydrate-bearing interval, below 678m.

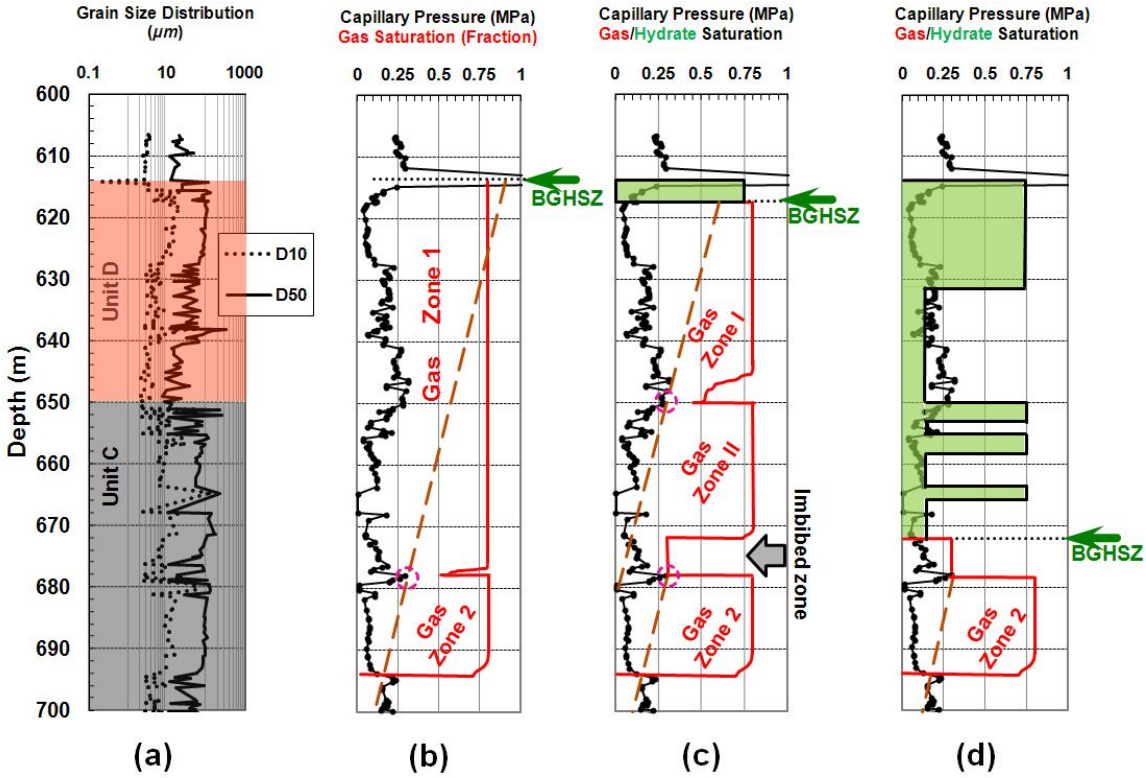

Fig. 3-8- Illustration of model of Fig. 3-2 with (a) grain size distribution from Mount Elbert well and a hypothetical initial gas column. (b) Capillary entry pressure, estimated from grain size distribution and Eqs. (3.1) through (3.7), versus depth (connected dots) along with an estimated initial gas saturation (red solid line) similar to that in Fig. 3-4 but assuming a deeper GWC at 694m. Gas/water capillary pressure along the gas column is shown as dashed line. The gas saturation profile changes as the BGHSZ moves down through the gas column and hydrate forms. (c) The BGHSZ has moved 4 meters downward. Gas transported from the lower portion of Gas zone 1 and water imbibed from below to create gas zone I. Gas zones I and II and 2 are no longer in communication due to the capillary barrier between them (shown with an hollow circle) at 650 m. (d) Gas saturation profile (red) when BGHSZ has moved downward through the gas column to a depth of 672m and the resulting hydrate saturation (green fill). Indicated gas zones 2 would convert to hydrate once the GHSZ expands into the gas zone. The final hydrate saturation profile when the BGHSZ has covered the whole gas column is shown in Fig. 3-9b-2.

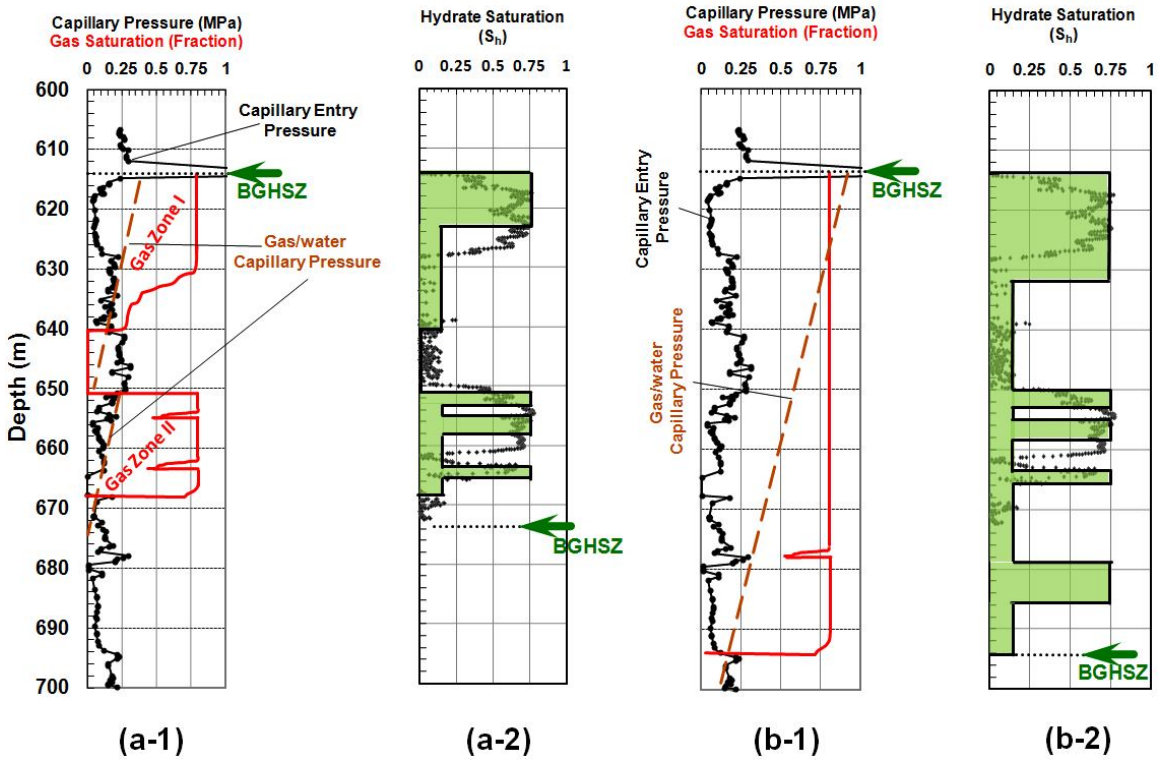

Fig. 3-9- Effect of initial gas column height on the resulting hydrate saturation profile: (a-1) shows two thinner (compared to Fig. 3-4), noncommunicating gas accumulations within the C and D Units of Mount Elbert well; (a-2) is the resulting hydrate accumulation after converting the gas accumulations in (a-1) into hydrate. The hydrate-bearing interval in both Units C and D are thinner than in Fig. 3-4. (b-1) shows a single long gas accumulation (614 m to 694 m). In contrast to (a-1), the gas phase is connected between the units. The resulting hydrate accumulation (b-2) after converting this long gas column into hydrate exhibits the same profile in the upper portion of Unit C (650 m to 673 m), indicating initial gas charge has little effect on the behavior. Conversion also yields a large hydrate-bearing interval below 678m. The hydrate-bearing interval in Unit D is thicker than in Fig. 3-4, because the initially continuous gas column allows a significant amount of gas to migrate from Unit C into Unit D before becoming disconnected.

This analysis shows that if fluid movement is only vertical, then the depth interval over which modern hydrate saturation is observed corresponds to the depth interval over which the original gas reservoir was established. That is why in the calculation of section

3.4) we tacitly assumed the initial gas column height was controlled by other factors (e.g. insufficient charge, a spill point elsewhere on the structure, etc.). In effect this is another inherent test of applicability of the vertical 1-D model: if an initial gas column corresponding to the range of depths where hydrate appears is not plausible, then flow along dip rather than vertically is likely to have occurred during BGHSZ descent.

3.6) SUMMARY AND CONCLUSION

A 1-D model was proposed to predict hydrate saturation profiles in "*converted free gas*" hydrate reservoirs considering three key elements: (i) volume change during hydrate formation within an existing gas accumulation, (ii) the descent of the base of GHSZ through the accumulation, and (iii) sedimentological variation with depth that causes variation in capillary entry pressure. Applied to a gas accumulation no longer connected to the charge, these elements combine to drive gas migration within the accumulation to the GHSZ. Substantial aqueous phase migration to and through the sediment column to the GHSZ accompanies the gas migration and hydrate formation. This leads to large hydrate saturations in the upper portion of the column and small saturations in the lower portion, even if the lower portion is sand-rich. Internal gas migration raises the gas/water contact, raising the possibility of disconnection of the remaining gas column at layers having relatively large capillary entry pressure. When this occurs, the disconnected subcolumns also yield large and small hydrate saturations in their upper and lower portions, respectively. The hydrate saturation profile resulting from these processes is nonuniform with rather sharp basal contacts, i.e. intervals of large S_h interspersed between intervals of small S_h, even if the initial gas saturation profile is uniform. The nonuniformity cannot be explained via association of major hydrate saturations with better quality sands.

Material balance analysis shows that a considerable amount of fluid (of order 1 pore volume of gaseous and aqueous phases) needs to be transported during hydrate formation. The fraction of this fluid that is gas strongly influences the magnitude of the final hydrate saturation. The model was applied on data from Mount Elbert well located in one of the methane hydrate reservoirs in Alaskan North Slope. With a physically reasonable choice for the fraction of gas in the total moving fluid, the model gives large S_h similar to those inferred from well logs. By orienting the flow direction in the model along dip rather than vertically, the model also predicts that small S_h will be found on the flanks of the Mount Elbert accumulation, if gas charged the flanks of the reservoir prior to or during BGHSZ descent, and that large S_h will fill the upper portion of Unit D. These predictions are consistent with interpretations of seismic anomalies and the Mount Elbert log-derived saturations.

The quantitative illustrations of the 1-D model presented here assumed all transport to be vertical. This maximizes the influence of sedimentological control on the final hydrate distribution. As the areal extent of the gas accumulation increases or the dip of the structure increases, the contribution of along-dip flow to the required gas transport increases, and the vertical flow model yields a lower bound on the thickness of the intervals with large hydrate saturation.

Chapter 4: Gas reservoir Conversion to Hydrate: Role of Pressure-Driven Fluid Phase Transport

4.1) OVERVIEW

The preceding chapters have laid out the main physical phenomena that drive the conversion of a gas reservoir into a hydrate-bearing formation. It was shown that conversion of gas reservoir into a hydrate reservoir would involve transport of substantial amounts of gaseous and aqueous phases into the hydrate stability zone (HSZ). Furthermore, it was assumed that during conversion the gas reservoir is no longer connected to the source of gas charge, and consequently the conversion of gas to hydrate causes the capillary pressure in the gas accumulation to decrease. That perspective, however, did not account explicitly for the mechanism by which gas and water were supplied to the GHSZ. We now turn to examine this transport problem from the bed scale.

The basic premise is simple: the decrease in gas phase pressure can drive viscous flow of both gas and aqueous phases to the hydrate stability zone. In the previous chapters that treated the overall volumetric changes associated with hydrate formation, it was shown that the fraction of fluid flow made up by the gas phase controlled the hydrate saturation in the upper portions of the reservoirs. Here a model of pressure-driven transport is developed to determine whether the calculated phase fluxes yield the hydrate saturation profile observed in Mount Elbert well.

The model is based on the same conceptual model for the conversion process used in the previous chapter. In summary, the conversion results from the descent of the base of gas hydrate stability zone (BGHSZ) through gas accumulated in a sediment. Given the measured grain size distribution in the sediment column, the initial gas phase saturation is estimated from the profile of capillary entry-pressure with depth. The gas accumulation is assumed to be isolated so that methane transport occurs only within it.

This chapter shows that if water transport occurs only by co-current viscous flow of gaseous and aqueous phases up to the hydrate stability zone (HSZ), it is not possible to create large hydrate saturations from large initial gas saturations. This is because typical relative permeability curves impose strong limitations on water flux. Thus the large hydrate saturations observed in Mount Elbert (Boswell et al., 2011) and Mallik (Kurihara et al., 2008) above the current BGHSZ would suggest another form of water flow: water moves down through accumulated hydrate from above. This requires the aqueous phase to remain connected within the hydrate-bearing sediment. The ratio of aqueous phase permeability in the hydrate-bearing sediment to the aqueous phase relative permeability at residual gas saturation determines hydrate saturation profile.

In the following, the context for the bed-scale transport model is reviewed. The goal is to recapitulate essential features from the preceding chapters of this dissertation, so that the model development is self-contained.

4.2) CONTEXT FOR PRESSURE-DRIVEN TRANSPORT MODEL

As overviewed earlier, substantial amount of research has been conducted to provide predictive models of hydrate formation in sediments. However, all the available models were developed for oceanic systems considering either (A) hydrate formation from methane-saturated water as it enters the GHSZ, or (B) hydrate formation at the interface between gas phase and aqueous phase as the methane gas phase enters the GHSZ. In chapter 3, the first mechanistic model for hydrate formation in terrestrial settings was developed (Behseresht and Bryant, 2012), presuming that the base of GHSZ moves through pre-established gaseous and aqueous phases instead of presuming fluxes of fluid(s) into the GHSZ.

Adapting the latter model, Behseresht and Bryant (2012) achieved satisfactory matches with the hydrate saturation distribution from field data, assuming that the structural geology of the location has allowed, over 1.8 Ma, for the long gas accumulation supported by grain size distribution data. In this model a stoichiometric fixed-pore-volume model of hydrate formation from water and methane was used. Through considering the vertical variation in capillary entry pressure, i.e. variation in grain size distribution, as well as volume reduction during hydrate formation, leading to continuous flow of fluid phases during hydrate formation, they could mechanistically explain/predict the currently observed hydrate saturation distribution in the Mount Elbert well deposits. Notably, the model explains why in unit C (Fig. 3-4) the major methane

hydrate accumulation is at the top lower-quality sand rather than the bottom better-quality deposit, and how a nearly uniform initial gas saturation profile leads to a sandwich-like hydrate saturation profile.

It was shown in section (3.5.3) that to have a hydrate saturation distribution as currently observed in Mount Elbert, abundant amount of fluids, up to 1.4 pore volumes for Mount Elbert case, should have been transported into the hydrate-bearing zones. It was also shown that the gas phase volume fraction, R_v in Eq. (2.41), of the total transported fluid volume, $\Delta V_g + \Delta V_w$, is directly related to the final hydrate saturation in a sediment zone, given the initial fluid phase saturations, $S_{w,i}$ and $S_{g,i}$ (Behseresht and Bryant, 2012). That work did not propose a mechanism for the fluid transport, however.

In the following some key elements of the stoichiometric model of chapter 2 applied to model hydrate formation in porous media are reviewed and then we discuss an important new aspect of the model: What parameters control the value of R_v and thus the resulting hydrate saturation in the host sediments. The main assumptions of the model, as mentioned earlier, are as follows: it is assumed that the alternative to fluid movement as a result of volume reduction associated with hydrate formation, which is compaction or grain rearrangement within the sediment, can be neglected (chapter 2). It was also assumed that methane that moves to the GHSZ is subsequently converted to hydrate (chapter 3). For simplicity CH_4 is treated to be the only constituent of the gas phase and the only guest molecule in the hydrate (chapter 1). The aqueous phase is assumed to have a small initial salinity, as reported for Mount Elbert well geochemistry data (Torres et al., 2011), and that any buildup in salinity caused by incorporation of H_2O into hydrate is rapidly dissipated into an unlimited reservoir of brine. The gas column is assumed to be no longer connected to its source and thus the gas mass is fixed. Finally, the heat

diffusion coefficient is about 500 times larger than the salinity transport coefficient (Clennell et al., 1999), so the effect of heat transfer on limiting hydrate formation is also neglected.

Given an initial gas/water saturation inside the sediment box of Fig. 2-8, the dimensionless volume of fluids transported into the sediment, $\Delta V_{g,d}$ and $\Delta V_{w,d}$, is related to the final hydrate saturation inside the sediment by Eqs. (2.48) and (2.49). Dimensionless volumes are in units of pore volume and are calculated by dividing the absolute volumes, ΔV_g and ΔV_w, by the total pore volume of the sediment, V_{tot}.

The gas phase fraction denoted by $R_{v,1:1}$, Eq. (2.47), represents a neutral point between imbibition (i.e. increase in S_w from its initial value, $S_{w,i}$) occurring during hydrate formation for $R_v < R_{v,1:1}$ and drainage (i.e. decrease in S_w from its initial value, $S_{w,i}$) occurring for $R_v > R_{v,1:1}$. As mentioned earlier, the value of $R_{v,1:1}$ is independent of initial saturations, $S_{w,i}$ and $S_{g,i}$.

In summary, this model introduced in preceding chapters allows the full range of behavior, from only aqueous phase entering the sediment box to fill the volume ($R_v = 0$) to only gas phase entering ($R_v = 1$). For $0 < R_v < R_{v,1:1}$ the aqueous phase coexists with hydrate at the final state and $S_{w,f} = 1 - S_{h,f} > S_{w,i}$, so that imbibition occurs during hydrate formation. For $R_{v,1:1} < R_v < R_{v,stoich}$, aqueous phase and hydrate coexist at the final state, but some drainage has occurred, so that $S_{w,f} = 1 - S_{h,f} < S_{w,i}$. Finally, for $R_{v,stoich} < R_v < 1$, the gas phase coexists with hydrate at the final state, with $S_{g,f} = 1 - S_{h,f}$. The situation commonly encountered in regions between the base of permafrost and the BGHSZ is an aqueous phase coexisting with hydrate. The hydrate phase can be present in trace amounts, $S_h < 0.1$, or in rich layers (many meters of sediment) with $0.6 < S_h < 0.8$. In the

latter case, of order one pore volume of gas and aqueous phases must move into the layer, with roughly equal volumes of each phase.

4.3) CAN CO-CURRENT VISCOUS FLOW PROVIDE THE REQUIRED AMOUNTS OF FLUIDS TO THE HYDRATE FORMATION ZONE?

As mentioned earlier, the conversion of methane and water (Fig. 4-1a) to hydrate reduces the volume occupied by the fluid phases, and this will give rise to a reduction in local fluid pressure. Hence a gradient in fluid pressure, i.e. nonzero flow potential, will arise when hydrate formation begins (Fig. 4-1b). The established potential gradient along the accumulation would in turn drive flow of gaseous, q_g, and aqueous, q_w, phase toward the GHSZ (Fig. 4-1b) so that hydrate keeps forming. We now consider how this gradient could move the required fluid phase volumes to the GHSZ. Because the model assumes the gas accumulation is no longer connected to the source of the gas charge, the gaseous phase must flow upwards within the accumulation towards the BGHSZ. It is of interest then to consider whether the aqueous phase can flow cocurrently with the gas.

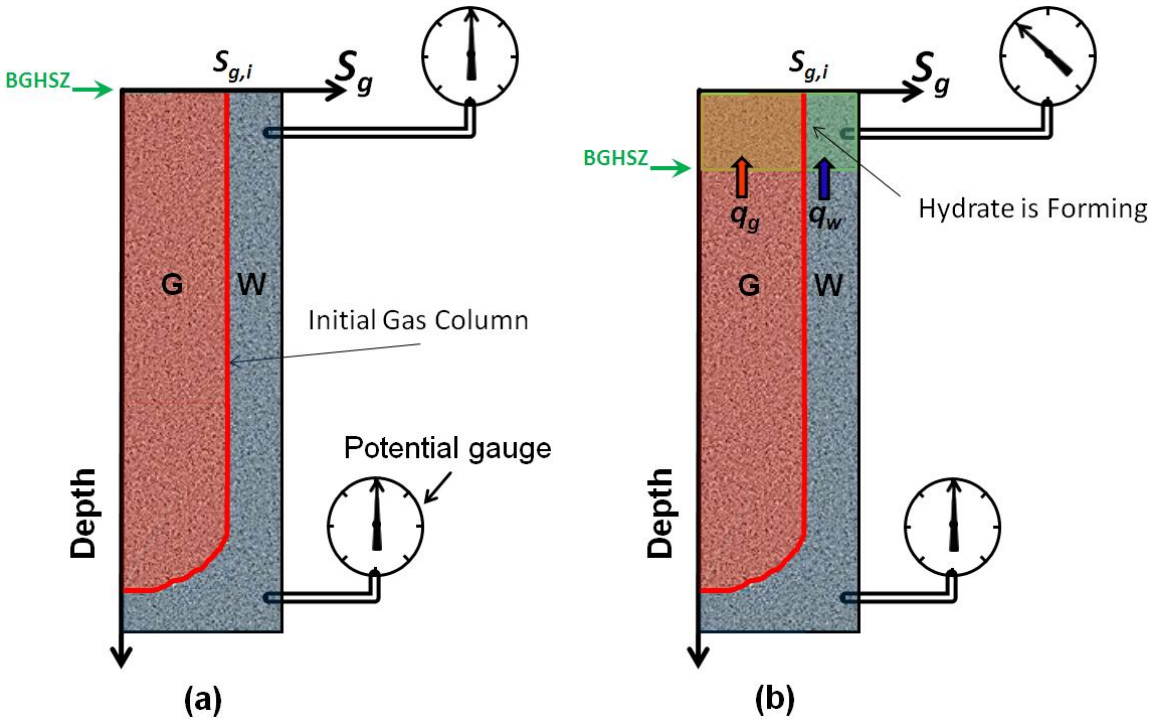

Fig. 4-1- (a) A gas accumulation established in an initially water saturated sediment column. The system is assumed to be in equilibrium when the BGHSZ is at the top of the column. The two potential gauges, thus, are reading the same values, i.e. potential gradient is zero. (b) The sediment column when its top portion is located inside the HSZ, i.e. through cooling from above: the local fluid pressure inside the HSZ is decreased. Hence a gradient in fluid pressure, i.e. nonzero flow potential, would established along the accumulation which in turn drives flow of gaseous, q_g, and aqueous, q_w, phase toward the GHSZ.

For the 1-D vertical model introduced above, Darcy's law for the aqueous phase is given by

$$u_w = \frac{-kk_{r,w}}{\mu_w}\frac{\partial}{\partial z}(P_w + \rho_w g z) \tag{4.1}$$

and thus:

$$u_w = \frac{-kk_{r,w}}{\mu_w}(\frac{\partial P_w}{\partial z} + \rho_w g) \tag{4.2}$$

Note that the positive direction is assumed upward as the cocurrent flow of gas and water would be upward. In this case the fluxes u_w and u_g would be positive. Here u_w is the Darcy velocity of aqueous phase, μ_w is the viscosity of aqueous phase, $k_{r,w}$ is the relative permeability of the sediment to the aqueous phase. P_w denotes the aqueous phase pressure and g is the acceleration due to gravity.

Similarly, for the gaseous phase we have:

$$u_g = \frac{-kk_{r,g}}{\mu_g}\left(\frac{\partial P_g}{\partial z} + \rho_g g\right) \tag{4.3}$$

For a quasi-steady-state model where gas and water are assumed to be in equilibrium, P_g and P_w are related through the Eq. (4.4):

$$P_g - P_w = P_c(z) = (\rho_w - \rho_g) g (z - z_0) \tag{4.4}$$

where $P_c(z)$ is capillary pressure as a function of depth, z and z_0 is the depth of the free water level at which the capillary pressure is zero.

Combining Eqs. (4.3) and (4.4) gives:

$$u_g = \frac{-kk_{r,g}}{\mu_g}\left(\frac{\partial P_w}{\partial z} + \frac{\partial P_c}{\partial z} + \rho_g g\right) \tag{4.5}$$

Eq. (4.4) also gives that:

$$\frac{\partial P_c}{\partial z} = (\rho_w - \rho_g) g \tag{4.6}$$

Combining Eqs. (4.5) and (4.6) gives:

$$u_g = \frac{-kk_{r,g}}{\mu_g}\left(\frac{\partial P_w}{\partial z} + \rho_w g\right) \tag{4.7}$$

Therefore, for a quasi-steady-state model considering the cocurrent flow of gaseous and aqueous phase Eq. (4.8) holds.

$$\frac{q_g}{q_w} = \frac{u_g}{u_w} = \frac{\lambda_g}{\lambda_w} \tag{4.8}$$

Here q_g and q_w are the volumetric flow rate of the gaseous and aqueous phases, respectively. ρ_g and ρ_w denote the effective mobility of gaseous and aqueous phases, respectively. Mobility of a phase, p, is defined as Eq. (4.9).

$$\lambda_p = \frac{kk_{r,p}}{\mu_p} \;;\; p = g, w \tag{4.9}$$

Combining Eqs. (2.41) and (4.9) gives,

$$R_v = \frac{\Delta V_g}{\Delta V_g + \Delta V_w} = \frac{q_g}{q_g + q_w} = \frac{\lambda_g}{\lambda_g + \lambda_w} \tag{4.10}$$

In other words, the assumption of cocurrent viscous flow of gaseous and aqueous phases leads to identifying R_v as the fractional flow of the gaseous phase. This provides an independent constraint on the value of R_v that could have occurred during hydrate formation. Interestingly, this constraint is independent of the magnitude of the pressure gradient induced by hydrate formation and independent of the permeability of the sediment.

Fig. 4-2a shows a typical relative permeability curve for a water wet porous medium. In this example the residual gas saturation, S_{gr}, is 0.3 and the irreducible wetting phase saturation, $S_{w,irr}$, is 0.2. Based on this relative permeability characteristics, using Eq. (4.10), the value of R_v is calculated for a range of values of water saturation, S_w, at which gas and aqueous phases can flow, i.e. $S_{w,irr}<S_w<1-S_{gr}$. The results of this calculation are shown in Fig. 4-2b. In the aforementioned calculations, dynamic methane viscosity, μ_g, is estimated to be $\approx 1.2\times10^{-5}$ Pa.s at P=6.5 MPa and T=2°C (Huang et al., 1966). The latter P and T are the average temperature and averaged hydrostatic pressure over depth along the hydrate-bearing interval in the Mount Elbert well[1]. At the same thermodynamic

[1] This pressure and temperature was picked primarily due to the fact that the observed hydrate saturation profile in Mount Elbert well was the main motivation behind developing the proposed terrestrial hydrate formation model in this dissertation.

condition, viscosity of water, μ_w, is estimated to be$\approx 1.7\times10^{-3}$ Pa.s (Stanley and Batten, 1969).

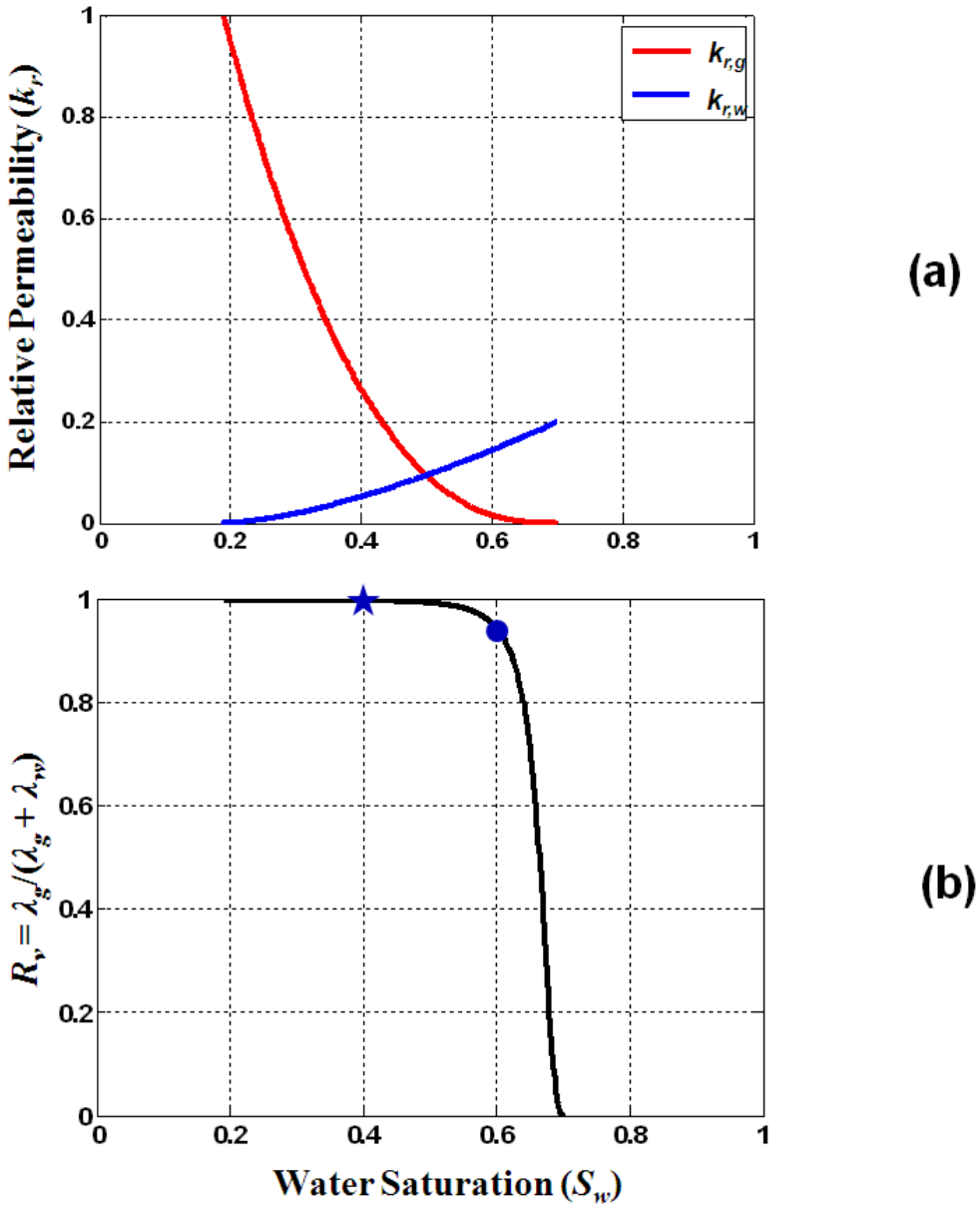

Fig. 4-2-Assuming cocurrent vertical viscous flow of gas and aqueous phases allows estimating R_v in terms of phase mobilities. (a) A typical relative permeability curve; red represents the relative permeability of gaseous phase and blue represents that of the wetting phase. (b) R_v versus water saturation at which cocurrent flow occurs calculated from Eq. (4.10).

Now that R_v could be estimated based on mobilities as a function of S_w, the next step would be predicting the final hydrate saturation, S_h, based on the estimated R_v values. To make a rough estimation of final hydrate saturation versus initial water saturation, $S_{w,i}$, suppose that cocurrent viscous flow occurs with the same value of R_v, throughout the hydrate formation time period, as the R_v calculated at the initial water saturation, $S_{w,i}$. For example, consider two values of initial water saturations $S_{wi} = 0.4$ and $S_{wi} = 0.6$, marked as a solid star and a solid circle, on Fig. 4-2b. The corresponding values of R_v are close to unity, Fig. 4-2b, and lead to final states in which hydrate and gas phases would coexist. These two states are also shown with the same symbols on Fig. 4-3a. Fig. 4-3a shows final hydrate saturation as a function of overall R_v. Therefore, along with Fig. 4-3a the calculated R_v values from Fig. 4-2b, assuming constant R_v during hydrate formation, can be used to estimate the final hydrate saturation from the initial water saturation for the relative permeability characteristics shown in Fig. 4-2a. Performing this calculation for the full range of initial saturations, $S_{w,irr}<S_w<1-S_{gr}$, yields the curve of Fig. 4-3b. The zones of excess methane (final state is hydrate and gas phases) and excess water (final state is hydrate and aqueous phases) are highlighted in red fill and blue fill, respectively.

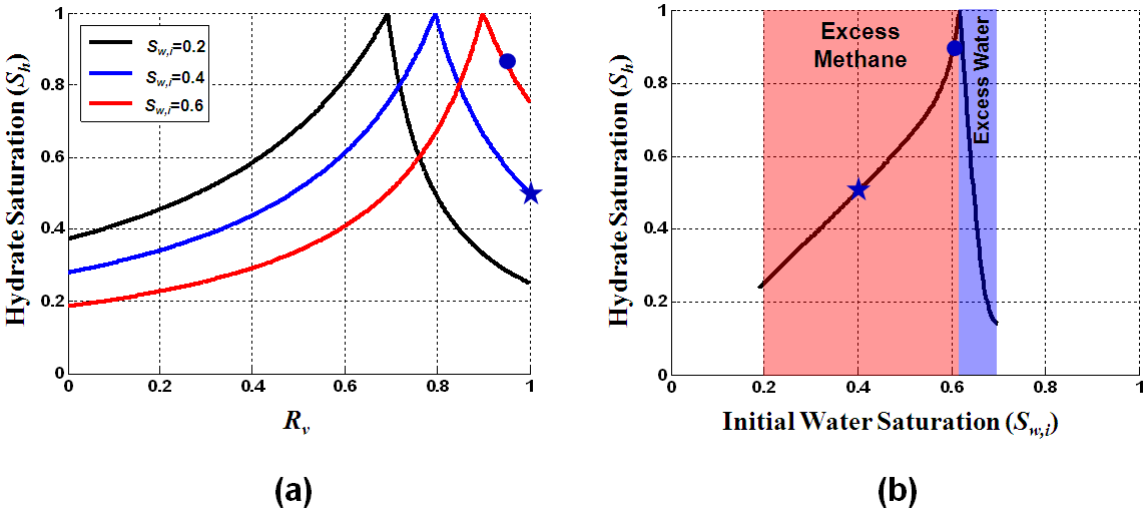

Fig. 4-3- Estimating hydrate saturation, S_h, from initial water saturation, $S_{w,i}$ and the R_v calculated for a co-current viscous flow of gaseous and aqueous phases at the initial aqueous phase saturation, $S_{w,i}$. (a) Hydrate saturation versus R_v for different initial water saturations. The points corresponding to the two arbitrary water saturations, marked as a solid star and a solid circle, on Fig. 4-2b are shown with the same symbols. (b) Hydrate saturation versus initial, flowing water saturation constructed through combining Fig. 4-2b and Fig. 4-3a.

Therefore, if the water and methane required during hydrate formation, $\Delta V_{w,d}$ and $\Delta V_{g,d}$, are provided through a co-current viscous flow of gas and aqueous phases, the final state of the sediment would be having hydrate and methane only (excess methane) for a rather wide range of initial water saturations, i.e. $S_{w,i}$<0.62 for the typical relative permeability curve in Fig. 4-2a. The latter, however, is in contradiction to the observed situation in Mount Elbert well of only hydrate and aqueous phases present (Lee and Collett, 2011).

Fig. 4-3b further shows that the observed state of the Mount Elbert well would arise only over a very narrow range of initial water saturation. This range corresponds to rather small initial gas saturations, $S_{g,i}$<0.38. The capillary entry pressure estimations, however, predict much larger initial gas saturations for Mount Elbert well (Fig. 3-4a).

This contradiction suggests that it is unlikely that cocurrent viscous flow can fulfill the phase flow requirements during conversion of a preexisting gas accumulation, with presumably moderate to large initial gas saturations, into a hydrate accumulation.

To constrain the saturations at which cocurrent viscous flow of aqueous and gaseous phases might have occurred, the classical fractional flow theory (Buckley and Leverett, 1942) is applied here. Fig. 4-4 shows the fractional flow of the aqueous phase corresponding to the relative permeability curves shown in Fig. 4-2a. The downstream boundary condition in the gas column is $S_w=S_{w,i}=1-S_{g,i}$ while the upstream boundary condition is $S_w = 1-S_{gr}$ with $f_w=1$ (Fig. 4-5). The latter corresponds to aqueous phase entering the sediment to raise the GWC. These boundary conditions give rise to an upward moving front at which a step change in saturation occurs, Fig. 4-5. The water saturation at the front can be determined graphically by drawing a tangent from the initial saturation point on the f_w-S_w curve to the f_w-S_w curve. The tangent lines for three values of initial saturation ($S_{w,i}$ =0.2, 0.4 and 0.6) are drawn on the fractional flow curve shown in Fig. 4-4.

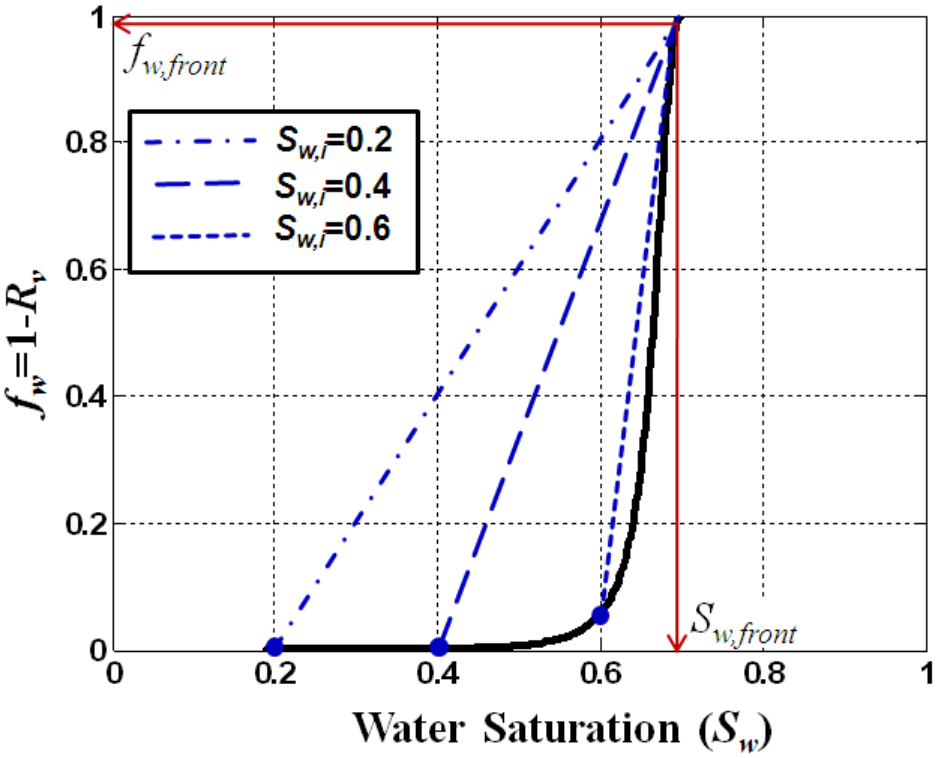

Fig. 4-4- Fractional flow of aqueous phase versus aqueous phase saturation for a co-current viscous flow of methane and water with the characteristic relative permeability curves shown in Fig. 4-2a. The shock front (tangent lines) suggests a piston type movement with $S_{w,front} \approx 1\text{-}S_{gr}$ for almost the whole range of initial water saturation $S_{w,irr} < S_w < 1\text{-}S_{gr}$.

Based on the tangent lines in shown in Fig. 4-4, the front saturation, $S_{w,front}$, would be practically the same for all three initial water saturations: $S_{w,front} \approx 1\text{-}S_{gr} = 0.7$ for which the corresponding fractional flow of aqueous phase would be $f_{w,front} \approx 1$. Ahead of the front, the water saturation is $S_w = S_{w,i}$ and $f_w \approx 0$. Thus only gas phase is arriving ($f_g \approx 1$) at the BGHSZ. This situation is expected for almost any set of relative permeability curves because the viscosity ratio dominates the mobility ratio, forcing λ_w / λ_g to be very small. Consequently, the displacement becomes piston type, where water pushes gas ahead in a piston type manner. This piston type movement of a methane bank ahead of the water

bank can provide the upper zones, in which hydrate is forming, with the required gas $\Delta V_{g,d}$. Simultaneously this piston type movement of aqueous phase would enable the transport of water, $\Delta V_{w,d}^{GWC}$, to replace transported gas from below and raise the GWC. But clearly the cocurrent viscous flow could not have transported water into the zone of hydrate formation

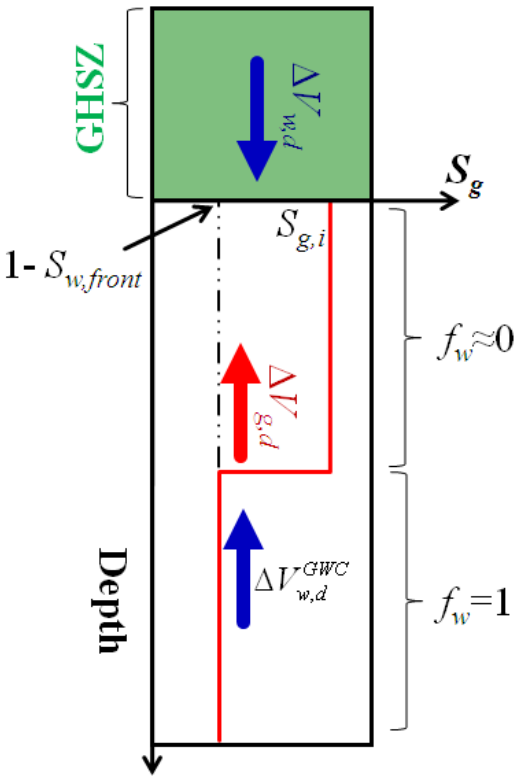

Fig. 4-5- Model for the transported volumes of aqueous and gas phase. Fractional flow theory proves it unlikely that the required amount of aqueous phase, $\Delta V_{w,d}$, has been transported through a co-current flow with the gas phase.

In the following section, an alternative path for aqueous phase viscous flow to the GHSZ is proposed. Thereafter, the corresponding viscous flow model is implemented and discussed in more detail.

4.4) FLOW MODEL FOR VISCOUS FLOW OF GASEOUS AND AQUEOUS PHASES INTO THE GHSZ

As mentioned earlier, the driving force for fluid phase movement is the reduction in volume occupied by the gas/aqueous/hydrate phases when hydrate forms from gas and aqueous phase components. Therefore, it is of great interest to determine gas phase and aqueous phase movements independently, and thereby determine the value of R_v. To do this it is first necessary to know the mechanisms through which gaseous and aqueous phase arrive into the zone of hydrate formation while hydrate is forming in an interval newly introduced into the GHSZ. Fig. 4-6 illustrates a sand unit with a gas column established below a seal at depth, h_1. The BGHSZ has just moved into the gas-bearing zone and hydrate can form inside the zone shown within a green box. In the previous section, it was shown that due to the very low ratio of aqueous to gas phase mobilities, steady co-current viscous flow of aqueous phase and gas phase from below the BGHSZ cannot supply the amount of water required, $\Delta V_{w,d}$ (Behseresht and Bryant, 2011). Instead, a piston-type movement of gas would arise, with the aqueous phase following from below, as shown in Fig. 4-5.

It was also shown that since aqueous phase viscosity is much larger than that of the gas phase, the aqueous phase mobility λ_w is much smaller than that of the gas phase λ_g for almost any reasonable set of relative permeability curves (Behseresht and Bryant, 2011). Thus only gas is arriving ($f_g = 1 - f_w \approx 1$) at the BGHSZ showing that the cocurrent viscous flow of gaseous and aqueous phases cannot have transported water into the zone of hydrate formation in “converted free gas reservoirs”.

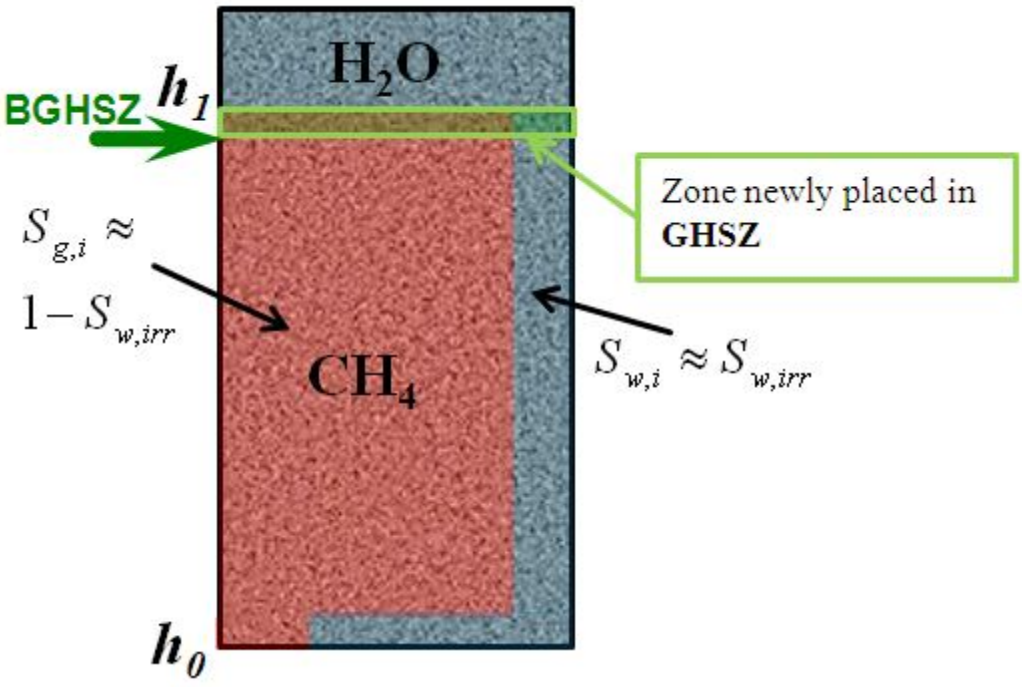

Fig. 4-6- A sand unit having a seal at depth, h_1 is shown. A gas accumulation is established below the seal. The BGHSZ was above the gas column when the gas column was established. The BGHSZ is descending through the sediment column. The zone recently placed in the GHSZ is highlighted by a green fill on the sediment column.

The need for considerable amount of water, $\Delta V_{w,d}$, during hydrate formation requires a different route for water flow. We propose that water moves down through accumulated hydrate from the unfrozen water above[2] (Fig. 4-5). For this to happen the water phase must remain connected within the hydrate-bearing sediment. This requires the final hydrate saturation at the upper zones to be less than $1-S_{w,irr}$ so the aqueous phase is connected at the final water saturation. Behseresht and Bryant (2012) predict that this condition will arise, because imbibition occurs in the upper zones as the GWC rises and causes the capillary pressure to decrease as the height of the gas column decreases.

[2] Such water exists, because the base of permafrost is always above the BGHSZ.

In the following, the model illustrated in Fig. 4-5 is formulated and applied on the D sand unit of Mount Elbert well. Following the discussion in section (4.3) gaseous phase is assumed to have a piston type cocurrent flow. Fig. 4-7 shows the sand unit of Fig. 4-6 when the BGHSZ has moved down through a portion of the original gas column. The figure shows the situation once the BGHSZ has moved from depth, h_1+L_h to $h_1+L_h+\Delta L_h$. The gas accumulation between h_1 and h_1+L_h has been fully consumed to form hydrate and the pore space is filled with hydrate and water only, i.e. $R_v<R_{v,stoich}$. As hydrate forms in the ΔL_h interval newly placed inside the GHSZ, the flow of aqueous phase, q_w, and gas phase, q_g, takes place. Aqueous phase pressure is assumed hydrostatic and the pressure at depths h_1 and h_0 are assumed undisturbed, i.e. hydrostatic, by the change in pressure due to the volume change associated with the hydrate formation in the ΔL_h interval (Fig. 4-7). At the moment shown in Fig. 4-7, the GWC is at a depth of h_0-L_w. As hydrate forms in the ΔL_h interval, GWC keeps moving upward to accommodate the transport of gas to the zone of hydrate formation above. Permeability to aqueous phase flow in the hydrate-bearing zone in the interval $[h_1,\ h_1+L_h]$ is denoted as $k_{w,h}$. The permeability to gas phase flow in the interval $[h_0-L_w,\ h_0-L_t]$ is denoted as k_g and the permeability to aqueous phase flow below the depth of h_0-L_w is shown as k_w.

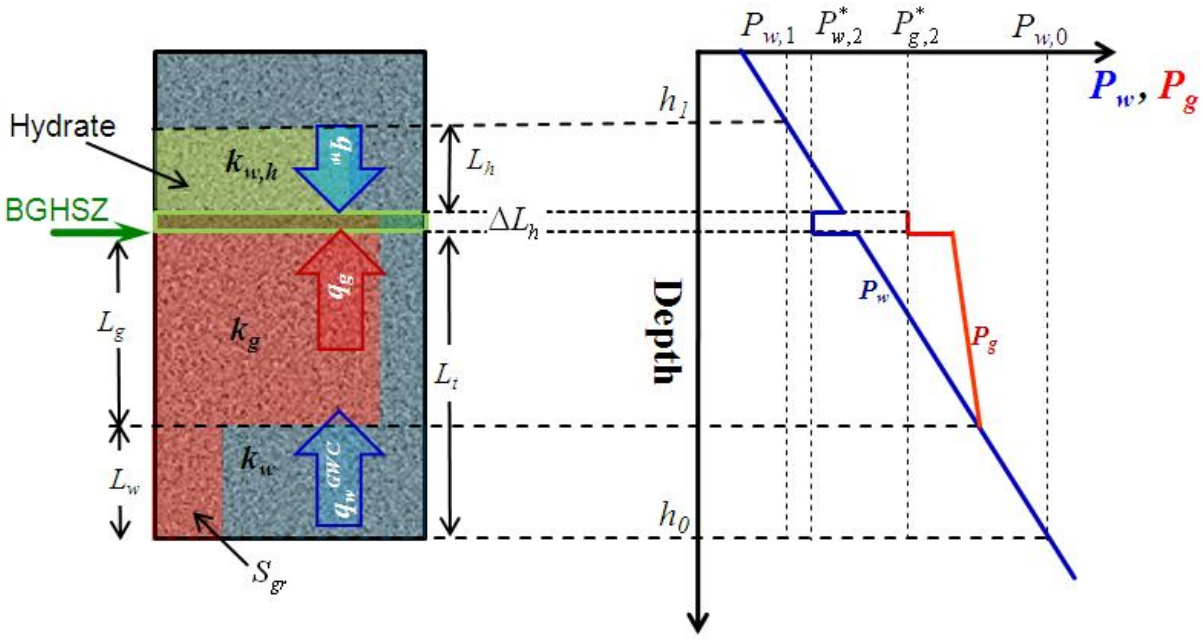

Fig. 4-7- The sand unit of Fig. 4-6 when the BGHSZ has moved down through a portion of the gas column. There is L_h meters accumulation of hydrate above the current location of the BGHSZ. The GWC has moved upward (compare to Fig. 4-6) to depth $h_0–L_w$. The gas below the GWC has been transported upward and the gas saturation is S_{gr}. The phase pressure state inside the sediment is shown by a companion graph of pressure versus depth. The capillary pressure $P_g – P_w$ is zero at the GWC. The decrement in pressure at the BGHSZ indicates schematically the effect of the phase volume reduction accompanying hydrate formation.

4.4.1) Model Formulation

The volume reduction associated with hydrate formation in the interval ΔL_h in Fig. 4-7 would decrease the aqueous phase pressure at the BGHSZ to a value $P^*_{w,2}$ from its original hydrostatic value $P_{w,2} = P_{w,1} + \rho_w g L_h$. For an increment of hydrate, dS_h, the corresponding consumed amount of water and gas is calculated from Eqs. (4.11) and (4.12) (Behseresht and Bryant, 2012).

$$dS_w^{used} = \frac{N\bar{V}_w}{\bar{V}_h} dS_h \tag{4.11}$$

$$dS_g^{used} = \frac{\bar{V}_g}{\bar{V}_h} dS_h \tag{4.12}$$

For the initial fluid phase saturations, a total fluid compressibility can be calculated as:

$$c_t = S_{w,i} c_w + S_{g,i} c_g \tag{4.13}$$

If no fluid were to enter the interval ΔL_h then the pressure change, dP, associated with the consumed volume of gaseous and aqueous phase, is calculated as

$$dP = -\frac{1}{c_t}\frac{dV}{V_{tot}} = -\frac{1}{c_t} dS = -\frac{1}{c_t}\left(dS_w^{used} + dS_g^{used} - dS_h \right) \tag{4.14}$$

Combining Eqs. (4.11), (4.12) and (4.14) gives:

$$dP = -\frac{1}{c_t}\left(\frac{N\bar{V}_w + \bar{V}_g}{\bar{V}_h} - 1 \right) dS_h \tag{4.15}$$

Therefore, the pressure $P_{w,2}^*$ after a decrement of dS_w^{used} and dS_g^{used} and an increment of dS_h is calculated as:

$$P_{w,2}^* = \left[1 - \frac{1}{c_t P_{w,2}} \left(\frac{N\bar{V}_w + \bar{V}_g}{\bar{V}_h} - 1 \right) dS_h \right] P_{w,2} \tag{4.16}$$

Substituting the hydrostatic relationship $P_{w,2} = P_{w,1} + \rho_w g L_h$ in Eq. (4.16) gives

$$P_{w,2}^* = \left[1 - \frac{1}{c_t \left(P_{w,1} + \rho_w g L_h \right)} \left(\frac{N\bar{V}_w + \bar{V}_g}{\bar{V}_h} - 1 \right) dS_h \right] \left(P_{w,1} + \rho_w g L_h \right) \tag{4.17}$$

The reduction in pressure will induce flow in both gaseous and aqueous phases. From Darcy's law, the downward flow of water through the hydrate-bearing zone, q_w, would be:

$$q_w = \frac{A k_{w,h}}{\mu_w} \left(\frac{P_{w,1} - P_{w,2}^*}{L_h} + \rho_w g \right) \tag{4.18}$$

where A is the cross sectional area across the flow, g is the acceleration due to gravity and ρ_w is density of aqueous phase. Substituting Eq. (4.17) in (4.18) after simplifying gives:

$$q_w = A\frac{1}{c_t}\left(\frac{N\bar{V}_w + \bar{V}_g}{\bar{V}_h} - 1\right)\frac{k_{w,h}}{\mu_w L_h} dS_h \tag{4.19}$$

As expected, if no hydrate forms, i.e. $dS_h = 0$, no water flux would take place, $q_w = 0$.

For the upward piston type flow of gas and water from below, Darcy's law can be applied as,

$$\begin{cases} q_w^{GWC} = \dfrac{Ak_w}{\mu_w}\left(\dfrac{P_{w,0} - P}{L_w} - \rho_w g\right) \\ q_g = \dfrac{Ak_g}{\mu_g}\left(\dfrac{P - P_{g,2}^*}{L_g} - \rho_g g\right) \end{cases} \tag{4.20}$$

where P is the flowing water pressure at the GWC and can be calculated from Eqs. (4.22) and (4.23). Note that the positive direction is assumed to be upward here and thus the flow rates of water and gas would be positive here. For the vertical flow of gaseous and aqueous phases the usual fractional flow theory assumption is applied,

$$q_{tot} = q_w^{GWC} = q_g \tag{4.21}$$

where q_g is the flow downstream of the front. Combining the two equations in (4.20) and Eq. (4.21) gives:

$$\begin{cases} P_{w,0} - P = q_g \dfrac{L_w}{A\lambda_w} + \rho_w g L_w \\ P - P_{g,2}^* = q_g \dfrac{L_g}{A\lambda_g} + \rho_g g L_g \end{cases} \tag{4.22}$$

Adding the two equations in (4.22) after rearrangement gives

$$q_g = \frac{A}{\dfrac{L_w}{\lambda_w} + \dfrac{L_g}{\lambda_g}}\left[\left(P_{w,0} - P_{g,2}^*\right) - \left(\rho_w L_w + \rho_g L_g\right) g\right] \tag{4.23}$$

Similar to $P^*_{w,2}$, the corresponding pressure for the gas phase in the hydrate formation zone, $P^*_{g,2}$, when an increment of hydrate, dS_h, forms can be expressed in terms of the equilibrium gas pressure, $P_{w,2}+\Delta\rho g L_g$, and Eq. (4.15).

$$P^*_{g,2} = \left[1 - \frac{1}{c_t P_{g,2}}\left(\frac{N\bar{V}_w + \bar{V}_g}{\bar{V}_h} - 1\right) dS_h\right] P_{g,2} \tag{4.24}$$

Substituting the hydrostatic relationship $P_{g,2} = P_{w,0} - \rho_w g L_t + \Delta\rho g L_g$ in Eq. (4.24) gives

$$P^*_{g,2} = \left[1 - \frac{1}{c_t\left(P_{w,0} - \rho_w g L_t + \Delta\rho g L_g\right) P_{g,2}}\left(\frac{N\bar{V}_w + \bar{V}_g}{\bar{V}_h} - 1\right) dS_h\right]\left(P_{w,0} - \rho_w g L_t + \Delta\rho g L_g\right) \tag{4.25}$$

Combining Eqs. (4.23) and (4.25) gives the upward gas flow as

$$q_g = \frac{1}{c_t}\left(\frac{N\bar{V}_w + \bar{V}_g}{\bar{V}_h} - 1\right)\frac{A}{\frac{L_w}{\lambda_w} + \frac{L_g}{\lambda_g}} dS_h \tag{4.26}$$

We now have the rate of aqueous phase transport to the BGHSZ from above, Eq. (4.19), and the rate of gaseous phase transport to the BGHSZ from below, Eq. (4.26). These equations will be used in the next section to determine R_v as a function of the phase relative permeabilities.

4.4.2) Calculating R_v From Aqueous and Gaseous Phase Flows

For this 1-D flow model, Eq. (4.27) holds.

$$\frac{q_g}{q_w} = \frac{u_g}{u_w} \tag{4.27}$$

By definition, $R_v = \dfrac{q_g}{q_g + q_w}$ and thus

$$\frac{u_g}{u_w} = \frac{R_v}{1 - R_v} \tag{4.28}$$

Based on the Buckley-Leverett shock (Buckley and Leverett, 1942), shown in Fig. 4-5, the upward Darcy velocity of gaseous phase, u_g, can be expressed in terms of the water front speed, dL_w/dt as in Eq. (4.29).

$$u_g = \left(S_{g,i} - S_{gr}\right)\phi \frac{dL_w}{dt} \tag{4.29}$$

where ϕ is the average porosity of the porous media through which the flow is taking place. Dividing Eq. (4.19) by Eq. (4.26) gives the left side of Eq. (4.28) from which R_v can be calculated:

$$\frac{u_g}{u_w} = \frac{k_w}{k_{w,h}} \frac{L_h}{ML_t + L_w\left(1-M\right)} \tag{4.30}$$

where M is the mobility ratio defined as

$$M = \frac{k_w / \mu_w}{k_g / \mu_g} \tag{4.31}$$

Defining a length L_w^* so that $u_w = \frac{dL_w^*}{dt}$ and combining it with Eq. (4.29), the ratio of phase velocities can be expressed as

$$\frac{u_g}{u_w} = \frac{\left(S_{g,i} - S_{gr}\right)\phi \frac{dL_w}{dt}}{\frac{dL_w^*}{dt}} \tag{4.32}$$

Eq. (4.32) can be simplified and expressed in integral from as

$$\frac{u_g}{u_w} = \left(S_{g,i} - S_{gr}\right)\phi \frac{\Delta L_w}{\Delta L_w^*} \tag{4.33}$$

R_v is then evaluated from Eq. (4.28) and (4.33) as

$$R_v = \frac{\left(S_{g,i} - S_{gr}\right)\phi \Delta L_w}{\left(S_{g,i} - S_{gr}\right)\phi \Delta L_w + \Delta L_w^*} \tag{4.34}$$

On the other hand, combining Eqs. (4.30) and (4.32) gives

$$\left(S_{g,i}-S_{gr}\right)\phi\frac{dL_w/dt}{dL_w^*/dt}=\frac{k_w}{k_{w,h}}\frac{L_h}{ML_t+L_w\left(1-M\right)} \tag{4.35}$$

which can be simplified as

$$\frac{dL_w}{dL_w^*}=\frac{\xi}{ML_t+L_w\left(1-M\right)} \tag{4.36}$$

where,

$$\xi=\frac{k_w}{k_{w,h}}\frac{L_h}{\left(S_{g,i}-S_{gr}\right)\phi} \tag{4.37}$$

The dynamic quantity in ξ is the thickness of the hydrate zone L_h and the overall permeability of the hydrate-bearing interval, $k_{w,h}$. Thus Eq. (4.36) relates the rate dL_w/dt at which the gas-water contact moves to the thicknesses of the hydrate zone, the remaining gas column L_t and the residual gas zone L_w. The influence of the relative permeability curves appears in the mobility ratio M because of co-current flow in the gas column. These curves also determine the ratio of aqueous phase permeability below the GWC, k_w, to the aqueous phase permeability in the hydrate-bearing sediment, $k_{w,h}$, which affects the magnitude of ξ in Eq. (4.36). Rearranging and integrating Eq. (4.36) gives

$$\int_0^{\Delta L_w}\left(1-M\right)L_w dL_w+\int_0^{\Delta L_w}ML_t dL_w=\int_0^{\Delta L_w^*}\xi\, dL_w^* \tag{4.38}$$

Simplifying Eq. (4.38) gives an expression for ΔL_w^* as

$$\Delta L_w^*=\frac{1}{\xi}\left(\frac{1-M}{2}\Delta L_w^2+ML_t\Delta L_w\right) \tag{4.39}$$

In the following section an iterative algorithm for implementing the above formulated model is provided.

4.4.3) Iterative Algorithm for Model Implementation

Based on the above discussion, when the BGHSZ moves down from h_1+L_h to $h_1+L_h+\Delta L_h$, the following algorithm can be followed to calculate R_v and thus hydrate saturation, S_h, in the ΔL_h interval newly introduced in the GHSZ.

A. Start with an initial guess for $R_v = R_{v,guess}$

B. Calculate ΔL_w, which is a function of R_v, from Eq. (4.41)

The pore volumes of gas, $\Delta V_{g,d}$, required to be transported into the new interval of hydrate formation, ΔL_h, is a function of R_v and can be calculated from Eq. (2.48). This amount of gas will be provided through sweeping ΔL_w meters of the gas column by the water front from below; therefore we have

$$A\phi\left(S_{g,i}-S_{gr}\right)\Delta L_w = A\phi\Delta L_h\Delta V_{g,d} \tag{4.40}$$

Hence,

$$\Delta L_w = \frac{\Delta V_{g,d}}{S_{g,i}-S_{gr}}\Delta L_h \tag{4.41}$$

C. Calculate ΔL_w^* from Eq. (4.39)

D. Update the value of $R_{v,guess}$ using Eq. (4.34)

E. If $|R_v/R_{v,guess} - 1| > 0.001$ go to step B.

$R_v=R_{v,guess}$ is the answer using which the final hydrate saturation in the ΔL_h new hydrate-bearing interval is calculated from Eq. (2.43), if $R_v<R_{v,stoich}$, or Eq. (2.44), otherwise. Hence this model provides an *a priori* method of estimating R_v, the gas phase fraction of the total phase volume arriving at the BGHSZ. The flowchart corresponding to the latter algorithm is presented in Fig. 4-8.

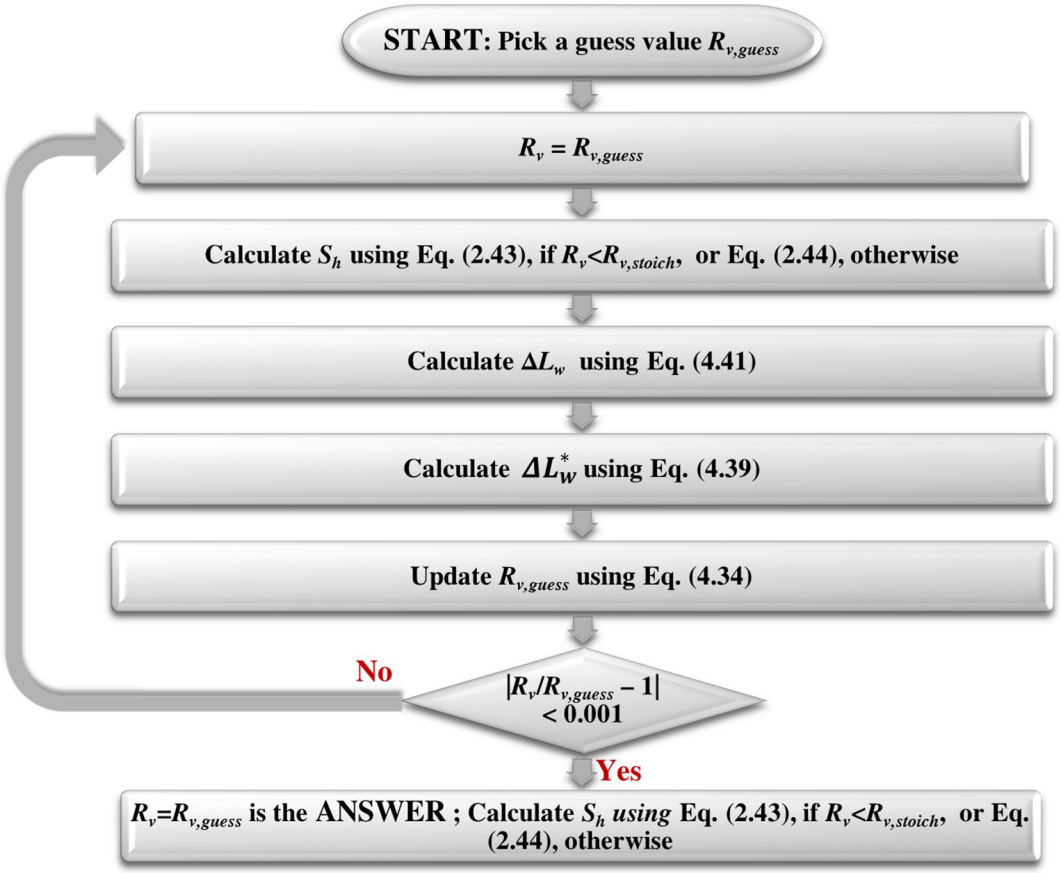

Fig. 4-8- Flowchart of the iterative algorithm, based on the model introduced in section (4.4) , for calculating hydrate saturation, S_h, inside a ΔL_h interval newly located inside the GHSZ.

As expressed in Eq. (4.37), $k_{w,h}$ is one of the key parameters in determining R_v and thus the final S_h inside a new interval ΔL_h encompassed by the GHSZ. Permeability to aqueous phase in a sediment containing hydrate is a strong function of the hydrate saturation. Therefore, once the final state of a new ΔL_h interval of hydrate-bearing sediment is determined using the above algorithm, the overall permeability to aqueous phase flow in the hydrate zone, $k_{w,h}$, needs to be updated as follows: let $k_{w,Lh}$ be the

permeability of the L_h interval of hydrate-bearing sediment and $k_{w,\Delta Lh}$ the permeability of the new hydrate-bearing interval, ΔL_h. Then the updated $k_{w,h}$, which is the overall permeability of the $L_h+\Delta L_h$ hydrate-bearing interval, is calculated from the rule of conductances in series, Eq. (4.42).

$$k_{w,h} = \frac{L_h + \Delta L_h}{\left(\frac{L_h}{k_{w,L_h}} + \frac{\Delta L_h}{k_{w,\Delta L_h}} \right)} \tag{4.42}$$

There are several models to estimate the aqueous phase permeability in the presence of hydrate. Here, it is assumed that hydrate fills center of the pores and thus a pore-filling permeability model applies. Let the permeability of a sediment in the ΔL_h interval in the absence of hydrate be denoted k. Based on the pore-filling model (Kleinberg et al., 2003), the permeability of the ΔL_h interval to aqueous phase, $k_{w,\Delta Lh}$, when a hydrate saturation S_h is formed inside the sediment can be calculated from Eq. (4.43),

$$k_{w,\Delta L_h} = \frac{\left(1+S_h\right)^{n+2}}{\left(1+\sqrt{S_h}\right)^2} k \tag{4.43}$$

where n is the hydrate saturation exponent. Neglecting the effect of capillary pressure, the saturation exponent increases from n = 0.4 at S_h = 0.1 to unity at S_h = 1 (Kleinberg et al., 2003; Spangenberg, 2001).

in the following section, the above algorithm is used to predict the hydrate saturation distribution, given the initial distribution of phase saturations (before descent of the BGHSZ), the P and T of the GHSZ, the residual gas saturation, the relative permeability characteristics of gaseous and aqueous phases, and the permeability to aqueous phase when hydrate occupies sediment pore space.

4.5) APPLICATION OF THE VISCOUS-DOMINATED TRANSPORT MODEL TO MOUNT ELBERT WELL

The above model is applied on the D sand unit of Mount Elbert well. First, the profile of absolute permeability for the D sand unit versus depth is estimated. As discussed in section (3.3) , based on the grain size distribution data from Mount Elbert well (Winters et al., 2011), Eq. (3.5) can be used to estimate the permeability at each depth as a function of grain size distribution at that depth. Fig. 4-9 shows the estimated permeability versus depth in the D sand unit based on the grain size distribution shown in Fig. 3-3a.

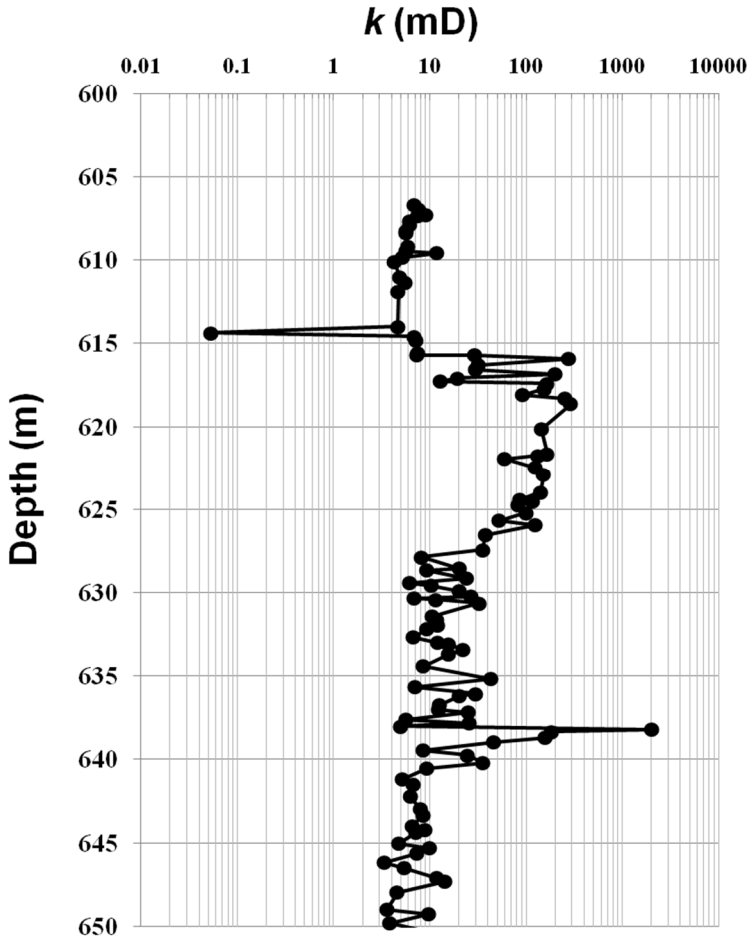

Fig. 4-9- Estimated permeability from Eq. (3.5) based on grain size distribution data of the D sand unit from Mount Elbert well. Grain size variation versus depth is shown in Fig. 3-3a.

To calculate the mobility ratio, M, of aqueous to gaseous phase, for the upward piston type co-current flow, the end-point relative permeabilities of aqueous, $k_{rw,0}$ and gaseous, $k_{rg,0}$, phase are required. Here, a typical pair of end-point relative permeability values for water-wet sediments is used: $k_{rw,0}$=0.3 for water and $k_{rg,0}$=0.7 for methane, as shown on Fig. 4-10. Similar to the values used in chapter 3, a dynamic methane viscosity of μ_g=1.2×10^{-5} Pa.s (Huang et al., 1966) and water viscosity of μ_w=1.7×10^{-3} Pa.s (Stanley

and Batten, 1969) is used here which give rise to a mobility ratio of M=3×10^{-3}. Note that due to the hundred-fold difference in gas and aqueous phase viscosities, we have $M << 1$ for typical ratios of end point relative permeabilities.

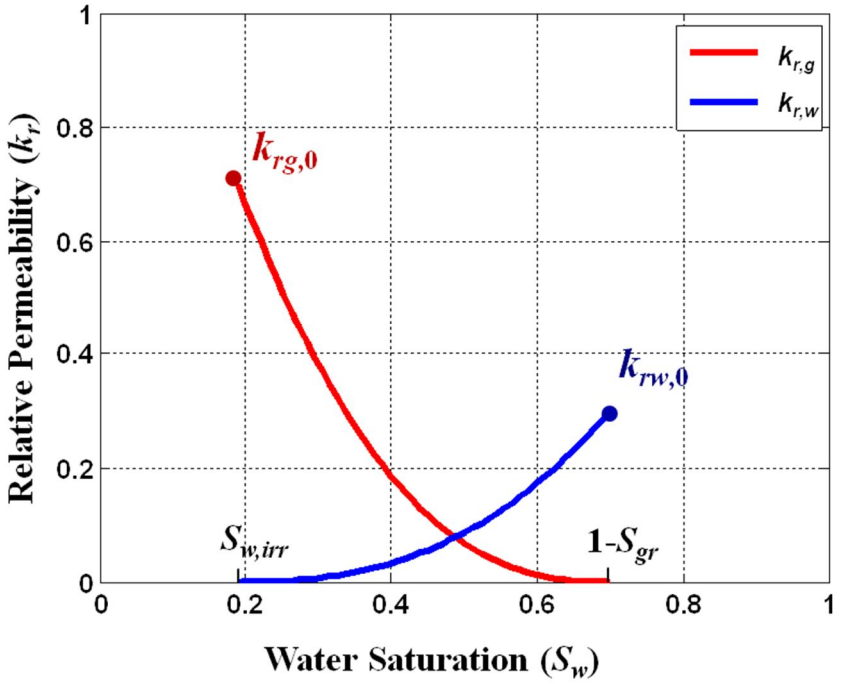

Fig. 4-10- Typical relative permeability curves for a water-wet sediment; red represents the relative permeability of gaseous phase and blue represents that of the aqueous phase. The end point relative permeabilities, along with the end point saturations are shown on the graph.

We apply the above model (Fig. 4-5), starting with the same initial gas saturation profile estimated by Behseresht and Bryant (2012) based on the capillary entry pressure profile calculated from the grain size distribution at each depth (Behseresht and Bryant, 2012). The initial gas saturation profile in the D sand unit, therefore, can be approximated by that shown in Fig. 4-6 having h_0 = 650 m, h_1 = 614 m, $S_{w,irr}$ = 0.2 and S_{gr} = 0.3 (Behseresht et al., 2009).

4.5.1) Results

Figure 36a shows the calculated R_v versus depth with a solid black line as the BGHSZ moves down through the methane/water bearing sediment. The reason that R_v values increase with depth from the upper part of the unit is that as the BGHSZ moves downward and the length of hydrate-bearing sediment, L_h, increases, the overall permeability of the hydrate bearing sediment, $k_{w,h}$ decreases. This reduction in permeability to aqueous phase reduces the water flow rate from above which is equivalent to an increase in R_v. The R_v in the imbibed zone below 630 m, swept by water to the end-point saturation $1-S_{gr}$, is zero. This is because when BGHSZ descends into the residual gas zone, no more gas is available to flow upwards as all gas saturation below the BGHSZ is at residual. Examination of Eqs. (4.34) and (4.39) shows that the calculated R_v, and hence the predicted hydrate saturation profile, is independent of the porosity, ϕ. Therefore, effectively for a given initial gas water saturation, the ratio $k_w/k_{w,h}$ is the main parameter governing R_v under a fixed thermodynamic condition (i.e. at fixed T and P, hence $\bar{V}_g \big/ N\bar{V}_w = const$).

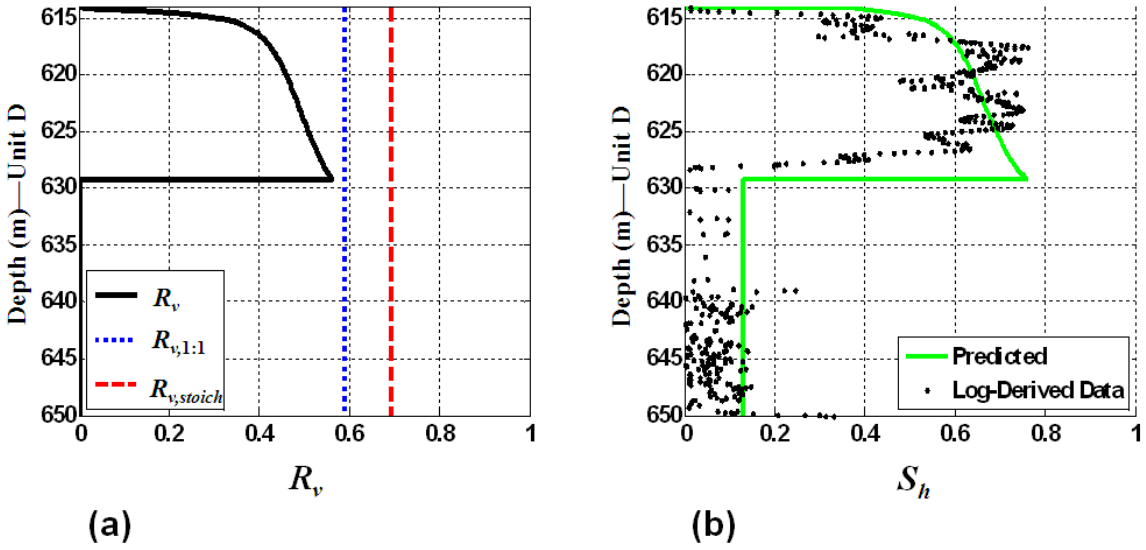

Fig. 4-11- Application of the pressure-driven fluid transport model to the D sand unit in Mount Elbert well using end-point relative permeability values of $k_{rw,0}$=0.3 and $k_{rg,0}$=0.7. (a) R_v versus depth shown in solid black line. R_v is zero below 629 m because the gas saturation dropped to residual there as gas moved upward to the GHSZ during hydrate formation. The values of $R_{v,1:1}$ and $R_{v,stoich}$ are shown in dotted line and dashed line, respectively. (b) Predicted hydrate saturation profile in green solid line versus dots representing the log-derived hydrate saturation data (Lee and Collett, 2011).

The calculated value of R_v determines the hydrate saturation at each depth. Fig. 4-11b shows the predicted hydrate saturation profile along with the log-derived hydrate saturation data of the D sand unit in Mount Elbert well (Lee and Collett, 2011). It is important to note that the hydrate saturation profile, shown in green solid line (Fig. 4-11b), evolved from an initially uniform gas saturation profile with $S_{g,i} \approx 1 - S_{w,irr}$ = 0.8 filling almost the entire D sand unit. The agreement with the measured values of S_h is reasonable. The trend of increasing S_h from 614 m to 620 m is evident, as is the small but nonzero S_h between 630 m and 650 m.

Applying the model on D sand unit in Mount Elbert well with a smaller end-point relative permeability for aqueous phase compared to that in Fig. 4-11, $k_{rw,0}$ = 0.1, predicts

a longer hydrate column but at smaller saturation as shown in Fig. 4-12. The reason is that the smaller aqueous phase end-point relative permeability slows the rate at which gas can move to the BGHSZ, causing R_v to be smaller, and hence S_h to be smaller. The mass of gas converted to hydrate is the same as in Fig. 4-11, so the smaller S_h requires a longer column in the upper hydrate-bearing zone than in Fig. 4-11.

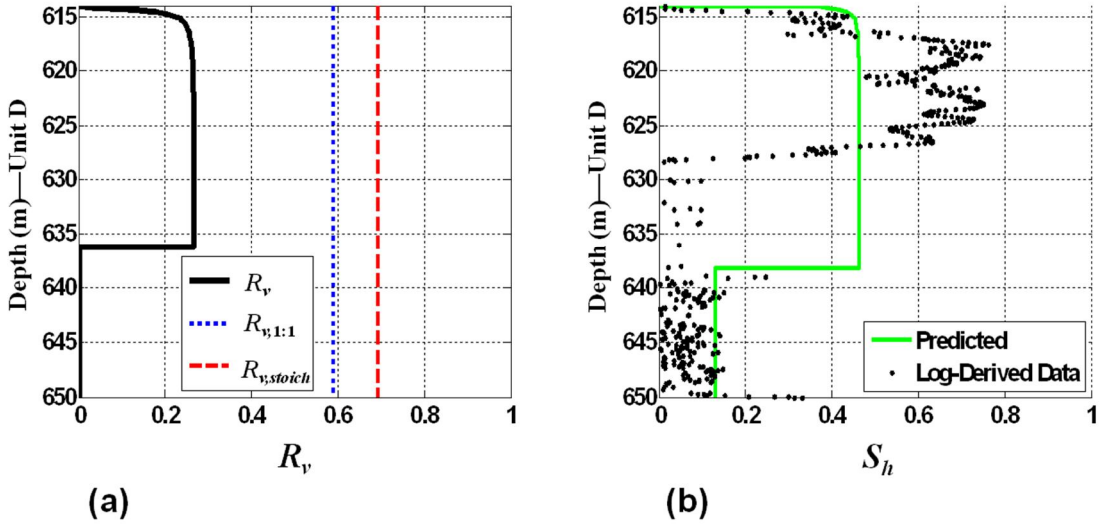

Fig. 4-12- Application of the pressure-driven fluid transport model to the D sand unit in Mount Elbert well using an end-point $k_{rw,0} = 0.1$ yields smaller R_v and correspondingly thicker upper zone of hydrate at a smaller saturation than in Fig. 4-11. (a) R_v versus depth shown in solid black line. (b) Predicted hydrate saturation profile in green solid line. Dots represent the log-derived hydrate saturation data (Lee and Collett, 2011).

Fig. 4-13b shows the predicted hydrate saturation profile when the end-point relative permeability to aqueous phase is changed from 0.3 (in Fig. 4-11) to 0.5. The larger value in effect enables more rapid transport of methane to the GHSZ, thus a larger R_v, which in turn results in a larger hydrate saturations at the top of the sand unit. A larger hydrate saturation at the top would reduce the permeability to aqueous phase in the hydrate-bearing sediment, causing R_v to increase further even more than $R_{v,stoich}$. In the

present model, this feedback leads to complete conversion of aqueous phase saturation to hydrate, yielding S_h = 1 in some upper part of the column. As one part of the column at the top is fully filled with hydrate, i.e. S_h=1, permeability to water from above would vanish. This prevents subsequent transport of water from above the GHSZ. Thus the hydrate saturation below this point corresponds only to converting the existing initial water saturation, with an R_v=0, and a large gas saturation is predicted to remain unconverted (pink box in Fig. 4-13). Neither the predicted hydrate saturation profile nor the presence of gaseous phase is consistent with observations (Boswell et al., 2011).

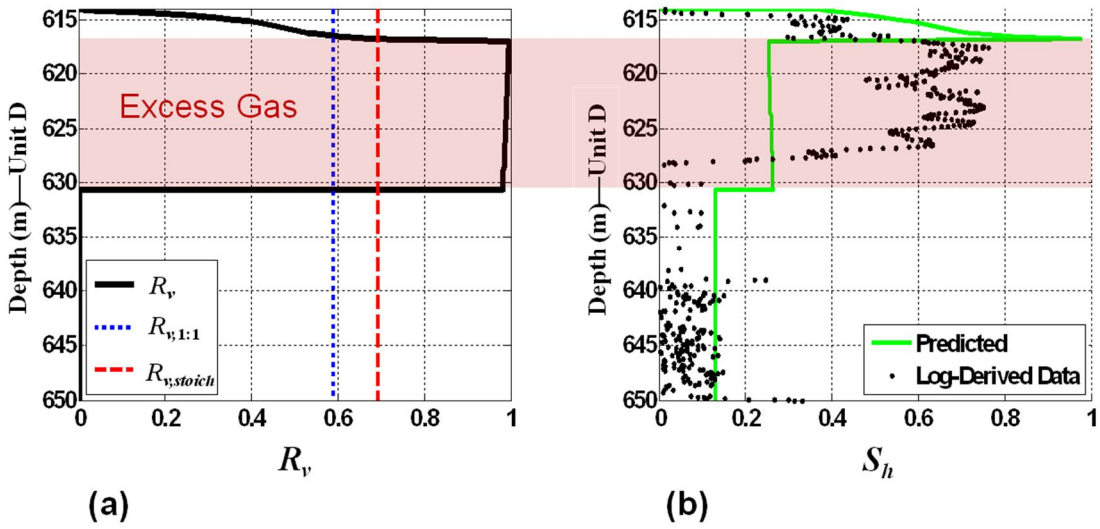

Fig. 4-13- Applying the viscous flow model along with the stoichiometric model of chapter 2 on the D sand unit in Mount Elbert well using an end-point $k_{rw,0}$=0.5 yields a qualitatively different behavior than Fig. 4-11 and Fig. 4-12. (a) R_v versus depth shown in solid black line. Calculated R_v from the flow model exceeds $R_{v,stoich}$ in part of the sand unit which is highlighted with a red fill. (b) Predicted hydrate saturation profile in green solid line. The zone identified with red fill contains hydrate and gas only which is in contradiction to the observed profile in field having hydrate and water only.

4.6) DISCUSSION OF THE PRESSURE-DRIVEN VISCOUS-DOMINATED TRANSPORT MODEL

Comparing the above figures it is evident that the observations in Mount Elbert well agrees more with $k_{rw,0} = 0.3$, Fig. 4-11. However, the model which only accounts for the viscous flow of aqueous and gaseous phases, is very sensitive to the endpoint aqueous phase relative permeability as well as the effective permeability to water in the hydrate zone. In fact, the ratio of $k_{rw,0}/k_{w,h}$ is very crucial to the behavior of the model. The same sensitivity shown in Fig. 4-12 and Fig. 4-13 would also apply if the value of permeability to aqueous phase in the hydrate-bearing sediment $k_{w,h}$ were to change by a factor of two. Laboratory experiments reported in the literature suggest that this permeability is highly sensitive to hydrate saturation, and in any case it will also depend strongly on the variation in grain size within the hydrate-bearing sediment. Moreover, the model contains a feedback loop, in that larger $k_{rw,0}$ yields larger hydrate saturations, which cause smaller values of $k_{w,h}$. This is the cause of the increase in S_h with depth between 614 and 629 m in Fig. 4-11, and between 614 m and 617 m in Fig. 4-13. The hydrate saturation profiles predicted for smaller or larger values of $k_{rw,0}/k_{w,h}$ shown in Fig. 4-12 and Fig. 4-13, respectively, are not observed at Mount Elbert well (Lee and Collett, 2011).

Numerous hydrate accumulations in the Alaska North Slope exhibit saturation profiles qualitatively similar to that observed in Mount Elbert well (see Fig. 1-9). Yet a pressure-driven transport model yields the behavior observed at Mount Elbert only for a rather narrow range of choices of $k_{rw,0}/k_{w,h}$. The range of choices seems particularly narrow considering the likely range of values in different accumulations. For these reasons, it seems unlikely that pressure-driven flow is responsible for supplying gas and aqueous phases to the hydrate stability zone during conversion. Physically, the problem with this model is that pressure-driven flow cannot supply aqueous phase from below the

BGHSZ. The gas phase is supplied from below the BGSHZ at a rate proportional to $k_{rw,0}$ while the aqueous phase must be supplied from above at a rate proportional to $k_{w,h}$. The ratio $k_{rw,0}/k_{w,h}$ fixes the relative rates of gas and aqueous phase transport. These rates must be rather finely balanced to yield the observed saturation profiles.

4.6.1) The Missing Piece: Capillary-driven Flow

The pressure-driven model neglects an important aspect of fluid flow in porous media, especially when water saturation approaches $S_{w,irr}$: capillary pressure gradients causing an extra water suction to keep the aqueous phase connected, i.e. $S_w \geq S_{w,irr}$. This is in analogy with the observed induced water suction during frost heave formation, which keeps the aqueous phase connected for continued heave formation (Hermansson and Spencerguthrie, 2005; Penner, 1959). Formation of hydrate is analogous in several respects to frost heave formation (Cook et al., 2008; Lee et al., 2011; Rees et al., 2011). Once the aqueous phase saturation becomes close to the $S_{w,irr}$, further decrement of the aqueous phase saturation due to hydrate formation would cause a large capillary pressure gradient. This imposed saturation gradient is expected to drive transport of aqueous phase to the GHSZ to counteract the decrement in saturation. Because the gradient dP_c/dS_w is largest near $S_{w,irr}$, this mechanism is likely to prevent R_v from increasing beyond $R_{v,1:1}$ if hydrate forms slowly enough. Fig. 4-14 shows the model prediction for the same parameters as in Fig. 4-13, but assuming R_v cannot exceed $R_{v,1:1}$. With the latter constraint on R_v, the predicted hydrate saturation fairly matches the log-derived data and predicts an excess water situation (having hydrate and water only), as expected.

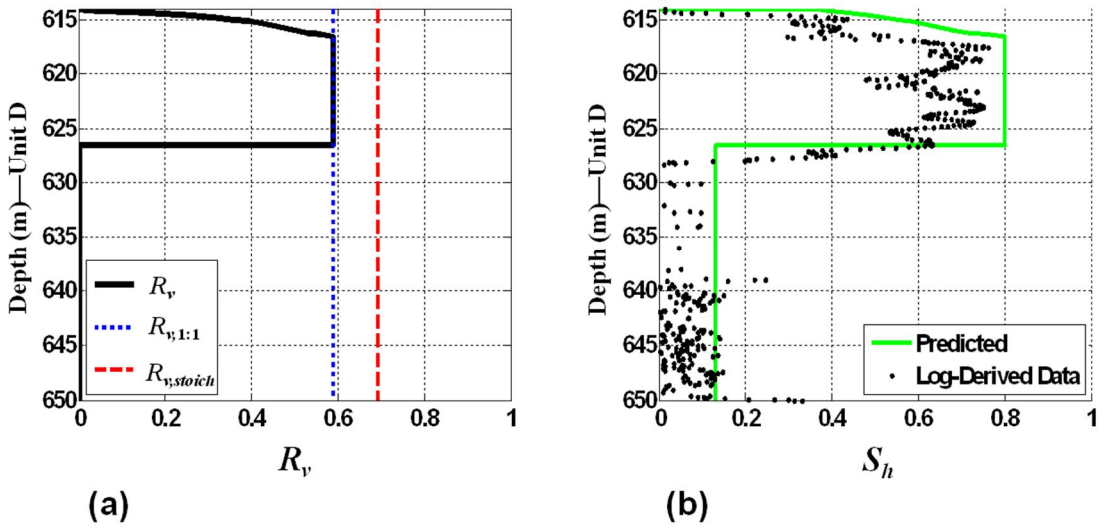

Fig. 4-14- Applying a constrained pressure-driven fluid transport model along with the stoichiometric model of chapter 2 on the D sand unit in Mount Elbert well using an end-point $k_{rw,0} = 0.5$; the constraint is that R_v is not allowed to exceed the value $R_{v,1:1}$. The predicted hydrate saturation profile overestimates the measurements in the upper part of the unit and yields a slightly thinner accumulation. The small hydrate saturation below 627 m is the result of converting residual gas saturation to hydrate.

Of course the aforementioned constraint on R_v is entirely *ad hoc*. The fact that overriding the pressure-driven flow model in this way yields a saturation profile close to what is observed raises the interesting hypothesis that capillarity-driven transport is a more general means of accounting for the behavior during conversion to hydrate. This observation is the motivation for the next chapter of this dissertation.

4.7) SUMMARY: APPLICABILITY OF PRESSURE-DRIVEN TRANSPORT MODEL FOR CONVERSION OF GAS RESERVOIRS TO HYDRATE

The conversion of a gas accumulation into hydrate reduces the volume occupied by fluid phases and thus drives the flow of fluid phases toward the zone of hydrate formation. Assuming this flow is driven by gradient in potential has significant

implications for the applicability of the model. In particular, a *cocurrent flow* of gas and aqueous phases from below a descending base of gas hydrate stability zone (BGHSZ) upward into the hydrate stability zone (GHSZ) *cannot provide the required amount of water* for hydrate formation. This is because the rising gas phase forms a sharp front, in accord with fractional flow theory, ahead of which only gas flows. Thus the pressure-driven model must transport water to the GHSZ from above. That is, water moves down into the hydrate formation zone through accumulated hydrate from overlying aquifers, while gas rises to the GHSZ from the remaining gas reservoir.

With suitable choices of the key transport coefficients (effective permeability to aqueous phase at the residual gas endpoint, and effective permeability to aqueous phase of sand containing large hydrate saturation), the *countercurrent transport* of gas and aqueous phases *provides the large volumes of both components needed* to form large hydrate saturations observed in Arctic sediments. The large saturations occur only in the upper portion of the original gas accumulation, with the thickness and the saturation depending on the ratio of aqueous phase end point relative permeability to aqueous phase permeability in hydrate-bearing sediment. A column of small hydrate saturations (10-15%) forms below the upper zone; this lower zone is where residual gas phase saturation was established as gas flowed upward to the GHSZ and aqueous phase imbibed. During hydrate formation in the imbibed zones the only phase flowing into the GHSZ due to the volume change is the aqueous phase.

For plausible endpoint relative permeabilities for aqueous phase and for a reasonable choice of a relationship between water effective permeability and hydrate saturation, the model prediction agrees with behavior observed in the Mount Elbert well. However the model prediction is highly sensitive to the ratio of these transport

coefficients. Small variations in grain size distribution, end point relative permeability, or hydrate-saturation dependence of permeability to water yield large variations in predicted hydrate profiles, including qualitatively different behavior, e.g. preservation of a large gas phase saturation. Thus the pressure-driven fluid transport model is unlikely to provide a robust explanation of the mechanism of conversion. Instead it offers useful insight into the likely role of capillarity-driven transport, which is discussed in the next chapter of this dissertation.

Chapter 5: Gas Reservoir Conversion to Hydrate: Role of Capillarity-Driven Fluid Phase Transport at Bed-Scale

5.1) OVERVIEW

The preceding chapter shows that pressure-driven, viscous-dominated flow is unlikely to account for the observed hydrate saturation distributions at Mount Elbert or elsewhere in the subpermafrost accumulations. In this chapter we generalize the fluid flow model to account for capillarity-driven transport. For this application, saturation gradients provide the driving force. The model is otherwise the same as that described in section (4.3) . Here we recapitulate the main features of that model and include the relevant terms for capillarity-driven transport.

Here, it is assumed that the required fluid flow for hydrate formation is being supported from below only, owing either to a strong seal at the top or the fact that permeability reduces significantly due to hydrate formation at the top of the gas column at early stages of the BGHSZ descent. Fig. 5-1 shows a schematic of the fluxes happening in the reactive flow model of this chapter to simulate the conversion of a gas accumulation into a hydrate reservoir owing to a descending BGHSZ, i.e. growing GHSZ.

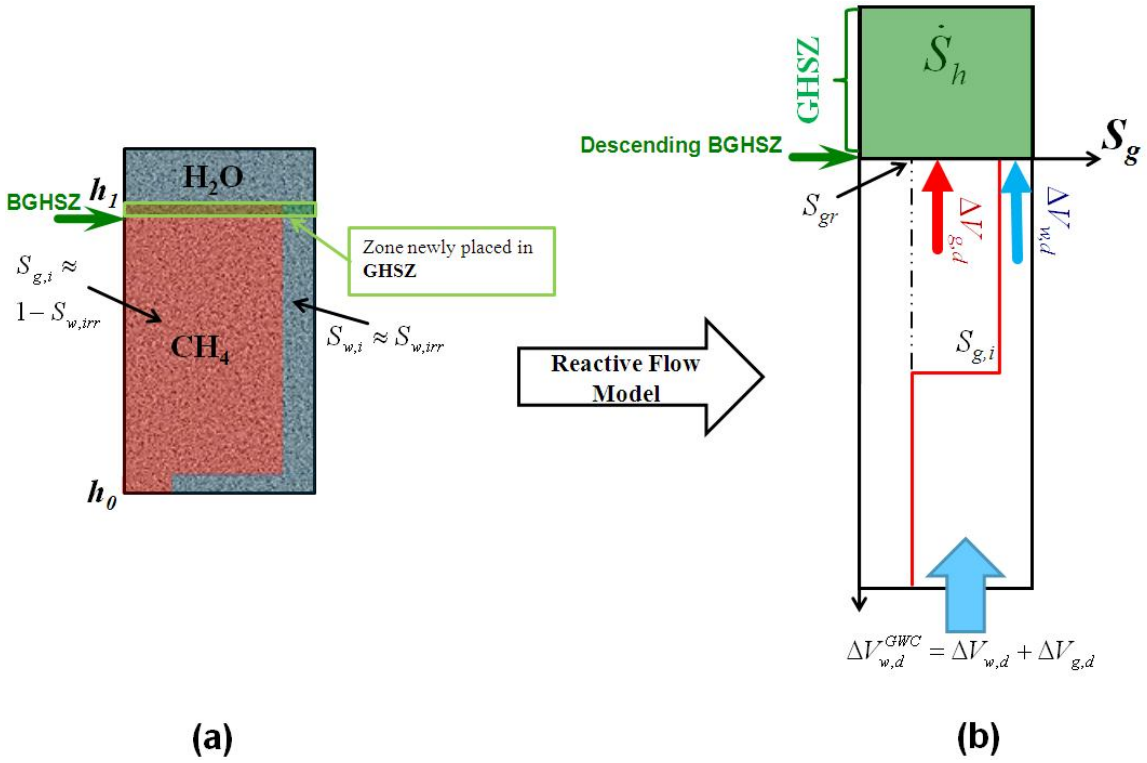

Fig. 5-1- Schematic of fluid flow induced by hydrate formation during descent of the BGHSZ. (a) a sand unit having a seal at depth, h_1 containing a gas accumulation below the seal. The BGHSZ is descending through the sediment column. The zone recently placed in the GHSZ is highlighted by a green fill on the sediment column. (b) Schematic of the reactive flow model developed in this chapter. Here, it is assumed that the required fluid flow for hydrate formation is being supported from below only, owing to a strong seal at the top or the fact that permeability reduces significantly due to hydrate formation at the top of the gas column.

5.2) NUMERICAL SIMULATION OF 1-D CONVERSION OF A GAS RESERVOIR TO A HYDRATE RESERVOIR

5.2.1) Model Formulation

In this section, the proposed model is formulated and a numerical approach is presented for implementing the model.

5.2.1.1) Flow Equations

Following the aforementioned assumption that flow of gaseous and aqueous phases occurs only from below in response to the formation of hydrate, the governing equations of this process is developed in this section. Considering the downward direction as positive direction, the multiphase flow of gaseous, u_g, and aqueous phase, u_w, based on Darcy's equation for 1-D vertical flow would be as follows:

$$u_w = -k\lambda_w\left(\frac{\partial P_w}{\partial z} - \rho_w g\right) \tag{5.1}$$

$$u_g = -k\lambda_g\left(\frac{\partial P_g}{\partial z} - \rho_g g\right) \tag{5.2}$$

where ρ_w and ρ_g are aqueous and gaseous phase mobilities, respectively, as defined in Eq. (4.9). The flow is assumed incompressible with only two mobile phases, gaseous and aqueous phases with a non-mobile hydrate phase.

As mentioned before, the difference between the gaseous phase pressure, P_g, and aqueous phase pressure, P_w, is known as capillary pressure, P_c. Therefore, the gradients of the two phase pressures are related as follows:

$$\frac{\partial P_g}{\partial z} = \frac{\partial P_w}{\partial z} + \frac{\partial P_c}{\partial z} \tag{5.3}$$

Defining u_T as the total flux of gaseous and aqueous phases combined with Eq. (5.3) gives

$$u_T = u_w + u_g = -k\lambda_w\left(\frac{\partial P_w}{\partial z} - \rho_w g\right) - k\lambda_g\left(\frac{\partial P_w}{\partial z} + \frac{\partial P_c}{\partial z} - \rho_g g\right) \tag{5.4}$$

Eq. (5.4) can be further simplified as

$$u_T = -k\left(\lambda_w + \lambda_g\right)\frac{\partial P_w}{\partial z} + k\left(\lambda_g\rho_g + \lambda_w\rho_w\right)g - k\lambda_g\frac{\partial P_c}{\partial z} \tag{5.5}$$

Solving for the aqueous phase pressure gradient from Eq. (5.5), and substituting in Eq. (5.1) gives Eq. (5.6) which avoids having to solve for the phase pressures.

$$u_w = \underbrace{\frac{\lambda_w}{\lambda_w + \lambda_g}u_T}_{\textit{Viscous}} + \underbrace{k\frac{\lambda_w\lambda_g}{\lambda_w + \lambda_g}\frac{\partial P_c}{\partial z}}_{\textit{Capillary}} + \underbrace{k\frac{\lambda_w\lambda_g}{\lambda_w + \lambda_g}\left(\rho_w - \rho_g\right)g}_{\textit{Gravity}} \tag{5.6}$$

As indicated in Eq. (5.6), three contributions to the water flux are viscous (pressure driven), capillary (saturation-gradient driven) and gravity (buoyancy) flows.

5.2.1.2) Mass Balance Equations

Consider an infinitesimal element of porous media with porosity ϕ, in which both gaseous and aqueous phases are present and hydrate is forming with a rate of $\dot{S}_h$ saturation unit per unit time (Fig. 5-2),

$$\frac{d}{dt}S_h = \dot{S}_h \tag{5.7}$$

The sediment is filled with water, methane and hydrate at any point in time, i.e.

$$S_w + S_g + S_h = 1 \tag{5.8}$$

As the proposed model is a 1-D model, the flows of aqueous and gaseous phases are assumed to happen only in the vertical direction. On Fig. 5-2 only the flow of aqueous phase is shown, but the same sketch and procedure can be repeated for the gaseous phase.

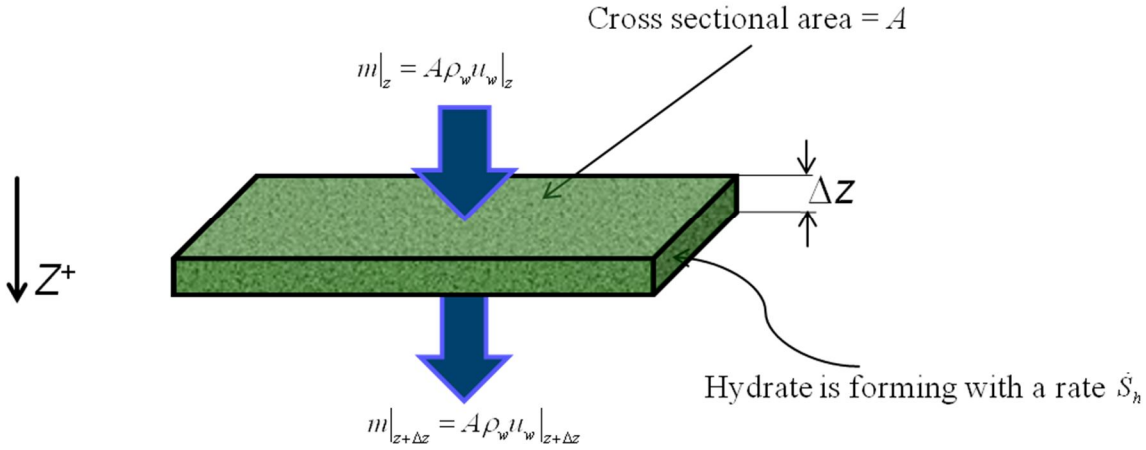

Fig. 5-2-A sediment layer of infinitesimal thickness, Δz, in which hydrate is forming. This illustrations is used in deriving Eq. (5.10). Note that positive z direction is downward.

The basic mass balance equation for water can be written as

$$\frac{\partial}{\partial t}\left(A\Delta z\phi S_w\rho_w\right) = A\rho_w u_w\big|_z - A\rho_w u_w\big|_{z+\Delta z} - \underbrace{A\Delta z\phi\rho_w\dot{S}_w}_{Sink} \tag{5.9}$$

Assuming water density is constant with depth and time, and porosity is constant (no compaction during hydrate formation) with time, Eq. (5.9) when $\Delta z \to 0$ is simplified as

$$\phi\frac{\partial}{\partial t}S_w + \frac{\partial}{\partial z}u_w + \alpha_w\dot{S}_h = 0 \tag{5.10}$$

where α_w, Eq. (5.11), is the stoichiometric conversion relating hydrate formation rate to consumption rate of water:

$$\alpha_w = \phi\frac{N\bar{V}_w}{\bar{V}_h} \tag{5.11}$$

where $\bar{V}_w$ and $\bar{V}_h$ are the molar volumes of water and hydrate, respectively.

Similarly, the continuity equation for the gaseous phase is as

$$\phi\frac{\partial}{\partial t}S_g + \frac{\partial}{\partial z}u_g + \alpha_g\dot{S}_h = 0 \tag{5.12}$$

where α_g, Eq. (5.13),is the stoichiometric conversion relating hydrate formation rate to consumption rate of methane; for simplicity we assume pure phases so that aqueous and gaseous phase saturations are synonymous with water component and methane component concentrations, respectively.

$$\alpha_g = \phi \frac{\bar{V}_g}{\bar{V}_h} \tag{5.13}$$

Summation of Eqs. (5.10) and (5.12) gives

$$\phi \frac{\partial}{\partial t}\left(S_w + S_g\right) + \frac{\partial}{\partial z}\left(u_w + u_g\right) + \left(\alpha_w + \alpha_g\right)\dot{S}_h = 0 \tag{5.14}$$

Substituting S_w+S_g=1-S_h in Eq. (5.14) and simplifying gives

$$\left(\alpha - \phi\right)\dot{S}_h + \frac{\partial}{\partial z} u_T = 0 \tag{5.15}$$

where $\alpha = \alpha_w + \alpha_g$.

5.2.1.3) Final Governing Equations for 1-D Conversion of a Gas Reservoir to a Hydrate Reservoir

Combining Eqs. (5.6) and (5.10) gives

$$\phi \frac{\partial}{\partial t} S_w + \frac{\partial}{\partial z}\left[\underbrace{\frac{\lambda_w}{\lambda_w + \lambda_g} u_T}_{Viscous} + \underbrace{k \frac{\lambda_w \lambda_g}{\lambda_w + \lambda_g} \frac{\partial P_c}{\partial S_w} \frac{\partial S_w}{\partial z}}_{Capillary} + \underbrace{k \frac{\lambda_w \lambda_g}{\lambda_w + \lambda_g} (\rho_w - \rho_g) g}_{Gravity} \right] + \underbrace{\alpha_w \dot{S}_h}_{Sink} = 0 \tag{5.16}$$

Given an $\dot{S}_h$ there would be four unknowns to solve in time and space: S_w, S_g, S_h, and u_T. The four equations required to identify the latter four unknowns would be Eqs. (5.7), (5.8), (5.15), and (5.16), summarized as the following system of equations:

$$
\begin{cases}
\phi \dfrac{\partial}{\partial t} S_w + \dfrac{\partial}{\partial z}\left[\underbrace{\dfrac{\lambda_w}{\lambda_w + \lambda_g} u_T}_{\textit{Viscous}} + \underbrace{k \dfrac{\lambda_w \lambda_g}{\lambda_w + \lambda_g} \dfrac{\partial P_c}{\partial S_w}}_{\textit{Capillary}} \dfrac{\partial S_w}{\partial z} + \underbrace{k \dfrac{\lambda_w \lambda_g}{\lambda_w + \lambda_g} (\rho_w - \rho_g) g}_{\textit{Gravity}} \right] + \underbrace{\alpha_w \dot{S}_h}_{\textit{Sink}} = 0 \\
\dfrac{d}{dt} S_h = \dot{S}_h \\
(\alpha - \phi) \dot{S}_h + \dfrac{\partial}{\partial z} u_T = 0 \\
S_w + S_g + S_h = 1
\end{cases}
\tag{5.17}
$$

The solution to the system of equations (5.17) depends on several rock and fluid properties: the relative permeability curves (for the phase mobilities), the capillary pressure curve (for the gradient of capillary pressure vs. saturation) and phase densities (for buoyancy). All flows are driven by hydrate formation, which is prescribed as a rate of hydrate formation and a descending BGHSZ. The domain includes the gas reservoir plus an infinite volume of aquifer below the gas/water contact; in fact the bottom boundary condition would be $S_w(t) = 1$. The top of the gas reservoir is assumed to be sealed to fluids (both gas and water).

The model assigns the rate of hydrate formation in a finite volume of sediment, GHSZ, which is growing with time, i.e. descending BGHSZ. We compute the fluxes in the gas/water region below the BGHSZ and fluxes within the GHSZ. The latter depends on the permeability to fluids in the presence of hydrate, for which an empirical correlation is used. The permafrost-associated hydrate reservoirs are commonly reported to exhibit pore-filling morphologies of hydrate distribution within the host sediment (Boswell et al., 2011; Dallimore and Collett, 2005). Therefore, for the permeability of the host sediment in the presence of hydrate an equation, Eq. (4.43), based on a pore-filling permeability model (Kleinberg et al., 2003; Spangenberg, 2001) is used.

As shown in Eq. (5.18), $\dot{S}_h = f(z,t)$ is a function of space and time. In fact a moving boundary condition is imposed on the system of equations (5.17) to mimic the descent of the BGHSZ happened in response to surface temperature cooling in the Arctic.

$$\dot{S}_h(z,t) = \begin{cases} \dot{S}_h & ; z \le z_{BGHSZ} \\ 0 & ; z > z_{BGHSZ} \end{cases} \tag{5.18}$$

In Eq. (5.18), z_{BGHSZ} is the depth of the BGHSZ which in turn is a function of time, $z_{BGHSZ} = f(t)$.

5.2.2) Numerical Model

As mentioned earlier, many rock properties as well as rock-fluid properties are involved in the model of this chapter including capillarity and relative permeability characteristics of the host sediment. For capillary characteristics, $P_c(S_w)$, Brooks-Corey model, Eq. (5.19), is used,

$$P_c = P_c^* \left(\frac{S_w - S_{w,irr}}{1 - S_{w,irr}} \right)^{-\frac{1}{\gamma}} \tag{5.19}$$

where P_c^* is the capillary entry pressure and γ is the pore-size distribution index (Brooks and Corey, 1964). Similarly, for relative permeability characteristics another correlation from Brooks and Corey (1964) is used, Eqs. (5.20) and (5.21).

$$k_{rw} = k_{w0} \left(\frac{S_w - S_{wirr}}{1 - S_{wirr} - S_{gr}} \right)^{N_w} \tag{5.20}$$

$$k_{rg} = k_{g0} \left(\frac{S_g - S_{gr}}{1 - S_{wirr} - S_{gr}} \right)^{N_g} \tag{5.21}$$

A fully implicit scheme is being used here to solve the system of equations (5.17). In order to discretize Eq. (5.16), two auxiliary functions, $F(S_w)$ and $G(S_w)$ are defined as follows:

$$F(S_w) = \frac{\lambda_w}{\lambda_w + \lambda_g} u_T + k \frac{\lambda_w \lambda_g}{\lambda_w + \lambda_g} (\rho_w - \rho_g) g \tag{5.22}$$

$$G(S_w) = k \frac{\lambda_w \lambda_g}{\lambda_w + \lambda_g} \frac{\partial P_c}{\partial S_w} \tag{5.23}$$

Therefore, water flux can be written as

$$u_w = F + G \frac{\partial S_w}{\partial z} \tag{5.24}$$

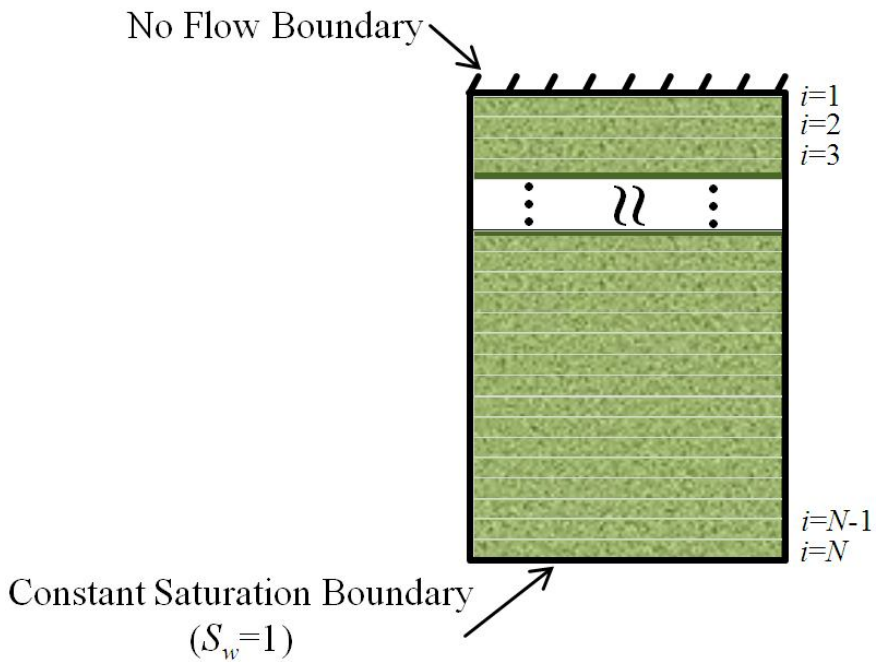

Fig. 5-3-A sediment column discretized into N grids with the specified boundary conditions: (i) no-flow boundary condition at the top and (ii) constant water saturation, S_w=1, at the bottom.

Fig. 5-3 shows the host sediment column discretized into N grids for each an objective function, f_i, needs to be defined and solved so that f_i=0, where i is the grid index, i.e. i = 1, 2, 3,…, N. The objective function for grids i=2 to i=N-1 can be generalized as

$$
\begin{aligned}
& f_i = \phi\left(S_{w,i}^{n+1} - S_{w,i}^{n}\right) + \\
& + \frac{\Delta t}{\Delta z}\left(F(S_{w,i}^{n+1}) - F(S_{w,i-1}^{n+1})\right) + \\
& + \frac{\Delta t}{(\Delta z)^2}\left[\left(G(S_{w,i}^{n+1}) - G(S_{w,i-1}^{n+1})\right)\left(S_{w,i}^{n+1} - S_{w,i-1}^{n+1}\right)\right] + \\
& + \frac{\Delta t}{(\Delta z)^2} G(S_{w,i}^{n+1})\left(S_{w,i+1}^{n+1} - 2S_{w,i}^{n+1} + S_{w,i-1}^{n+1}\right) + \\
& + \Delta t \alpha_w \dot{S}_{h,i}^{n+1} = 0
\end{aligned}
\tag{5.25}
$$

where $S_{w,i}^{n}$ denotes aqueous phase saturation at grid *i* at time step *n*. Note that a central discretization scheme is used for the diffusion terms, $\frac{\partial^2 S_w}{\partial z^2}$, and a backward scheme is used for convective terms, $\frac{\partial S_w}{\partial z}$. For the boundary grid *N*=1, the objective function is

$$
\begin{aligned}
& f_1 = \phi\left(S_{w,1}^{n+1} - S_{w,0}^{n}\right) + \\
& + \frac{\Delta t}{\Delta z}\left(F(S_{w,1}^{n+1}) - F(S_{w,0}^{n+1})\right) + \\
& + \frac{\Delta t}{(\Delta z)^2}\left[\left(G(S_{w,1}^{n+1}) - G(S_{w,0}^{n+1})\right)\left(S_{w,1}^{n+1} - S_{w,0}^{n+1}\right)\right] + \\
& + \frac{\Delta t}{(\Delta z)^2} G(S_{w,1}^{n+1})\left(S_{w,2}^{n+1} - 2S_{w,1}^{n+1} + S_{w,0}^{n+1}\right) + \\
& + \Delta t \alpha_w \dot{S}_{h,1}^{n+1} = 0
\end{aligned}
\tag{5.26}
$$

Considering the no-flow boundary condition at the top of grid *i*=1, the water flux would be zero at an imaginary grid *i*=0, i.e. $u_w\big|_{i=0} = 0$:

$$
\begin{aligned}
& f_1 = \phi\left(S_{w,1}^{n+1} - S_{w,1}^{n}\right) + \\
& + \frac{\Delta t}{\Delta z}\left(u_w\big|_1 - \cancel{u_w\big|_0}\right) + \\
& + \Delta t \alpha_w \dot{S}_{h,1}^{n+1} = 0
\end{aligned}
\tag{5.27}
$$

Substituting the water flux at grid *i*=1 from Eq. (5.27) into Eq. (5.26) gives the simplified objective function for grid *i*=1 as

$$f_1 = \phi\left(S_{w,1}^{n+1} - S_{w,0}^{n}\right) + \frac{\Delta t}{\Delta z}\left(F\left(S_{w,1}^{n+1}\right) + G\left(S_{w,1}^{n+1}\right)\frac{\left(S_{w,2}^{n+1} - S_{w,1}^{n+1}\right)}{\Delta z}\right) + \Delta t \alpha_w \dot{S}_{h,1}^{n+1} = 0 \tag{5.28}$$

For the bottommost grid, *i*=*N*, a Dirichlet boundary condition applies as $S_{w,N+1}^{n} = 1$.

Therefore, the objective function would be

$$\begin{aligned} f_N &= \phi\left(S_{w,N}^{n+1} - S_{w,N}^{n}\right) + \\ &+ \frac{\Delta t}{\Delta z}\left(F(S_{w,N}^{n+1}) - F(S_{w,N-1}^{n+1})\right) + \\ &+ \frac{\Delta t}{(\Delta z)^2}\left[\left(G(S_{w,N}^{n+1}) - G(S_{w,N-1}^{n+1})\right)\left(S_{w,N}^{n+1} - S_{w,N-1}^{n+1}\right)\right] + \\ &+ \frac{\Delta t}{(\Delta z)^2} G(S_{w,N}^{n+1})\left(1 - 2S_{w,N}^{n+1} + S_{w,N-1}^{n+1}\right) + \\ &+ \Delta t \alpha_w \dot{S}_{h,N}^{n+1} = 0 \end{aligned} \tag{5.29}$$

The Jacobian matrix, (5.30), for solving the above objective functions, or equivalently solve Eq. (5.16), would be a three diagonal matrix since the model is one dimensional.

$$J = \begin{bmatrix} \frac{\partial f_1}{\partial S_{w,1}^{n+1}} & \frac{\partial f_1}{\partial S_{w,2}^{n+1}} & & & 0 & 0 & 0 \\ \frac{\partial f_2}{\partial S_{w,1}^{n+1}} & \frac{\partial f_2}{\partial S_{w,2}^{n+1}} & \frac{\partial f_2}{\partial S_{w,3}^{n+1}} & & & 0 & 0 \\ & \frac{\partial f_3}{\partial S_{w,2}^{n+1}} & \frac{\partial f_3}{\partial S_{w,3}^{n+1}} & \frac{\partial f_3}{\partial S_{w,4}^{n+1}} & & & 0 \\ & & \ddots & \ddots & \ddots & & \\ 0 & & & \frac{\partial f_{N-2}}{\partial S_{w,N-3}^{n+1}} & \frac{\partial f_{N-2}}{\partial S_{w,N-2}^{n+1}} & \frac{\partial f_{N-2}}{\partial S_{w,N-1}^{n+1}} & \\ 0 & 0 & & & \frac{\partial f_{N-1}}{\partial S_{w,N-2}^{n+1}} & \frac{\partial f_{N-1}}{\partial S_{w,N-1}^{n+1}} & \frac{\partial f_{N-1}}{\partial S_{w,N}^{n+1}} \\ 0 & 0 & 0 & & & \frac{\partial f_N}{\partial S_{w,N-1}^{n+1}} & \frac{\partial f_N}{\partial S_{w,N}^{n+1}} \end{bmatrix} \tag{5.30}$$

Therefore, the tridiagonal matrix algorithm (TDMA) also known as Thomas algorithm may be used here. Using this algorithm, the solution can be obtained in $O(n)$ operations instead of $O(n^3)$ required by Gaussian elimination. In Thomas algorithm a first sweep of J eliminates the elements below the main diagonal and then a backward substitution generates the solution (Conte, 1980).

In the following results, the applied rates of descent of the BGHSZ are assumed constant. It is also possible to assign variable, with time t, rates of descent of the BGHSZ. The main outputs of the model are profiles of flux and saturation for each phase. The three contributions to the flux of each fluid phase are also extracted.

5.2.3) Results: Numerical Simulations

In this section we consider an initial gas reservoir through which gaseous and aqueous phase saturations are distributed based on capillarity/gravity equilibrium below a seal at the top. The gas reservoir is then gradually encompassed by the GHSZ from the top to mimic the descent of the BGHSZ due to temperature cooling at the surface. The emerged gaseous and aqueous phase fluxes, derived by hydrate formation inside the growing GHSZ, are then predicted. It is shown that the rate of hydrate formation along with the rate of descent of the BGHSZ, i.e. the rate of temperature cooling at the surface, plays a key role in determining the final hydrate saturation as well as the final state of the system, i.e. hydrate coexists with aqueous phase (excess water) versus hydrate coexists with gas phase (excess methane). For the following set of simulations a 25m thick sand unit having similar thickness to that of Unit D of Mount Elbert well is used. In the first round of simulations, the effect of hydrate formation rate, $\dot{S}_h$, relative to the rate of descent of the BGHSZ is addressed, keeping the physical rock properties fixed at values

reported in Table 5-1. The characteristic relative permeability and capillary pressure curves associated with the values of Table 5-1 are shown in Fig. 5-4.

Table 5-1-Sand Unit physical properties used in simulations of section (5.2.3)

Capillary Characteristics				**Relative Permeability Characteristics**			
γ	P_c^* (Pa)	K (md)	ϕ	N_g	$k_{rg,0}$	N_w	$k_{rw,0}$
1	5×10^3	250	0.25	2.5	0.7	2.5	0.5

For simplification, the densities of gaseous and aqueous phases are assumed constant during hydrate formation, being the same as the values used in chapter 3. These values are summarized in Table 5-2.

Table 5-2-methane, water and hydrate properties used in simulations of section (5.2.3)

Molecular Weights (kg/kg-mole)			**Hydration Number**	**Density (kg/m^3)**			**Molar Volume (m^3/kg-mole)**		
Water	methane	Hydrate	N	ρ_w	ρ_g	ρ_h	$\bar{V}_w$	$\bar{V}_g$	$\bar{V}_h$
18	16	124	6	1000	55	914	0.018	0.291	0.136

Numerous realizations of the proposed model were investigated to capture the characteristic behaviors associated with conversion of a pre-established gas accumulation into a hydrate accumulation through temperature cooling at the surface, i.e. descent of the BGHSZ. Some of these cases are studied in detail in this section. Later in the discussion, these various realizations are synthesized together for characterizing the observed behavior over a broad range of $\dot{S}_h$ versus the rate of descent of the BGHSZ. The latter constant rates for the cases presented in this section are summarized in Table 5-3. Other

pertinent parameters used in this set of realizations are summarized in Table 5-1 and Table 5-2.

Table 5-3- Rate of hydrate formation and rate of descent of the BGHSZ for the cases discussed in section (5.2.3) .

Case #	$\dot{S}_h$ (sat. unit/day)	$\dot{z}_{BGHSZ}$ (m/year)
1	8.64E-04	2.37E-03
2	8.64E-04	2.37E-01
3	8.64E-04	9.46E+00
4	8.64E-04	9.46E+04

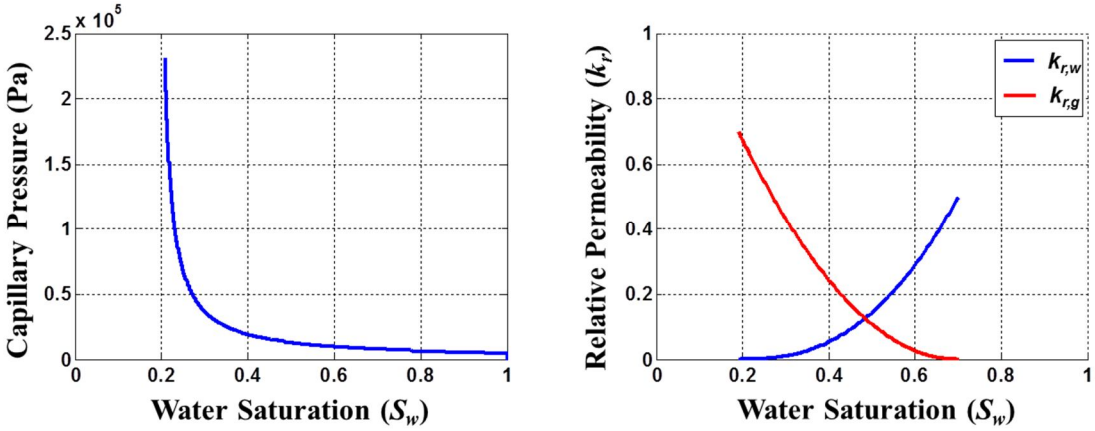

Fig. 5-4-(Left) Capillary pressure versus water saturation, and (right) relative permeability characteristics for gaseous and aqueous phases associated with parameters in Table 5-1.

Case 1

In this case a relatively small hydrate formation rate of $\dot{S}_h = 8.6\times10^{-4}$ saturation-unit/day inside the GHSZ is considered with the thickness of the GHSZ increasing downward, i.e. the BGHSZ descends, at a rate of 2.7×10^{-3} m/year. Fig. 5-5 shows the evolution of hydrate saturation profile (left panel) and that of the gaseous and aqueous

phases (right panel) at five different steps in time. The highlighted green area indicates the part of the sand unit inside the HSZ at each point in time. As hydrate is forming inside the expanding GHSZ, gaseous and aqueous phases flow into the GHSZ to support the required amounts of phases (see Fig. 5-6). As a result, the GWC is gradually rising towards the descending BGHSZ. Once the BGHSZ passes the GWC, the zone newly placed inside the GHSZ would contain residual gas saturation, S_{gr} (See t = 7772 yrs.). Therefore, the only moving phase is aqueous phase, i.e. R_v=0. As discussed in chapter 3, for S_{gr} = 0.3, Fig. 2-9 (curve for $S_{w,i}$ = 0.7 evaluated at R_v = 0) yields a hydrate saturation S_h = 0.13. The corresponding fluxes of gaseous and aqueous phases are shown in Fig. 5-6.

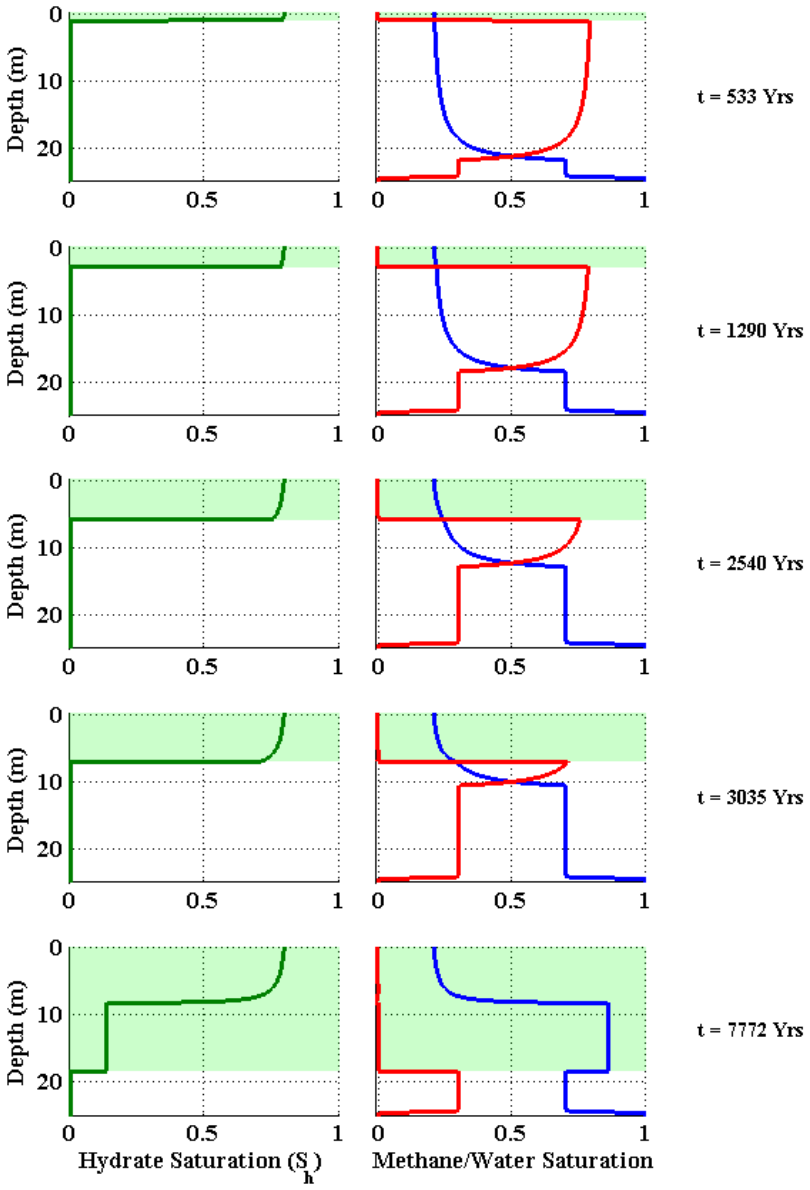

Fig. 5-5- Model results for Case 1 where rate of hydrate formation and rate of descent of the BGHSZ are both small. The highlighted green area indicates the part of the sand unit inside the HSZ. As hydrate is forming inside the expanding GHSZ, gaseous and aqueous phases flow into the GHSZ to support the required amounts of phases. As a result, the GWC gradually rises towards the descending BGHSZ. The left panel shows the evolution of hydrate saturation profiles and the right panel shows the methane (red) and water (blue) saturation profiles for different locations of the BGHSZ. The corresponding fluxes of gaseous and aqueous phases are shown in Fig. 5-6.

Simulation results show that in this case the required fluxes of gas and water are proportionately small, as seen in Fig. 5-6 (left panel). Based on the convention used earlier, the positive *z*-direction is downwards; therefore, the negative values of fluxes in Fig. 5-6 means upward flux of gaseous and aqueous phases towards the GHSZ. As seen in Fig. 5-6 (right panel), the pressure-driven, viscous, flow of aqueous phase is quite small, while the saturation-gradient driven, capillary, flow accounts for most of the aqueous phase flux especially in the region between the BGHSZ and the gas-water contact (GWC). The gaseous and aqueous phase fluxes, as well as the total flux, change in time owing to the two counteracting reasons: (i) the GHSZ is growing and hydrate is forming inside a larger portion of the sand unit leading to an increase in fluxes, and (ii) some parts of the sand unit already inside the GHSZ, on the other hand, run out of the gaseous phase and thus hydrate formation stops in those parts leading to a reduction in fluxes.

It is worth emphasizing that the flux of water is almost entirely due to capillarity, until the BGHSZ and the GWC meet. Before the HSZ encompasses the residual gas zone, although the methane and water fluxes vary with time, the value of R_v, the fraction of total flux which is gas phase, stays in the range $0.55<R_v<0.59$. It was shown in chapter 3 that Mount Elbert well hydrate accumulation is consistent with an $R_v \approx 0.55$, and in any case for a capillary dominated flow, R_v is expected to be less than $R_{v,1:1}$ that is 0.59 for the density values of Table 5-2. The final hydrate saturation, when no more hydrate can form due to exhaustion of the gaseous phase, is shown in Fig. 5-7. The final hydrate saturation profile exhibits a sharp basal contact, i.e. hydrate saturation changes from large values to values less than 15% over a narrow depth range. Besides during the conversion process within the GHSZ the aqueous phase could always maintain its existence throughout the

sand unit, i.e. the sand unit remained wet at all times. Based on the latter two characteristics, sharp basal contact and being wet at all times, a symbol  is used to describe such mode of conversion of gas accumulation into a hydrate reservoir. In the following, other cases with qualitatively different behaviors are introduced and symbolized accordingly.

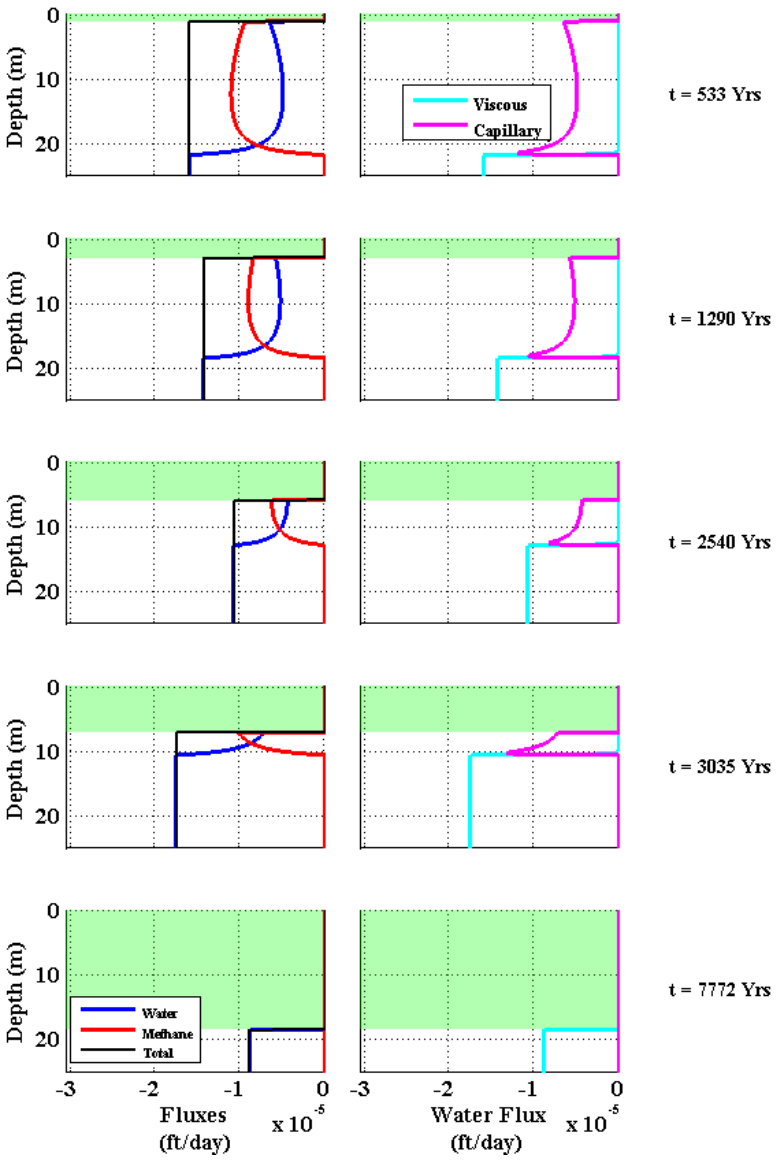

Fig. 5-6- Model results for Case 1 where rate of hydrate formation and rate of descent of the BGHSZ are both small. Left panel: Phase fluxes (blue = water, red = gas) in the formation at the times indicated on the right hand side. The highlighted area (in green) indicates the part of the sand unit inside the HSZ at each time. Negative values of flux mean upward flow. The flux of gas and water are changing through time as the BGHSZ encompasses larger portion of the gas column; however, at the same time some portions of the sand unit already inside the GHSZ run out of gaseous phase and thus hydrate formation stops. Right panel: the contribution of viscous flow and capillarity flow in aqueous phase flux is demonstrated. It is clear that capillarity plays a key role in providing the GHSZ with the required amounts of water.

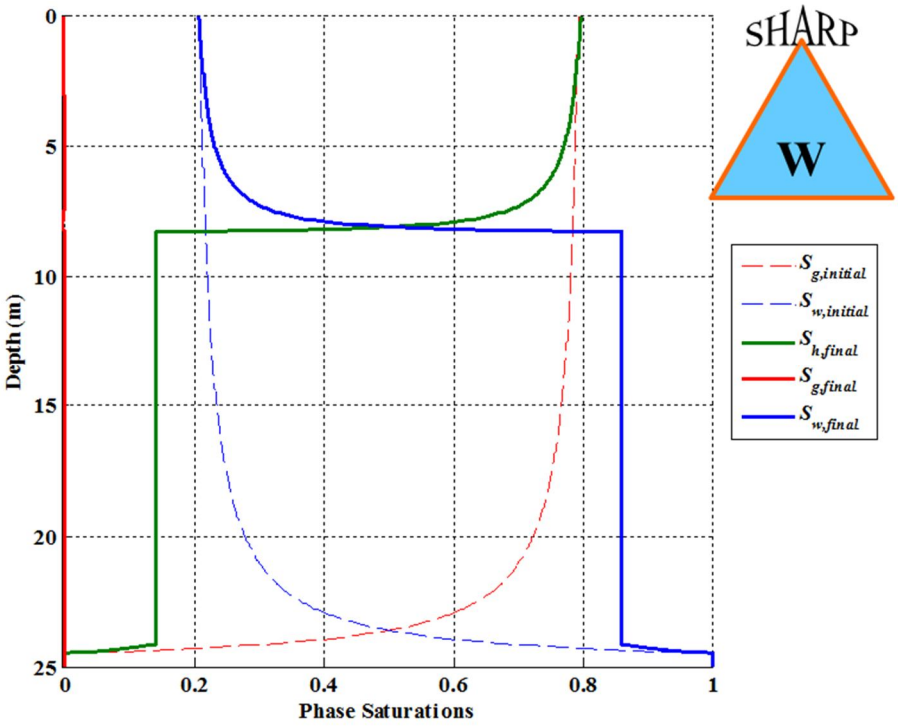

Fig. 5-7- Model results for Case 1 where rate of hydrate formation and rate of descent of the BGHSZ are both small: Initial gaseous and aqueous phase saturations are shown in red and blue dashed lines, respectively. The final hydrate saturation, when no more hydrate forms because the gaseous phase is exhausted, is shown in solid green line. The solid blue and red lines represent the final aqueous phase and gaseous phase saturation profiles, respectively. The corresponding symbol to this case, showing that the final hydrate saturation profile exhibits a sharp basal contact through a process in which the sand unit remained wet at all times, is shown at the top right corner.

Case 2

In this case the hydrate formation inside the GHSZ is the same as that in Case 1, i.e. $\dot{S}_h = 8.6\times10^{-4}$ saturation-unit/day. However, a descent rate of the BGHSZ considered in Case 2 is two orders of magnitude larger than that in Case 1 (see Table 5-3). Fig. 5-8 shows the evolution of hydrate saturation profile (left panel) and that of the gaseous and aqueous phases (right panel) at five different steps in time. Similar to that in Case 1, as

hydrate is forming inside the expanding GHSZ, green fill, the GWC gradually rises towards the descending BGHSZ pushing the required phase volumes towards the GHSZ. Considering the larger rate of descent of the BGHSZ, compared to that in Case 1, the sand unit is encompassed by the GHSZ much faster and thus the total amount of hydrate formation would grow much faster than that in Case 1. Larger amounts of hydrate growth require larger fluxes of gaseous and aqueous phases. That is why the fluxes in Fig. 5-9 are about two orders of magnitude larger than those in Fig. 5-6.

Simulation results (Fig. 5-9) shows that, in the upper three meters of the sand unit, although the aqueous phase flow is mainly derived by saturation gradient, i.e. capillary flow, the viscous flow of the gaseous phase dominates that of the aqueous phase flow so that $R_v > R_{v,stoich}$.[3] That is why the upper three meter of the sand unit would eventually run out of the aqueous phase, i.e. an excess gas situation evolves (see Fig. 5-8). However, as the BGHSZ descends further and gets closer to the rising GWC, the contribution of the aqueous phase in the total flux becomes larger so that R_v becomes smaller than $R_{v,stoich}$ and quickly becomes smaller than $R_{v,1:1}$. The final hydrate saturation, when no more hydrate can form due to exhaustion of either the gaseous phase, below 3 m depth, or the aqueous phase, top 3 meters, is shown in Fig. 5-10. Similar to that in Case 1, the final hydrate saturation exhibits a sharp basal contact; however, the top section of the sand, above 3 m depth which was initially wet, dried out during the conversion and remained filled by gas and hydrate phases. Therefore, a symbol  is used to describe this mode of gas accumulation conversion showing a sharp basal contact and a wet/dry, i.e. initially wet (W) but dried out (D) eventually, situation for the host sediment.

[3] $R_{v,stoich}$ is about 0.7 for the densities of Table 5-2 and an initial gas saturation of about 80%.

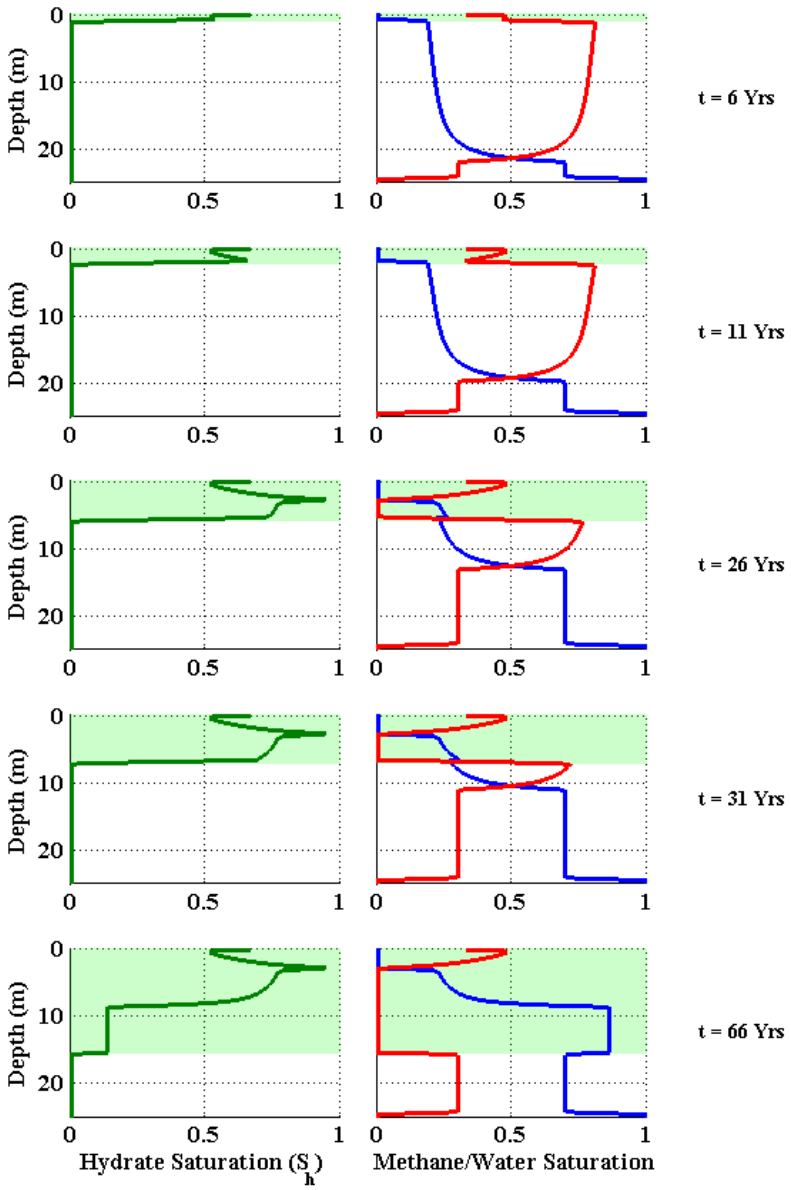

Fig. 5-8- Model results for Case 2 with a faster rate of descent of the BGHSZ, compared to that in Case 1. The green fill indicates the part of the sand unit inside the HSZ. As hydrate is forming inside the expanding GHSZ, gaseous and aqueous phases flow into the GHSZ to support the required amounts of phases. As a result, the GWC gradually rises towards the descending BGHSZ. The left panel shows the evolution of hydrate saturation profiles and the right panel shows the methane (red) and water (blue) saturation profiles for different locations of the BGHSZ. The corresponding fluxes of gaseous and aqueous phases are shown in Fig. 5-9.

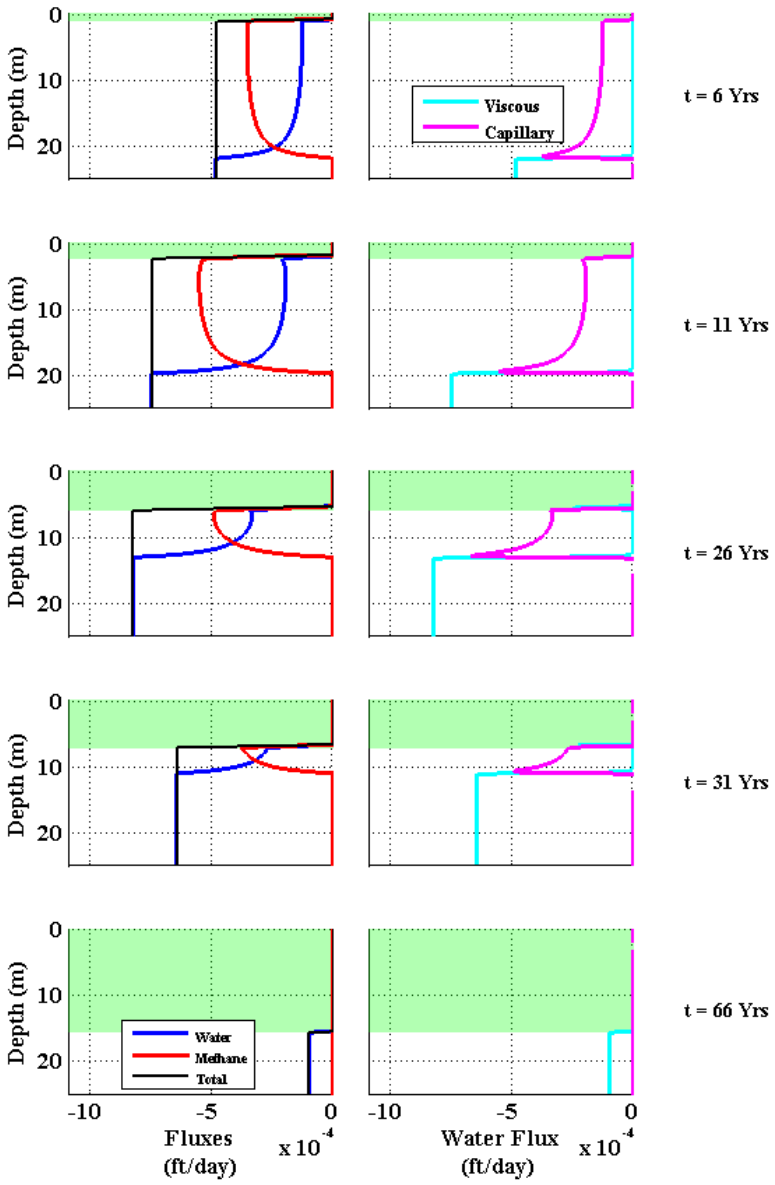

Fig. 5-9- Model results for Case 2 where a faster rate of descent of the BGHSZ, compared to that in Case 1. Left panel: Phase fluxes (blue = water, red = gas) in the formation at the times indicated on the right hand side. Right panel: the contribution of viscous flow and capillarity flow in aqueous phase flux is demonstrated. Capillarity plays a key role in providing the required amount of water to the GHSZ.

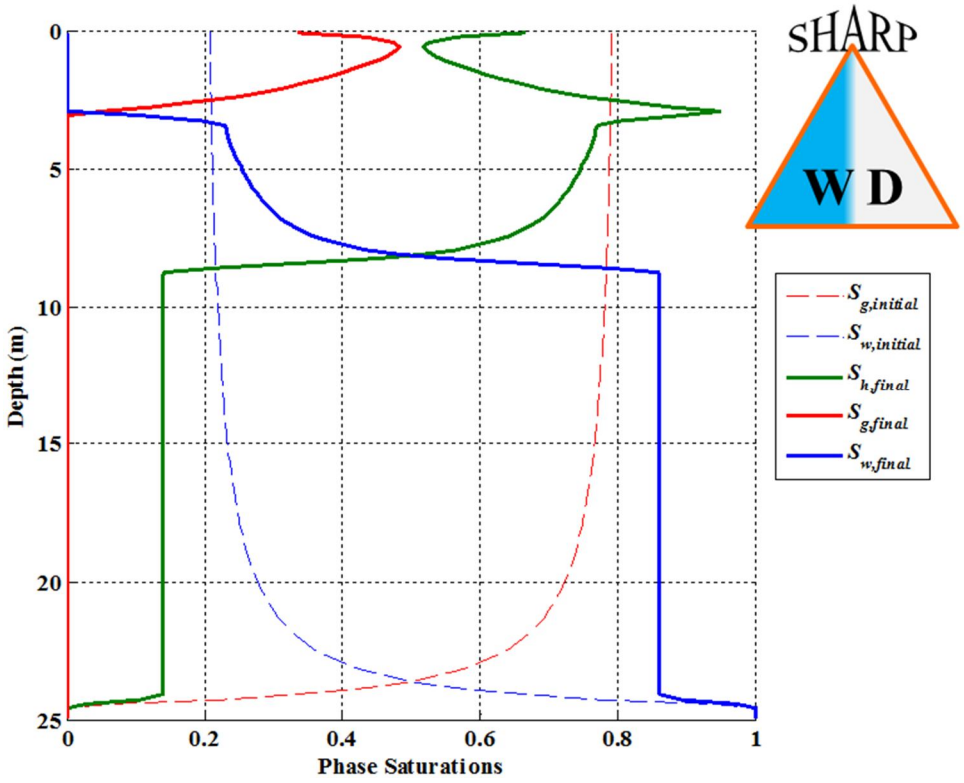

Fig. 5-10- Model results for Case 2 with a faster rate of descent of the BGHSZ, compared to that in Case 1: Initial gaseous and aqueous phase saturations are shown in red and blue dashed lines, respectively. The final hydrate saturation, when no more hydrate forms inside the system, because either the gaseous phase or the aqueous phase is exhausted, is shown in solid green line. The solid blue and solid red lines represent the final aqueous phase and gaseous phase saturation profiles, respectively. The corresponding symbol for this case, showing that the final hydrate saturation profile exhibits a sharp basal contact through a process in which the sand unit was initially wet but eventually dried out at the top, is shown at the top right corner.

Case 3

Consider a case with the same rate of hydrate formation as that in Case 2, but with a rate of descent of the BGHSZ an order of magnitude faster than that in Case 2. Therefore, compared to Case 2, a larger amount of hydrate is forming at a given time period owing to placing larger portion of the sand unit inside the GHSZ in a given time.

Large growth rates require large fluxes of gaseous and aqueous phases. These can be provided only by pressure driven flow; the product of saturation gradient and the slope of the P_c-S_w characteristic curve is simply not large enough to provide large enough water fluxes. This leads to a viscous-dominated fractional flow in which gas flux overwhelms the capacity for water flux. (See Fig. 5-12, t=0.7 and t=1 Yrs.). The GWC rises almost at the speed of the classical Buckley-Leverett shock front (Fig. 5-12, left panel); before (t=2 Yrs.), the flux of aqueous phase is negligible compared to that of the gaseous phase (Fig. 5-12, left panel). Therefore, during the latter time period since mainly gas is arriving at the GHSZ, hydrate formation is essentially limited to the water available in the GHSZ. Therefore, prior to (t=2 Yrs.) the final state in the GHSZ shows a modest S_h of ~25% (Fig. 5-11 left panel) and gas saturation of ~75% (Fig. 5-11, right panel), slightly below the initial value of ~80%.

After (t=2 Yrs.), however, a different mechanism comes into play: counter-current imbibition. The top section wherein the aqueous phase was exhausted owing to hydrate formation would become adjacent to a section below wherein movable saturations of water exist. This situation would be similar to putting a dry water-wet core in touch with a wetting phase where counter-imbibition would take place. Similarly, here when aqueous phase gets in touch with the water-free region at the top, the aqueous phase flows upward into the top section and converts incremental amounts of gas into hydrate. As indicated on Fig. 5-12 with red and blue arrows, during the counter-current imbibition as aqueous phase flows upward, i.e. negative flux, the gaseous phase moves downward, i.e. positive flux. The counter-current imbibition, and thus upward conversion of the remaining gas at the top into hydrate, continues until all the gaseous phase is converted to hydrate.

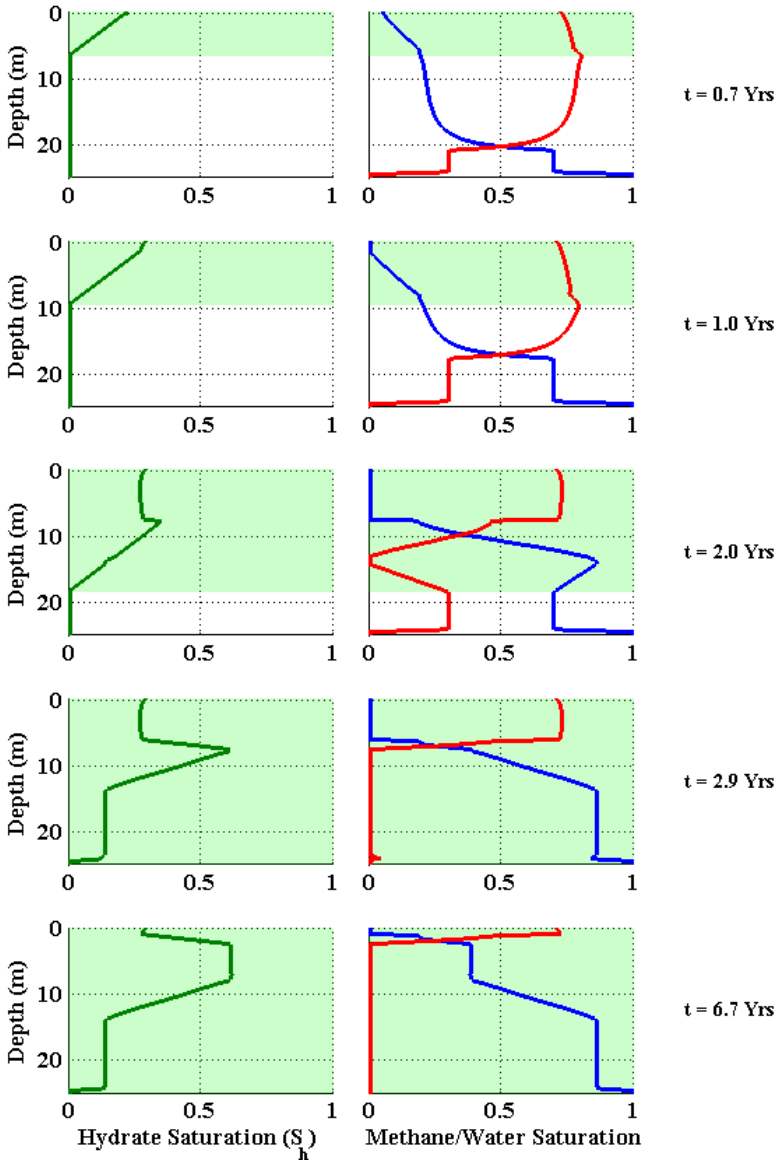

Fig. 5-11- Model results for Case 3 where a faster rate of descent of the BGHSZ, compared to that in Case 2, is considered. The highlighted green area indicates the part of the sand unit inside the HSZ. As hydrate is forming inside the expanding GHSZ, gaseous and aqueous phases flow into the GHSZ to support the required amounts of phases. Similar to that in Case 2 the top portion of sand unit started having an excess methane situation, i.e. aqueous phase was exhausted (see t=2 Yrs.). However, after further descent of the BGHSZ, as the GWC becomes closer to the remaining amount of methane in the excess methane part, counter imbibition initiates hydrate formation again and freezing happens upward this time. The corresponding fluxes of gaseous and aqueous phases are shown in Fig. 5-12.

The final state of the sand unit in Case 3 is shown in Fig. 5-13. Similar to case 1, all the available gas turned into hydrate; however, as discussed above, the mechanism led to excess water situation here is quite different from that in Case 1. In Case 1, the required aqueous phase flux for hydrate formation was basically a co-current imbibition only. In Case 3, however, the process started with a co-current imbibition, which could not provide the top section of the sand unit with the required amounts of aqueous phase and led to exhaustion of the aqueous phase, but concluded with a time period of counter-current imbibition converting the remaining amount of gas at the top into hydrate. In Case 2, however, such counter-current flow of gaseous and aqueous phase did not happen. The reason is that before the GWC becomes close enough to the water-free section at the top, a section of large hydrate saturation at around 3m (see Fig. 5-10) reduced the saturations of both gaseous and aqueous phases below their residual values. Consequently, this zone of immobile gaseous and aqueous phases stopped the communication between free aqueous phase below and the water-free section at the top, not allowing for any counter-current flow.

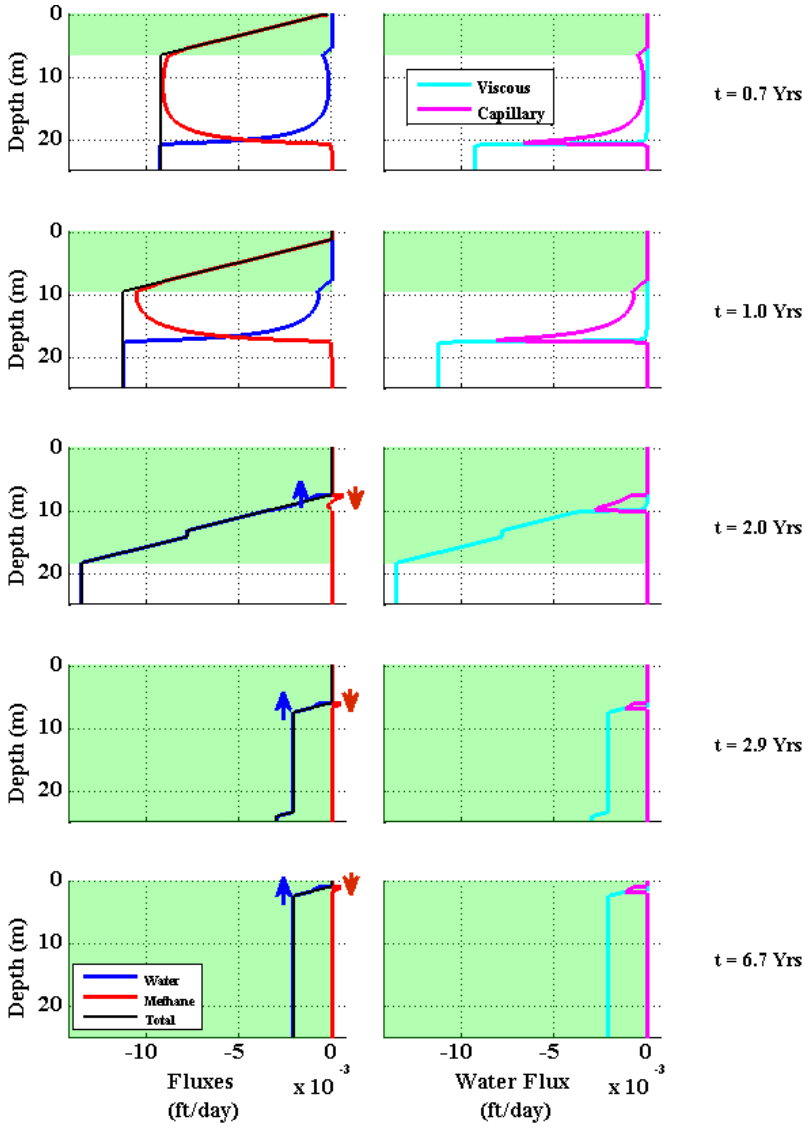

Fig. 5-12- Model results for Case 3 where a faster rate of descent of the BGHSZ, compared to that in Case 2, is considered. Left panel: Phase fluxes (blue = water, red = gas) in the formation at the times indicated on the right hand side. As discussed in Fig. 5-11, after (*t*=2Yrs.) counter imbibition initiates an upward hydrate formation into the upper part of the sand unit wherein the aqueous phase was initially exhausted. The red and blue arrows show the direction of gaseous and aqueous phase flow, respectively, owing to the counter-flow taking place at the interface of aqueous and gaseous phases. Right panel: the contribution of viscous flow and capillarity flow in aqueous phase flux is demonstrated. It is evident that before (*t*=2Yrs.) the aqueous phase contribution in the total flux is negligible leading to leaving a large portion of the initial gas column unconverted at the upper parts of the sand unit.

Compared to the final hydrate saturation profiles of Cases 1 and 2, a more diffuse basal contact is predicted for Case 3. (Compare Fig. 5-13 with Fig. 5-10 and Fig. 5-7). In Cases 1 and 2 the hydrate saturation changes from large values >70% to values less than 15% over a depth range of 2 meters while in Case 3 a reduction in S_h from 60% to less than 20% occurs over a depth range of about 6 m. The main reason behind this difference between Case 3 and the previous cases is that the faster rate of descent of the BGHSZ leads to having a slightly shorter column of residual gas saturation encompassed by the GHSZ. To describe the mode of conversion in Case 3 a diamond[4] symbol  is used to reflect that the final hydrate saturation profile exhibits a basal contact which is slightly more diffuse than that in cases 1 and 2. Furthermore, the latter symbol shows that the sand unit which was initially wet (W), dried out (D) at some point during the conversion process but became wet (W) eventually owing to countercurrent imbibition.

[4] Diamond symbol is used here to reflect that the final hydrate saturation profile exhibits a basal contact which is not too sharp (like a triangle) and not too diffuse (like a circle)

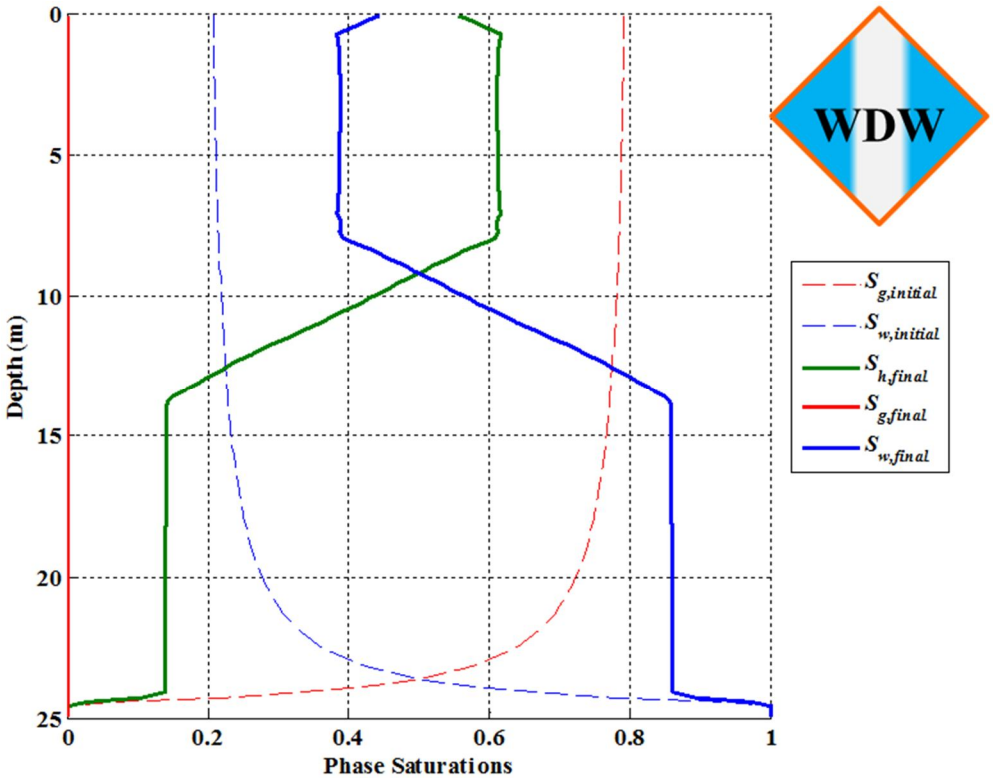

Fig. 5-13- Model results for Case 3 with a faster rate of descent of the BGHSZ, compared to that in Case 2: initial gaseous and aqueous phase saturations are shown in red and blue dashed lines, respectively. The final hydrate saturation, when no more hydrate forms because the gaseous phase is exhausted, is shown in solid green line. The solid blue and solid red lines represent the final aqueous phase and gaseous phase saturation profiles, respectively. Compared to Cases 1 and 2, the hydrate saturation profile in this case exhibits a more diffuse basal contact, i.e. hydrate saturation changes from ~60% to ~15% over a depth range of more than 6 meters. The corresponding symbol for this case, showing that the final hydrate saturation profile exhibits a slightly sharp basal contact through a process in which the sand unit was initially wet (W) at the top then dried out (D) but eventually became wet (W) again, is shown at the top right corner.

Case 4

To show the effect of rate of descent of the BGHSZ on the final hydrate saturation profile, an imaginary case 4 is considered having the same characteristics as that of Case

3 except for a four orders of magnitude larger rate of descent of the BGHSZ. The processes leading to the final hydrate saturation profile is quite similar to that explained for Case 3, i.e. both co-current and counter-current imbibition are responsible for providing the required amounts of phases. However, the final hydrate saturation profile for Case 4 would be much more diffuse than that observed in Case 3 owing to a faster rate of temperature cooling. The final hydrate saturation profile for Case 4 is shown in Fig. 5-14. For such mode of conversion with a final hydrate saturation profile which exhibits a very diffuse basal contact a symbol  is used in this dissertation. The latter symbol also reflects the fact that the top section of the sand unit which was initially wet (W), dried out (D) at some point during the conversion process but eventually became wet (W) owing to the upward front of hydrate formation and the countercurrent imbibition took place meanwhile.

In the following section the results of numerous scenarios for conversion of a gas accumulation are compiled and characterized based on the aforementioned symbolized qualitative behaviors and two dimensionless groups.

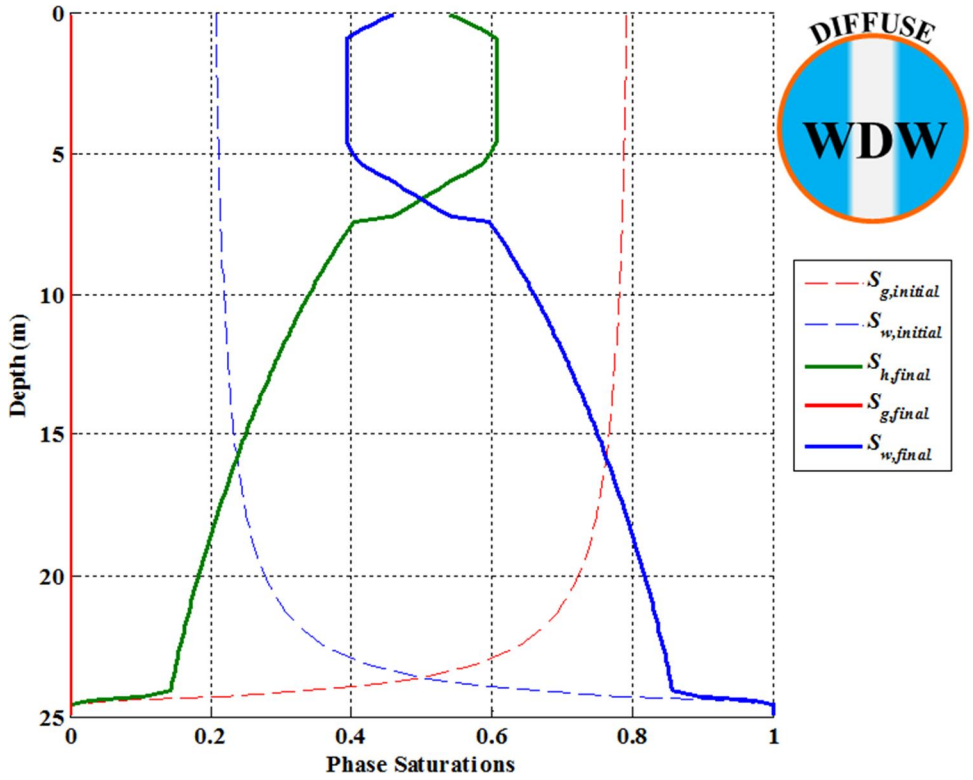

Fig. 5-14- Model results for Case 4 with a faster rate of descent of the BGHSZ compared to that in Case 3: Compared to previous cases, the hydrate saturation profile in this case exhibits a much more diffuse basal contact, i.e. hydrate saturation changes from ~60% to ~15% over a depth range of more than 20 meters. The corresponding symbol for this case, showing that the final hydrate saturation profile exhibits a diffuse basal contact through a process in which the sand unit was initially wet (W) at the top then dried out (D) but eventually became wet (W) again, is shown at the top right corner.

5.3) DISCUSSION

5.3.1) Generalization of 1-D conversion of a gas accumulation, with a seal at the top, through dimensional analysis

As mentioned earlier, numerous simulations of conversion of a gas accumulation into hydrate accumulation with different rates of hydrate formation and rates of descent of the BGHSZ as well as various rock and fluid properties were performed. The specifications of these various cases are summarized in Table 5-4. Here the two dimensionless groups N_{CC} and N_{Pe}^{*}, introduced in Appendix B, are used to characterize the physical processes behind the conversion as well as the final hydrate saturation profiles.

N_{CC}, Eq. (5.32), is the ratio of the rate of descent of the BGHSZ, $\dot{z}_{BGHSZ}$, to the rate of hydrate formation within the GHSZ, $\dot{S}_h$, normalized by the length of gas-bearing section, L_0, of the sand unit and the maximum gaseous phase saturation, $S_g^{\max}$, below the seal at the top, prior to imposition of the gas accumulation inside the GHSZ. In other words, N_{CC} is a measure of the ratio of conversion time scale to the cooling time scale.

$$S_g^{\max} = \left(1 - S_{w,irr}\right)\left[1 - \left(1 + \frac{\Delta\rho g L_0}{P_c^{*}}\right)^{-\gamma}\right] \tag{5.31}$$

$$N_{CC} = \frac{\left(1 - S_{w,irr}\right)}{L_0}\left[1 - \left(1 + \frac{\Delta\rho g L_0}{P_c^{*}}\right)^{-\gamma}\right]\frac{\dot{z}_{BGHSZ}}{\dot{S}_h} \tag{5.32}$$

where P_c^{*} is the capillary entry pressure and γ is the pore-size distribution index (Brooks and Corey, 1964) and $\Delta\rho = \rho_w - \rho_g$. For small enough N_{CC} the flow of gaseous and aqueous phase due to hydrate formation would mainly happen outside the GHSZ "toward" the GHSZ. For large values of N_{CC}, on the other hand, the cocurrent flow of gaseous and aqueous phases would mainly happen "within" the GHSZ. The fact that flow

happens “within” or “toward” the GHSZ would have direct effect on the final hydrate saturation profile. When the flow is mainly taking place “within” the GHSZ during hydrate formation the final hydrate saturation profile would exhibit a diffuse basal contact, meaning that the hydrate saturation would change from large values at the top to small values at the bottom over a rather large depth range. In contrast, when the gaseous and aqueous phases flow “toward” the GHSZ, the GHSZ would eventually encompass a considerable zone with residual gas phase, S_{gr}, and thus the final hydrate saturation would show a rather sharp basal contact.

In appendix B, a dimensionless group named complete Peclet number, N_{Pe}^{*}, is proposed as a scaling dimensionless group to characterize the physical process behind the conversion of a gas accumulation in terms of aqueous phase transport to the GHSZ. In other words, for a given N_{CC} and for any given porous medium characteristics and any given rate of hydrate formation and rate of temperature cooling, all conversions corresponding to the same N_{Pe}^{*} would exhibit the same mode of conversion in terms of being wet (W), wet/dry (WD) or wet/dry/wet (WDW). As derived in detail in Appendixes A and B, N_{Pe}^{*} can be calculated as

$$N_{Pe}^{*} = \frac{N_{Pe}\big|_{u_T = u_T^{*}}}{D_c(S\big|_{S_w = 1 - S_g^{\max}})} \tag{5.33}$$

where

$$N_{Pe} = \frac{u_T L_0}{k \lambda_{rw,0} P_c^{*}} \tag{5.34}$$

$$u_T^{*} = \begin{cases} \phi K_{trans}\left(1 - S_{w,irr}\right)\left[1 - \left(1 + \dfrac{\Delta\rho g L_0}{P_c^{*}}\right)^{-\gamma}\right]\dot{z}_{BGHSZ} & ;\ if\ \ N_{CC} \le 1 \\ \phi K_{trans}\dot{S}_h L_0 & ;if\ \ N_{CC} \ge 1 \end{cases} \tag{5.35}$$

where K_{trans}, as introduced in chapter 2, is the total phase (gaseous + aqueous) volume transported into the GHSZ per unit volume of hydrate formed, so that the total system volume is fixed. In the denominator of Eq. (5.33),

$$S = \frac{S_w - S_{w,irr}}{1 - S_{gr} - S_{w,irr}} \tag{5.36}$$

and

$$D_C(S) = -\frac{1}{\gamma}\left(\frac{1 - S_{gr} - S_{w,irr}}{1 - S_{w,irr}}\right)^{-\frac{1}{\gamma}} \frac{(1-S)^{N_g} S^{N_w - \frac{\gamma+1}{\gamma}}}{(1-S)^{N_g} + MS^{N_w}} \tag{5.37}$$

The calculated values of u_T^*, N_{Pe}, N_{Pe}^* and N_{CC} for all the simulation cases are reported in Table 5-4. The results of these realizations are characterized as sharp versus diffuse hydrate saturation profiles as well as wet, wet/dry or wet/dry/wet mode of conversion. The aforementioned terms were introduced earlier in the results. These realizations are then mapped on a graph of complete Peclet number, N_{Pe}^*, versus the ratio of conversion time scale to cooling time scale, N_{CC} (Fig. 5-15).

Two threshold values are evident on Fig. 5-15: $N_{Pe,threshold}^* = 0.4$ and $N_{CC,threshold} = 1$. For all the cases with complete Peclet number smaller than the threshold value, i.e. $N_{Pe}^* < N_{Pe,threshold}^*$, the sand unit remained wet (W) at all times during the conversion of gas accumulation into hydrate accumulation, meaning that the aqueous phase flow, i.e. capillary contribution, is strong enough to compete with the viscous dominated flow of gaseous phase even at the top of the gas column. In fact, complete Peclet number is a measure of the ratio of viscous forces to the capillary forces; thus the smaller N_{Pe}^* the larger the capillary flow contribution. Based on Fig. 5-15, for any given porous media and any value of $\dot{S}_h$ and $\dot{z}_{BGHSZ}$, as far as $N_{Pe}^* < 0.4$ the sand unit would remain in excess-

water situation during the conversion, i.e. $R_v < R_{v,stoich}$ along the sand unit. For this regime, the main flow mechanism involved would be cocurrent flow of gaseous and aqueous phases towards or within the GHSZ.

In contrast, when the $N^*_{Pe} > N^*_{Pe,threshold}$, the capillary contribution in aqueous phase flow would not be large enough to guarantee R_v values less than $R_{v,stoich}$ specially at the top of the sand unit with larger gas saturations. Therefore, the aqueous phase becomes exhausted during the conversion process in the upper sections of the sand unit and the initially wet sand dries out (WD). The dried out part of the sand unit, however, could be imbibed by the aqueous phase once a large enough aqueous phase saturation establishes below the dried section. At this time, as discussed for Case 3 in the results section, a different flow mechanism, countercurrent imbibition, supports water into the dried out part and converts the gas remainder into hydrate exhibiting an upward freezing front. Therefore, an initially wet part of the sand, which dried out at some point during the conversion process, become wet again owing to a countercurrent imbibition process; that's why we describe this mode of conversion as wet/dry/wet (WDW).

As seen in Fig. 5-15, the cases with N_{CC}<0.1 and $N^*_{Pe} > 0.4$, the dried out portion of the sediment never got a chance to be imbibed by the aqueous phase again. The situation here is similar to that discussed earlier for Case 2 where the hydrate saturation at a zone, between the dried out portion and the wet portion, becomes so large that both aqueous and gaseous phases become disconnected. Therefore, countercurrent imbibition cannot take place and thus the dried out portion would remain dry. The aforementioned phenomena is a consequence of the stiff residual phase saturations, S_{gr} and $S_{w,irr}$, imposed on the model. In nature, however, the areal and vertical heterogeneity and the time scale of the process, i.e. geologic time scale, would likely facilitate the countercurrent

imbibition. That is why in the graph of Fig. 5-15, all the cases wherein the upper part of the sand unit dries out at some point during the conversion process is categorized as WDW. The symbols, however, reflect the actual behavior predicted by the present model.

Table 5-4-Numerous simulations of the conversion process of a gas-accumulation are performed. Specifications of these realizations are summarized below. The calculated dimensionless numbers N_{Pe}, N_{Pe}^{*} and N_{CC} are also reported.

Case #	$\dot{S}_h$ (saturation/day)	$\dot{z}_{BGHSZ}$ (m/year)	Capillary Characteristics				Relative Permeability Characteristics				Length of Gas Column, L_0, (m)	u_T^* (ft/day)	N_{Pe}	N_{Pe}^{*}	N_{CC}
			γ	$P_{c,entry}$ (Pa)	ϕ	k (md)	N_g	$k_{rg,0}$	N_w	$k_{rw,0}$					
1	8.64E-04	2.37E-03	1	5000	0.25	250	2.5	0.7	2.5	0.5	24.5	8.35E-06	1.96E-03	6.68E-03	2.43E-04
2	8.64E-04	2.37E-01	1	5000	0.25	250	2.5	0.7	2.5	0.5	24.5	8.35E-04	1.96E-01	6.68E-01	2.43E-02
3	8.64E-04	9.46E+00	1	5000	0.25	250	2.5	0.7	2.5	0.5	24.5	3.34E-02	7.86E+00	2.67E+01	9.70E-01
4	8.64E-04	9.46E+04	1	5000	0.25	250	2.5	0.7	2.5	0.5	24.5	3.37E-02	7.92E+00	2.69E+01	9.70E+03
5	8.64E-08	2.37E-03	1	5000	0.25	250	2.5	0.7	2.5	0.5	24.5	3.37E-06	7.92E-04	2.69E-03	2.43E+00
6	8.64E-08	9.46E+00	1	5000	0.25	250	2.5	0.7	2.5	0.5	24.5	3.37E-06	7.92E-04	2.69E-03	9.70E+03
7	8.64E-04	$z_{BGHSZ} = 5m$	1	5000	0.25	250	2.5	0.7	2.5	0.5	24.5	3.37E-02	7.92E+00	2.69E+01	∞
8	0.0864	47.93472	1	5000	0.25	250	2.5	0.7	2.5	0.5	24.5	1.69E-01	3.98E+01	1.35E+02	4.92E-02

Table 5-4, cont.

#	$\dot{S}_h$	$\dot{z}_{BGHSZ}$	γ	$P_{c,entry}$ (Pa)	ϕ	k (md)	N_g	$k_{rg,0}$	N_w	$k_{rw,0}$	L_0	u_T^*	N_{Pe}	N_{Pe}^*	N_{CC}
9	0.0864	126.144	1	5000	0.25	250	2.5	0.7	2.5	0.5	24.5	4.46E-01	1.05E+02	3.56E+02	1.29E-01
10	8.64E-06	2.37E-01	1	5000	0.25	250	2.5	0.7	2.5	0.5	24.5	3.37E-04	7.92E-02	2.69E-01	2.43E+00
11	8.64E-06	2.37E+02	1	5000	0.25	250	2.5	0.7	2.5	0.5	24.5	3.37E-04	7.92E-02	2.69E-01	2.43E+03
12	0.0864	12614.4	1	5000	0.25	250	2.5	0.7	2.5	0.5	24.5	3.37E+00	7.92E+02	2.69E+03	1.29E+01
13	0.0864	12614400	1	5000	0.25	250	2.5	0.7	2.5	0.5	24.5	3.37E+00	7.92E+02	2.69E+03	1.29E+04
14	8.64E-05	9.46E-03	1	5000	0.25	250	2.5	0.7	2.5	0.5	24.5	3.34E-05	7.86E-03	2.67E-02	9.70E-03
15	8.64E-03	2.37E+00	1	5000	0.25	250	2.5	0.7	2.5	0.5	24.5	8.35E-03	1.96E+00	6.68E+00	2.43E-02
17	8.64E-08	12614400	1	5000	0.25	250	2.5	0.7	2.5	0.5	24.5	3.37E-06	7.92E-04	2.69E-03	1.29E+10
18	8.64E-08	1.26144E+11	1	5000	0.25	250	2.5	0.7	2.5	0.5	24.5	3.37E-06	7.92E-04	2.69E-03	1.29E+14
19	0.0864	0.4793472	1	5000	0.25	250	2.5	0.7	2.5	0.5	24.5	1.69E-03	3.98E-01	1.35E+00	4.92E-04
20	8.64E-04	2.37E-01	0.5	5000	0.25	250	2.5	0.7	2.5	0.5	24.5	8.35E-04	1.96E-01	1.88E-02	2.12E-02
21	8.64E-04	2.37E-01	2	5000	0.25	250	2.5	0.7	2.5	0.5	24.5	8.35E-04	1.96E-01	4.22E+02	2.48E-02
22	8.64E-04	9.46E+00	2	5000	0.25	250	2.5	0.7	2.5	0.5	24.5	3.34E-02	7.86E+00	1.69E+04	9.91E-01
23	8.64E-04	2.37E-03	1	5000	0.25	250	2.5	0.9	2.5	0.3	24.5	8.35E-06	1.96E-03	6.68E-03	2.43E-04
24	8.64E-08	9.46E+00	1	5000	0.25	0.25	2.5	0.7	2.5	0.5	24.5	3.37E-06	7.92E-01	2.69E+00	9.70E+03

Table 5-4, cont.

#	$\dot{S}_h$	$\dot{z}_{BGHSZ}$	γ	$P_{c,entry}$ (Pa)	ϕ	k (md)	N_g	$k_{rg,0}$	N_w	$k_{rw,0}$	L_0	u_T^*	N_{Pe}	N_{Pe}^*	N_{CC}
25	8.64E-06	2.37E-01	1	2500	0.25	250	2.5	0.7	2.5	0.5	24.5	3.37E-04	1.58E-01	7.58E-01	2.45E+00
26	8.64E-04	2.37E-01	1	12500	0.25	250	2.5	0.7	2.5	0.5	24	8.35E-04	7.70E-02	1.67E-01	2.40E-02
27	8.64E-06	2.37E-01	1	2500	0.25	250	2.5	0.7	4	0.5	24.5	3.37E-04	1.58E-01	3.33E+02	2.45E+00
28	8.64E-06	2.37E-01	1	2500	0.25	250	2.5	0.7	1.75	0.5	24.5	3.37E-04	1.58E-01	3.62E-02	2.45E+00
29	8.64E-05	0.000479347	0.8	2500	0.25	25	2.5	0.8	3	0.3	24.5	1.69E-06	7.96E-03	3.80E-02	4.89E-04
30	0.0864	4.793472	1	5000	0.25	250	2.5	0.7	3	0.3	24.5	1.69E-02	3.98E+00	7.32E+01	0.004916953

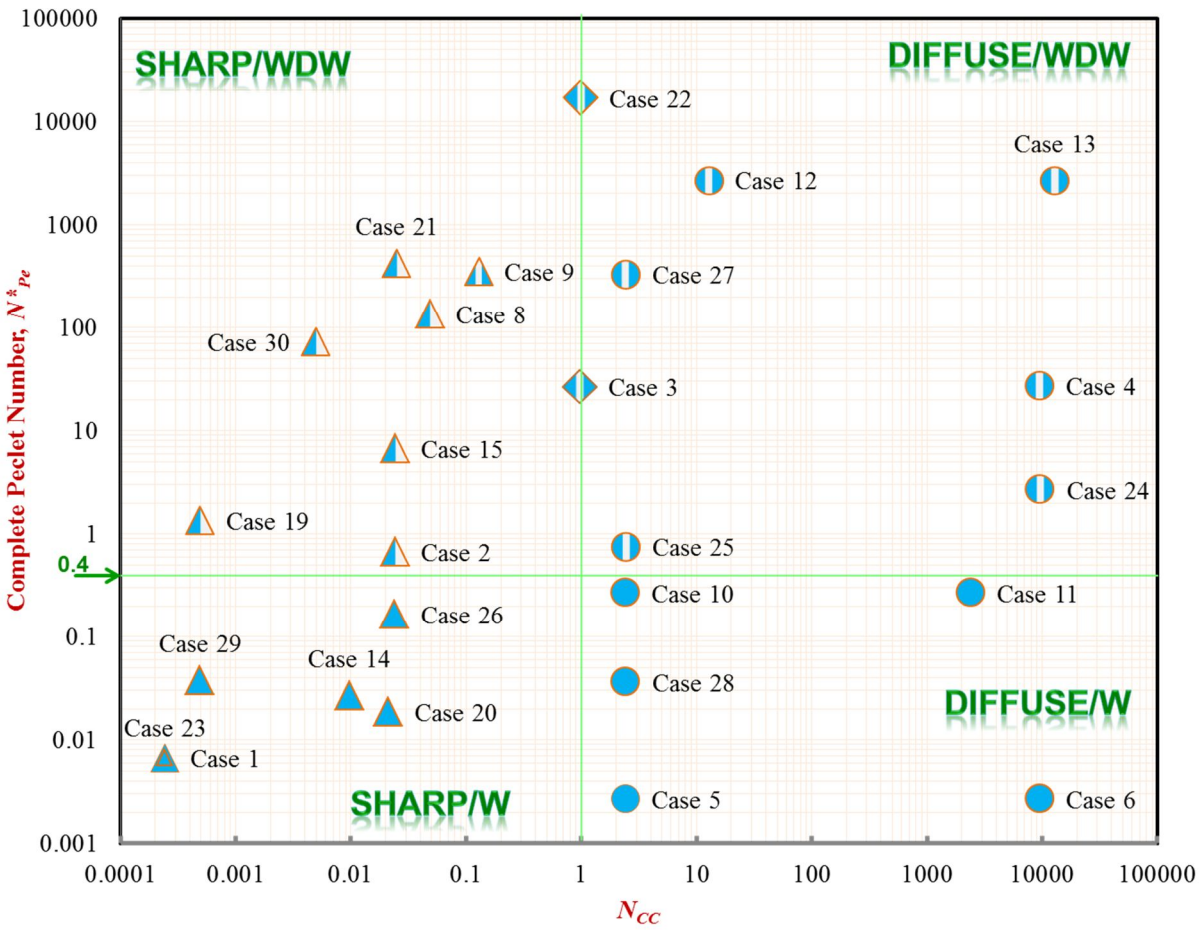

Fig. 5-15- Complete Peclet number, N^*_{Pe} versus N_{CC} for thirty different cases of gas accumulation conversion. Two thresholds N_{CC}=1 and $N^*_{Pe} = 0.4$ are evident which can be used to characterize the hydrate saturation profile for various porous media characteristics and any arbitrary set of rate of hydrate formation, $\dot{S}_h$, and rate of descent of the BGHSZ, $\dot{z}_{BGHSZ}$.

The other dimensionless number, N_{CC}, as the horizontal axis of the graph of Fig. 5-15 provides a measure of the ratio of rate of temperature cooling to the rate of hydrate formation which would in turn determine the sharpness of the final hydrate saturation profile. As observed in Fig. 5-15, the final hydrate saturation profile in all the cases for which $N_{CC}<1$ exhibit a sharp basal contact while in cases with $N_{CC}>1$ the final hydrate saturation changes from large values, $S_h>0.6$, to $S_h<0.15$ over a rather long depth interval. As discussed earlier, when $N_{CC}>1$ the phases flow takes place "within" the GHSZ for a significant part of the gas accumulation conversion time and thus the final hydrate saturation tends to exhibit a rather diffuse basal contact as opposed to cases with $N_{CC}<1$ where sharp basal contacts are evident in their final hydrate saturation profiles. There are two cases on Fig. 5-15 for which $N_{CC}\approx1$, Case 3 (discussed earlier in results section) and Case 22. As expected, the final hydrate saturation profiles in these two cases exhibit a slightly more diffuse basal contact compared to those with $N_{CC}<1$.

Overall, Fig. 5-15 can be used to qualitatively predict the final hydrate saturation profile, in terms of being sharp or diffuse, and the main transport mechanisms leading to the conversion of the gas accumulation, either through cocurrent imbibition or through cocurrent and countercurrent imbibition, using the dimensionless numbers N^*_{Pe} and N_{CC}. The two threshold values, $N^*_{Pe,threshold}=0.4$ and $N_{CC,threshold}=1$ divide the graph of Fig. 5-15 into four subsections within each the qualitative behavior during the conversion process and the final hydrate saturation profile is similar. These four subsections are summarized in Table 5-5.

Table 5-5- Generalization of the gas accumulations conversions based on the two dimensionless numbers for the density values of Table 5-2, consistent with the averaged thermodynamic conditions, *P* and *T*, of hydrate-bearing sand unit of Mount Elbert well

$N^*_{Pe} > 0.4$	 **Sharp** basal contact; cocurrent/countercurrent imbibition (**WDW**)	 **Diffuse** basal contact; cocurrent/countercurrent imbibition (**WDW**)
$N^*_{Pe} < 0.4$	 **Sharp** basal contact; cocurrent imbibition (**W**)	 **Diffuse** basal contact; cocurrent imbibition (**W**)
	N_{CC}<1	N_{CC}>1

5.3.2) Effect of hydrate formation rate, $\dot{S}_h$, versus rate of descent of the BGHSZ on hydrate saturation profiles in "converted free gas accumulations"

The first 19 realizations specified in Table 5-4 are cases with exactly the same rock physical properties and relative permeability characteristics, summarized in Table 5-1, with the only changing parameters being rate of hydrate formation, $\dot{S}_h$, and rate of descent of the BGHSZ, $\dot{z}_{BGHSZ}$. Therefore, these cases would be appropriate for examining the effect of rate of hydrate formation versus rate of surface temperature cooling on the mode of conversion of a gas accumulation to a hydrate reservoir. Fig. 5-16 shows these cases on a log-log plot of $\dot{S}_h$ versus $\dot{z}_{BGHSZ}$.

As discussed earlier, the dimensionless number N_{CC}=1 provides a threshold for the sharpness of the final hydrate saturation profile. For example, when N_{CC}>1 diffuse basal contacts are expected in the final hydrate saturation profile. Solving for N_{CC}=1 gives,

$$\frac{\dot{z}_{BGHSZ}}{\dot{S}_h} = \frac{L_0}{\left(1-S_{w,irr}\right)\left[1-\left(1+\frac{\Delta\rho g L_0}{P_c^*}\right)^{-\gamma}\right]} \tag{5.38}$$

which can be simplified using the rock and fluid properties used in Cases 1 through 19 as[5] $\dot{z}_{BGHSZ}/\dot{S}_h \approx 1100$ which forms a line in log-log scale. This line (in red) is plotted on the log-log graph of Fig. 5-16. As expected, for the cases which fall above this line, i.e. N_{CC}<1, a sharp basal contact is observed in their final hydrate saturation profile. Conversely, for the cases below the red line a rather diffuse basal contacts is exhibited by their hydrate saturation profile.

As discussed in the previous section, complete Peclet number, N_{Pe}^*, provides a threshold as $N_{Pe,threshold}^* = 0.4$ which separates "wet" cases (W) from "wet/dry/wet" cases (WDW). For the cases shown on Fig. 5-16, with the same specifications summarized in Table 5-1 and Table 5-2, $N_{Pe}^* = 0.4$ simplifies to $u_T^* = 1.76\times10^{-9}\,\frac{m}{s}$. Eq. (5.35) then gives,

$$u_T^* = 1.76\times10^{-9}\,\frac{m}{s} \Rightarrow \begin{cases} \dot{z}_{BGHSZ} = 0.145\ \dfrac{m}{year} & ;\ if\ \ N_{CC} \le 1 \\ \dot{S}_h = 1.28\times10^{-5}\ \dfrac{sat.unit}{day} & ;if\ \ N_{CC} \ge 1 \end{cases} \tag{5.39}$$

The calculated threshold values of $\dot{S}_h$ and $\dot{z}_{BGHSZ}$ are plotted on Fig. 5-16 as two perpendicular green lines.

---

[5] $\dot{S}_h\left[\dfrac{sat.unit}{day}\right]$ and $\dot{z}_{BGHSZ}\left[\dfrac{m}{year}\right]$

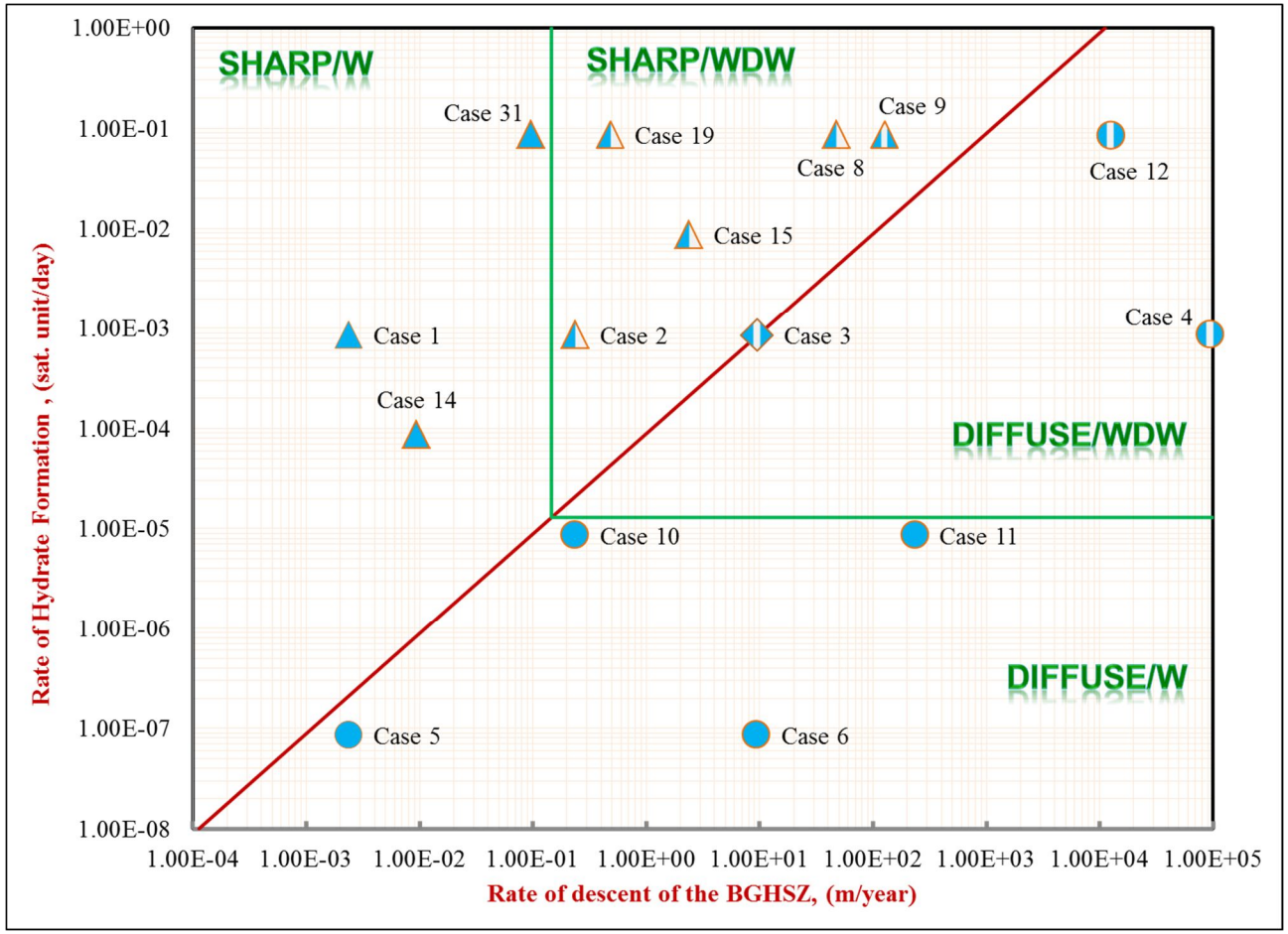

Fig. 5-16- Effect of rate of hydrate formation, $\dot{S}_h$, versus rate of descent of the BGHSZ, $\dot{z}_{BGHSZ}$, on the mode of hydrate formation and the final hydrate saturation profile. The cases shown have the same sand unit properties with the only difference among them being $\dot{S}_h$ and $\dot{z}_{BGHSZ}$.

Fig. 5-16 reflects the effect of rate of hydrate formation, $\dot{S}_h$, versus rate of descent of the BGHSZ, $\dot{z}_{BGHSZ}$, on the mode of hydrate formation and the final hydrate saturation profile for a series of simulation cases with the same sand unit properties with the only differences among them being $\dot{S}_h$ and $\dot{z}_{BGHSZ}$. Based on the two threshold lines (red and green), consistent with the threshold values $N_{CC}=1$ and $N_{Pe}^{*}=0.4$, four regions of different behaviors are distinguishable as indicated on Fig. 5-16. Generally, as $\dot{S}_h$ and $\dot{z}_{BGHSZ}$ increase a WDW mode of conversion tend to happen as the aqueous phase cannot feed the upper parts of the sand unit, during hydrate formation, to maintain the aqueous phase saturation. Therefore, at some periods of time during the conversion unconverted gas would be left behind in a dried out region at the top. However, for the specific sand unit properties of Table 5-1, when $\dot{S}_h < 1.28\times10^{-5}\ sat.unit/day$ and N_{CC}>1 or when $\dot{z}_{BGHSZ} < 0.145 m/year$ and N_{CC}<1 the sand unit would remain wet (W) at all times during the conversion process. It can be shown that for a fixed set of rock properties the longer the length of the gas accumulation, L_0, the narrower the region where a wet (W) mode of conversion takes place, i.e. the threshold values of $\dot{S}_h$ and $\dot{z}_{BGHSZ}$ become smaller.

Generally, however, not only the rate of hydrate formation and the rate of descent of the BGHSZ, but also the petrophysical properties of the sand unit such as capillarity and relative permeability characteristics play key roles in determining the mode of conversion of a gas accumulation to hydrate accumulation. In the following the effect of capillarity and relative permeability characteristics are further discussed.

5.3.3) Effect of capillary characteristics on hydrate saturation profiles in "converted free gas accumulations"

Based on Brooks-Corey model, Eq. (5.19), there are two parameters involved in the capillary characteristics: pore-size distribution index, γ and capillary entry pressure, P_c^{*}.

To examine the effect of pore-size distribution index two cases, Cases 20 and 21, are considered for which all the specifications, except for γ, are the same as Case 2 discussed in the results section. Case 20[††] represents a sand unit with a wider pore size distribution compared to that in Case 2[‡‡], while Case 21[§§] represents sediment with a narrow pore size distribution.

Simulation results for Case 20 are summarized in Fig. 5-17 through Fig. 5-19. Comparing the aqueous phase flux for Case 20 (Fig. 5-18) with the fluxes in Case 2 (Fig. 5-9), it is evident that in Case 20, in contrast to Case 2, the capillary contribution of the aqueous phase flux is strong enough to keep $R_v<R_{v,1:1}$ and thus the conversion mechanism keeps the sand unit wet (W) at all times. The reason is that due to a wider pore size distribution the saturation gradients and thus capillary flow in Case 20 is larger than that in Case 2 with narrower pore size distribution. The latter effect is clearly reflected in N_{Pe}^* as $N_{Pe}^*\big|_{Case\,2} > 0.4$ and $N_{Pe}^*\big|_{Case\,20} < 0.4$; consequently Case 20 exhibits a wet (W) mode of conversion. In terms of N_{CC} the two cases are similar since $\dot{S}_h$ and $\dot{z}_{BGHSZ}$ are the same in both cases and thus the final hydrate saturation profiles in both cases are similarly exhibiting a sharp basal contact. The final hydrate saturation profile along with the initial gaseous and aqueous phase saturation profiles are plotted in Fig. 5-19.

[††] γ=0.5
[‡‡] γ=1
[§§] γ=2

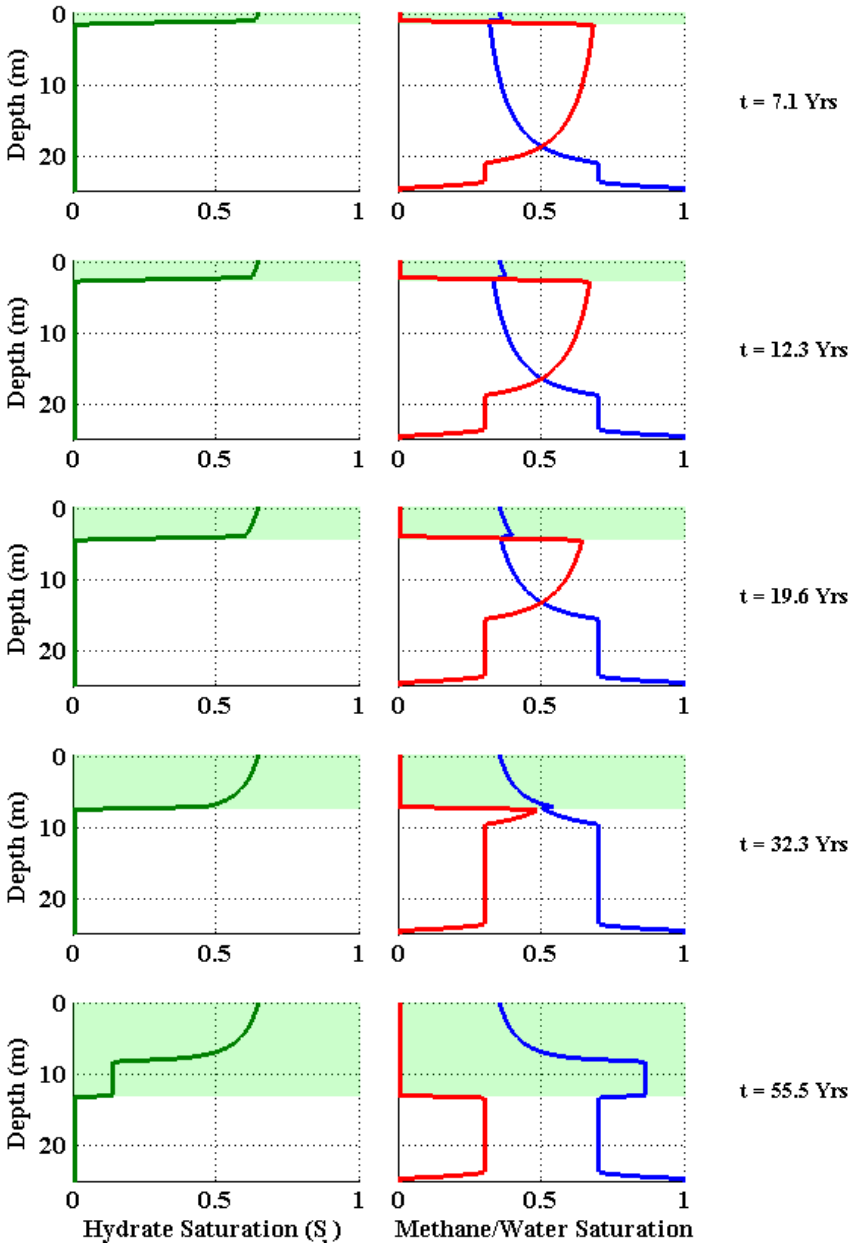

Fig. 5-17- Model results for Case 20 with a wider pore size distribution, compared to that in Case 2. The highlighted green area indicates the part of the sand unit inside the HSZ. As hydrate is forming inside the expanding GHSZ, gaseous and aqueous phases flow into the GHSZ to support the required amounts of phases. As a result, the GWC is gradually rising towards the descending BGHSZ. The left panel shows the evolution of hydrate saturation profiles and the right panel shows the methane (red) and water (blue) saturation profiles for different locations of the BGHSZ. The corresponding fluxes of gaseous and aqueous phases are shown in Fig. 5-18.

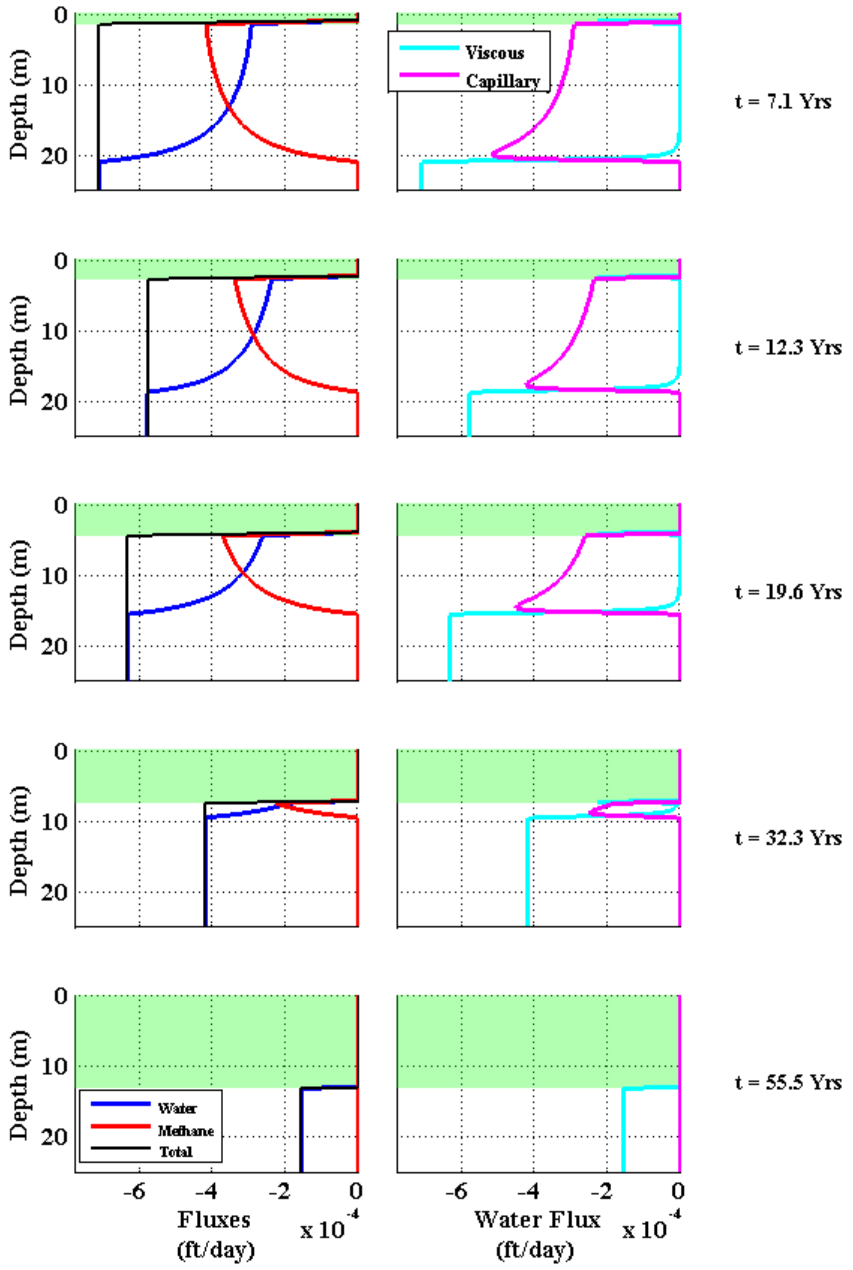

Fig. 5-18- Model results for Case 20 with a wider pore size distribution, compared to that in Case 2. Left panel: Phase fluxes (blue = water, red = gas) in the formation at the times indicated on the right hand side. Right panel: the contribution of viscous flow and capillarity flow in aqueous phase flux is demonstrated. In contrast to Case 2 (Fig. 5-9) the capillary contribution of the aqueous phase flux is strong enough to keep $R_v<R_{v,1:1}$ and thus the conversion mechanism keeps the sand unit wet (W) at all times. The reason is that due to a wider pore size distribution the saturation gradients and thus capillary flow in Case 20 is larger than that in Case 2 with relatively narrower pore size distribution.

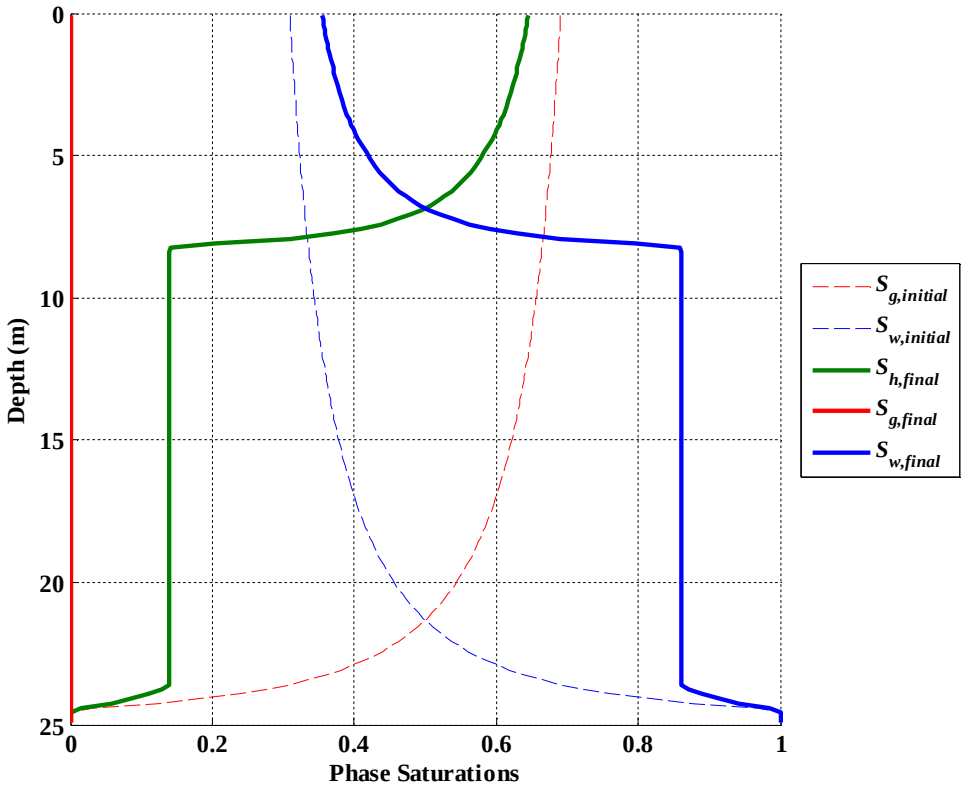

Fig. 5-19- Model results for Case 20 with a wider pore size distribution, compared to that in Case 2: Initial gaseous and aqueous phase saturations are shown in red and blue dashed lines, respectively. The final hydrate saturation, when no more hydrate forms, because the gaseous phase is exhausted, is shown in solid green line. The solid blue and solid red lines represent the final aqueous phase and gaseous phase saturation profiles, respectively. Unlike Case 2, the mode of conversion for Case 20 is wet (W) meaning that the sand unit remains wet at all times during the conversion.

On the other hand, Case 21 represents a sediment with narrower pore size distribution and thus a much sharper capillary pressure curve compared to that in Case 2. In this case the complete Peclet number, N_{Pe}^{*}, is even larger than that in Case 2 (see Fig. 5-15) since the gas saturations at the top of the sand unit are larger, closer to 1-$S_{w,irr}$, than that in Case 2. Consequently, in Case 21 at the top of the sand unit, smaller saturation

gradients, dS_w/dz, would establish and thus the capillary contribution to aqueous phase flow would be even smaller than that in Case 2.

Fig. 5-21 shows the gaseous and aqueous phase fluxes through time for Case 21. The smaller capillarity-driven flux of water proves insufficient to supply the imposed rate of hydrate growth. Hence the flow in this case reverts to a viscous dominated flow of gaseous and aqueous phases. Essentially, a piston type flux of gaseous and aqueous phase is established especially during the conversion of the upper parts of the sand unit and thus the conventional Buckley-Leverett shock would provide a reasonable approximation of the gaseous and aqueous phase fluxes. Therefore, the gas flux becomes dominant and prevents any water reaching the GHSZ, i.e. R_v=0. The resulting hydrate saturation at the upper sections is about 25% (cf. Fig. 2-9), gas remains in the GHSZ and thus a wet/dry (WD) mode of conversion. The overall mode of conversion, sharp/WD, is similar to that in Case 2 as in both cases $N_{Pe}^{*} > 0.4$ and $N_{CC} < 1$; however since $N_{Pe}^{*}\big|_{Case\,21} > N_{Pe}^{*}\big|_{Case\,2}$ with the same value of N_{CC}, although having the same mode of conversion, a larger column of gas was left unconverted at the end of hydrate formation in Case 21 compared to that in Case 2. The final hydrate saturation profile in Case 21 is shown in Fig. 5-22.

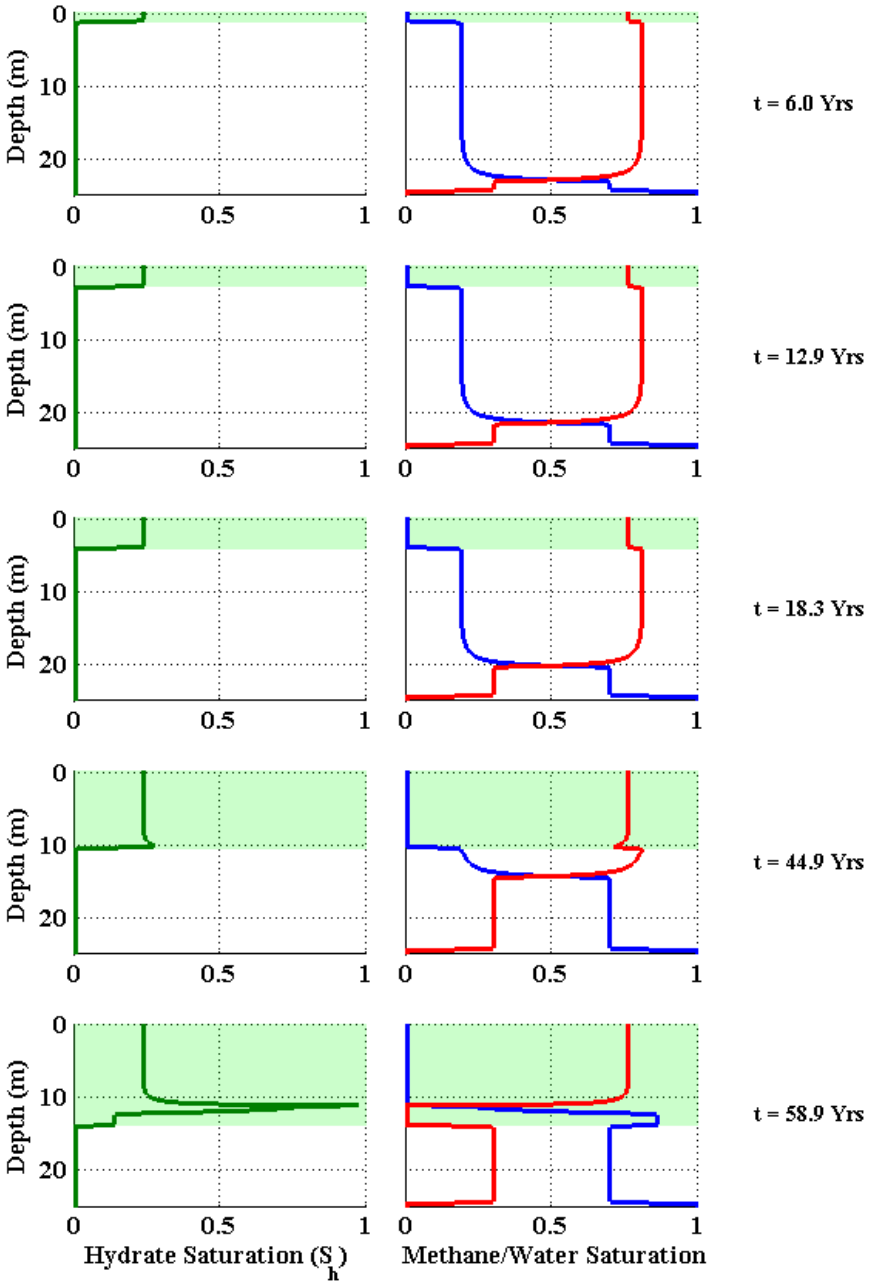

Fig. 5-20- Model results for Case 21 with a narrower pore size distribution, compared to that in Case 2. As hydrate is forming inside the expanding GHSZ (highlighted green fill), gaseous and aqueous phases flow into the GHSZ. Consequently, the GWC gradually rises towards the descending BGHSZ. The left panel shows the evolution of hydrate saturation profiles and the right panel shows the methane (red) and water (blue) saturation profiles for different locations of the BGHSZ. The corresponding fluxes of gaseous and aqueous phases are shown in Fig. 5-21.

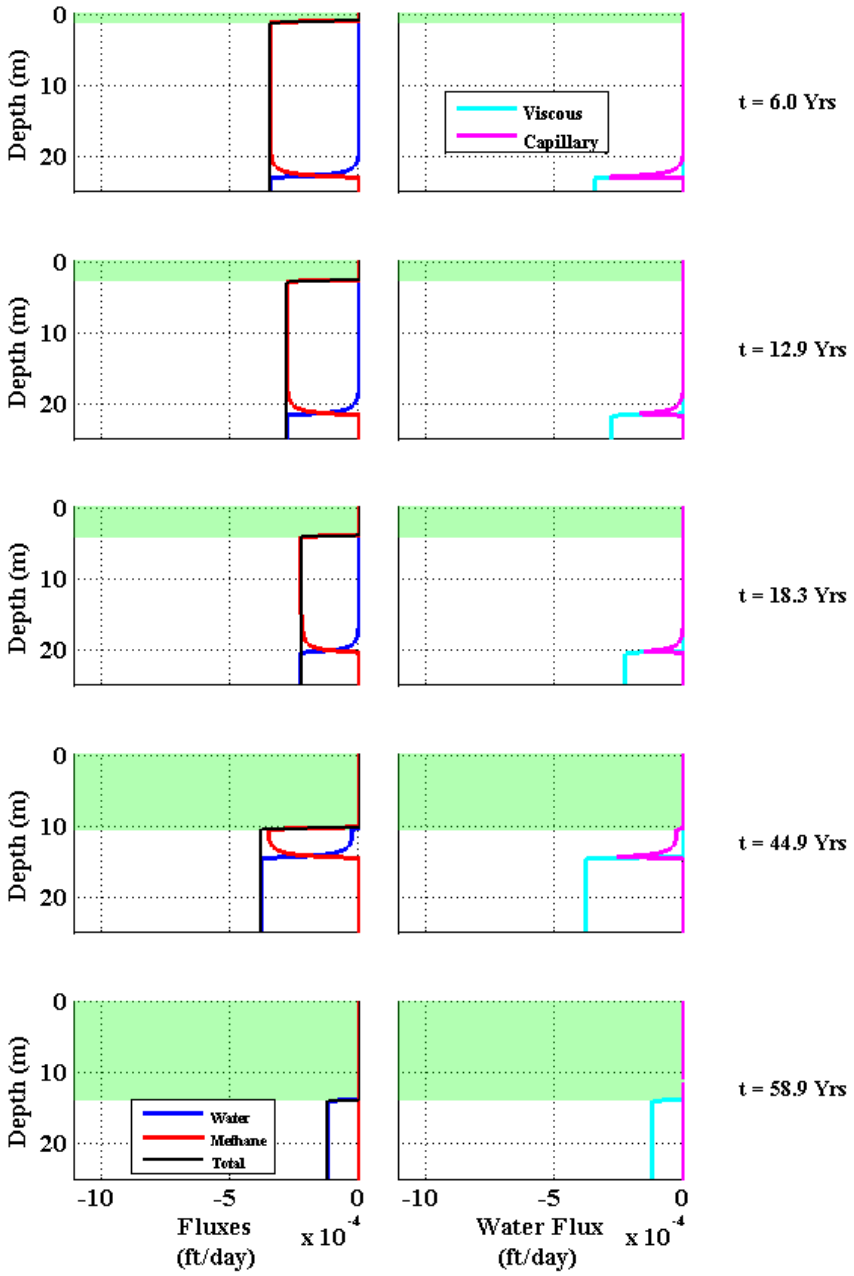

Fig. 5-21- Model results for Case 21 with a narrower pore size distribution, compared to that in Case 2. Left panel: Phase fluxes (blue = water, red = gas) in the formation at the times indicated on the right hand side. Right panel: the contribution of viscous flow and capillarity flow in aqueous phase flux is demonstrated. The capillary contribution of the aqueous phase flux is negligible and the aqueous phase flux is essentially the same as that predicted by the conventional Buckley-Leverett shock. Therefore, R_v=0 for a major section of the accumulation at the top, leading to a wet/dry (WD) mode of conversion similar to that in Case 2.

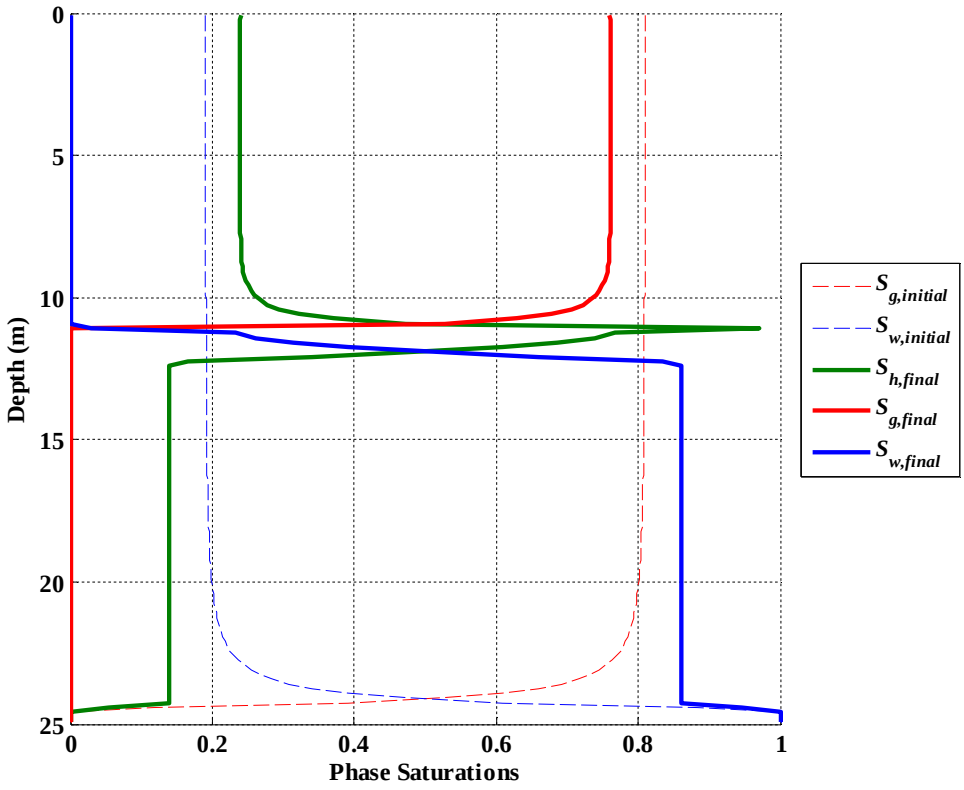

Fig. 5-22- Model results for Case 21 with a narrower pore size distribution, compared to that in Case 2: Initial gaseous and aqueous phase saturations are shown in red and blue dashed lines, respectively. The final hydrate saturation, when no more hydrate forms inside the system, because either the gaseous phase or the aqueous phase is exhausted, is shown in solid green line. The solid blue and solid red lines represent the final aqueous phase and gaseous phase saturation profiles, respectively. Similar to Case 2, the mode of conversion for Case 21 is Sharp/WD.

The other aspect of capillarity characteristics that plays a key role in determining the mode of conversion, is the capillary entry pressure, P_c^*, which is primarily governed by the size of grains in a porous media as well as the size distribution. To examine the effect of capillary entry pressure two cases with similar specifications except for P_c^* are

simulated: Case 10[***] and Case 25[†††]. As the capillary entry pressure increases, for similar length of gas accumulation L_0, the gas saturation at the top of the accumulation decreases and thus larger saturation gradients establishes at the upper parts. Larger saturation gradients, in turn, increase the capillary flow contribution in aqueous phase flux. The effect of P_c^* is also reflected in the complete Peclet number, N_{Pe}^*, as the $N_{Pe}^*\big|_{Case10} = 0.27$ and $N_{Pe}^*\big|_{Case25} \approx 0.76$; as is shown in Fig. 5-15, Case 10 falls below the threshold value $N_{Pe}^* = 0.4$ and thus a wet (W) mode of conversion is observed (see Fig. 5-23 and Fig. 5-24). In contrast, Case 25 falls above the threshold complete Peclet number which, as expected, led to a wet/dry/wet (WDW) mode of conversion (see Fig. 5-25 and Fig. 5-26).

Overall, capillary characteristics of the host sediment impose a key effect on the conversion process, specifically on the mode of conversion in terms of being wet (W) or wet/dry/wet (WDW). Generally, provided that all other specification of a gas accumulation and the host sediment are fixed, as the capillary entry pressure, P_c^*, increases or the Brooks-Corey model exponent, γ, decreases the complete Peclet number, N_{Pe}^*, decreases leading to a greater contribution of capillary flow in aqueous phase flux. This would, in turn, lead the mode of conversion toward being wet (W).

[***] $P_c^* = 5000\,Pa$

[†††] $P_c^* = 2500\,Pa$

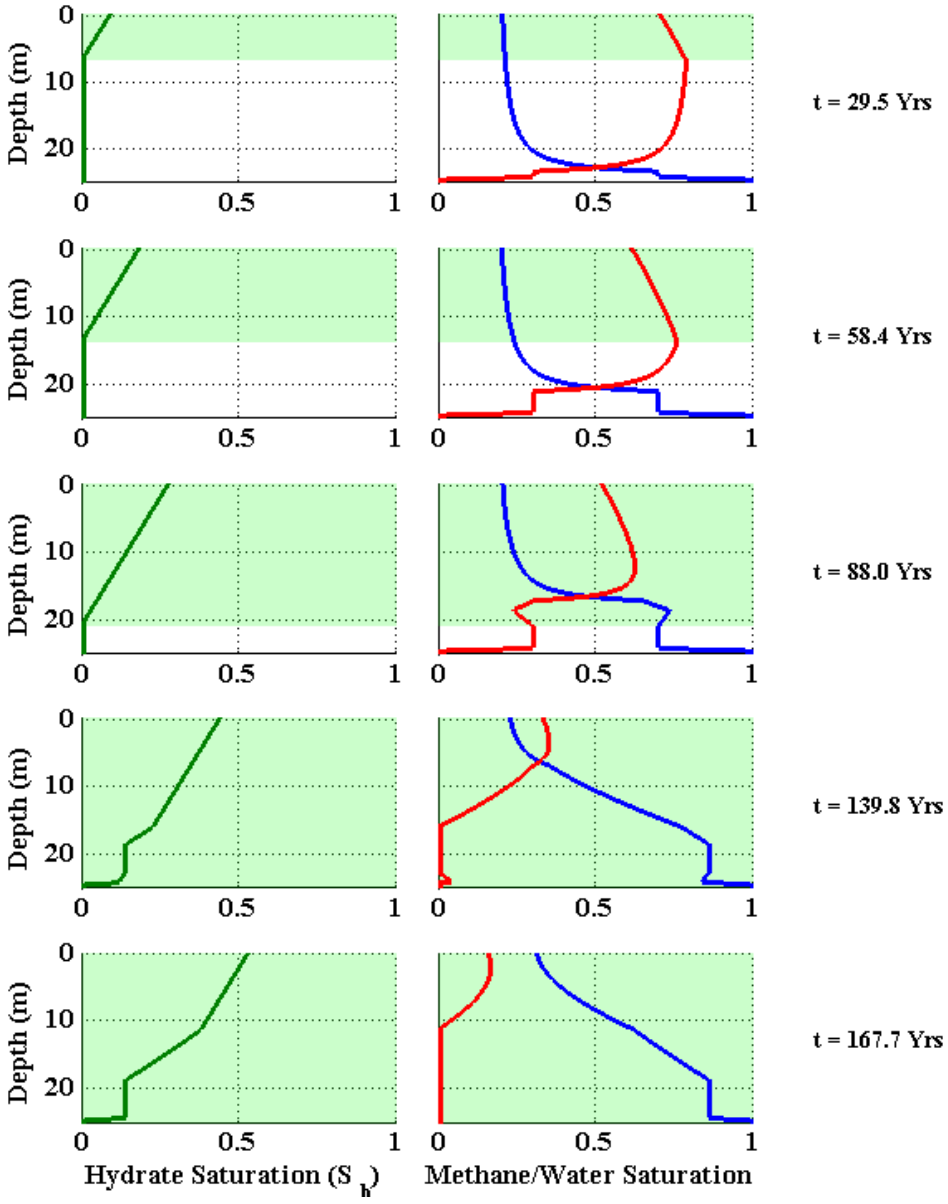

Fig. 5-23- Model results for Case 10 (see Table 5-4 for specifications): As hydrate is forming inside the expanding GHSZ (highlighted green fill), gaseous and aqueous phases flow into the GHSZ. Consequently, the GWC gradually rises towards the descending BGHSZ. The left panel shows the evolution of hydrate saturation profiles and the right panel shows the methane (red) and water (blue) saturation profiles through time. The final hydrate saturation profile is shown in Fig. 5-24 .

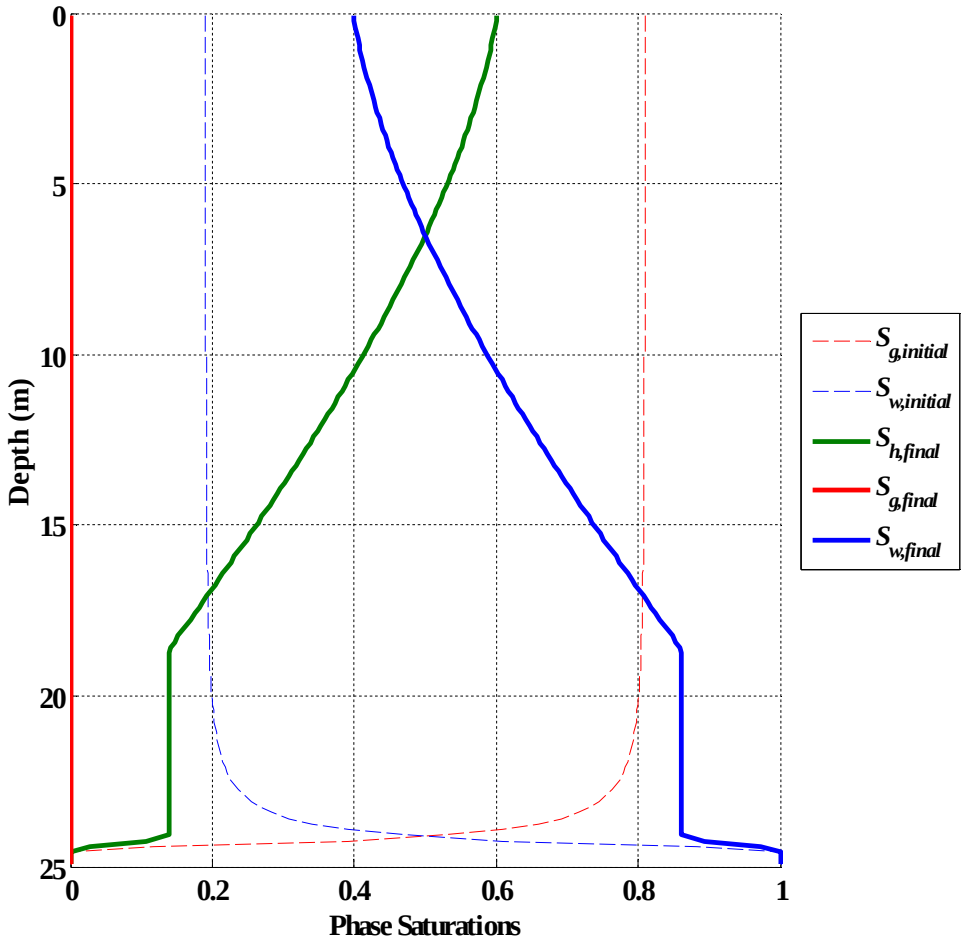

Fig. 5-24- Model results for Case 10: Initial gaseous and aqueous phase saturations are shown in red and blue dashed lines, respectively. The final hydrate saturation, when no more hydrate forms inside the sand unit, because the gaseous phase is exhausted, is shown in solid green line. The solid blue and solid red lines represent the final aqueous phase and gaseous phase saturation profiles, respectively. The mode of conversion for this case is Diffuse/W.

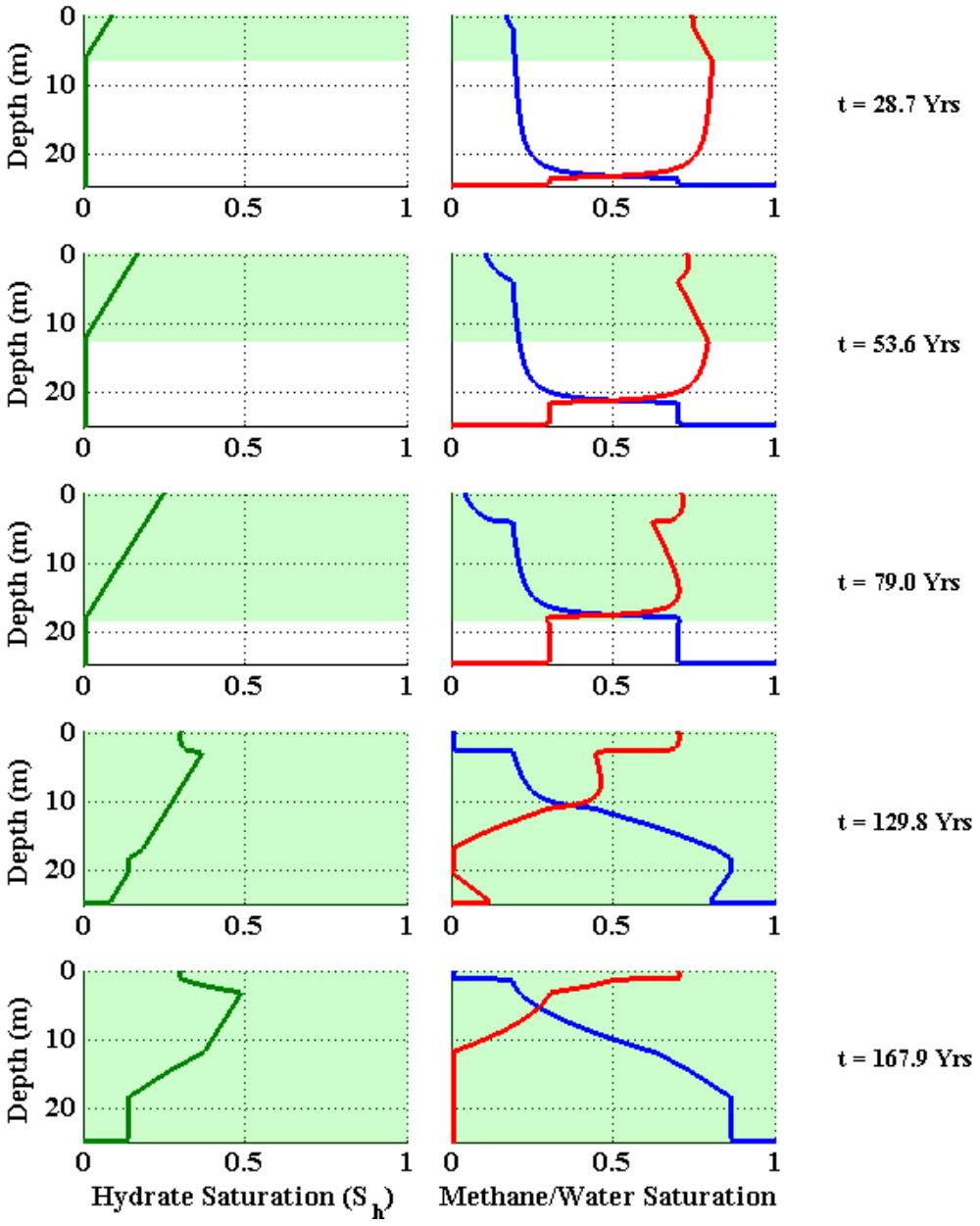

Fig. 5-25- Model results for Case 25 with a smaller capillary entry pressure P_c^*, compared to that in Case 10: In contrast to Case 10, in this case a top portion of the sand unit dries out at some point during the conversion process. Later, however, countercurrent imbibition wets the upper portion converting the gas remainder into hydrate. The left panel shows the evolution of hydrate saturation profiles and the right panel shows the methane (red) and water (blue) saturation profiles for different locations of the BGHSZ. The final hydrate saturation profile is shown in Fig. 5-26.

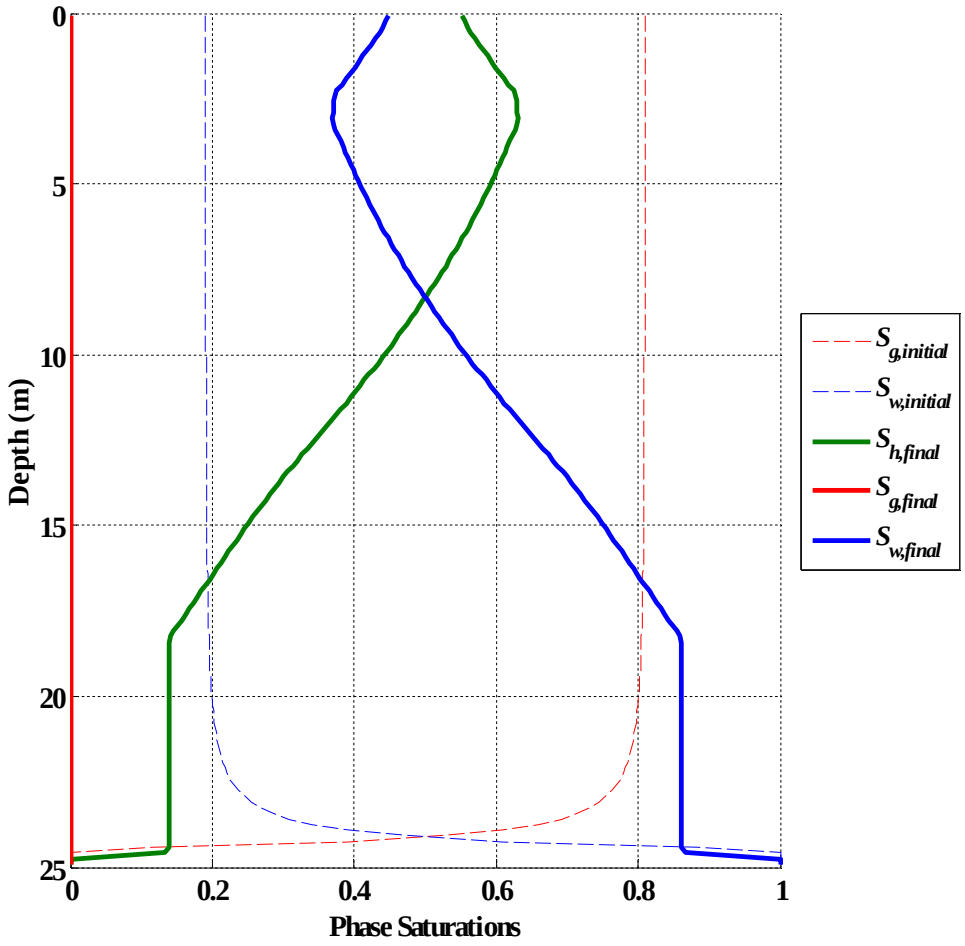

Fig. 5-26- Model results for Case 25 with a smaller capillary entry pressure P_c^*, compared to that in Case 10: Initial gaseous and aqueous phase saturations are shown in red and blue dashed lines, respectively. The final hydrate saturation, when no more hydrate forms inside the sand unit, because the gaseous phase is exhausted, is shown in solid green line. The solid blue and solid red lines represent the final aqueous phase and gaseous phase saturation profiles, respectively. The mode of conversion for this case is Diffuse/WDW.

5.3.4) Effect of permeability and relative permeability characteristics on hydrate saturation profiles in "converted free gas accumulations"

Permeability, k, and relative permeability characteristics, N_w, N_g, $k_{rw,0}$, and $k_{rg,0}$, are also role playing in determining the mode of conversion in terms of being wet (W) or wet/dry/wet (WDW). The latter is expected as permeability characteristics are key parts of the complete Peclet number, N_{Pe}^{*}.

A decrease in permeability of the host sediment, keeping all other characteristics fixed, would increase the complete Peclet number since a lower permeability would lead to a smaller capillary flow contribution in the aqueous phase flux. As an example, consider Case 6 and Case 24 with all the specification being the same except that absolute permeability in Case 6 is three orders of magnitude larger than that in Case 24. While Case 6 exhibits a wet (W) mode of conversion, Case 24 clearly exhibits a wet/dry/wet (WDW) mode of conversion. The reason is that $N_{Pe}^{*}\big|_{Case\,24} > 0.4$ and thus the capillary flow contribution is not large enough to maintain $R_v < R_{v,stoich}$. In terms of having diffuse basal contact, however, both cases 6 and 24 are similar since a change in absolute permeability would not change the dimensionless number N_{CC}.

As mentioned earlier, relative permeability characteristics are also expected to play a role in determining the mode of conversion and the final hydrate saturation profile. To investigate this effect, consider Case 28[###] which possesses a relative permeability curve of slightly less water-wet sediment compared to that in Case 25[§§§], with all other specifications being the same. As shown on Fig. 5-15, this variation would lead to different modes of conversion as the complete Peclet number in Case 28 fall below the threshold value $N_{Pe}^{*} = 0.4$ and thus exhibiting a wet (W) mode of conversion.

[###] N_w=1.75
[§§§] N_w=2.5

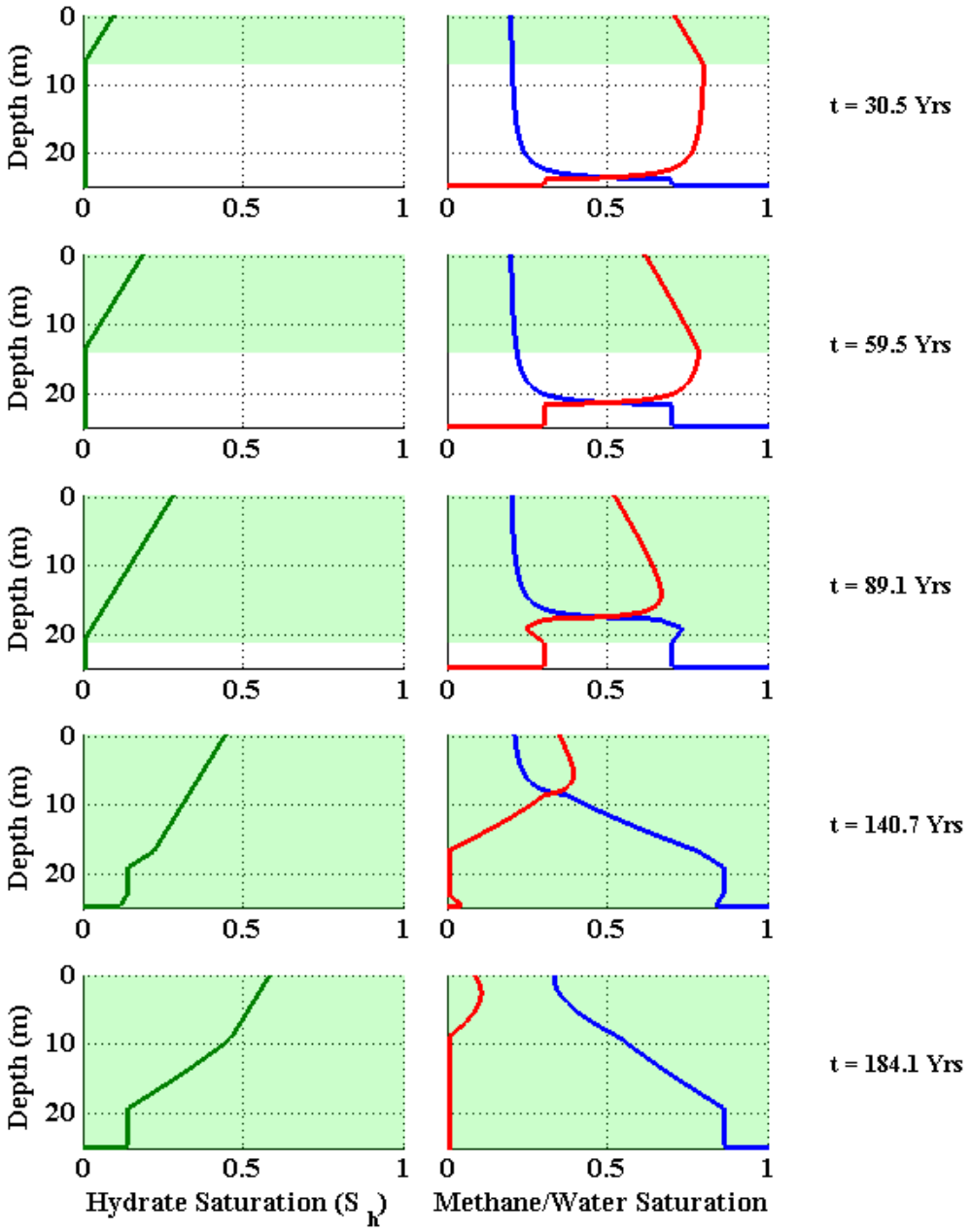

Fig. 5-27- Model results for Case 28 with a less water wet sand unit compared to that in Case 25: In contrast to Case 25, the mode of conversion is wet (W) here. The left panel shows the evolution of hydrate saturation profiles and the right panel shows the methane (red) and water (blue) saturation profiles for different locations of the BGHSZ. The final hydrate saturation profile is shown in Fig. 5-28.

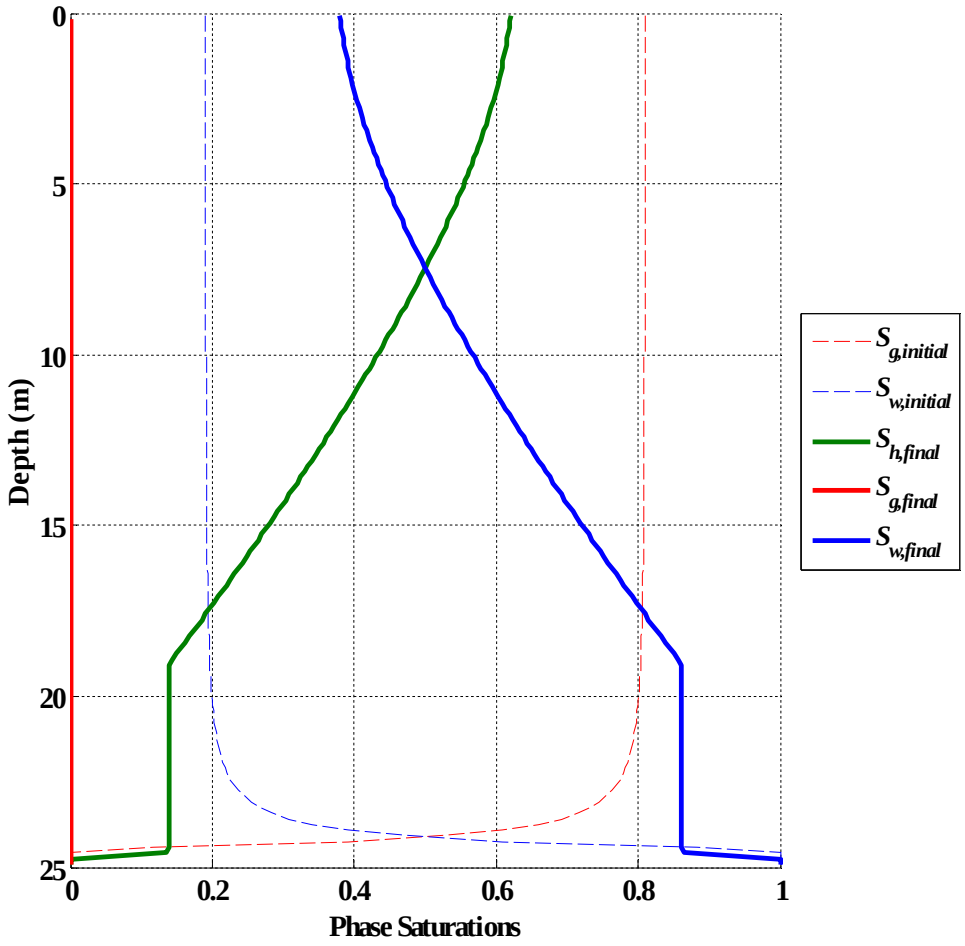

Fig. 5-28- Model results for Case 28 with a less water wet sand unit compared to that in Case 25: Initial gaseous and aqueous phase saturations are shown in red and blue dashed lines, respectively. The final hydrate saturation, when no more hydrate forms inside the sand unit, because the gaseous phase is exhausted, is shown in solid green line. The solid blue and solid red lines represent the final aqueous phase and gaseous phase saturation profiles, respectively. The mode of conversion for this case is Diffuse/W.

Overall, as the host sediment becomes more water wet or its absolute permeability decreases, the mode of conversion tends towards wet/dry/wet (WDW) since the capillary flow contribution in aqueous phase flux decreases.

5.3.5) Plausible mode of conversion during hydrate formation in Mount Elbert hydrate prospect

Based on the earlier discussions, it is evident that the mode of conversion and the physical processes behind conversion of the gas accumulation in Mount Elbert hydrate prospect, would be a complex function of not only the physical properties of the host sediment, being vertically heterogeneous, but also the rate of hydrate formation and the temperature cooling regime at the time of conversion. Dai et al. (2011) analyzed a comprehensive set of data from Mount Elbert well, including ground surface elevation, stratigraphy, surface temperature, the base of the ice-bearing permafrost, BIPF and the BGHSZ (Fig. 5-29). Fig. 5-29 suggests that the bottom of the GHSZ has moved down through the depth range of interest (Depth of 600 m to 700 m) in Mount Elbert well in a course of about 50,000 years, inferring an average rate of descent of the BGHSZ to be $\dot{z}_{BGHSZ} \approx 2\times10^{-3}\, m/year$. After descended through the depth interval 600m-700m, the BGHSZ did some oscillations (Fig. 5-29); however, as mentioned in chapter 1, the hydrate-bearing section of the Mount Elbert well, i.e. Units C and D, remained well inside the GHSZ and were not disturbed by the oscillations of the BGHSZ.

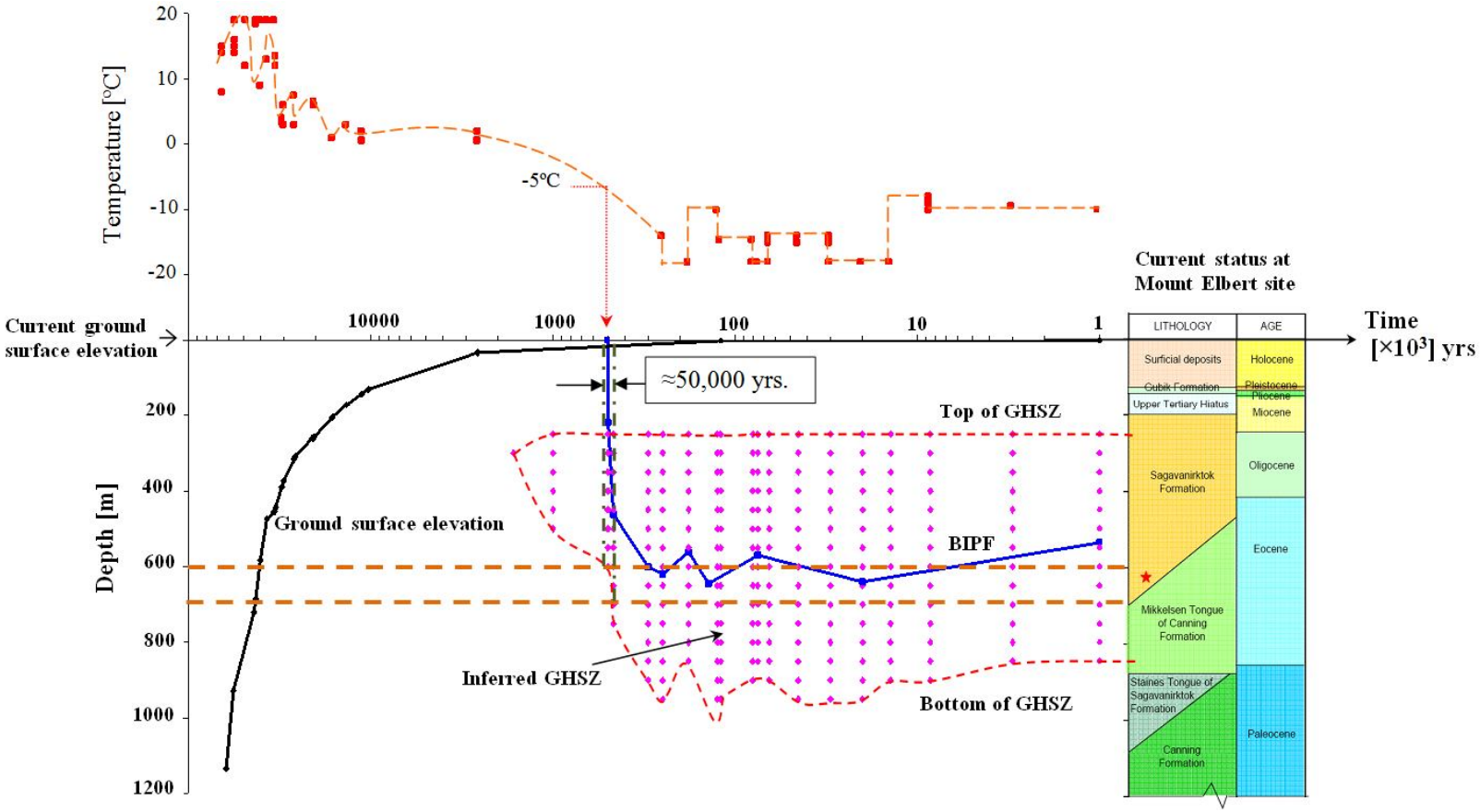

Fig. 5-29-A simultaneous analysis of different data from Mount Elbert stratigraphic test well including ground surface elevation, stratigraphy, surface temperature and the base of the ice-bearing permafrost, BIPF. The analysis shows that the Bottom of GHSZ has moved down through the depth range of interest (Depth of 600m to 700 m) in Mount Elbert well in a course of about 50,000 years, inferring the average rate of descent of the BGHSZ to be $\dot{z}_{BGHSZ} \approx 2\times10^{-3}\, m/year$. Figure is adopted and modified from Dai et al. (2011).

Considering that the rate of descent of the BGHSZ had been in order 10^{-3} m/y or less for the relevant cooling period of the Alaska North Slope, and considering that sharp basal contacts are exhibited by the observed hydrate saturation profiles in Mount Elbert well (Boswell et al., 2011), it is most likely that Mount Elbert hydrate prospect experienced a wet (W) mode of conversion (cf. Fig. 5-16). In other words, in terms of $\dot{S}_h$ versus $\dot{z}_{BGHSZ}$, Mount Elbert falls in the "Sharp/W" region identified on Fig. 5-16, meaning that capillarity driven flux has been the primary means of transporting fluid phases to the GHSZ during hydrate formation. Furthermore, the capillary flow contribution in the aqueous phase flux have been strong enough to keep $R_v<R_{v,1:1}$ and the sand units D and C remained wet (W) during the conversion process.

In any case, there are numerous factors playing role in the way hydrate accumulations formed in Mount Elbert prospect. For example, along dip flows of gaseous and aqueous phase flow, lateral heterogeneity, variable rate of descent of the BGHSZ as well as hydrate formation rate all play roles in determining the final hydrate saturation profile. The proposed 1-D hydrate formation model here permits analysis of some key processes involved in conversion of gas accumulations to hydrate reservoirs, especially in terms of accompanied fluid flow during hydrate formation. As some key features observed in Mount Elbert data are replicated by this 1-D model, it would be useful to extend the process model to 2- and 3-D geology. But it is beyond the scope of this dissertation to fully explain the Mount Elbert accumulation per se, and in any case the one-dimensionality of the model is too simple for that task.

5.4) SUMMARY AND CONCLUSION

Capillarity-driven transport to the GHSZ is the key mechanism of aqueous phase transport when a gas reservoir is converted to hydrate owing to surface temperature cooling, i.e. a descending BGHSZ. The model of this chapter computes fluxes due to buoyancy, pressure gradient and saturation gradient in response to the volume changes associated with hydrate formation. The model predicts that capillarity-driven flux is dominant mode of water transport and that this flux is sufficient to supply the needs of relatively slow rates of temperature cooling, i.e. $\dot{z}_{BGHSZ} < 10^{-2}\ m/yr$. The model yields an *a priori* value of R_v, the volumetric parameter (fraction of total fluid phases movement made up by gas) which determines the final hydrate saturation, given the initial gas saturation. For typical multiphase flow characteristics (relative permeability and capillary pressure curves) the predicted R_v gives a large hydrate saturation close to those observed in Mount Elbert and Mallik wells.

1-D conversion of gas accumulations into hydrate accumulation was characterized through dimensional analyses. Two dimensionless groups N_{Pe}^{*} and N_{CC} were identified to be controlling the mode of conversion in terms of the flow mechanisms and the final hydrate saturation profile. These two dimensionless numbers invoke key information about the host sediment, gas accumulation and rate of hydrate formation as well as rate of temperature cooling at the time of gas accumulation conversion.

It was shown that if the rate of hydrate formation, $\dot{S}_h$, or the rate of descent of the BGHSZ, $\dot{z}_{BGHSZ}$, are less than their corresponding threshold values (which is a function of rock physical properties and height of gas accumulation), the aqueous phase flux could always be supported to keep the host sediment wet (W) during the conversion, i.e. $S_w > 0$. If $\dot{S}_h$ and $\dot{z}_{BGHSZ}$ are both larger than their corresponding thresholds, the aqueous phase, at the upper section of the accumulation, would be exhausted at some point during the

conversion process. However, the countercurrent imbibition would eventually imbibe the exhausted region and convert the gas remainder into hydrate through an upward freezing process.

The model results suggest that in nature, fluxes of gas and water from below the GHSZ establish saturation profiles that balance the gradients due to buoyancy, pressure and capillarity. At any given location of the BGHSZ, the balance leads to a characteristic value of R_v, the fraction of fluid phase transport made up of gas. This value combined with the presumed value of residual gas saturation in the GHSZ leads to hydrate saturations less than or equal to the initial gas saturation at that location, depending on the magnitude of residual saturation. This is the reason that the simpler bed-scale model (presented in chapter 3 accounting for volumetric changes and sedimentological variation for a user-prescribed value of R_v) correctly predicts the Mount Elbert well saturation profile when the appropriate value of R_v is given.

Chapter 6: Conclusions and Future Works

6.1) SUMMARY AND CONCLUSIONS

A series of 1-D models were proposed to predict hydrate saturation profiles in "*converted free gas*" hydrate reservoirs considering that many of the Arctic hydrate prospects are believed to be preexisting natural gas reservoirs converted to modern hydrate accumulations in response to the ancient temperature cooling, i.e. during the last ice age. Augmenting various qualitative descriptions of this phenomena, the proposed models of this dissertation, for the first time, explore the physical basis for how this conversion of gas accumulation to hydrate might proceed, considering implications and effects of variable geology/petrophysics as well as volume change during hydrate formation on the response of a free-gas/water system to the imposition of gas hydrate stability conditions.

The model of chapter 3 considers three key elements during the conversion of a gas accumulation into hydrate: (i) volume change during hydrate formation within an existing gas accumulation, (ii) the temperature cooling which maps to a descending BGHSZ through the accumulation, and (iii) variation of grain size distribution with depth that causes variation in capillary entry pressure. The model is primarily developed for a gas accumulation no longer connected to the source of the gas charge. Mass balance analysis of the observed hydrate saturation profiles in the Arctic, such as that in Mount Elbert hydrate prospect, suggests that substantial aqueous phase migration to the GHSZ had accompanied the gas migration to the GHSZ and hydrate formation. The large volumes of transported aqueous phase are essential for forming large hydrate saturations in the upper portion of the column as observed in nature. The model also predicts small saturations in the lower portion, as observed in terrestrial hydrate prospects, even if the lower portion is sand-rich and initially gas saturated. Internal gas migration raises the gas/water contact, raising the possibility of disconnection of the remaining gas column at layers having relatively large capillary entry pressure. When this occurs, the disconnected subcolumns also yield large and small hydrate saturations in their upper and lower portions, respectively. This model assumes that the rate of descent of the BGHSZ is much smaller than the rate of hydrate formation. Therefore, the hydrate saturation profile predicted by the model is nonuniform with rather sharp basal contacts, i.e. intervals of large S_h interspersed between intervals of small S_h, even if the initial gas saturation profile is uniform. As discussed in chapter 3, such nonuniformities as observed in Mount Elbert well cannot be explained via “rule of thumb” association of major hydrate saturations with better quality sands.

It was shown that a considerable amount of fluid (of order 1 pore volume of gaseous and aqueous phases) needs to be transported during conversion of pre-

established natural gas reservoirs. As discussed in chapter 2, the fraction of this fluid that is gas, i.e. R_v, governs the magnitude of the final hydrate saturation. The model was applied on data from Mount Elbert well located in one of the methane hydrate reservoirs in Alaskan North Slope. With a physically reasonable choice for R_v, the model gives large S_h similar to those inferred from well logs. By orienting the flow direction in the model along dip rather than vertically, the model also predicts that small S_h will be found on the flanks of the Mount Elbert accumulation, if gas charged the flanks of the reservoir prior to or during BGHSZ descent, and that large S_h will fill the upper portion of Unit D. These model predictions were also consistent with interpretations of seismic anomalies and the Mount Elbert log-derived saturations.

As the model of chapter 3 required a prescribed value of R_v it was of high interest to study the elements controlling the value of R_v, and thus the magnitude of final hydrate saturation. A transport model based on pressure-driven viscous flow of phases was proposed in chapter 4 to provide an *a priori* estimate of R_v. As the effect of vertical heterogeneity was addressed in chapter 3, for simplicity the transport models were mainly discussed on homogeneous cases. It was shown that a cocurrent flow of gas and aqueous phases from below a descending base of gas hydrate stability zone (BGHSZ) upward into the hydrate stability zone (GHSZ) cannot provide the required amount of water for hydrate formation. Therefore, the pressure-driven model must transport water to the GHSZ from above. That is, water moves down into the hydrate formation zone through accumulated hydrate from overlying aquifers, while gas rises to the GHSZ from the remaining gas reservoir.

It was shown, however, that only with suitable choices of the key transport coefficients can the countercurrent transport of gas and aqueous phases provides the large volumes of both components needed to form large hydrate saturations observed in Arctic

sediments. For plausible endpoint relative permeabilities for aqueous phase and for a reasonable choice of a relationship between water effective permeability and hydrate saturation, the model prediction agrees with behavior observed in the Mount Elbert well. However, the viscous-dominated transport model prediction is highly sensitive to the ratio of these transport coefficients. Small variations in grain size distribution, end point relative permeability, or hydrate-saturation dependence of permeability to water yield large variations in predicted hydrate profiles, including qualitatively different behavior, e.g. preservation of a large gas phase saturation. Thus the pressure-driven fluid transport model is unlikely to provide a robust explanation of the mechanism of conversion. Instead it offers useful insight into the likely role of capillarity-driven transport, which was then discussed in chapter 5 of this dissertation.

In chapter 5, a numerical 1-D transport model is proposed for converted gas accumulations considering all different contributions to flow of gaseous and aqueous phases, including viscous, gravity and capillary flows. This general model also allows for different rates of hydrate formation versus rate of descent of the BGHSZ. It was shown that capillary flow derived by saturation gradients, dS_w/dz, are essential for providing the required volumes of transported aqueous phase. There are many parameters involved in determining whether the saturation gradients would be large enough to maintain the aqueous phase flow so that $R_v<R_{v,stoich}$, including permeability, relative permeability and in turn mobility of the phases, capillary characteristics (including capillary entry pressure and pore size distribution index), rate of descent of the BGHSZ, rate of hydrate formation within the GHSZ, and the length of gas-bearing section of the host sediment.

Two characterizing dimensionless groups: (i) complete Peclet number, N_{Pe}^{*}, and ratio of conversion time scale to cooling time scale, N_{CC} were identified to be keys in determining the mode of conversion of the gas accumulation as well as shape of the final

hydrate saturation profile. The strength of such characterization is that any change in the host sediment properties or rates of hydrate formation and descent of the BGHSZ would directly be reflected in N_{Pe}^{*} and N_{CC} determining the resulting mode of conversion and the hydrate saturation profile; consequently based on the threshold values, $N_{Pe}^{*}=0.4$ and $N_{CC}=1$, the mode of conversion would be predictable. The discussed modes of conversion are as follow: wet (W) versus wet/dry/wet (WDW) and sharp versus diffuse basal contacts of hydrate saturation profile. It was shown for $N_{Pe}^{*}<0.4$ the mode of conversion would be wet (W) meaning that the capillary contribution to aqueous phase flux is large enough to keep the sand unit wet, i.e. without exhausting the aqueous phase, at all times during the conversion process. When $N_{Pe}^{*}>0.4$, however, the aqueous phase in the upper parts of the gas accumulation would be exhausted at some point during the conversion as the cocurrent flow of gaseous and aqueous phase could not provide the required amount of aqueous phase to keep $R_v<R_{v,stoich}$. The aqueous-phase-exhausted portion of the sand unit would later be imbibed by the aqueous phase through a countercurrent imbibition process when the BGHSZ gets close enough to the GWC. The latter phenomenon would lead to an upward conversion of the gas remainder at the top of the sand unit as the upper portion is already well within the GHSZ.

Applying the model on the case of Mount Elbert well where the rate of descent of the BGHSZ had been in order 10^{-3} m/y, and considering the sharp basal contacts exhibited by the observed hydrate saturation profiles in Mount Elbert well (Boswell et al., 2011), suggests that Mount Elbert hydrate prospect experienced a wet (W) mode of conversion (cf. Fig. 5-16). In other words, Mount Elbert is consistent with a "Sharp/W" mode of conversion, meaning that capillarity driven flux has been the primary means of transporting fluid phases to the GHSZ during hydrate formation. Moreover, the capillary

flow contribution in the aqueous phase flux have been strong enough to keep $R_v<R_{v,1:1}$ and the sand units D and C remained wet (W) during the conversion process.

Although the models of this dissertation replicate many of the key features observed in Arctic hydrate accumulations, such as that in Mount Elbert well, they assume all transport to be vertical. This maximizes the influence of sedimentological control on the final hydrate distribution. Furthermore, as the areal extent of the gas accumulation increases or the dip of the structure increases, the contribution of along-dip flow to the gas transport increases, and a 1-D vertical flow model yields a lower bound on the thickness of the intervals with large hydrate saturation. Yet, 1-D models are of paramount interest in terms of identifying fundamental features playing role during conversion of gas accumulations into modern hydrate prospects.

6.2) FUTURE WORKS

6.2.1) Model extension to 2-D and 3-D

As discussed in chapter 2, the phase flow pathway, the extent of gas charge and the dip angle of the bedding are key controls on final hydrate distribution in a multilayer column of sediment. The 1-D model of chapter 3 quantitatively addresses the extent-of-charge explanation, i.e. original gas reservoirs in multiple layers are insufficiently charged to be in communication across layers. Moreover, it generalizes the extent-of-charge model to show how a stack of partially filled hydrate reservoirs can result even from initially communicating layers that host a single continuous column of gas. However, some key contributions such as bedding inclinations, presence of high conductivity conduits such as fractures, spill points and areal heterogeneity are not considered in the 1-D models of this work. Therefore, it would be of interest to extend the present models to 2- and 3-D to incorporate the effects neglected in 1-D models. Mount

Elbert hydrate prospect has an inclination of less than 2° and thus a 1-D model could be reasonable representation of the structural setting. However, a 2-D or 3-D model would be more appropriate for Mallik hydrate setting which has a structural setting much steeper than that of Mount Elbert hydrate prospect.

6.2.2) Implementing the effect of salinity on hydrate stability

The isotopic composition of the fluid recovered from Mount Elbert well characterizes the formation water as the same as modern day local *fresh water* bodies (Torres et al., 2011). Therefore, in the models of this work the salinity of the aqueous phase is neglected for simplicity and owing to the fact that the primary data of interest in this dissertation are from Mount Elbert well. In general, salinity can affect the hydrate saturation profiles especially in marine systems. When salinity builds up to values more than a threshold, hydrate formation would be inhibited until the salinity decreases, through diffusion, to values lower than the threshold. Therefore, in natural systems with brine (not fresh water) the aqueous phase can never be exhausted since the salinity limit on hydrate stability does not allow for further hydrate formation once the aqueous phase saturation becomes small enough so that salinity reaches its limit.

Therefore, it would have interesting implications to account for the effect of salinity on the stability of gas hydrates during their formation. It is anticipated that considering the effect of salinity could potentially change the conversion mode from being wet/dry/wet (WDW) to wet (W), especially if the aqueous phase is not fresh water. However, considering that in the order of 1 pore volume of water would transport into the hydrate formation zone during the conversion process, any salinity buildup would eventually be diluted if the formation water is not too saline.

6.2.3) Accounting for the effect of hydrate on capillary characteristics of hydrate-bearing sediments

In the models of this work, capillary characteristics of the host sediment are considered unchanged by the presence of gas hydrate. In other words, when a part of the sand unit is encompassed by the GHSZ as hydrate grows inside the host sediment the capillary characteristics of the hydrate-bearing zone are considered the same as that prior to the imposition of the GHSZ.

In natural systems, however, it is expected that the presence of hydrate, especially when hydrate coats the surface of grains, would affect the capillary characteristics of the host sediment. The reason is that once the surface of the grains are coated by hydrate, or when hydrate is pore-filling or even grows at the grain contacts, the interfacial tensions between aqueous phase and the solid, and that between gaseous phase and the solid would partially change. The change in interfacial tensions would change the contact angle and theoretically changes the capillary pressure curve. This would need detail knowledge of how the presence of hydrate changes the interfacial tension between liquids and the solid phase as well as the way that hydrate is distributed within porous media which can change from case to case. It is expected that the mode of hydrate saturation distribution, i.e. whether it is pore filling or grain-coating, would make substantial difference in terms of the capillary characteristics of the hydrate-bearing sediment.

6.2.4) Incorporating the kinetics of hydrate formation in transport models

In the model of chapter 5, a wide spectrum of rate of hydrate formation, $\dot{S}_h$, and rate of descent of the BGHSZ, $\dot{z}_{BGHSZ}$, was investigated. However, for each case a fixed $\dot{S}_h$ and $\dot{z}_{BGHSZ}$ was adopted for simplicity. However, the rate of hydrate formation is a function of the difference between the phase equilibrium fugacity, f_{eq}, and the methane

fugacity at the hydrate crystal surface, f, (Kim et al., 1987) which are both functions of pressure, P, and temperature, T.

Earlier, it was pointed out that non-uniformity of descent of the BGHSZ, i.e. variable rate of descent of the BGHSZ, would impact the hydrate saturation profiles. We also believe that a variable rate of hydrate formation would affect the hydrate saturation profiles as the hydrate formation rate also affects the gas portion of the total flux, R_v, and in turn the magnitude of final hydrate saturation. Therefore, it would be of interest to incorporate the kinetics of hydrate formation into the transport models proposed in this dissertation.

Appendix A: A dimensionless form of convection-diffusion transport equation

In chapter 5, it was shown that aqueous phase flux in the convection-diffusion equation, Eq. (5.16), can be written as

$$u_w = \underbrace{\frac{\lambda_w}{\lambda_t} u_T}_{Viscous} + \underbrace{k \frac{\lambda_w \lambda_g}{\lambda_t} \frac{\partial P_c}{\partial z}}_{Capillary} + \underbrace{k \frac{\lambda_w \lambda_g}{\lambda_t} \Delta \rho g}_{Gravity} \tag{A.1}$$

and thus the governing equation for aqueous phase saturation, in the absence of hydrate formation, can be written as

$$\phi \frac{\partial}{\partial t} S_w + \frac{\partial}{\partial z} \left[\underbrace{\frac{\lambda_w}{\lambda_t} u_T}_{Viscous} + \underbrace{k \frac{\lambda_w \lambda_g}{\lambda_t} \frac{\partial P_c}{\partial z}}_{Capillary} + \underbrace{k \frac{\lambda_w \lambda_g}{\lambda_t} \Delta \rho g}_{Gravity} \right] = 0 \tag{A.2}$$

where $\lambda_t = \lambda_w + \lambda_g$ and $\Delta\rho = \rho_w - \rho_g$. Equation (A.1) can be written in dimensionless form using some normalized parameters introduced in the following. The dimensionless space variable is defined as

$$z_D = \frac{z}{L_0} \tag{A.3}$$

where L_0 is the thickness of the sand unit along which the initial gas accumulation is established. A dimensionless aqueous phase saturation, S, is also defined as

$$S = \frac{S_w - S_{w,irr}}{1 - S_{gr} - S_{w,irr}} \tag{A.4}$$

where S_{gr} and $S_{w,irr}$ are residual gaseous phase saturation and irreducible aqueous phase saturation, respectively. A dimensionless time, t_D, is defined as

$$t_D = \frac{u_T}{\phi^* L_0} t \tag{A.5}$$

where u_T is the total flux, i.e. $u_T = u_w + u_g$, and

$$\phi^* = \phi\left(1 - S_{gr} - S_{w,irr}\right) \tag{A.6}$$

Substituting equations (A.3) through (A.6) into Eq. (A.2) yields

$$\frac{\partial S}{\partial t_D} + \frac{\partial}{\partial z_D}\left[\underbrace{\frac{\lambda_w}{\lambda_t}}_{Viscous} + \underbrace{\frac{k}{u_T L_0}\frac{\lambda_w \lambda_g}{\lambda_t}\frac{\partial P_c}{\partial S}\frac{\partial S}{\partial z_D}}_{Capillary} + \underbrace{\frac{k}{u_T}\frac{\lambda_w \lambda_g}{\lambda_t}\Delta\rho g}_{Gravity}\right] = 0 \tag{A.7}$$

For capillarity and relative permeability characteristics, Brooks-Corey model, Eqs. (A.8) through (A.10) are used.

$$P_c = P_c^*\left(\frac{1 - S_{gr} - S_{w,irr}}{1 - S_{w,irr}}\right)^{-\frac{1}{\gamma}} S^{-\frac{1}{\gamma}} \tag{A.8}$$

$$\lambda_w = \lambda_{rw,0} S^{N_w} \tag{A.9}$$

$$\lambda_g = \lambda_{rg,0}\left(1 - S\right)^{N_g} \tag{A.10}$$

Substituting Brooks-Corey model equations into Eq. (A.7) after simplification gives:

$$\frac{\partial S}{\partial t_D} + \frac{\partial}{\partial z_D}\left[\underbrace{V(S)}_{Viscous} + \underbrace{\frac{1}{N_{Pe}} D_C(S)\frac{\partial S}{\partial z_D}}_{Capillary} + \underbrace{N_G G(S)}_{Gravity}\right] = 0 \tag{A.11}$$

where N_{Pe} and N_G are Peclet number and gravity numbers, respectively, written as

$$N_{Pe} = \frac{u_T L_0}{k \lambda_{rw,0} P_c^*} \tag{A.12}$$

$$N_G = \frac{k\lambda_{rw,0}}{u_T}\Delta\rho g \tag{A.13}$$

Peclet number, N_{Pe}, represents the ratio of viscous forces to capillary forces while gravity number, N_G, represents the ratio of gravity forces to the viscous forces. Combining Eqs. (A.11) through (A.13) it can be shown that functions $V(S)$, $D_C(S)$, and $G(S)$ are

$$D_C(S) = -\frac{1}{\gamma}\left(\frac{1-S_{gr}-S_{w,irr}}{1-S_{w,irr}}\right)^{-\frac{1}{\gamma}} \frac{(1-S)^{N_g}\, S^{N_w-\frac{\gamma+1}{\gamma}}}{(1-S)^{N_g}+MS^{N_w}} \tag{A.14}$$

$$G(S) = \frac{(1-S)^{N_g}\, S^{N_w}}{(1-S)^{N_g}+MS^{N_w}} \tag{A.15}$$

$$V(S) = \frac{MS^{N_w}}{(1-S)^{N_g}+MS^{N_w}} \tag{A.16}$$

where M is the mobility ratio, i.e. ratio of aqueous phase mobility to that of the gas phase,

$$M = \frac{\lambda_{rw,0}}{\lambda_{rg,0}} \tag{A.17}$$

Appendix B: Introduction to dimensionless groups, N_{CC} and N_{Pe}^{*}

To extract the influence of each of the viscous, gravity and capillary forces, an aqueous phase dimensionless flux, u_{wD}, can be obtained from Eq. (A.11):

$$u_{wD} = u_{wDC} + u_{wDG} + u_{wDV} \tag{B.1}$$

where the elements can be written as Eqs. (B.2) through (B.4).

$$u_{wDC} = \frac{1}{N_{Pe}} D_C(S) \frac{\partial S}{\partial z_D} \tag{B.2}$$

$$u_{wDG} = N_G G(S) \tag{B.3}$$

$$u_{wDV} = V(S) \tag{B.4}$$

To calculate the Peclet number a characteristic total flux, $u_T = u_T^*$, is required which is characterized by the rate of hydrate formation, $\dot{S}_h$ and the rate of descent of the BGHSZ, $\dot{z}_{BGHSZ}$. It can be shown that if hydrate forms in sediment of porosity, ϕ, over a thickness, Δz, the required total flux for hydrate formation, with a rate of $\dot{S}_h$ saturation unit per unit time, would be

$$u_T = \phi K_{trans} \dot{S}_h \Delta z \tag{B.5}$$

Therefore, to calculate the characteristic total flux, u_T^*, a characteristic Δz^* needs to be calculated. Δz^* is a characteristic length of the gas-bearing sediment over which the rate of hydrate formation is nonzero, i.e. both gaseous and aqueous phases are present.

When the BGHSZ is descending at rate of $\dot{z}_{BGHSZ}$, Δz would tend to grow with the same rate; however, the top portions of the sediment in which hydrate formation started earlier might run out of aqueous phase or gaseous phase at the same time which limits the growth of Δz. The maximum amount of time, $\Delta t^{\max}$, that Δz is growing with the rate $\dot{z}_{BGHSZ}$ can be calculated from the maximum hydrate saturation expected and the rate of hydrate formation $\dot{S}_h$ as in Eq. (B.6).

$$\Delta t^{\max} = \frac{S_h^{\max}}{\dot{S}_h} \tag{B.6}$$

Consequently, Δz^* can be calculated from Eq. (B.7).

$$\Delta z^* = \dot{z}_{BGHSZ} \Delta t^{\max} \tag{B.7}$$

As discussed in chapters 2 and 3, it is expected that hydrate saturation is bounded by the initial gas saturation at the zone of hydrate formation, i.e. $S_{h,\,final} \le S_{g,i}$. For homogeneous sand, the maximum gas saturation occurs at the top below the seal and can be written as

$$S_g^{\max} = \left(1 - S_{w,irr}\right)\left[1 - \left(1 + \frac{\Delta\rho g L_0}{P_c^*}\right)^{-\gamma}\right] \tag{B.8}$$

Combining the equations (B.5) through (B.8), the characteristic total flux, u_T^*, can be calculated as

$$u_T^* = \phi K_{trans}\left(1 - S_{w,irr}\right)\left[1 - \left(1 + \frac{\Delta\rho g L_0}{P_c^*}\right)^{-\gamma}\right]\dot{z}_{BGHSZ} \tag{B.9}$$

However, u_T^* is certainly bounded by a maximum amount of flux required for hydrate formation within the whole gas-bearing section, L_0. Therefore,

$$u_T^* = \phi K_{trans}\left(1-S_{w,irr}\right)\left[1-\left(1+\frac{\Delta\rho g L_0}{P_c^*}\right)^{-\gamma}\right]\dot{z}_{BGHSZ} \le \phi K_{trans}\dot{S}_h L_0 \tag{B.10}$$

Based on the simplified version of (B.10) the true representation of u_T^* would be

$$u_T^* = \begin{cases} \phi K_{trans}\left(1-S_{w,irr}\right)\left[1-\left(1+\frac{\Delta\rho g L_0}{P_c^*}\right)^{-\gamma}\right]\dot{z}_{BGHSZ} & ;\ if\ \ N_{CC} \le 1 \\ \phi K_{trans}\dot{S}_h L_0 & ;if\ \ N_{CC} \ge 1 \end{cases} \tag{B.11}$$

wherein N_{CC} is a dimensionless number as

$$N_{CC} = \frac{\left(1-S_{w,irr}\right)}{L_0}\left[1-\left(1+\frac{\Delta\rho g L_0}{P_c^*}\right)^{-\gamma}\right]\frac{\dot{z}_{BGHSZ}}{\dot{S}_h} \tag{B.12}$$

N_{CC} is a normalized version of the ratio of rate of descent of the BGHSZ, $\dot{z}_{BGHSZ}$, to hydrate formation rate, $\dot{S}_h$, inside the GHSZ. In chapter 5, it is shown how this dimensionless group can be used to predict the final hydrate saturation profile in terms of having a sharp or diffuse basal contact.

In chapter 4 it was shown that owing to the very low mobility ratio of aqueous to gaseous phase, M<<1, in the process of conversion of a gas accumulation into hydrate accumulation, viscous contribution in aqueous phase flow is negligible, i.e. $u_{wDV} \approx 0$. In the simulations of chapter 5 it was shown that the capillary flow, u_{wDC}, derived by saturation gradients, are in charge of the aqueous phase flow towards the GHSZ. Examination of Eq. (A.11) shows that the behavior of the flow towards the GHSZ is determined not only by the nature of the porous medium and the fluid system, i.e. permeability, porosity, viscosities, relative permeability and capillary characteristics, but also by the length of gaseous-phase-containing section, L_0, and the characteristic total

flux, u_T^*. Considering that capillarity flow is the major contribution to aqueous phase flow, we propose that a complete version of Peclet number,

$$N_{Pe}^* = \frac{N_{Pe}\big|_{u_T = u_T^*}}{D_c(S\big|_{S_w = 1 - S_g^{\max}})} \tag{B.13}$$

may be qualified as a scaling dimensionless group and it can be stated that for a given N_{CC} and for any given porous medium and any given rate of hydrate formation and rate of temperature cooling, all conversions corresponding to the same N_{Pe}^* behave similarly (same physical processes) in terms of aqueous phase transport to the GHSZ. This assertion is investigated in chapter 5 through compiling numerous numerical realizations of Eq. (A.7) for a wide range of relevant porous media characteristics along with various rates of hydrate formation and descent of the BGHSZ.

Glossary

Nomenclature

A	Cross sectional area (L^2)
c	Compressibility ($M^{-1}LT^2$)
D_{10}, D_{50}, D_{60}	10^{th} , 50^{th} and 60^{th} percentile of grain size distribution, respectively (L)
f	Fractional flow (dimensionless)
g	Gravitational acceleration (LT^{-2})
h	Depth (L)
J	Jacobian matrix
K	Hydraulic conductivity (LT^{-1})
K_{trans}	Total phase (gas + aqueous) volume transported per unit volume of hydrate formed (dimensionless)
k	Permeability (L^2)
$k_{w,h}$	Permeability of hydrate-bearing sediment (L^2)
L	Length (L)
M	Mobility ratio (dimensionless)
MW	Molecular weight (M/M)
N	Hydration number
N_G	Gravity number (dimensionless)
N_g	Gaseous phase relative permeability exponent (dimensionless)
N_{Pe}	Peclet number (dimensionless)
N_{Pe}^*	Complete Peclet number (dimensionless)
N_{CC}	Ratio of conversion time scale to cooling time scale (dimensionless)
N_w	Aqueous phase relative permeability exponent (dimensionless)
n	Number of moles (M)
P, P_c	Phase pressure, and capillary pressure, respectively ($ML^{-1}T^{-2}$)
$P_{c,entry}$	Capillary entry pressure ($ML^{-1}T^{-2}$)
P_c^*	Capillary entry pressure ($ML^{-1}T^{-2}$)
q	Flow rate (L^3T^{-1})
R_n	Gas phase molar ratio of transported phases (dimensionless)
R_v	Gas phase volume ratio of transported phases (dimensionless)
r_{avg}, r_{eq}	Average radius and equivalent radius, respectively (L)
S	Saturation (dimensionless)
S_{gr}	Residual gas saturation (dimensionless)
$\dot{S}_h$	Rate of hydrate formation (T^{-1})
$S_{w,irr}$	Irreducible water saturation (dimensionless)
T	Temperature (Θ)
t	Time (T)

t_D	Dimensionless time (dimensionless)
U	Coefficient of uniformity (dimensionless)
u	Flux (LT^{-1})
u_T^*	Characteristic total flux (LT^{-1})
V	Volume (L^3)
$\bar{V}$	Molar volume (L^3M^{-1})
z	Depth (L)
z_D	Dimensionless depth (dimensionless)
$\dot{z}_{BGHSZ}$	Rate of descent of the BGHSZ (LT^{-1})

Greek

α	Total gaseous and aqueous phases volume required to form one unit volume of gas hydrate (dimensionless)
δ	Incremental amount of a quantity
ϕ	Porosity (dimensionless)
ϕ^*	Normalized porosity (dimensionless)
γ	Pore size distribution index (dimensionless)
λ	Mobility ($M^{-1}L^3T$)
λ_r	Relative mobility ($M^{-1}LT$)
μ	Dynamic viscosity ($ML^{-1}T^{-1}$)
ρ	Density (ML^{-3})
σ	Interfacial tension (MT^{-2})
Δn	Transported number of moles (M)
ΔV	Transported volume (L^3)

Subscripts

BGHSZ	Base of Gas Hydrate Stability Zone
C	Capillary contribution
G	Gravity contribution
g, h, w	Gaseous, hydrate, and aqueous phases, respectively
D, d	Dimensionless
i, f	Initial and final, respectively
front	Of a moving front
stoich	Associated with having the maximum possible hydrate saturation
1:1	Associated with having the final hydrate saturation equal to the initial gas saturation
r	Relative [permeability or mobility]
T, t, tot	Total amount of a quantity

threshold	Threshold value of a quantity
V	Viscous contribution

Superscripts

GWC	Gas-water contact
max	Maximum amount of a quantity

Bibliography

Behseresht, J., Bryant, S.L., 2011. Sedimentological and Transport Control on Hydrate Saturation Distribution in Arctic Gas-Hydrate-Bearing Deposits, in: Proceedings of the 7th International Conference on Gas Hydrates. Presented at the International Conference on Gas Hydrates, Edinburgh, Scotland, United Kingdom.

Behseresht, J., Bryant, S.L., 2012. Sedimentological control on saturation distribution in Arctic gas-hydrate-bearing sands. Earth and Planetary Science Letters 341-344, 114–127.

Behseresht, J., Bryant, S.L., Sepehrnoori, K., 2009. Infinite-Acting Physically Representative Networks for Capillarity-Controlled Displacements. SPEJ 14, 568–578.

Bhatnagar, G., Chapman, W.G., Dickens, G.R., Dugan, B., Hirasaki, G.J., 2007. Generalization of gas hydrate distribution and saturation in marine sediments by scaling of thermodynamic and transport processes. American Journal of Science 307, 861–900.

Boswell, R., Collett, T., 2006. The Gas Hydrates Resource Pyramid, Fire in the Ice. Office of Fossil Energy, National Energy Technology Laboratory.

Boswell, R., Collett, T., McConnell, D., Frye, M., shedd, B., Mrozewski, S., Guerin, G., Cook, A., Godfriaux, P., Dufrene, R., Roy, R., Jones, E., 2009. Joint Industry Project Leg II discovers rich gas hydrate accumulations in sand reservoirs in the Gulf of Mexico (No. 9), Fire in the Ice. US Department of Energy, National Energy Technology Laboratory, Office of Fossil Energy.

Boswell, R., Rose, K., Collett, T.S., Lee, M., Winters, W., Lewis, K.A., Agena, W., 2011. Geologic controls on gas hydrate occurrence in the Mount Elbert prospect, Alaska North Slope. Marine and Petroleum Geology 28, 589–607.

Brooks, R.H., Corey, A.T., 1964. Hydraulic properties of porous media (No. 3), Hydraulic paper. Colorado State University,, Colorado State University.

Bryant, S.L., King, P.R., Mellor, D.W., 1993. Network model evaluation of permeability and spatial correlation in a real random sphere packing. Transp Porous Med 11, 53–70.

Buckley, S.E., Leverett, M.C., 1942. Mechanism of fluid displacement in sands. Petroleum Transactions, AIME 146, 107–116.

Buffett, B., 2000. Formation of gas hydrate from dissolved gas in natural porous media. Marine Geology 164, 69–77.

Buffett, B., Archer, D., 2004. Global inventory of methane clathrate: sensitivity to changes in the deep ocean. Earth and Planetary Science Letters 227, 185–199.

Clennell, B.M., Hovland, M., Booth, J.S., Henry, P., Winters, W.J., 1999. Formation of natural gas hydrates in marine sediments 1. Conceptual model of gas hydrate

growth conditioned by host sediment properties. J. Geophys. Res. 104, 22985–23003.
Collett, T.S., 1993. Natural Gas Hydrates of the Prudhoe Bay and Kuparuk River Area, North Slope, Alaska. AAPG bulletin 77, 793–812.
Collett, T.S., Johnson, A., Knapp, C., Boswell, R., 2009. Natural Gas Hydrates – A Review, in: Natural Gas Hydrates – Energy Resource Potential and Associated Geologic Hazards, AAPG Memoir, Vol. 89. pp. 146–219.
Collett, T.S., Lee, M.W., Agena, W.F., Miller, J.J., Lewis, K.A., Zyrianova, M.V., Boswell, R., Inks, T.L., 2011. Permafrost-associated natural gas hydrate occurrences on the Alaska North Slope. Marine and Petroleum Geology 28, 279–294.
Conte, S.D., 1980. Elementary Numerical Analysis: An Algorithmic Approach, 3 Sub. ed. Mcgraw-Hill College.
Cook, A., Goldberg, D., Kleinberg, R., 2008. Fracture-controlled gas hydrate systems in the northern Gulf of Mexico. Marine and Petroleum Geology 25, 932–941.
Cook, A.E., Anderson, B.I., Malinverno, A., Mrozewski, S., Goldberg, D.S., 2010. Electrical anisotropy due to gas hydrate-filled fractures. Geophysics 75, F173–F185.
Cook, A.E., Goldberg, D., 2008. Extent of gas hydrate filled fracture planes: Implications for in situ methanogenesis and resource potential. Geophys. Res. Lett. 35, L15302.
Dai, S., Lee, C., Santamarina, J.C., 2011. Formation history and physical properties of sediments from the Mount Elbert Gas Hydrate Stratigraphic Test Well, Alaska North Slope. Marine and Petroleum Geology 28, 427–438.
Dallimore, S., Collett, T., 2005. Scientific results from the Mallik 2002 gas hydrate production research well program, Mackenzie delta, Northwest Territories, Canada. Geological Survey of Canada Bulletin 585.
Davie, M.K., Buffett, B.A., 2001. A numerical model for the formation of gas hydrate below the seafloor. Journal of Geophysical Research 106, 497–514.
Dawe, R.A., Wheat, M.R., Bidner, M.S., 1992. Experimental investigation of capillary pressure effects on immiscible displacement in lensed and layered porous media. Transp Porous Med 7, 83–101.
Dickens, G.R., 2003. Rethinking the global carbon cycle with a large, dynamic and microbially mediated gas hydrate capacitor. Earth and Planetary Science Letters 213, 169–183.
Dickens, G.R., Castillo, M.M., Walker, J.C.G., 1997. A blast of gas in the latest Paleocene: Simulating first-order effects of massive dissociation of oceanic methane hydrate. Geology 25, 259.
Dickens, G.R., O'Neil, J.R., Rea, D.K., Owen, R.M., 1995. Dissociation of oceanic methane hydrate as a cause of the carbon isotope excursion at the end of the Paleocene. Paleoceanography 10, 965.
Fujii, T., Saeki, T., Kobayashi, T., Inamori, T., Hayashi, M., Takano, O., Takayama, T., Kawasaki, T., Nagakubo, S., Nakamizu, M., Yokoi, K., 2008. Resource

Assessment of Methane Hydrate in the Eastern Nankai Trough, Japan. The Offshore Technology Conference.
Garg, S.K., Pritchett, J.W., Katoh, A., Baba, K., Fujii, T., 2008. A mathematical model for the formation and dissociation of methane hydrates in the marine environment. Journal of Geophysical Research 113.
Ginsburg, G.D., 1998. Gas hydrate accumulation in deep-water marine sediments. Geological Society, London, Special Publications 137, 51–62.
Ginsburg, G.D., Soloviev, V.A., 1997. Methane migration within the submarine gas-hydrate stability zone under deep-water conditions. Marine Geology 137, 49–57.
Gudmundsson, J.., Børrehaug, A., 1996. Frozen hydrate for transport of natural gas. Presented at the 2nd International Conference on Natural Gas Hydrate, Toulouse, France.
Hadley, C., Peters, D., Vaughan, A., Bean, D., 2008. Gumusut-Kakap Project: Geohazard Characterisation and Impact on Field Development Plans. Society of Petroleum Engineers.
Hancock, S., Collett, T.., Dallimore, S.., Satoh, T., Huenges, E., Henninges, J., 2005. Overview of thermal stimulation production test results for the Japex/JNOC/GSC Mallik 5L- 38 Gas Hydrate Research Well, in: Scientific Results from Mallik 2002 Gas Hydrate Production Research Well Program, Mackenzie Delta, Northwest Territories, Canada, Geological Survey of Canada Bulletin 585.
Hancock, S., Collett, T.., Pooladi-Darvish, M., Gerami, S., Moridis, G., Okazawa, T., Osadetz, K., Dallimore, S., Weatherill, B., 2004. A preliminary investigation on the economics of onshore gas hydrate production based on the Mallik Field discovery, in: American Association of Petroleum Geologists Hedberg Conference. Presented at the Hedberg Conference, Vancouver, CA.
Handa, Y.P., 1986. Calorimetric determinations of the compositions, enthalpies of dissociation, and heat capacities in the range 85 to 270 K for clathrate hydrates of xenon and krypton. The Journal of Chemical Thermodynamics 18, 891–902.
Henry, P., Thomas, M., Clennell, M., 1999. Formation of natural gas hydrates in marine sediments 2. Thermodynamic calculations of stability conditions in porous sediments. Journal of Geophysical Research 104, 23005–23022.
Hensen, C., Wallmann, K., 2005. Methane formation at Costa Rica continental margin—constraints for gas hydrate inventories and cross-décollement fluid flow. Earth and Planetary Science Letters 236, 41–60.
Hermansson, A., Spencerguthrie, W., 2005. Frost heave and water uptake rates in silty soil subject to variable water table height during freezing. Cold Regions Science and Technology 43, 128–139.
Hilpert, M., McBride, J.F., Miller, C.T., 2000. Investigation of the residual–funicular nonwetting-phase-saturation relation. Advances in Water Resources 24, 157–177.
Holland, M., Schultheiss, P., Roberts, J., Druce, M., 2008. Observed Gas Hydrate Morphologies in Marine Sediment. Presented at the Proceedings of the 6th International Conference on Gas Hydrates (ICGH 2008), Vancouver, British Columbia, CANADA.

Howe, S.., 2004. Production modeling and economic evaluation of a potential gas hydrate pilot production program on the North Slope of Alaska (MS Thesis).
Huang, E.T.S., Swift, G.W., Kurata, F., 1966. Viscosities of methane and propane at low temperatures and high pressures. AIChE J. 12, 932–936.
Hunter, R., Collett, T., Patil, S., Casavant, R., Mroz, T., 2004. Characterization, appraisal, and economic viability of Alaska North Slope gas hydrate accumulations. Presented at the AAPG Hedberg Conference, Vancouver, Canada.
Hunter, R.B., Collett, T.S., Boswell, R., Anderson, B.J., Digert, S.A., Pospisil, G., Baker, R., Weeks, M., 2011. Mount Elbert Gas Hydrate Stratigraphic Test Well, Alaska North Slope: Overview of scientific and technical program. Marine and Petroleum Geology 28, 295–310.
Hyndman, R.D., Davis, E.E., 1992. A Mechanism for the Formation of Methane Hydrate and Seafloor Bottom-Simulating Reflectors by Vertical Fluid Expulsion. Journal of Geophysical Research 97, 7025–7041.
Inks, T., Lee, M., Agena, W., Taylor, D., Collett, T., Hunter, R., Zyrianova, M., 2009. Seismic prospecting for gas hydrate and associated free gas prospects in the Milne Point area of northern Alaska, in: Collett, T., Johnson, A., Knapp, C., Boswell R., Eds., Natural Gas Hydrates – Energy Resource Potential and Associated Geologic Hazards. AAPG Memoir.
Iversen, N., Jorgensen, B., 1993. Diffusion coefficients of sulfate and methane in marine sediments: Influence of porosity. Geochimica et Cosmochimica Acta 57, 571–578.
Jho, C., Nealon, D., Shogbola, S., King, A.D., 1978. Effect of pressure on the surface tension of water: Adsorption of hydrocarbon gases and carbon dioxide on water at temperatures between 0 and 50UC. Journal of Colloid and Interface Science 65, 141–154.
Kaiho, K., Arinobu, T., Ishiwatari, R., Morgans, H.E.G., Okada, H., Takeda, N., Tazaki, K., Zhou, G., Kajiwara, Y., Matsumoto, R., Hirai, A., Niitsuma, N., Wada, H., 1996. Latest Paleocene benthic foraminiferal extinction and environmental changes at Tawanui, New Zealand. Paleoceanography 11, 447.
Kennett, J.P., Cannariato, K.., Hendy, I.., Behl, R.., 2003. Methane hydrates in Quaternary climate change : the clathrate gun hypothesis. American Geophysical Union, Washington, DC.
Kim, H.C., Bishnoi, P.R., Heidemann, R.A., Rizvi, S.S.H., 1987. Kinetics of methane hydrate decomposition. Chemical Engineering Science 42, 1645–1653.
Klauda, J.B., Sandler, S.I., 2003. Predictions of gas hydrate phase equilibria and amounts in natural sediment porous media. Marine and Petroleum Geology 20, 459–470.
Kleinberg, R.L., Flaum, C., Griffin, D.D., Brewer, P.G., Malby, G.E., Yesinowski, J.P., 2003. Deep sea NMR: Methane hydrate growth habit in porous media and its relationship to hydraulic permeability, deposit accumulation, and submarine slope stability. J. Geophys. Res. 108.

Koh, C., Westacott, R.., Zhang, W., Hirachand, K., Creek, J.., Soper, A.., 2002. Mechanisms of gas hydrate formation and inhibition. Fluid Phase Equilibria 194-197, 143–151.

Kurihara, M., Funatsu, K., Ouchi, H., Masuda, Y., Yasuda, M., Yamamoto, K., Numasawa, M., Fujii, T., Narita, H., Dallimore, S.., Wright, J.., 2008. Analysis of the JOGMEC/NRCan/Aurora Mallik gas hydrate production test through numerical simulation, in: 6th International Conference on Gas Hydrates (ICGH 2008). Presented at the Proceedings of the 6th International Conference on Gas Hydrates (ICGH 2008), Vancouver, British Columbia, CANADA.

Kvenvolden, K., 1988. Methane hydrate — A major reservoir of carbon in the shallow geosphere? Chemical Geology 71, 41–51.

Lee, J.Y., Ryu, B.J., Yun, T.S., Lee, J., Cho, G.-C., 2011. Review on the gas hydrate development and production as a new energy resource. KSCE J Civ Eng 15, 689–696.

Lee, M.W., Collett, T., 2011. In-situ gas hydrate saturation estimated from various well logs at the Mount Elbert Gas Hydrate Stratigraphic Test Well, Alaska North Slope. Marine and Petroleum Geology 28, 439–449.

Lee, M.W., Collett, T.S., 2009. Gas hydrate saturations estimated from fractured reservoir at Site NGHP-01-10, Krishna-Godavari Basin, India. J. Geophys. Res. 114, B07102.

Liu, X., Flemings, P., 2006. Passing gas through the hydrate stability zone at southern Hydrate Ridge, offshore Oregon. Earth and Planetary Science Letters 241, 211–226.

Liu, X., Flemings, P.B., 2007. Dynamic multiphase flow model of hydrate formation in marine sediments. J. Geophys. Res. 112.

Lund, P.C., Shindo, Y., Fujioka, Y., Komiyama, H., 1994. Study of the pseudo-steady-state kinetics of CO2 hydrate formation and stability. International Journal of Chemical Kinetics 26, 289–297.

Majorowicz, J.A., Osadetz, K., Safanda, J., 2008. Modeling temperature profiles considering the latent heat of physical-chemical reactions in permafrost and gas hydrates: The Mackenzie Delta terrestrial case, in: Ninth International Conference on Permafrost. Fairbanks, Alaska USA, pp. 1113–1118.

Maslin, M., Owen, M., Betts, R., Day, S., Dunkley Jones, T., Ridgwell, A., 2010. Gas hydrates: past and future geohazard? Philosophical Transactions of the Royal Society A: Mathematical, Physical and Engineering Sciences 368, 2369–2393.

Mason, G., Mellor, D.W., 1995. Simulation of Drainage and Imbibition in a Random Packing of Equal Spheres. Journal of Colloid and Interface Science 176, 214–225.

Mehta, A.P., Hebert, P.B., Cadena, E.R., Weatherman, J.P., 2003. Fulfilling the Promise of Low-Dosage Hydrate Inhibitors: Journey From Academic Curiosity to Successful Field Implementation. SPE Production & Facilities 18.

Milkov, A.V., 2004. Global estimates of hydrate-bound gas in marine sediments: how much is really out there? Earth-Science Reviews 66, 183–197.

Milkov, A.V., Sassen, R., 2002. Resource and economic potential of gas hydrates in the northwestern gulf of Mexico, in: 4th International Conference Gas Hydrates. Presented at the 4th International Conference Gas Hydrates, pp. 111–114.
Milkov, A.V., Xu, W., 2005. Comment on "Gas hydrate growth, methane transport, and chloride enrichment at the southern summit of Hydrate Ridge, Cascadia margin off Oregon" by Torres et al. [Earth Planet. Sci. Lett. 226 (2004) 225–241]. Earth and Planetary Science Letters 239, 162–167.
Moridis, G.J., 2003. Numerical Studies of Gas Production From Methane Hydrates. SPE Journal 8.
Moridis, G.J., Collett, T.S., Dallimore, S.R., Satoh, T., Hancock, S., Weatherill, B., 2004. Numerical studies of gas production from several CH4 hydrate zones at the Mallik site, Mackenzie Delta, Canada. Journal of Petroleum Science and Engineering 43, 219–238.
Odong, J., 2008. Evaluation of Empirical Formulae for Determination of Hydraulic Conductivity based on Grain-Size Analysis. The Journal of American Science 4, 1–6.
Osadetz, K.., Chen, Z., 2004. Progress toward a petroleum system approach to gas hydrate resource assessment. Presented at the AAPG Hedberg Conference, Vancouver, Canada.
Peng, Y., Prodanovic, M., Bryant, S.L., 2009. Improving Fidelity of Network Models for Drainage and Imbibition, in: Proceedings of SPE Annual Technical Conference and Exhibition. Presented at the SPE Annual Technical Conference and Exhibition.
Penner, E., 1959. The mechanism of frost heaving in soils. BULLETIN of HIGHWAY RESEARCH BOARD 225, 1–22.
Rees, E.V.L., Priest, J.A., Clayton, C.R.I., 2011. The structure of methane gas hydrate bearing sediments from the Krishna–Godavari Basin as seen from Micro-CT scanning. Marine and Petroleum Geology 28, 1283–1293.
Rempel, A.W., Buffett, B.A., 1997. Formation and accumulation of gas hydrate in porous media. J. Geophys. Res. 102, 10151–10164.
Ripmeester, J.A., Ratcliffe, C.I., 1988. Low-temperature cross-polarization/magic angle spinning 13C NMR of solid methane hydrates: Structure, cage occupancy, and hydration number. J. Phys. Chem. 92, 337–339.
Rose, K., Boswell, R., Collett, T., 2011. Mount Elbert Gas Hydrate Stratigraphic Test Well, Alaska North Slope: Coring operations, core sedimentology, and lithostratigraphy. Marine and Petroleum Geology 28, 311–331.
Ruppel, C., 2011. Methane Hydrates and the Future of Natural Gas (No. Supplementary Paper 4), Gas Hydrates Project. U.S. Geological Survey, Woods Hole, MA.
Schoderbek, D., Boswell, R., 2011. Ignik Sikumi #1, gas hydrate test well, successfully installed on the Alaska North Slope (No. 11(1)), Fire in the Ice. US Department of Energy, Office of Fossil Energy, National Energy Technology Laboratory.
Seol, Y., Kneafsey, T.., 2008. Fluid flow through heterogeneous methane hydrate-bearing sand: Observations using x-ray CT scanning, in: 6th International Conference on

Gas Hydrates (ICGH 2008). Presented at the Proceedings of the 6th International Conference on Gas Hydrates (ICGH 2008), Vancouver, British Columbia, CANADA.
Shindo, Y., Lund, P.C., Fujioka, Y., Komiyama, H., 1993. Kinetics of formation of CO2 hydrate. Energy Conversion and Management 34, 1073–1079.
Sloan, E., 1998. Clathrate hydrates of natural gases, 2nd ed., rev. and expanded. ed. Marcel Dekker, New York.
Sloan, E.D., 2000. Hydrate Engineering. Society of Petroleum Engineers, Richardson, Tex.
Sloan, E.D., 2003. Fundamental principles and applications of natural gas hydrates. Nature 426, 353–363.
Soloviev, V., Ginsburg, G., Telepnevm, E., Mikhailyk, Y., 1987. Cryogeothermy and Natural Gas Hydrates of the Arctic Ocean Sediments. Ministry of Geology USSR, Leningrad.
Spangenberg, E., 2001. Modeling of the influence of gas hydrate content on the electrical properties of porous sediments. J. Geophys. Res. 106, 6535–6548.
Stanley, E.M., Batten, R.C., 1969. Viscosity of water at high pressures and moderate temperatures. J. Phys. Chem. 73, 1187–1191.
Takahisa, I., 2005. Overview of production test results for the Mallik 2002 gas hydrate production research well program. J. Japan Inst. Energy 84, 106–111.
Teng, H., Yamasaki, A., Shindo, Y., 1996. Stability of the hydrate layer formed on the surface of a CO2 droplet in high-pressure, low-temperature water. Chemical Engineering Science 51, 4979–4986.
Tohidi, B., Anderson, R., Clennell, B.M., Burgass, R.W., Biderkab, A.., 2001. Visual observation of gas-hydrate formation and dissociation in synthetic porous media by means of glass micromodels. Geology 29, 867–870.
Torres, M.E., Collett, T.S., Rose, K.K., Sample, J.C., Agena, W.F., Rosenbaum, E.J., 2011. Pore fluid geochemistry from the Mount Elbert Gas Hydrate Stratigraphic Test Well, Alaska North Slope. Marine and Petroleum Geology 28, 332–342.
Torres, M.E., Wallmann, K., Tréhu, A.M., Bohrmann, G., Borowski, W.S., Tomaru, H., 2004. Gas hydrate growth, methane transport, and chloride enrichment at the southern summit of Hydrate Ridge, Cascadia margin off Oregon. Earth and Planetary Science Letters 226, 225–241.
Tréhu, A.M., Flemings, P.B., Liu, C.-S., Liu, X., Riedel, M., Torres, M., 2004. Feeding methane vents and gas hydrate deposits at south Hydrate Ridge. Geophysical Research Letters 31.
Waite, W.F., Santamarina, J.C., Cortes, D.D., Dugan, B., Espinoza, D.N., Germaine, J., Jang, J., Jung, J.W., Kneafsey, T.J., Shin, H., Soga, K., Winters, W.J., Yun, T.-S., 2009. Physical properties of hydrate-bearing sediments. Rev. Geophys. 47.
Winters, W., Walker, M., Hunter, R., Collett, T., Boswell, R., Rose, K., Waite, W., Torres, M., Patil, S., Dandekar, A., 2011. Physical properties of sediment from the Mount Elbert Gas Hydrate Stratigraphic Test Well, Alaska North Slope. Marine and Petroleum Geology 28, 361–380.

Xu, W., Ruppel, C., 1999. Predicting the occurrence, distribution, and evolution of methane gas hydrate in porous marine sediments. Journal of Geophysical Research 104, 5081–5095.

Vita

Javad Behseresht earned his undergraduate degrees, B.Sc. degrees in Electrical Engineering and Petroleum Engineering, from Sharif University of Technology in May 2006. He then started his graduate studies in Petroleum and Geosystems Engineering Department at the University of Texas at Austin and earned a M.Sc. degree in Petroleum Engineering in 2008. In 2009 he started his Ph.D. on the formation of terrestrial natural gas hydrate prospects with the focus on the effects of multiphase flow and sedimentology on hydrate saturation distribution in the subsurface. Javad is the author of more than ten technical articles and has served as reviewer for several technical journals. He is recipient of research and presentation awards and has held offices in student organizations at the University of Texas at Austin. His research interests include multiphase flow in porous media (micro-scale and field scale), petrophysics, reservoir engineering, and gas hydrate reservoirs as energy resources.

Email: jbehseresht@utexas.edu

This dissertation was typed by the author.